Charles University in Prague
Faculty of Mathematics and Physics

HABILITATION THESIS

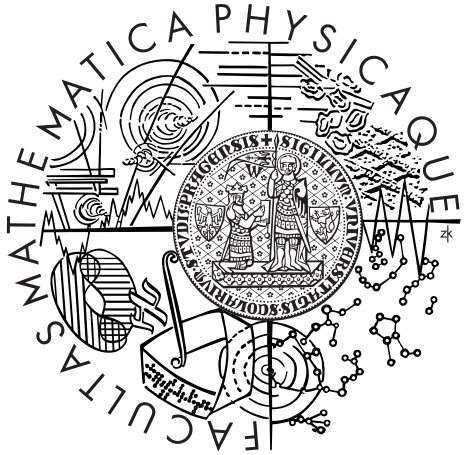

Jiří Pavlů

Interaction of space environment with dust grains: experimental and numerical simulations

Department of Surface and Plasma Science

Physics — Physics of Plasmas

Prague 2016

Many thanks belong to my colleagues and family.

„Co jste vlastně proti vesmíru, když považíte, že nejbližší nám stálice je od tohoto vojenského vlaku vzdálena 275 000krát, než je Slunce, aby její paralaxa tvořila jednu obloukovou vteřinu. Kdyby vy jste se nacházel ve vesmíru jako stálice, byl byste rozhodně příliš nepatrným, aby vás mohly postřehnout nejlepší hvězdářské přístroje. Pro vaši nepatrnost ve vesmíru není pojmu. Za půl roku udělal byste na obloze takový maličký oblouček, za rok maličkou elipsu, pro vyjádření kteréž číslicemi není vůbec pojmu, jak je nepatrná. Vaše paralaxa byla by neměřitelnou.“

(Jaroslav Hašek — Osudy dobrého vojáka Švejka za světové války)

Contents

Preface **3**

1 Introduction **5**
- 1.1 Dust in Space . . . 5
- 1.2 Dust in Laboratory . . . 5
- 1.3 Dust Charge . . . 6
- 1.4 Laboratory Observations . . . 7

2 Experimental Facilities **9**
- 2.1 3D Quadrupole Trap . . . 9
- 2.2 Linear Quadrupole With Three Orthogonal Fields . . . 10
- 2.3 Measurement Techniques . . . 11

3 Dust Charging Studies **13**
- 3.1 Fundamental Processes . . . 13
  - 3.1.1 Photoemission . . . 13
  - 3.1.2 Secondary Electron Emission — Experiment . . . 14
  - 3.1.3 Secondary Electron Emission — Model . . . 15
  - 3.1.4 Ion Interactions . . . 17
- 3.2 Applications . . . 20
  - 3.2.1 Lunar Surface . . . 20
  - 3.2.2 Martian Atmosphere . . . 22
  - 3.2.3 Icy Satellites of Saturn . . . 23
  - 3.2.4 Tokamak . . . 23

4 Concluding Remarks **27**

References **29**

Appendices **37**

A Pavlů et al. [2004] **39**

B Beránek et al. [2012] **47**

C Nouzák et al. [2016] **57**

D Pavlů et al. [2009] **67**

E Pavlů et al. [2008] **87**

F Richterová et al. [2006] **107**

G Richterová et al. [2012] **117**

H Richterová et al. [2016] **125**

I Pavlů et al. [2007] **135**

J Beránek et al. [2010] **143**

K Němeček et al. [2011] **151**

L Vaverka et al. [2013] **161**

M Pavlů et al. [2014] **169**

N Richterová et al. [2011] **183**

O Vaverka et al. [2014] **191**

Preface

THE THESIS surveys our progress in laboratory experiments and numerical simulations in which I've been involved over the last ten years. The work is devoted to experiments on single dust grains caught in electrodynamic traps, where particular charging processes can be observed separately. Such a unique approach brings attainments and fine details that cannot be easily seen by other facilities. We focus our study to the basic understanding of charging processes that are evoked by particle (no matter which) impacts. Materials of interest are often insulators and other space-related substances. The focus is split into three domains:

1. development and construction of the technical equipment and experimental techniques — outlined in section 2 and in Pavlů et al. [2004, Appendix A] and Beránek et al. [2012, Appendix B],

2. study of particular dust–particle interactions (that includes all kinds of charging processes, ion sputtering, neutral diffusion, surface and structural modifications, etc.) — referred in sections 3.1 and in Nouzák et al. [2016, Appendix C], Pavlů et al. [2009, Appendix D], Pavlů et al. [2008, Appendix E], Richterová et al. [2006, Appendix F], Richterová et al. [2012, Appendix G], Richterová et al. [2016, Appendix H], Pavlů et al. [2007, Appendix I], and Beránek et al. [2010, Appendix J],

3. application of our knowledge on particular processes (and their combination complemented with numerical simulations) to real plasma environments — mentioned in sections 3.2 and in Němeček et al. [2011, Appendix K], Vaverka et al. [2013, Appendix L], Pavlů et al. [2014, Appendix M], Richterová et al. [2011, Appendix N], and Vaverka et al. [2014, Appendix O].

The research included in this thesis was in course of time supported by Ministry of Education Research Plan MSM 0021620834, Czech Science Foundation projects 202/04/0912, 202/08/P066, 202/08/0063, 209/11/1412, and 16-05762S, and finally, by Charles University in Prague through various projects. We greatly acknowledge all funders.

1. Introduction

SPACE (COSMIC) DUST is present across the whole universe. It is generally small object having a few molecules up to about millimeter in size. Stardust is a small fraction that consists of larger refractory minerals that condensed as matter left the stars. Cosmic dust can be also distinguished by its location: intergalactic, interstellar, interplanetary (such as in the zodiacal cloud), and circumplanetary dust (such as in a planetary ring). Solar system dust origins are mostly comets, asteroids, Kuiper belt, and also interstellar dust passing through the solar system. Zook [2001] estimated that as much as 40 000 tons of cosmic dust reach the Earth's surface every year.

In the past, the dust annoyed astronomers, as it obscures objects they are observing. With growth od infrared astronomy, those dust particles were observed to be a significant part of astrophysical processes. Similarly, in the laboratory plasma, the dust was often considered as an unwanted rubbish. Last several decades brought up the attention to the so-called "complex plasmas" (also referred as "dusty plasmas") where dust grains play a role of the third plasma constituent.

1.1 Dust in Space

Dust plays an important role in the overall scenario of structure and evolution of the universe. It's generally agreed that dust is present from almost the beginning of the universe to present time. Dust is at the center of all important events there, influences thermal, dynamical, ionization, and chemical states of matter of the interstellar and also intergalactic medium. Since the dust grains are effective absorbers of radiation (shielding each other), they often form low-temperature clouds serving as small chemical laboratories in outer space. While optical properties are most important for studies of dust clouds far beyond the solar system, the dust within the reach of the Sun (and thus within the influence of the solar wind) is located inside plasma, therefore its electrical charge plays a key role.

Various space missions have been conducted to sound and to investigate the composition, size distribution, and structural characteristics of interstellar and interplanetary dust, such as Ulysses, Cassini, and Galileo [Altobelli et al., 2003, Krüger et al., 2010a,b]. The dust grains provide an excellent window into interstellar and interplanetary processes, carry information on the origin and evolution of their parent bodies, and reveal the intrinsic properties of the environments where these grains were born. *In situ* measurements also provide opportunities to test and to validate various theories related to cosmic dust.

1.2 Dust in Laboratory

Dust grains immersed in ionized media acquire charges whose signs and magnitudes strongly affect the properties of the surrounding plasma as well as of the ensemble of dust grains itself. The various crystalline and liquid phases of dust grains found in special laboratory experiments are the most important manifestations of this effect [Fortov et al., 2005, Ishihara, 2007, Ivlev et al., 2015]. The fact that dust grains and plasma are significantly coupled is known for a long time. Not only from astrophysical plasma environments [Horanyi, 1996, Mann, 2008, Sakai et al., 2013] but also from processing discharges, where the grains are not the intentional constituents studied for their properties but contaminants which need to be controlled because

they are detrimental to the performance of the discharge [Bouchoule, 1999, Smirnov et al., 2015].

1.3 Dust Charge

Since the charge acquired by a dust grain is an important parameter, it has been measured in a number of experiments [Melzer et al., 1994, Trottenberg et al., 1995, Walch et al., 1995, Tomme et al., 2000a,b, Samarian and Vladimirov, 2003, Khrapak et al., 2005, Lisin et al., 2012, and many others]. The dust grain is often considered being a electric probe and thus reaches the floating potential. For a spherical particle it can be immediately translated into a charge. In the most cases, however, the charges calculated using this approach are not in agreements with experimental data [e.g., Bronold et al., 2009].

Similarly, any unprotected surface in the space charges in response to incident currents, reaching a floating potential with respect to the surrounding plasma such that positive and negative currents to the surface balance [Whipple, 1981]. Typically, currents from lighter and faster electrons dominate over ion currents, acting to drive the surface negative, while photoelectron and secondary electron emission currents tend to charge the surface/grain positively [Halekas et al., 2009]. For example, on the Moon sunward side photoemission usually dominates, leading to a small positive potential. On the other hand, in a lunar shadow, depending on the secondary electron yield, surfaces can reach either positive or negative charges [e.g., Vaverka et al., 2013, Appendix L]. Further complicating this environment, although less understood, is an effect of the presence of surface relief, typically in the form of craters and/or boulders. It has been suggested that such non-trivial surface topography can lead to complex electrostatic potentials and fields, including "mini-wakes" behind small obstacles to the solar wind flow and "supercharging" near sunlit-shadow boundaries [Poppe et al., 2012]. The knowledge of electric fields and dust charge near the surface may have important implications for robotic and human explorations of the Moon and for forming of dust ponds on various asteroids [Stubbs et al., 2007].

As it was already mentioned, photoemission is one of the most important positive currents. Although it was widely studied on metals and semiconductors, it lacks observations for dielectrics and especially rather small samples. For its description, one would usually need only the work function of a given material and knowledge of photoelectron spectra but both remain generally unknown for space-related materials. Thus, half-empirical formulas are often used [Ma et al., 2013] for setting these constants in space-like simulations. Light absorption and reflection (complex refractive index or dielectric constant) for various wavelengths depend not only on the material itself but also on the shape and size of an object. Although there was a number of theoretical and numerical attempts in order to describe and to simulate light scattering from arbitrary shaped space-related grains [e.g., Kolokolova et al., 2006, Zubko et al., 2009, 2013], the laboratory experiments are rare.

Although the spherical grain shape is widely used for simulations, there is an evidence which suggests that many grains in astrophysical environments are irregularly shaped aggregates. Recent studies have shown that aggregates acquire higher charge-to-mass ratios due to their complex structures, which in turn may alter their subsequent dynamics and evolution [Wiese et al., 2010, Okuzumi et al., 2011, Ilgner, 2012]. However, the study of complex shapes numerically is rather difficult and it opens a playground for experiments.

1.4 Laboratory Observations

In this context, laboratory experiments bring a new approach to this field because the investigations of individual grains in equilibrium or steady state may provide their electrical and optical parameters and may separate particular processes.

Several laboratory experiments have been focused on various aspects of grain charging. Suszcynsky et al. [1992] measured secondary electron yields from ammonia and methanol ices as a function of the electron beam energy in the energy range of 2–30 keV and summarized that secondary electron yields are at the low end of the range for insulators. Barkan et al. [1994] studied charging of micron-sized dust grains dispersed into a fully ionized, magnetized plasma and found that the charge on a dust grain in a dense dust cloud can be substantially reduced with respect to the charge on an isolated grain. Walch et al. [1994, 1995] measured the charge on small grains of different non-conducting materials in a plasma containing both thermal and suprathermal electrons. Sickafoose et al. [2001] studied the photoemission and triboelectric charging of single dust grains levitating upon the metal surface. They have shown that triboelectric charging may be the dominant charging process for silicate planetary regolith analogs and thus it will play an important role in the subsequent behavior of dust grains released from planetary surfaces.

A technique developed in the 1950s for ion spectroscopy [Paul and Steinwedel, 1956], generally referred to as a quadrupole trap, has been successfully employed for the investigation of single micron-sized grains [Wuerker et al., 1959]. Using this technique, photoemission experiments with the UV radiation [Abbas et al., 2003], secondary electron emission experiments [e.g., Spann et al., 2001], and rotation and alignment of dust grains by the radiation [Abbas et al., 2004, Kane, 2010] have been performed. A similar technique was used in laboratory experiments where micron-sized grains bombarded by keV electrons were stored and a size dependence (observed by Švestka et al. [1993] and qualitatively explained by Chow et al. [1994]) was identified. Quadrupole traps were also used for studying ensembles of dust [e.g., Vasilyak et al., 2013].

Čermák et al. [1995] applied an electrodynamic quadrupole inside an ultra-high vacuum chamber to trap grains of micron and submicron sizes which were charged by electron and ion beams of energies up to 5 keV. The authors developed a new method for determination of the dust grain size, surface potential, and electric field strength, and they measured the effects of electron and ion beam energies on the dust surface potential. They obtained energy spectrum of emitted secondary electrons and estimated the yield of the secondary electron emission. In last ten years, the experimental set-up was further gradually extended [Žilavý et al., 1998, Čermák et al., 2004, Pavlů et al., 2004, Appendix A] and used to study different kinds of charging processes in well-defined laboratory conditions.

2. Experimental Facilities

AFOREMENTIONED INVESTIGATIONS are based on two laboratory set-ups where a single dust grain levitates in traps — both are based on the quadrupole trap principle. The first is a standard 3D quadrupole as originally designed by Paul and Steinwedel [1956], the geometry of the second reminds the linear quadrupole filter. Its electrodes are split and the applied voltages are combined in such a way that they form three independent quadrupole fields that together create the trap. The main advantage of the latter trap is a wider space between electrodes allowing of use of the UV light source. Furthermore, observations from different angles and accessing the trapping area with another instruments are much easier.

2.1 3D Quadrupole Trap

The electrodynamic quadrupole together with the dust reservoir are placed inside an ultra-high vacuum chamber [pressure in the chamber is less than 10^{-8} mbar, Pavlů et al., 2004, Appendix A]. The quadrupole is supplied symmetrically, i.e., there is zero potential in the middle of the trap. The quadrupole theory gives the vertical electrodes supplied by the same voltage. However, we are using two different amplifiers for them in order to apply a dumping voltage and DC voltage for the compensation of gravity. The scheme of the experiment is depicted in Figure 2.1.

A trapped grain is irradiated by a laser beam modulated by 10 kHz. The scattered

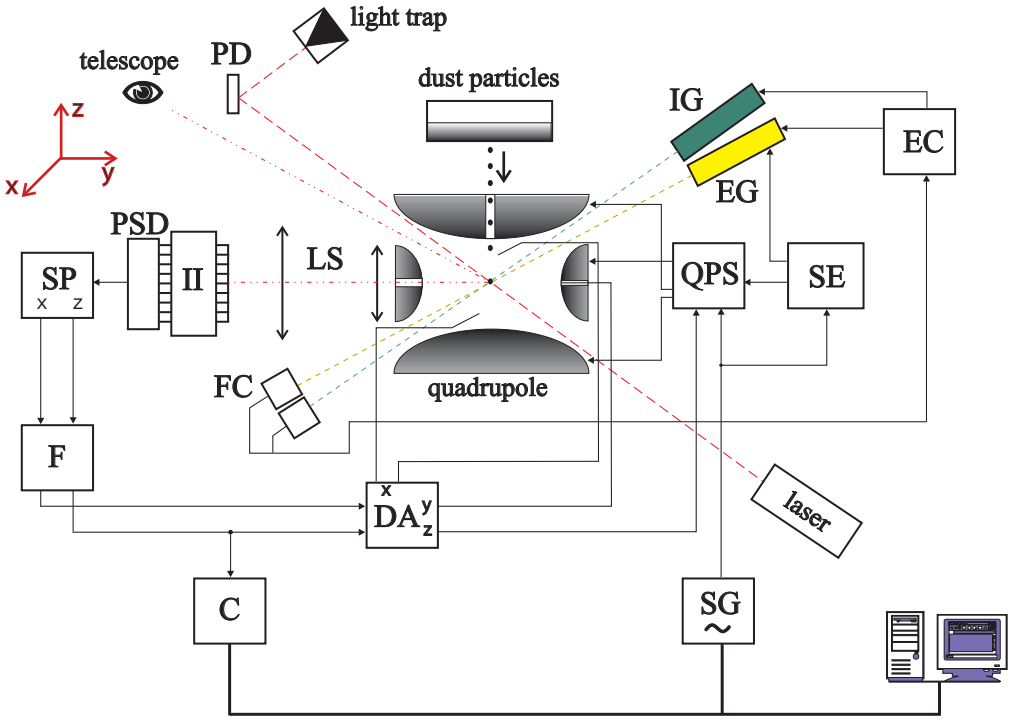

Figure 2.1: Experimental set-up of 3D quadrupole trap: C — counter, DA — damping amplifier, EC — emissivity control, EG — electron gun, FC — Faraday cups, F — filter, IG — ion gun, II — image intensifier, LS — lens system, M — acousto-optical modulator, PD — photodiode, PSD — position sensitive detector, QPS — quadrupole power supply, SE — sampling electronics, SG — signal generator, SP — signal processing.

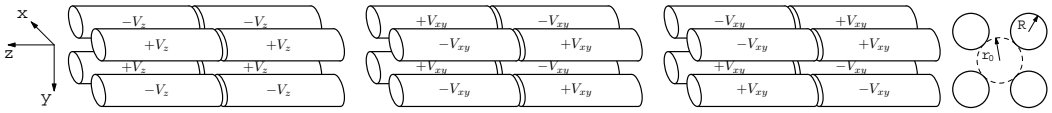

Figure 2.2: Sketch of the voltages on electrodes forming the electric potential of a linear trap. The voltage applied on a particular segment of the rod is a sum of partial voltages shown in the figure. Adopted from Beránek et al. [2012, Appendix B].

light is collected by a simple lens system and the magnified grain image is projected onto the entrance fiber optic of an image intensifier. The intensifier output is optically coupled to a PIN diode serving as a position sensitive detector. Signals from the PIN diode are amplified by narrow-band and lock-in amplifiers prior to the coordinates of the light spot are determined. We control the motion of the particle by a damping system. Actual charge-to-mass ratio, Q/m, is calculated from the particle secular frequency, f_z, the quadrupole supply voltage, $V_{\mathrm{ac}}^{\mathrm{eff}}$, and its frequency, f_{ac}. The Q/m is given by the expression:

$$\frac{Q}{m} = \pi^2 r_0 \frac{f_{\mathrm{ac}} f_z}{V_{\mathrm{ac}}^{\mathrm{eff}}} \cdot c(f_z, f_{\mathrm{ac}}), \tag{2.1}$$

where r_0 stands for the inner radius of the middle quadrupole electrode and c is a correction function close to unity which reflects the $f_{\mathrm{z}}/f_{\mathrm{ac}}$ ratio and actual field geometry inside the trap.

2.2 Linear Quadrupole With Three Orthogonal Fields

This experiment differs from the previous mainly in the geometry of the trap. Except that, the rest of the equipment is very similar, thus, we will further focus on the trap principle only.

The design originated in the classical (four-rod) linear quadrupole in which we split each electrode into two parts with a small insulating gap in between. The idea of the trap is based on a superposition of three AC quadrupole fields. Figure 2.2 schematically demonstrates the voltages providing three quadrupole fields. If we neglect the insulating gap, the voltages $\pm V_z$ shown in the left part of the figure will create the quadrupole field in the plane $z = 0$ because this is a standard linear quadrupole. The middle and right panels show the potentials creating the quadrupole fields in planes $x = 0$ and $y = 0$, respectively. We would like to note that we expect the same frequency and zero phase shift of both V_z and V_{xy}. The voltage applied onto the particular electrode is a sum of partial voltages shown in Fig. 2.2. The simplified view suggests that only three different HV supplies (amplifiers) can be used. This is true for the grain confinement but additional requirements like a compensation of the gravity force or damping of the grain oscillation amplitude lead to a requirement of a dedicated supply for each half-rod.

The voltage supplying the trap maintains the central symmetry (the voltage on the electrodes and the potential inside the trap does not change if we invert the coordinates). The lowest multipole term that such field can form is the quadrupole term. The electric potential φ inside the trap is a result of superposition of three partial potentials generated by an alternating voltages of amplitude V_z and V_{xy} applied to the rods according to Fig. 2.2. The resulting electric field does not change the sign if we invert direction of the z axis but changes the sign if the direction of any of remaining two axes is inverted. Therefore, the only possible quadrupole term is proportional to xy. The quadrupole term does not depend explicitly on the rod radius R in this approximation. The exact solution of the potential inside the trap [Beránek et al., 2007]

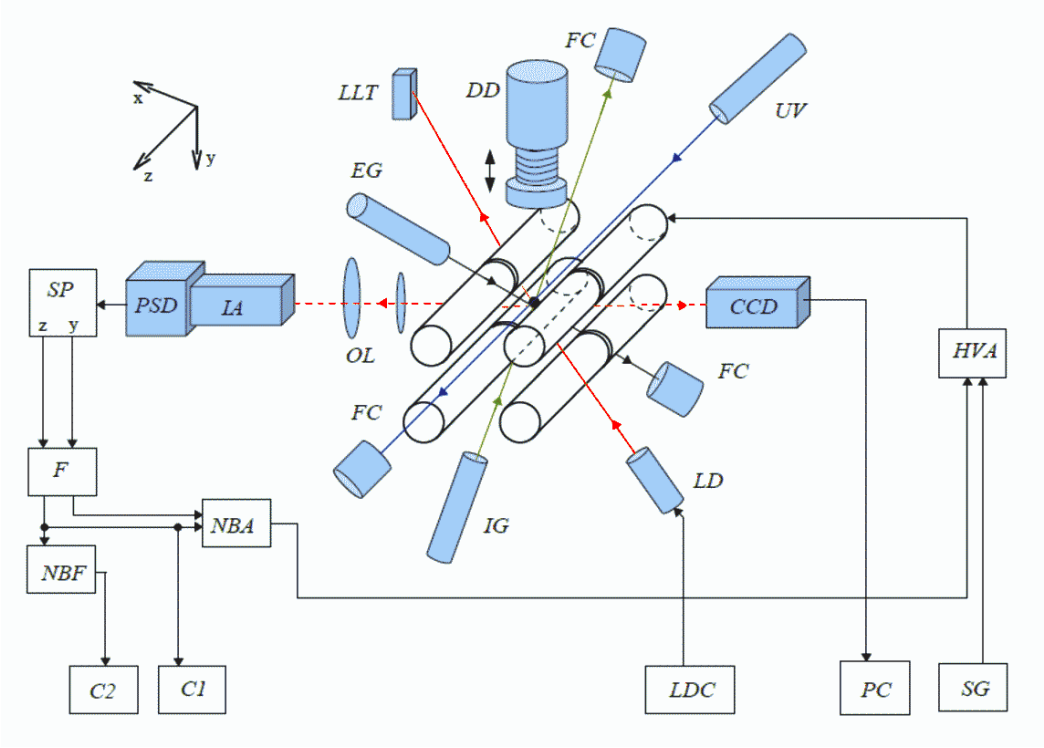

Figure 2.3: The scheme of the linear quadrupole trap with 3 orthogonal fields: C1,C2 — counters, CCD — camera, DD — dust dropper EG — electron gun, FC — Faraday cup, F — filter, HVA — high-voltage amplifiers, IA — image amplifier, IG — ion gun, LDC — laser diode controller, LD — laser diode, LLT — laser light trap, NBA — narrow band amplifier, NBF — narrow band filter, OL — lenses, PC — computer PSD — position sensitive detector, SG — signal generator, SP — signal processing, UV — discharge UV lamp.

shows that the geometric factor weakly depends on the ratio R/r_0 that determines the content of higher multipole terms. Finally, we can state the equation 2.1 applies similarly (up to the constant) in this case, too [see Beránek et al., 2012, Appendix B, for details]. As mentioned before, the scheme of this experiment is similar — compare Figures 2.1 and 2.3.

2.3 Measurement Techniques

Both experiments are equipped with a reservoir of dust grains that are falling through the trap, then the grain is charged by the electron or ion beams from the respective gun. If the grain is trapped, it oscillates with a frequency proportional to its charge-to-mass ratio. The grain is illuminated by a red laser, the scattered light is amplified and processed in order to determine the frequency of grain oscillations. This frequency is measured by a sophisticated system controlled by the computer which then provides the specific charge, Q/m of the grain as a result. Since Q/m is important but insufficient for the complete description of charging processes, we developed some techniques to measure the actual surface potential (i.e., the grain electrical capacitance) and the mass of the grain (by a variation of the Millikan oil-drop experiment). Then, we can calculate all important quantities describing the charging/discharging processes, i.e., currents and the electric field as well as material constants.

The detail description of our set-up including its gradual extension and descriptions of aforementioned techniques was given by Čermák [1994], Čermák et al. [1995], Žilavý et al. [1998], and Pavlů et al. [2004, Appendix A]. The second trap with a new design was described by Beránek et al. [2007, 2012, Appendix B].

3. Dust Charging Studies

THE CHARGING PROPERTIES of dust grains are studied in our laboratory for several years already. This section reports the results achieved in our group with author's contribution. The particular results are ordered rather thematically than chronologically. The first part deals with fundamental processes themselves while the second part concatenates experimental and numerical simulations of several processes in order to explain or describe phenomena at various environments.

3.1 Fundamental Processes

Dust can interact with all elementary particles — photon, electron, and ion. We will focus only on several selected processes, although their variety is much broader.

3.1.1 Photoemission

Nouzák et al. [2014] described initial observations of the photoemission from glass dust. We measured the work function of 5 μm glass grain ($W \approx 4.7$ eV) and the photoelectric yield (for HeI UV emission line), $\eta \approx 0.04$. Nouzák et al. [2016, Appendix C] studied the same phenomena on lunar soil simulants — broad variety of UV emission lines was used in this experiment. The grain was alternately charged and discharged by different photon energies (see Figure 3.1 for reference). We associated these lines with grain surface potentials and extrapolated them to zero grain potentials (i.e., work functions, see Figure 3.2). We got values of $W_{4.7\mu\mathrm{m}} = (5.9 \pm 0.3)$ eV and $W_{4.0\mu\mathrm{m}} = (5.1 \pm 0.7)$ eV, respectively. The measured grain work function is in a full accordance with the value of $W \approx 5.8$ eV obtained by Sternovsky et al. [2002] for the JSC-1 lunar regolith simulant by the contact charging method. According to theories of Brus [1983], Makov et al. [1988], the work function would depend on the curvature of the surface — this effect would be negligible for grains with a radius in the micrometer range, nevertheless, it would be seen for nanometer-sized grains. On the other hand, sharp edges that can be expected on the grain surface can lead to decrease of the measured work function.

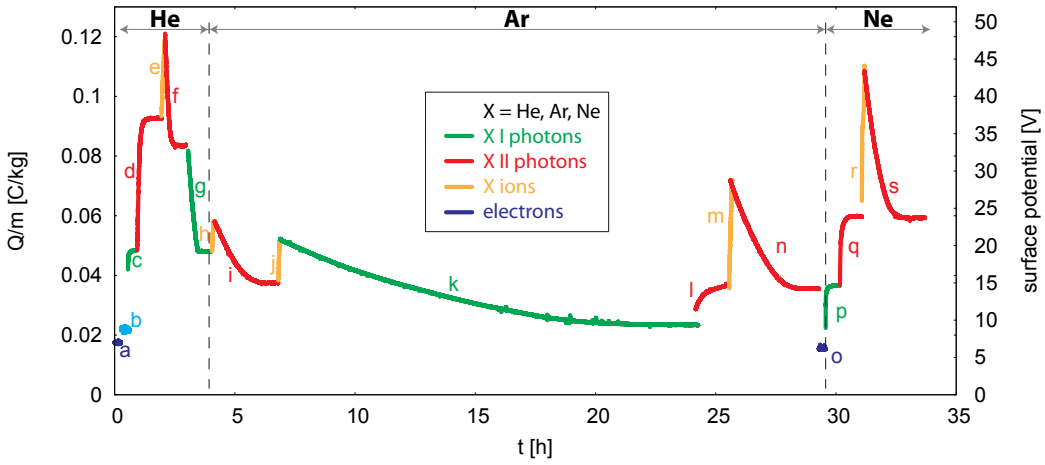

Figure 3.1: The course of the UV experiment when various gases and their emission lines were used to influence the grain charge. Adopted from Nouzák et al. [2016, Appendix C].

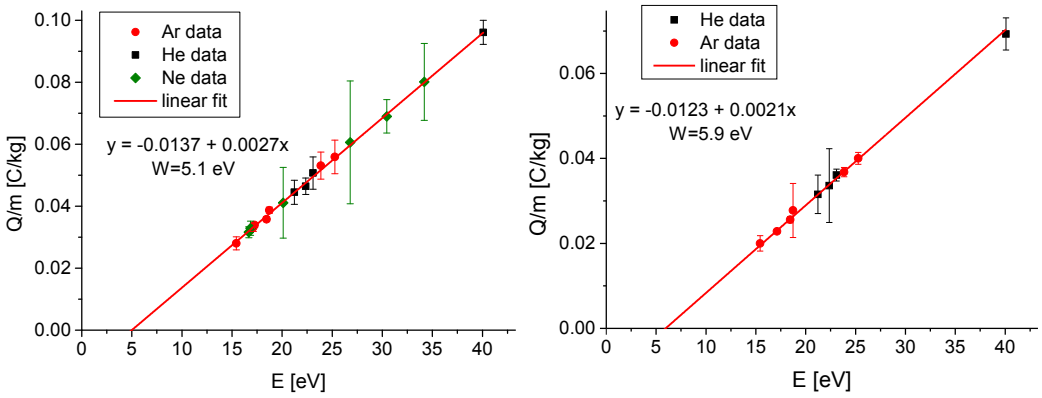

Figure 3.2: The determination of the work function for two different grains. Adopted from Nouzák et al. [2016, Appendix C].

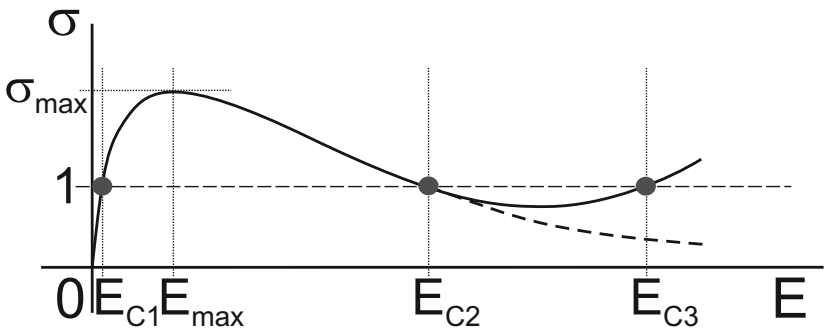

Figure 3.3: An example of electron emission yield profile as a function of the primary beam energy and an determination of parameters. The full line represents small grains and the dashed line stands for planar samples.

3.1.2 Secondary Electron Emission — Experiment

Primary electrons impacting the sample surface interact with a bulk material and they lose their energy in many types of collisions that often result in excitations of material electrons and some of them can then leave the surface. These electrons, so-called true secondary electrons, have typically energies of a few electronvolts. In the case of large planar samples, the energetic dependence of the secondary emission yield, δ, defined as the mean number of secondary electrons per one primary electron can be described by the Sternglass universal curve [Sternglass, 1951, 1957] that was later extended toward higher primary energies by Draine and Salpeter [1979]. This curve exhibits a maximum at a few tenths of kiloelectronvolts and decreases to zero at very high and low beam energies. Its parameters, the maximum yield, $\delta_{\max}$ and the corresponding energy, $E_{\max}$, depend only on a sample material at a certain incident angle. In collisions inside the target, primary electrons change their directions and thus they may be backscattered from the material before losing the whole energy. The backscattered yield, η increases with the material density and the atomic number up to ≈ 0.5 for a normal incident angle. It grows only slowly with the beam energy above a few hundreds of electronvolts. Thus, the total secondary yield σ ($\sigma = \delta + \eta$) and δ vary in a similar way with the beam energy [Bronstein and Fraiman, 1969]. Figure 3.3 depicts the typical shape of the yield dependence on the primary electron energy. The 2–3 unity points (E_{C1}, E_{C2}, and sporadic E_{C3}) show the energy when a sign of the surface potential switches, when an object is exposed to the electron beam.

In the case of grains, the energy dependence of a total secondary yield of dust

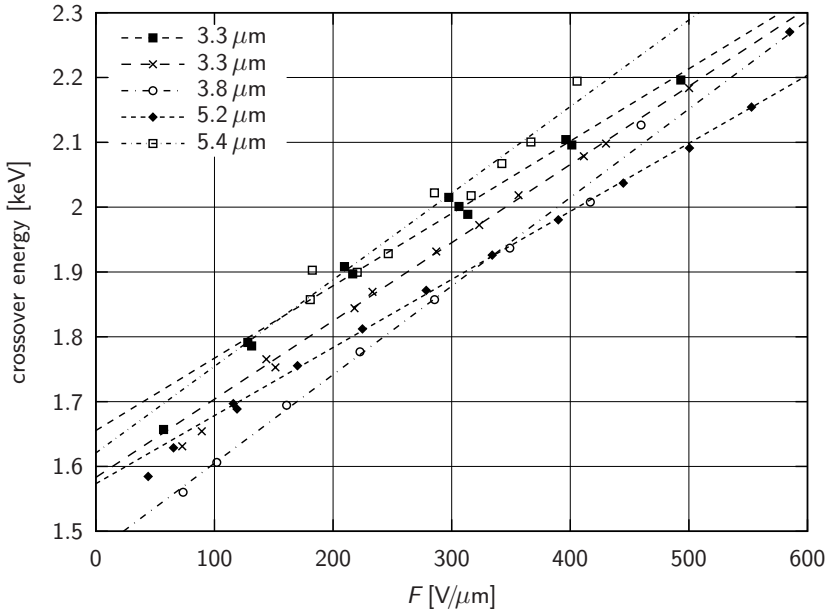

Figure 3.4: The crossover energy as a function of the surface electric field for different grain diameters. Adopted from Beránek et al. [2009].

grains does not fully follow the universal curve that was suggested for large samples. It is enhanced due to a surface curvature that results in a variation of the incident angle along the grain surface because σ (and both constituents) increases with the incident angle [Hachenberg and Brauer, 1959]. The dependence of the secondary emission yield on the incident angle was measured and fitted by different analytical expressions or simulated [Lu et al., 2005]. Since the whole grain is illuminated by the parallel electron beam in our experiment, the described angular dependence leads to an enhancement of the yield measured on the spherical grain with respect to planar samples by a factor of ≈ 1.3.

Pavlů et al. [2009, Appendix D] surveyed most of our both experimental and model results dealing with the process the of secondary electron emission. Among all, we just want to point out that we showed that the grain surface potential established by the secondary emission depends neither on the work function nor on the secondary emission yield but rises with the mean atomic number of the grain material [Pavlů et al., 2008, Appendix E]. That is non-trivial, since it is generally expected that the high yield means also the high potential which is misguiding — the point is that the important quantity is the secondary electron energy profile, not the yield. Beránek et al. [2009] observed the dependence of the secondary emission yield — a shift in the second cross-over point, i.e., unity point E_{C2} of the secondary emission yield when the yield decreases for higher electron energies — on the electric field (Figure 3.4). It seems, this field is not only fully screened by the surface electrons but penetrates deeper inside the conducting grains.

3.1.3 Secondary Electron Emission — Model

To explain the laboratory experiments, Richterová et al. [2004] developed a simple numerical model of the secondary emission from small dust grains. Since the model assumptions were very simplified, we have revisited it in order to include more complex principles of the electron-solid interaction using a well-tested Monte Carlo technique developed for scanning electron microscopy [Joy, 1995]. A new hybrid Monte Carlo

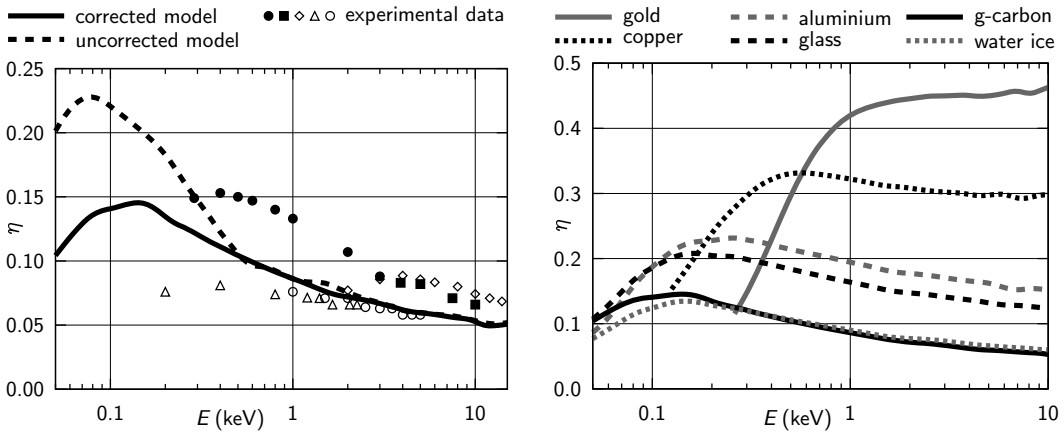

Figure 3.5: Influence of a slowing-down correction and a total elastic cross-section sampling on profiles of the modeled scattered yields, η for a normal angle of incidence and for (a) glassy carbon, and (b) other planar materials. Experimental points: • Bronstein and Fraiman [1969], ■ Hunger and Küchler [1979], ◇ Palluel [1947], △ Sternglass [1954], ○ Assad and El Gomati [1998]. Adopted from Richterová et al. [2010].

model [Richterová et al., 2006, Appendix F] shows that the increase of the grain potential occurs for grain sizes comparable to a penetration depth of primary electrons and that it is caused by a larger portion of primary electrons being scattered out of the grain. The corresponding increase of the secondary yield is rather tiny and has a minor effect on the resulting potential. This model was successfully verified by laboratory experiments dealing with charging of gold [Richterová et al., 2006, Appendix F] and glass [Richterová et al., 2007] dust grains. However, further investigations revealed a few differences between model predictions and experiments for some light species like carbon. The Richterová et al. [2010] paper analyzes sources of these differences and suggests appropriate corrections (Figure 3.5). This corrected model is then used for calculations of the scattered yield and energy spectra of scattered electrons.

Similarly to the secondary emission yield, the spectrum of secondary electrons is composed of two parts — the spectrum of backscattered primary electrons $F_B(E)$ and the spectrum of true secondary electrons $F_S(E)$. Many authors use the Maxwellian distribution with a temperature of several eV [e.g., Bronstein and Fraiman, 1969] but Draine and Salpeter [1979] and Grard et al. [1987] suggested a little different forms of this distribution. Richterová et al. [2008] examined the validity of the model and computed a contribution of the secondary electrons to the surface potential profile measured on gold and glass grains. We concluded that the spectrum of electrons emitted from gold grains exhibits a large portion of energetic electrons (above 10 eV), and thus it resembles the Draine and Salpeter distribution, whereas the Maxwellian one is more appropriate for glass grains. Rather small differences between energetic spectra of secondary electrons result in large differences in the grain equilibrium potential.

Both the scattered and secondary electrons contribute to the charging of the dust grains. For a description of charging by the secondary emission, an effective charging yield, $\delta^* = \delta/(1-\eta)$ is more appropriate because it is roughly proportional to the surface potential that the dust grain would reach under bombardment by electrons of the particular energy if all other charging currents can be neglected. This condition is fulfilled in many laboratory experiments [Mann et al., 2011].

The paper of Richterová et al. [2012, Appendix G] discusses our improvement of the secondary emission model that was successfully complemented with the possibility of defining complex shapes and the roughness of the surface. It has revealed an

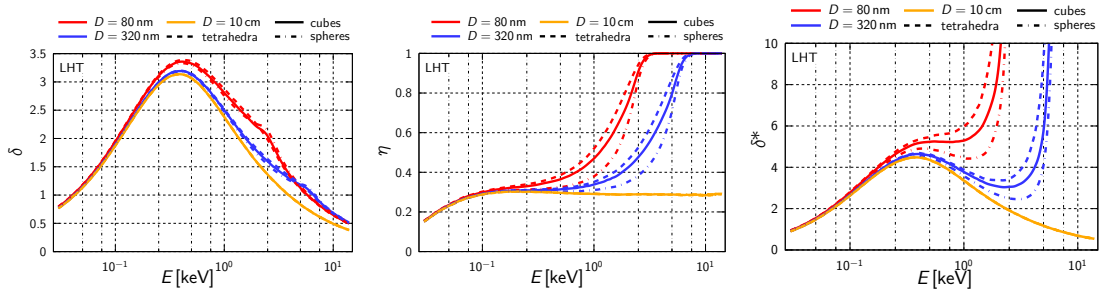

Figure 3.6: Demonstration of the grain shape effect. The panels show: left—the secondary yield, δ, middle—the scattered yield, η, and right—the effective charging yield, δ^* as a function of the primary energy for different shapes (spheres—dashed-dotted; cubes—full; and tetrahedrons—dashed). Adopted from Richterová et al. [2012, Appendix G].

important role of the surface quality as well as of special shape features (like sharp edges or steps) on the secondary electron emission. Both effects become mixed when any of the grain dimensions goes down to micron-sizes but generally, for low electron energies (below about 200 eV) the roughness is important, while for higher energies the shape is playing a major role (see, e.g., Figure 3.6). It has been shown that with increasing coarseness the maximum of the secondary emission yield decreases and shifts towards higher primary energies. Also rough surfaces scatter out a smaller number of primary electrons than smooth grains. Such a behavior was already observed and thus, it should be taken into account, when comparing observations of different groups. Finally, we note that the grain shape and surface roughness are usually unknown and thus a direct comparison with experiments is difficult. On the other hand, the model provides limits on the uncertainty of the experimental data.

Richterová et al. [2016, Appendix H] present a systematic study of electron interaction with well-defined systems — clusters consisting of different numbers of small spherical micron-sized grains which can be considered as examples of real space grains. The charges acquired by investigated objects as well as their secondary emission yields were calculated using the existing secondary emission model. We have found that the charge and surface potential of clusters exposed to the electron beam are influenced by a number of grains and by their geometry within a particular cluster (compact configuration of clusters exhibited the lower yield, see Figure 3.7) and that there is a large difference between charging of a cluster levitating in the free space and that attached to a planar surface. The calculation provides a reduction of the secondary electron emission yield of the surface covered by dust clusters by a factor of 1.5 with respect to the yield of a smooth surface. However, this reduction still seems to be too small to explain observed potentials of the lunar surface in the Earth's magnetosphere [Halekas et al., 2009].

3.1.4 Ion Interactions

Pavlů et al. [2007, Appendix I] observed sputtering of gold dust grains caused by the ion bombardment (Figure 3.8) and we described implications to the space-related processes. In order to check a possible relevance of the measurements to the interplanetary space, we have calculated [Pavlů et al., 2007, Appendix I] the sputtering times of a gold grain in typical solar wind conditions. At 1 AU, we assume that the solar wind has a velocity of 400 km/s and a number density of 10 cm^{-3}. In our estimates, we consider all solar wind ions as singly ionized atoms with keV energies. However,

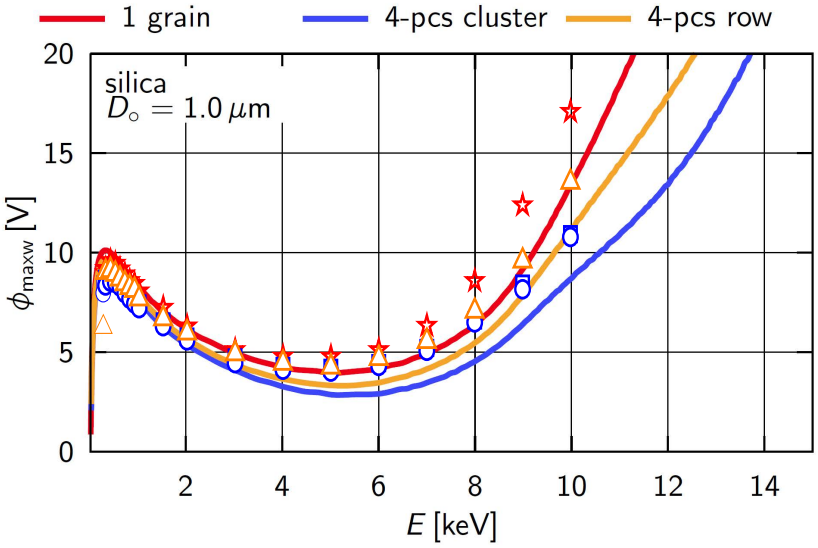

Figure 3.7: A comparison of measured (different points) and modeled (lines) surface potentials for one grain (red stars and line), for four grains in a line (yellow triangles and line), and for four grains in a compact configuration (blue circles, rectangles and line). The measured potentials were computed from the specific charge. Adopted from Richterová et al. [2016, Appendix H].

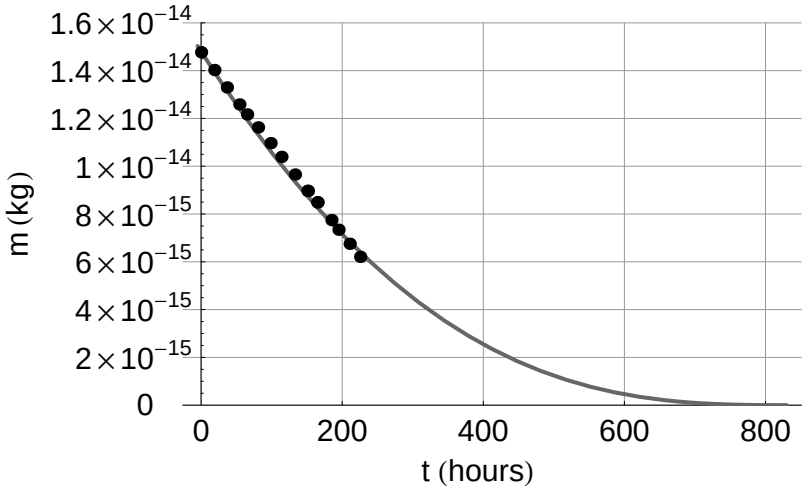

Figure 3.8: The time evolution of the Au grain mass during Ar^+ ion bombardment and comparison of model (solid line) and experimental results (dots). Adopted from Pavlů et al. [2007, Appendix I].

Insepov et al. [2006] show that the sputtering yield of multiply ionized ions can be much larger (by an order of magnitude). Indeed, all species (except protons) in the solar wind are in high ionization states. A typical mass composition of the solar wind was considered, however, the abundance of heavy ions can be significantly enhanced during coronal mass ejections, and these species are very effective for dust sputtering.

Pavlů et al. [2006] and Jeřáb et al. [2007] performed laboratory experiments where impacts of energetic ions led to a deposition of a huge positive charge onto a spherical grain causing a subsequent discharging (ion field emission). The surprisingly variable discharging behavior occurred — the increase of the discharge current with the time of

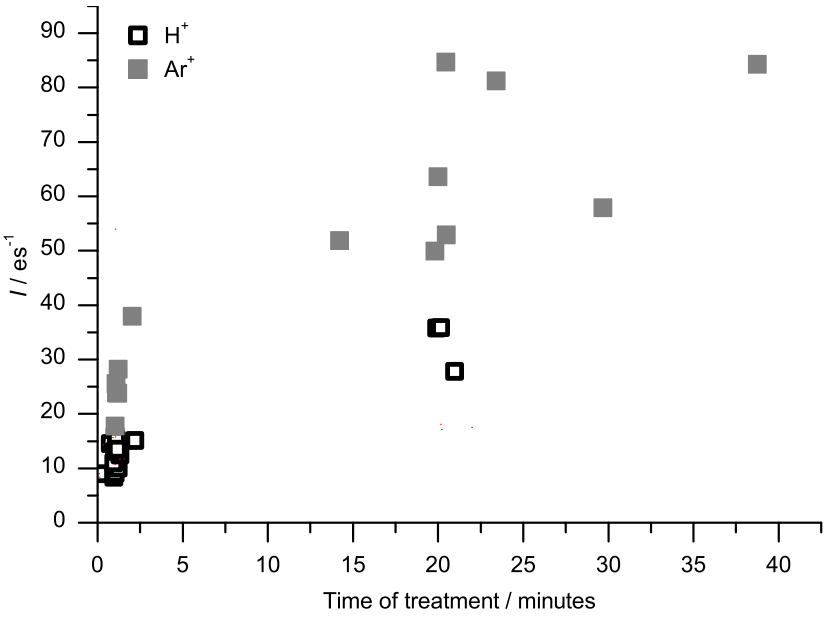

Figure 3.9: Field ion emission currents from one gold grain after different treatment times and for two ion species. Currents were measured at 1 kV of the grain surface potential. The full squares denote the Ar^+ bombardment, while the open circles show bombardment by H^+. Adopted from Pavlů et al. [2008, Appendix E].

treatment was unexpected because one would expect that grain charging is stopped at the point when the number of incoming and outgoing atoms are in equilibrium. Our experiments suggested that there is a mechanism that stores and gradually releases a portion of incoming ions. Our tentative explanation [Pavlů et al., 2008, Appendix E] was based on the implantation of beam ions into the grain material. Since the diffusion of the implanted ions toward the surface is probably a very slow process, it opened the question whether it could considerably contribute to the discharge current. In this experiment, the grain was exposed to a 5 keV ion beam for a time that is called "time of treatment" in Figure 3.9. After the beam was switched off, the discharge current was recorded together with the grain surface potential for several hours.

Beránek et al. [2010, Appendix J] analyzed heavily bombarded carbon grain and observed subsequent mass decrease after turning off the ion beam (Figure 3.10). These observations not only confirmed previous speculations but they are also important for space-related processes because the implantation of solar wind ions and their subsequent release in the form of neutral atoms was suggested as a possible source of the so-called pick-up ions in the solar system [e.g., Mann et al., 2004].

Vyšinka et al. [2016] sputtered silica grains by impacts of energetic ions in free space and on the surface. We found that the increase of the sputtering yield due to the simultaneous electron impact is probably much larger than expected and it can enhance the sputtering yield by a factor of 1.6 in a comparison with the sole ion bombardment. On the other hand, the influence of the electric field is probably not as strong as we anticipated. Sputtering of the grains fixed on a surface revealed that the angular profile of the yield is flatter than that frequently used for a description of the sputtering process.

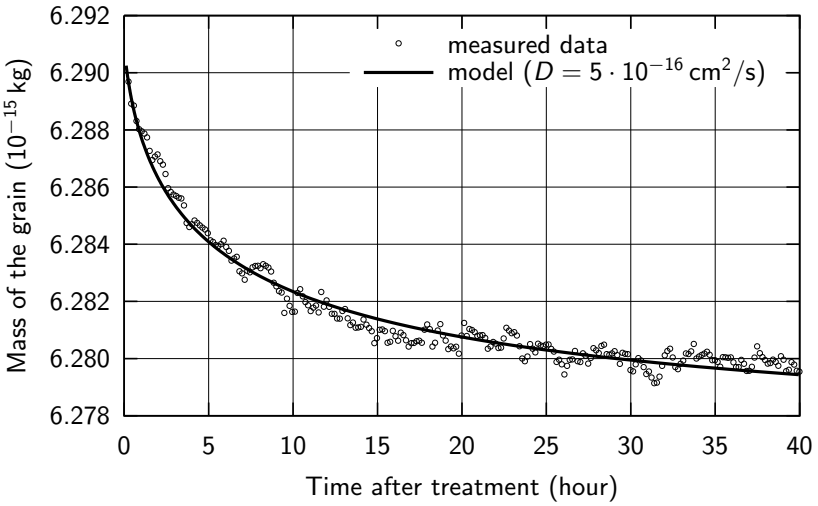

Figure 3.10: The change of the grain mass in time. The parameters of the model ($D = 5 \cdot 10^{-16}\,\mathrm{cm}^2/\mathrm{s}$, treatment 8 hours, incident current $32\,400$ particles per second). Adopted from Beránek et al. [2010, Appendix J].

3.2 Applications

In following pages, we will focus on applications of aforementioned knowledge obtained from experiments as well as from simulations. Since the dust is often surrounded by a plasma, the particular studies typically connect together our understanding of more processes and combine experimental and numerical simulations. We concretized simulation conditions to correspond to Moon and Mars and Saturn icy satellite environments (surfaces). Moreover, although space plasmas is a kind of extreme, our conclusions can be successfully applied also to other plasmas — a nice example is the last one where we use our results and our knowledge to study a real dust from tokamak (COMPASS-D) and to speculate on its behavior inside the tokamak plasma.

3.2.1 Lunar Surface

Němeček et al. [2011, Appendix K] discusses our first results of the measurements of the secondary emission yield and surface potential carried out on dust samples from LHT lunar regolith simulants with sizes between 0.3 and 3 μm using the electron beam with the energy below 700 eV. The interpretation of experimental results was again supported by the computer model of the secondary electron emission from spherical samples that reflects the LHT mass composition. They found that the equilibrium surface potential of this simulant does not depend on the grain size in discussed ranges of grain dimensions and the beam energies [as it was reported by Abbas et al., 2004], however, it is a function of the primary electron beam energy (see Figure 3.11). These conclusions are different from those that Abbas et al. [2010] derived from their laboratory experiment and we point out some of physical inconsistencies in their data interpretation. Notable is also the difference between our experimental results and that inferred from Lunar Prospector measurements above the lunar surface [Halekas et al., 2009]. The authors attributed a low value of the yield to the lunar surface roughness, thus we are preparing investigations of this effect in the laboratory experiment as well as in simulations.

The paper of Vaverka et al. [2013, Appendix L] studied the interaction of space

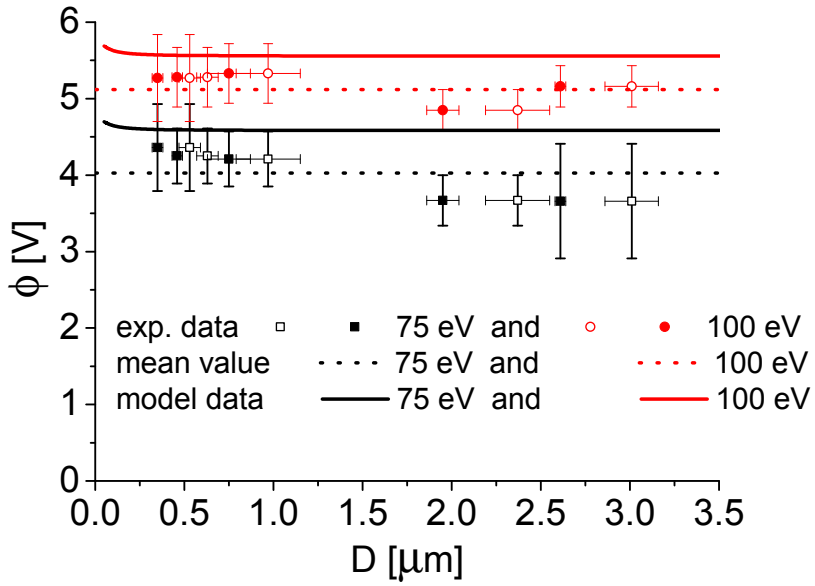

Figure 3.11: A dependence of the equilibrium surface potential on the energy of the primary electron beam. The crosses show the experimental data and the full line presents the model prediction [Richterová et al., 2010]. Adopted from Němeček et al. [2011, Appendix K].

plasma particles with dust grains. We presented the results of calculations of the surface potential of dust grains in high-temperature plasma such as that in the Earth's plasma sheet. The calculation reveals that the grain potential is a function of its size. Large (> 100 μm) grains would be negatively charged by hot electrons, whereas the positive potential of smaller grains is a descending function of their size. The negative potentials can be observed only in the shadow because the photocurrent caused by the solar UV radiation is large enough to compensate effects of the secondary emission. Nevertheless, the size dependence of the secondary emission current would cause different positive potentials of grains of different sizes even under sunlight. It has been suggested that the secondary emission can lead to multiple roots of the charging equations, but we did not find such behavior under the conditions studied in this paper.

Furthermore, Vaverka et al. [2016] combines numerical simulations of one Moon pass through the magnetospheric tail with the real plasma parameters measured by THEMIS (the data are used as an input of the model). The calculations are concentrated on different charges of the lunar surface itself and a dust grain lifted above this surface. We showed that the secondary electron emission leads to a positive charging of parts of the lunar surface even in the magnetosphere where a high negative potential is expected. It ensued the secondary electron emission is generally more important for isolated dust grains than for the lunar surface covered by these grains. The time constant of charging (depends on dust grains diameters) was estimated to be of the order of hours for sub-micrometer grains unlike the lunar surface which charges up within second. A polarity of the dust charge in a shadow depends on the temperature of surrounding electrons; it is negative for $T_\mathrm{e} < 10$ eV and positive for $T_\mathrm{e} > 20$ eV. We finally discussed the conditions under and the areas where a levitation of the lifted dust grains could be observed. Figure 3.12 shows the model result for plasma conditions referred near the lunar surface.

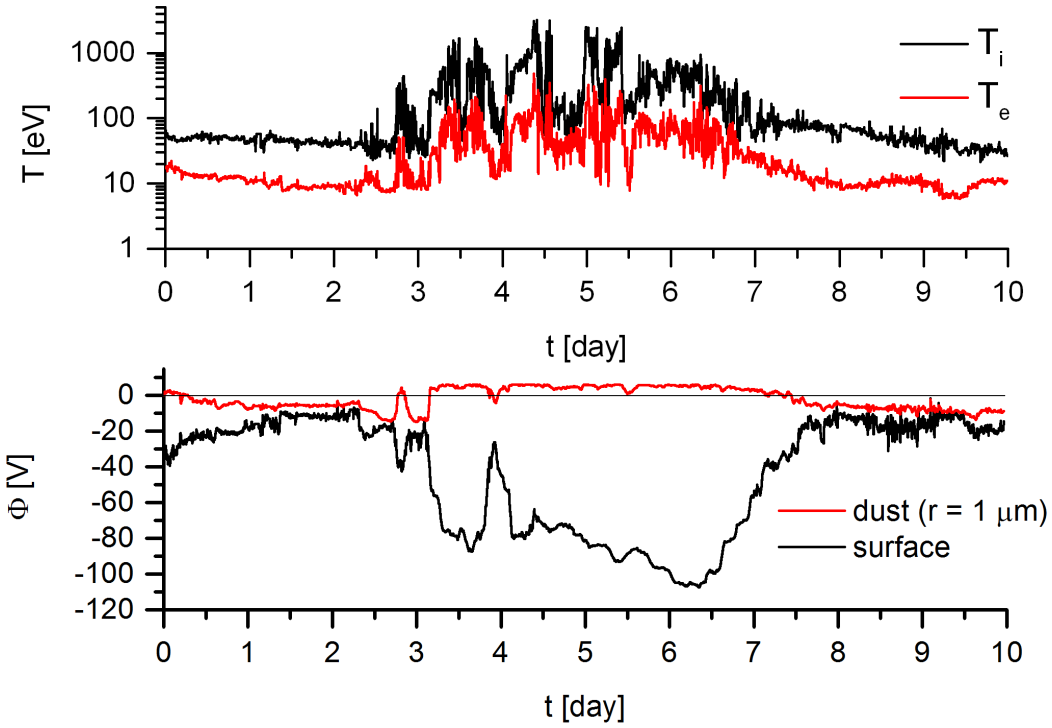

Figure 3.12: Upper panel — plasma temperature as measured by the THEMIS C (ARTEMIS P2) spacecraft during a crossing of the Earth's magnetosphere on 22–31 January, 2013. Lower panel — model of a temporal evolution of the lunar surface and dust grain potentials. The micron-sized grain is "levitated" above the surface during the lunar transit through the magnetosphere for the solar zenith angle of 90°. Adopted from Vaverka et al. [2016, submitted].

3.2.2 Martian Atmosphere

The study of Pavlů et al. [2014, Appendix M] deals with charging of the Martian soil simulant. In the recent years, a wide attention was paid to Mars. One of the unrevealed mysteries is the lack of presence of lightnings in the Martian atmosphere. We have investigated a Martian soil simulant (prepared at the Johnson Space Center under name JSC Mars-1) and its exposure to the electron beam revealed that the grain surface potential is low and generally determined by a mean atomic number of the grain material at a low-energy range (< 1 keV), whereas it can reach a limit of the field ion emission being irradiated by more energetic electrons. A comparison of model and experimental results reveals an influence of the grain shape and size predominantly in the range of higher (> 2 keV) electron energies. Moreover, generally used Maxwellian approximation of the energy spectrum of secondary electrons cannot be applied for the dust grains from SiO_2 or similar (e.g., JSC Mars-1) materials. The Draine and Salpeter [1979] distribution provides a better approximation in a broad range of energies (Figure 3.13), whereas the Sickafus [1977] distribution with $\mu \approx 0.5$ is appropriate for the description of a contribution of backscattered electrons (above 50 eV). We concluded that the models of electric circuits within the Martian dust clouds should include a description of the secondary electron emission that should reflect the effects of finite dimensions of dust grains. Finally, we tried to enlighten the missing lightnings issue by discussing possible implications of the secondary electron emission — our results led us to the conclusion that it can cause the lack of lightnings in the Martian tenuous atmosphere.

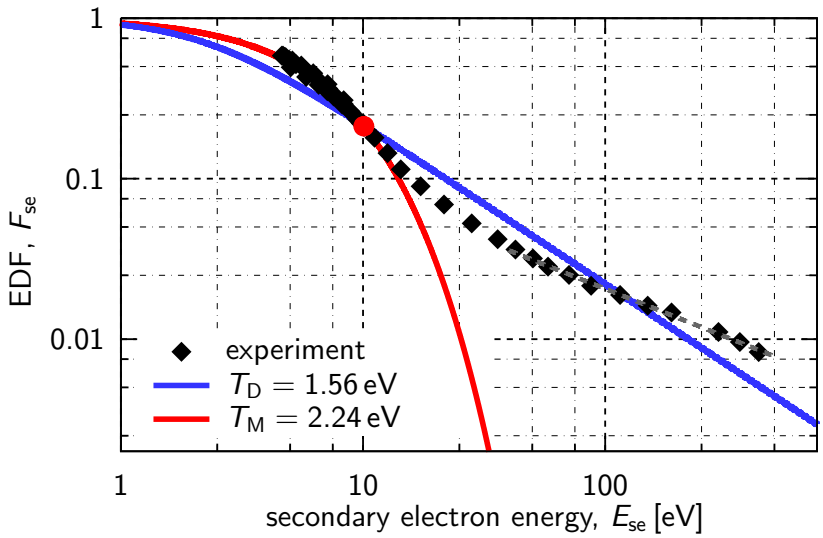

Figure 3.13: The electron distribution of secondary electrons. Points — experimental data; red curve — the Maxwellian fit to a low-energy part; blue line — the best fit to all experimental data by the Draine and Salpeter distribution; grey dashed line — the fit to experimental points with $E_{se} > 50$ eV by the power-law form. Adopted from Pavlů et al. [2014, Appendix M].

3.2.3 Icy Satellites of Saturn

Richterová et al. [2011, Appendix N] calculated the secondary electron emission yield of water ice grains and showed that the yield is greater than unity from ≈ 30 eV to several keV. Thus, these grains can achieve a negative equilibrium potential only if the Saturn E-ring plasma is cold enough (i.e., the secondary emission does not contribute significantly to the charging current) and the contribution of photoemission would be negligible. Furthermore, the calculations revealed that any reasonable admixture of NaCl does not change the secondary emission properties of small icy dust grains of a given diameter. It seems that the same conclusions would hold for the photoemission because the emission of electrons excited by energetic photons proceeds the same way as the emission of true secondary emission.

3.2.4 Tokamak

Based on the previous simulation results, the paper of Vaverka et al. [2014, Appendix O] discusses the role of dust in tokamaks. A dust production and its transport into the core plasma is an important issue for magnetic confinement fusion. Dust grains are charged by various processes — among these often underestimated processes, the secondary electron emission from the dust is investigated. Figure 3.15 shows COMPASS-D samples in comparison with in-tokamak-expected materials. The numerical model balances all currents including the backscattered electrons and takes into account the effects of grain size, material, and it is also able to handle both spherical and non-spherical grains. The role of the secondary electron emission under tokamak conditions is widely discussed and it's shown that the secondary electron emission is an important process for the grains crossing the scrape-off layer from the edge to core plasma. We demonstrated that a realistic description of the secondary electron yield from the dust grains is principal for a correct estimation of their floating potential in hot plasmas. Since the Sternglass [1957] formula that underestimates the secondary electron yield of dust grains is a part of widely used numerical codes (e.g., DTOKS,

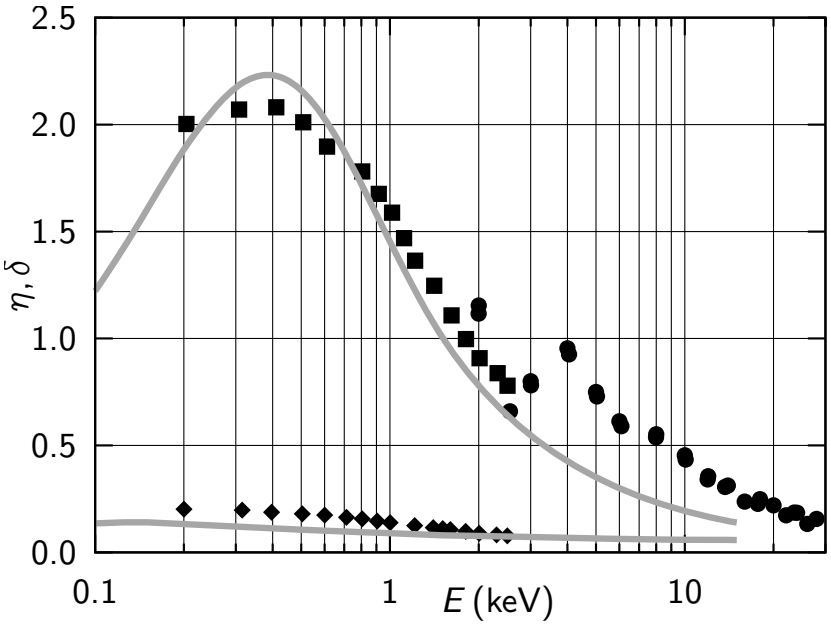

Figure 3.14: A comparison of modeled profile of the true secondary electron emission yield, δ (top curve) and backscattered yield, η (bottom curve) with experimental data (diamonds — η according to Matskevich and Mikhailova [1960] for pure water ice; squares — δ according to Matskevich and Mikhailova [1960]; and circles — δ according to Suszcynsky et al. [1992]). Adopted from Richterová et al. [2011, Appendix N].

DUSTT), calculations of the dust dynamics within tokamaks using these codes should be taken with a care. The results of our calculations are relevant for materials related to fusion experiments in ITER.

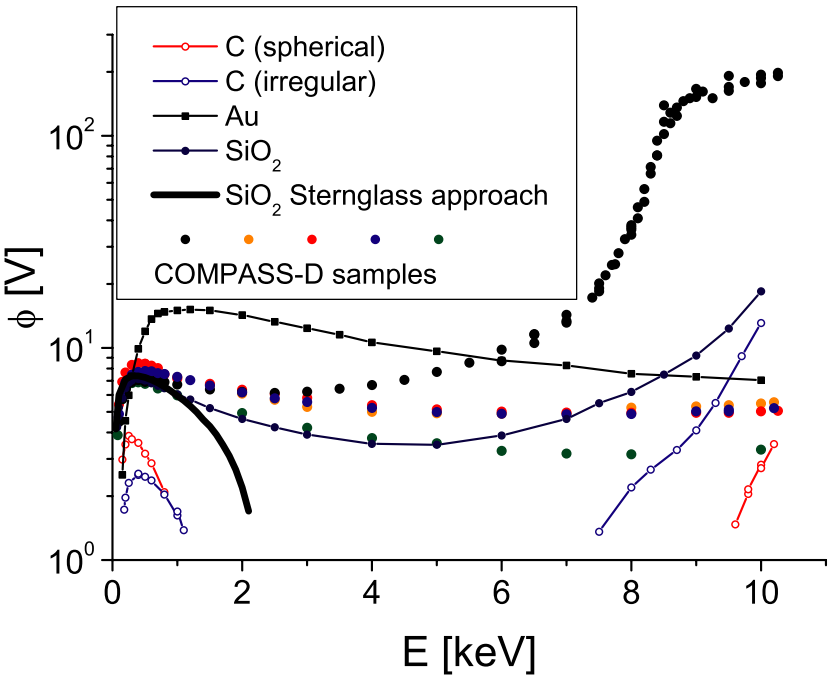

Figure 3.15: The surface potential as a function of the primary electron energy for several grains collected from the COMPASS-D tokamak (dots) and their comparison with glassy carbon, gold, and glass samples (lines). The full line presents the theoretical floating potential of the 1-μm SiO_2 grain computed according to the Sternglass [1957] theory. Adopted from Vaverka et al. [2014, Appendix O].

4. Concluding Remarks

IN THE PRESENT THESIS, we highlighted the scientific results in the dust–plasma interaction in course of the last ten years with an emphasis on directions covered by our department. The results are summarized according to different processes that affect to dust grain charging, no as a simple list of papers. Moreover, the thesis also shows a significant contribution to a development of new experimental methods and techniques that are an in-separable part of our investigations. We present experimental results as well as numerical simulations that are supporting each another and, in this way, they further enhance our knowledge and understanding of a wide range of different processes. Our complex study of the secondary electron emission can act as an example such reciprocal influence of the experiment and simulations (models) that leads to including this process to theories and interpretations of observations at various fields of the plasma research.

Finally, we would like to note that our results are only a first step to a full understanding all processes leading to dust charging. Nevertheless, due to both experimental sets-up built in our group in the last years, we have an excellent background for further investigations of the interaction of dust grains with electron, ion, and photon beams with an accent to contribute to a full description of the processes in dusty plasma.

Bibliography

Abbas, M., Craven, P., Spann, J., Tankosic, D., LeClair, A., Gallagher, D., West, E., Weingartner, J., Witherow, W., Tielens, A., Laboratory experiments on rotation and alignment of the analogs of interstellar dust grains by radiation. *Astrophys. J.* 614 (2): 781–795, 2004.

Abbas, M., Craven, P., Spann, J., Witherow, W., West, E., Gallagher, D., Adrian, M., Fishman, G., Tankosic, D., LeClair, A., Sheldon, R., Thomas, E., Radiation pressure measurements on micron-size individual dust grains. *J. Geophys. Res.* 108 (A6): 1229, 2003.

Abbas, M. M., Tankosic, D., Craven, P. D., LeClair, A. C., Spann, J. F., Lunar dust grain charging by electron impact: Complex role of secondary electron emissions in space environments. *Astrophys. J.* 718 (2): 795–809, 2010.

Altobelli, N., Kempf, S., Landgraf, M., Srama, R., Dikarev, V., Krüger, H., Moragas-Klostermeyer, G., Grün, E., Cassini between Venus and Earth: Detection of interstellar dust. *J. Geophys. Res.* 108: 8032, 2003.

Assad, A. M. D., El Gomati, M. M., Inelastic scattering in copper. *Scanning Electron Microsc.* 12: 185–192, 1998.

Barkan, A., D'Angelo, N., Merlino, R., Charging of dust grains in a plasma. *Phys. Rev. Lett.* 73 (23): 3093–3096, 1994.

Beránek, M., Čermák, I., Jeřáb, M., Pavlů, J., Šafránková, J., Němeček, Z., Proposal of an electrodynamic trap for photoemission measurements on dust grains. *In: Šafránková, J., Pavlů, J. (Eds.), WDS'07 Proceedings of Contributed Papers: Part II – Physics of Plasmas and Ionized Media*. Matfyzpress, Prague, pp. 111–118, 2007.

Beránek, M., Richterová, I., Němeček, Z., Pavlů, J., Šafránková, J., Secondary electron emission from highly charged carbon grains. *Eur. Phys. J. D* 54 (2): 299–304, 2009.

Beránek, M., Čermák, I., Němeček, Z., Šafránková, J., Jeřáb, M., Pavlů, J., Linear trap with three orthogonal quadrupole fields for dust charging experiments. *Rev. Sci. Instrum.* 83 (11): 115109, 2012.

Beránek, M., Vyšinka, M., Pavlů, J., Richterová, I., Němeček, Z., Šafránková, J., Dust as a gas carrier. *IEEE Trans. Plasma Sci.* 38 (4): 886–891, 2010.

Bouchoule, A., *Dusty Plasmas: Physics, Chemistry, and technological impacts in plasma processing*. Wiley and Sons, New York, 1999.

Bronold, F. X., Fehske, H., Kersten, H., Deutsch, H., Towards a Microscopic Theory of Particle Charging. *Contrib. to Plasma Phys.* 49: 303–315, 2009.

Bronstein, I. M., Fraiman, B. S., *Secondary Electron Emission*. Nauka, Moskva, 1969. In Russian.

Brus, L. E., A simple model for the ionization potential, electron affinity, and aqueous redox potentials of small semiconductor crystallites. *J. Chem. Phys.* 79 (11): 5566–5571, 1983.

Chow, V., Mendis, D., Rosenberg, M., Secondary emission from small dust grains at high electron energies. *IEEE Trans. Plasma Sci.* 22 (2): 179–186, 1994.

Čermák, I., Laboruntersuchung elektrischer Aufladung kleiner Staubteilchen. PhD thesis, Naturwissenschaftlich-Mathematischen Gesamtfakultät, Ruprecht-Karls-Universität, Heidelberg, 1994.

Čermák, I., Grün, E., Švestka, J., New results in studies of electric charging of dust particles. *Adv. Sp. Res.* 15 (10): 59–64, 1995.

Čermák, I., Pavlů, J., Žilavý, P., Němeček, Z., Šafránková, J., Richterová, I., 3D electrodynamic quadrupole: A nondestructive analysis of single dust grains. *In: Šafránková, J. (Ed.), WDS'04 Proceedings of Contributed Papers: Part II – Physics of Plas-*

mas and Ionized Media. Matfyzpress, Prague, pp. 279–286, 2004.

Draine, B., Salpeter, E., On the physics of dust grains in hot gas. *Astrophys. J.* 231 (1): 77–94, 1979.

Fortov, V. E., Ivlev, A. V., Khrapak, S. A., Khrapak, A. G., Morfill, G. E., Complex (dusty) plasmas: Current status, open issues, perspectives. *Phys. Rep.* 421: 1–103, 2005.

Grard, R. J. L., McDonnell, J. A. M., Grun, E., Gringauz, K. I., Secondary electron emission induced by gas and dust impacts on Giotto, Vega-1 and Vega-2 in the environment of comet P/Haley. *Astron. Astrophys.* 187 (1–2): 785–788, 1987.

Hachenberg, O., Brauer, W., Secondary electron emission from solids. *Advances in electronics and electron physics* 11: 413–499, 1959.

Halekas, J. S., Delory, G. T., Lin, R. P., Stubbs, T. J., Farrell, W. M., Lunar Prospector measurements of secondary electron emission from lunar regolith. *Planet. Space. Sci.* 57: 78–82, 2009.

Horanyi, M., Charged Dust Dynamics in the Solar System. *Annu. Rev. Astron. Astrophys.* 34: 383–418, 1996.

Hunger, H.-J., Küchler, L., Backscattering coefficients for elements from 1 to 20 keV. *Phys. Status Solidi A* 56: K45–K50, 1979.

Ilgner, M., Grain charging in protoplanetary discs. *Astron. Astrophys.* 538: A124, 2012.

Insepov, Z., Allain, J. P., Hassanein, A., Terasawa, M., Surface erosion by highly-charged ions. *Nucl. Instrum. Methods Phys. Res., Sect. B* 242: 498–502, 2006.

Ishihara, O., TOPICAL REVIEW: Complex plasma: dusts in plasma. *J. Phys. D* 40: R121–R147, 2007.

Ivlev, A. V., Nosenko, V., Roecker, T. B., Equilibrium and Non-Equilibrium Melting of Two-Dimensional Plasma Crystals. *Contrib. Plasma Phys.* 55 (1): 35–57, 2015.

Jeřáb, M., Richterová, I., Pavlů, J., Šafránková, J., Němeček, Z., Influence of charging conditions on field ion emission from dust grains. *IEEE Trans. Plasma Sci.* 35 (2): 292–296, 2007.

Joy, D., *Monte Carlo Modeling for Electron Microscopy and Microanalysis*. Oxford University Press, New York, 1995.

Kane, B. E., Levitated spinning graphene flakes in an electric quadrupole ion trap. *Phys. Rev. B* 82 (11): 115441, 2010.

Khrapak, S. A., Ratynskaia, S. V., Zobnin, A. V., Usachev, A. D., Yaroshenko, V. V., Thoma, M. H., Kretschmer, M., Höfner, H., Morfill, G. E., Petrov, O. F., Fortov, V. E., Particle charge in the bulk of gas discharges. *Phys. Rev. E* 72 (1): 016406, 2005.

Kolokolova, L., Kimura, H., Ziegler, K., Mann, I., Light-scattering properties of random-oriented aggregates: Do they represent the properties of an ensemble of aggregates? *J. Quanti. Spectrosc. Radiat. Transfer* 100: 199–206, 2006.

Krüger, H., Bindschadler, D., Dermott, S. F., Graps, A. L., Grün, E., Gustafson, B. A., Hamilton, D. P., Hanner, M. S., Horányi, M., Kissel, J., Linkert, D., Linkert, G., Mann, I., McDonnell, J. A. M., Moissl, R., Morfill, G. E., Polanskey, C., Roy, M., Schwehm, G., Srama, R., Galileo dust data from the jovian system: 2000 to 2003. *Planet. Space. Sci.* 58: 965–993, 2010a.

Krüger, H., Dikarev, V., Anweiler, B., Dermott, S. F., Graps, A. L., Grün, E., Gustafson, B. A., Hamilton, D. P., Hanner, M. S., Horányi, M., Kissel, J., Linkert, D., Linkert, G., Mann, I., McDonnell, J. A. M., Morfill, G. E., Polanskey, C., Schwehm, G., Srama, R., Three years of Ulysses dust data: 2005 to 2007. *Planet. Space. Sci.* 58: 951–964, 2010b.

Lisin, E. A., Vaulina, O. S., Petrov, O. F., Fortov, V. E., Dust-particle charge in weakly ionized gas-discharge plasma. *EPL* 97 (5), 2012.

Lu, Q., Zhou, Z., Shi, L., Zhao, G., Incident angle dependence of secondary electron emission from carbon induced by swift H_2^+. *Chin. Phys.* 14 (7): 1465–1470, 2005.

Ma, Q., Matthews, L. S., Land, V., Hyde, T. W., Charging of aggregate grains in astrophysical environments. *Astrophys. J.* 763 (2), 2013.

Makov, G., Nitzan, A., Brus, L. E., On the ionization potential of small metal and dielectric particles. *J. Chem. Phys.* 88 (8): 5076–5085, 1988.

Mann, I., Interplanetary medium – A dusty plasma. *Adv. Sp. Res.* 41 (1): 160–167, 2008.

Mann, I., Kimura, H., Biesecker, D. A., Tsurutani, B. T., Grün, E., McKibben, R. B., Liou, J.-C., MacQueen, R. M., Mukai, T., Guhathakurta, M., Lamy, P., Dust Near The Sun. *Space Science Reviews* 110: 269–305, 2004.

Mann, I., Pellinen-Wannberg, A., Murad, E., Popova, O., Meyer-Vernet, N., Rosenberg, M., Mukai, T., Czechowski, A., Mukai, S., Safrankova, J., Nemecek, Z., Dusty plasma effects in near earth space and interplanetary medium. *Space Sci. Rev.* 161 (1–4): 1–47, 2011.

Matskevich, T. L., Mikhailova, E. G., Secondary electron emission in ice and anthracene films. *Solid State Phys.* 2: 709–715, 1960.

Melzer, A., Trottenberg, T., Piel, A., Experimental determination of the charge on dust particles forming Coulomb lattices. *Phys. Lett. A* 191: 301–308, 1994.

Němeček, Z., Pavlů, J., Šafránková, J., Beránek, M., Richterová, I., Vaverka, J., Mann, I., Lunar dust grain charging by electron impact: Dependence of the surface potential on the grain size. *Astrophys. J.* 738 (1): 14, 2011.

Nouzák, L., Richterová, I., Pavlů, J., Němeček, Z., Šafránková, J., Investigations of photoemission from lunar dust simulant. *IEEE Trans. Plasma Sci.* 44 (2): in print, 2016.

Nouzák, L., Vaverka, J., Pavlů, J., Němeček, Z., Šafránková, J., Investigations of the photoemission from glass dust grains. *In: Šafránková, J., Pavlů, J. (Eds.), WDS'14 Proceedings of Contributed Papers — Physics*. Matfyzpress, Prague, pp. 361–370, 2014.

Okuzumi, S., Tanaka, H., Takeuchi, T., Sakagami, M.-a., Electrostatic Barrier Against Dust Growth in Protoplanetary Disks. II. Measuring the Size of the "Frozen" Zone. *Astrophys. J.* 731: 96, 2011.

Palluel, P., Composante rediffusée du rayonnement électronique secondaire des métaux. *Comptes Rendus* 224: 1492, 1947.

Paul, W., Steinwedel, H., Apparatus for separating charged particles of different specific charges. Patent 944,900, German Patent, 1956.

Pavlů, J., Beránek, M., Vaverka, J., Šafránková, J., Němeček, Z., Richterová, I., Secondary electron emission from martian soil simulant. *J. Geophys. Res.* 119 (1): 199–209, 2014.

Pavlů, J., Richterová, I., Němeček, Z., Šafránková, J., Wild, J., The sputtering of dust grains: Aspects of experimental observations. *IEEE Trans. Plasma Sci.* 35 (2): 297–302, 2007.

Pavlů, J., Richterová, I., Němeček, Z., Šafránková, J., Čermák, I., Interaction between single dust grains and ions or electrons: laboratory measurements and their consequences for the dust dynamics. *Faraday Discuss.* 137: 139–155, 2008.

Pavlů, J., Velyhan, A., Richterová, I., Němeček, Z., Šafránková, J., Čermák, I., Žilavý, P., Mass-loss rate for MF resin microspheres. *IEEE Trans. Plasma Sci.* 32 (2): 704–708, 2004.

Pavlů, J., Velyhan, A., Richterová, I., Šafránková, J., Němeček, Z., Wild, J., Jeřáb, M., Ion beam effects on dust grains: 2 — influence of charging history. *Vacuum* 80 (6): 542–547, 2006.

Pavlů, J., Šafránková, Němeček, Z., Richterová, I., Dust charging in space-related laboratory experiments: A review focused on secondary emission. *Contrib. Plasma Phys.* 49 (3): 169–186, 2009.

Poppe, A. R., Piquette, M., Likhanskii, A., Horanyi, M., The effect of surface topogra-

phy on the lunar photoelectron sheath and electrostatic dust transport. *Icarus* 221 (1): 135–146, 2012.

Richterová, I., Beránek, M., Pavlů, J., Němeček, Z., Šafránková, J., Electrons scattered inside small dust grains of various materials. *Phys. Rev. B* 81 (7): 075406, 2010.

Richterová, I., Němeček, Z., Šafránková, J., Pavlů, J., A model of secondary emission from dust grains and its comparison with experiment. *IEEE Trans. Plasma Sci.* 32 (2): 617–622, 2004.

Richterová, I., Němeček, Z., Šafránková, J., Pavlů, J., Beránek, M., Secondary emission from glass grains: Comparison of the model and experiment. *IEEE Trans. Plasma Sci.* 35 (2): 286–291, 2007.

Richterová, I., Němeček, Z., Beránek, M., Šafránková, J., Pavlů, J., Secondary emission from non-spherical dust grains with rough surfaces: Application to lunar dust. *Astrophys. J.* 761 (2): 108, 2012.

Richterová, I., Němeček, Z., Pavlů, J., Beránek, M., Šafránková, J., Modeling the secondary emission yield of salty ice dust grains. *Icarus* 212 (1): 367–372, 2011.

Richterová, I., Němeček, Z., Pavlů, J., Šafránková, J., Vaverka, J., Secondary emission from clusters composed of spherical grains. *IEEE Trans. Plasma Sci.* 44 (2): in print, 2016.

Richterová, I., Pavlů, J., Němeček, Z., Šafránková, J., Model of secondary emission and its application on the charging of gold dust grains. *Phys. Rev. B* 74 (23): 235430, 2006.

Richterová, I., Pavlů, J., Němeček, Z., Šafránková, J., An application of the dust grain charging model to determination of secondary electron spectra. *Eur. Phys. J. D* 48 (3): 375–381, 2008.

Sakai, S., Watanabe, S., Morooka, M. W., Holmberg, M. K. G., Wahlund, J.-E., Gurnett, D. A., Kurth, W. S., Dust-plasma interaction through magnetosphere-ionosphere coupling in Saturn's plasma disk. *Planet. Space. Sci.* 75: 11–16, 2013.

Samarian, A. A., Vladimirov, S. V., Charge of a macroscopic particle in a plasma sheath. *Phys. Rev. E* 67 (6): 066404, 2003.

Sickafoose, A. A., Colwell, J. E., Horányi, M., Robertson, S., Experimental investigations on photoelectric and triboelectric charging of dust. *J. Geophys. Res.* 106 (A5): 8343–8356, 2001.

Sickafus, E. N., Linearized secondary-electron cascades from the surfaces of metals. i. clean surfaces of homogeneous specimens. *Phys. Rev. B* 16 (4): 1436–1447, 1977.

Smirnov, R. D., Krasheninnikov, S. I., Pigarov, A. Y., Rognlien, T. D., Tungsten dust impact on ITER-like plasma edge. *Phys. Plasmas* 22 (1), 2015.

Spann, J., Abbas, M., Venturini, C., Comfort, R., Electrodynamic balance for studies of cosmic dust particles. *Phys. Scr.* T89: 149–153, 2001.

Sternglass, E., Theory of secondary electron emission under electron bombardment. Scientific Paper 6-94410-2-P9, Westinghouse Research Laboratories, Pittsburgh 35, 1957.

Sternglass, E. J., On the phenomenon of secondary electron emission from solids. master thesis, Cornell University, 1951.

Sternglass, E. J., Backscattering of Kilovolt Electrons from Solids. *Phys. Rev.* 95 (2): 345–358, 1954.

Sternovsky, Z., Robertson, S., Sickafoose, A., Colwell, J., Horányi, M., Contact charging of lunar and Martian dust simulants. *J. Geophys. Res.* 107 (E11): 5105, 2002.

Stubbs, T. J., Vondrak, R. R., Farrell, W. M., Impact of dust on lunar exploration. *In: Krüger, H., Graps, A. L. (Eds.), Dust in Planetary Systems*. Vol. 310 of *ESA Publications*. pp. 239–344, 2007.

Suszcynsky, D. M., Borovsky, J. E., Goertz, C. K., Secondary electron yields of solar system ices. *J. Geophys. Res.* 97 (E2): 2611–2619, 1992.

Švestka, J., Čermák, I., Grün, E., Electric charging and electrostatic fragmentation of dust particles in laboratory. *Adv. Sp. Res.* 13 (10): 199–202, 1993.

Tomme, E. B., Annaratone, B. M., Allen, J. E., Damped dust oscillations as a plasma sheath diagnostic. *Plasma Sources Sci. Technol.* 9: 87–96, 2000a.

Tomme, E. B., Law, D. A., Annaratone, B. M., Allen, J. E., Parabolic Plasma Sheath Potentials and their Implications for the Charge on Levitated Dust Particles. *Phys. Rev. Lett.* 85: 2518–2521, 2000b.

Trottenberg, T., Melzer, A., Piel, A., Measurement of the electric charge on particulates forming Coulomb crystals in the sheath of a radiofrequency plasma. *Plasma Sources Sci. Technol.* 4: 450–458, 1995.

Vasilyak, L. M., Vladimirov, V. I., Deputatova, L. V., Lapitsky, D. S., Molotkov, V. I., Pecherkin, V. Y., Filinov, V. S., Fortov, V. E., Coulomb stable structures of charged dust particles in a dynamical trap at atmospheric pressure in air. *New J. Phys.* 15 (4): 043047, 2013.

Vaverka, J., Richterová, I., Pavlů, J., Němeček, Z., Šafránková, J., Lunar surface and dust grain potentials during the Earth's magnetosphere crossing. *Astrophys. J.*: submitted, 2016.

Vaverka, J., Richterova, I., Pavlu, J., Safrankova, J., Nemecek, Z., Numerical Calculation of an Equilibrium Dust Grain Potential in Lunar Environment. *IEEE Trans. Plasma Sci.* 41 (4, 2, SI): 740–744, 2013.

Vaverka, J., Richterová, I., Vyšinka, M., Pavlů, J., Šafránková, J., Němeček, Z., The influence of secondary electron emission on the floating potential of tokamak-born dust. *Plasma Phys. Contr. F.* 56 (2): 025001, 2014.

Vyšinka, M., Němeček, Z., Šafránková, J., Pavlů, J., Vaverka, J., Lavková, J., Sputtering of spherical SiO_2 samples. *IEEE Trans. Plasma Sci.*: submitted, 2016.

Walch, B., Horanyi, M., Robertson, S., Measurement of the charging of individual dust grains in a plasma. *IEEE Trans. Plasma Sci.* 22 (2): 97–102, 1994.

Walch, B., Horányi, M., Robertson, S., Charging of Dust Grains in Plasma with Energetic Electrons. *Phys. Rev. Lett.* 75 (5): 838–841, 1995.

Whipple, E. C., Potentials of surfaces in space. *Rep. Prog. Phys.* 44 (11): 1197–1250, 1981.

Wiese, R., Sushkov, V., Kersten, H., Ikkurthi, V. R., Schneider, R., Hippler, R., Behavior of a porous particle in a radiofrequency plasma under pulsed argon ion beam bombardment. *New J. Phys.* 12 (3): 033036, 2010.

Wuerker, R., Shelton, H., Langmuir, R., Electrodynamic containment of charged particles. *J. Appl. Phys.* 30 (3): 342–349, 1959.

Zook, H. A., 2001. Spacecraft measurements of the cosmic dust flux. In: Peucker-Ehrenbrink, B., Schmitz, B. (Eds.), Accretion of Extraterrestrial Matter Throughout Earth's History. Springer US, pp. 75–92.

Zubko, E., Kimura, H., Shkuratov, Y., Muinonen, K., Yamamoto, T., Okamoto, H., Videen, G., Effect of absorption on light scattering by agglomerated debris particles. *J. Quanti. Spectrosc. Radiat. Transfer* 110: 1741–1749, 2009.

Zubko, E., Muinonen, K., Muñoz, O., Nousiainen, T., Shkuratov, Y., Sun, W., Videen, G., Light scattering by feldspar particles: Comparison of model agglomerate debris particles with laboratory samples. *J. Quanti. Spectrosc. Radiat. Transfer* 131: 175–187, 2013.

Žilavý, P., Sternovský, Z., Čermák, I., Němeček, Z., Šafránková, J., Surface potential of small particles charged by the medium-energy electron beam. *Vacuum* 50 (1–2): 139–142, 1998.

Appendices

A. Pavlů, J., Velyhan, A., Richterová, I., Němeček, Z., Šafránková, J., Čermák, I., Žilavý, P., Mass-loss rate for MF resin microspheres. *IEEE Trans. Plasma Sci.* 32 (2): 704–708, 2004.

B. Beránek, M., Čermák, I., Němeček, Z., Šafránková, J., Jeřáb, M., Pavlů, J., Linear trap with three orthogonal quadrupole fields for dust charging experiments. *Rev. Sci. Instrum.* 83 (11): 115109, 2012.

C. Nouzák, L., Richterová, I., Pavlů, J., Němeček, Z., Šafránková, J., Investigations of photoemission from lunar dust simulant. *IEEE Trans. Plasma Sci.* 44 (2): in print, 2016.

D. Pavlů, J., Šafránková, Němeček, Z., Richterová, I., Dust charging in space-related laboratory experiments: A review focused on secondary emission. *Contrib. Plasma Phys.* 49 (3): 169–186, 2009.

E. Pavlů, J., Richterová, I., Němeček, Z., Šafránková, J., Čermák, I., Interaction between single dust grains and ions or electrons: laboratory measurements and their consequences for the dust dynamics. *Faraday Discuss.* 137: 139–155, 2008.

F. Richterová, I., Pavlů, J., Němeček, Z., Šafránková, J., Model of secondary emission and its application on the charging of gold dust grains. *Phys. Rev. B* 74 (23): 235430, 2006.

G. Richterová, I., Němeček, Z., Beránek, M., Šafránková, J., Pavlů, J., Secondary emission from non-spherical dust grains with rough surfaces: Application to lunar dust. *Astrophys. J.* 761 (2): 108, 2012.

H. Richterová, I., Němeček, Z., Pavlů, J., Šafránková, J., Vaverka, J., Secondary emission from clusters composed of spherical grains. *IEEE Trans. Plasma Sci.* 44 (2): in print, 2016.

I. Pavlů, J., Richterová, I., Němeček, Z., Šafránková, J., Wild, J., The sputtering of dust grains: Aspects of experimental observations. *IEEE Trans. Plasma Sci.* 35 (2): 297–302, 2007.

J. Beránek, M., Vyšinka, M., Pavlů, J., Richterová, I., Němeček, Z., Šafránková, J., Dust as a gas carrier. *IEEE Trans. Plasma Sci.* 38 (4): 886–891, 2010.

K. Němeček, Z., Pavlů, J., Šafránková, J., Beránek, M., Richterová, I., Vaverka, J., Mann, I., Lunar dust grain charging by electron impact: Dependence of the surface potential on the grain size. *Astrophys. J.* 738 (1): 14, 2011.

L. Vaverka, J., Richterova, I., Pavlu, J., Safrankova, J., Nemecek, Z., Numerical Calculation of an Equilibrium Dust Grain Potential in Lunar Environment. *IEEE Trans. Plasma Sci.* 41 (4, 2, SI): 740–744, 2013.

M. Pavlů, J., Beránek, M., Vaverka, J., Šafránková, J., Němeček, Z., Richterová, I., Secondary electron emission from martian soil simulant. *J. Geophys. Res.* 119 (1): 199–209, 2014.

N. Richterová, I., Němeček, Z., Pavlů, J., Beránek, M., Šafránková, J., Modeling the secondary emission yield of salty ice dust grains. *Icarus* 212 (1): 367–372, 2011.

O. Vaverka, J., Richterová, I., Vyšinka, M., Pavlů, J., Šafránková, J., Němeček, Z., The influence of secondary electron emission on the floating potential of tokamak-born dust. *Plasma Phys. Contr. F.* 56 (2): 025001, 2014.

A. Pavlů et al. [2004]

Pavlů, J., Velyhan, A., Richterová, I., Němeček, Z., Šafránková, J., Čermák, I., Žilavý, P., Mass-loss rate for MF resin microspheres. *IEEE Trans. Plasma Sci.* 32 (2): 704–708, 2004.

Mass-Loss Rate for MF Resin Microspheres

Jiří Pavlů, Andriy Velyhan, Ivana Richterová, Zdeněk Němeček, Jana Šafránková, Ivo Čermák, and Peter Žilavý

***Abstract*—This paper deals with the influence of experimental conditions on properties of melamine formaldehyde resin particles. Motivation for this study was the fact that many laboratories and experimenters use these particles as samples for dust plasma investigations. We have found that the mass of these grains decreases during long-time exposure in vacuum. This decrease proceeds much faster if the temperature of grains is increased.**

***Index Terms*—Charging of dust grains, dusty plasma, melamine formaldehyde (MF) resin.**

I. Introduction

IMMERSING of small particles into plasma leads to a new and unusual plasma behavior [1]. Like small probes, these grains become charged. This opens the possibility for modified or entirely new collective modes of oscillation, instabilities, and linear or nonlinear waves. Because the charge state of particulate varies with plasma conditions, and actually fluctuates in time, and the dust grains have a distribution of sizes as well as shapes, the plasma state of this system, so-called dusty plasma, is much more complicated. Indeed, sometimes the term *complex plasmas* has been used to give a somewhat more accurate description of dusty plasma systems [2], [3].

In the last 20 years, the subject of dusty plasmas was studied not only theoretically, but there were *in situ* measurements of charged dust grains in space and laboratory experiments. Now, there are observations from space, e.g., close-up views of planetary rings, observations of dust streams in space, data from rocket flights through noctilucent clouds in the upper atmosphere, as well as numerous measurements of particle contaminants in plasma processing systems. Moreover, a wide variety of laboratory experiments exist, and others are planned for the International Space Station [4], [5].

These experiments usually apply the melamine formaldehyde (MF) resin particles as a dust simulant (e.g., [5]–[8]). Advantages of this simulant are spherical shape with guaranteed diameter and well-defined mass density. Note that the manufacturer checks the mass density of the MF grains themselves. However, we have found that some parameters of these particles change during experiments. Since such changes would be of interest for interpretation of results obtained in other laboratories, this paper is devoted to their extensive study.

Manuscript received August 14, 2003; revised October 16, 2003. This work was supported in part by the Charles University Grant Agency under Contract 176/01, by the Czech Republic Grant Agency under Contracts 205/02/D113 and 202/04/0912, and by the *Vakuum Praha* Corporation.

J. Pavlů, A. Velyhan, I. Richterová, Z. Němeček, J. Šafránková, and P. Žilavý are with the Faculty of Mathematics and Physics, Charles University, Prague, Czech Republic.

I. Čermák is with the Technical University, Chemnitz, Germany.

Digital Object Identifier 10.1109/TPS.2004.826120

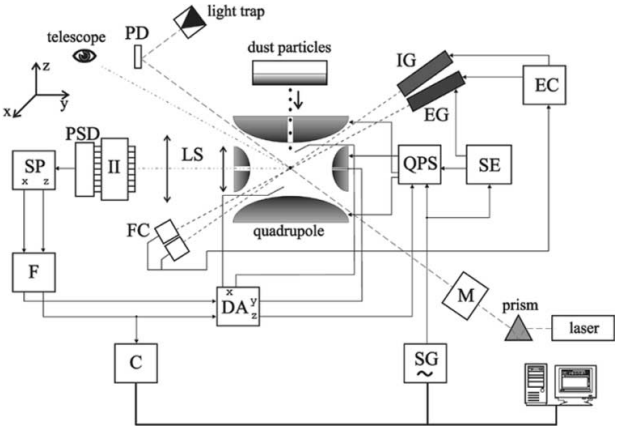

Fig. 1. Experimental setup: SG is signal generator, QPS is quadrupole power supply, SE is sampling electronics, FC are Faraday cups, EC is emissivity control, IG is ion gun, EG is electron gun, LS is lens system, II is image intensifier, PSD is position sensitive detector, SP is signal processing, F is filter, C is counter, DA is damping amplifier, M is acoustooptical modulator, and PD is photodiode.

II. Experimental Facility

Our experimental investigation is based on trapping a single dust grain in an electrodynamic quadrupole and its influencing by tunable mono-energetic ion and/or electron beams (Fig. 1). The electrodynamic quadrupole together with the dust reservoir are placed inside an ultrahigh vacuum chamber (pressure in the chamber is less than 10^{-8} mbar) [9]. The quadrupole is supplied symmetrically so that there is zero potential in the middle of the trap. From the quadrupole theory, it follows that the vertical electrodes should be supplied by the same voltage. However, we are using two different amplifiers for them in order to apply a dumping voltage and dc voltage for the compensation of the gravity force.

A trapped grain is irradiated by an He–Ne laser beam modulated by 10 kHz by an acoustooptical modulator. The laser light scattered by the grain is collected by a simple lens system, and the magnified grain image is projected onto the entrance fiber optic of an image intensifier. The intensifier output is optically coupled to a PIN diode serving as a position sensitive detector. Signals from the PIN diode are amplified by narrow band, and lock-in amplifiers prior to the coordinates of the light spot are determined. These coordinates are used to control the motion of the particle by a damping system. The current charge-to-mass ratio Q/m is calculated from the measured particle secular frequency f_z, and the currently used values of the quadrupole supply voltage V_{ac} and its frequency f_{ac}. The information of the particle Q/m ratio is used to influence the frequency f_{ac} of the quadrupole voltage V_{ac}, in order to ensure the stability of

the trapped particle. According to [9], the Q/m ratio is given by

$$\frac{Q}{m} = \pi^2 r_0 \frac{f_{ac} f_z}{V_{ac}} \cdot c(f_z, f_{ac}) \tag{1}$$

where r_0 stands for the inner radius of the middle quadrupole electrode and c is a correction function closed to unity which reflects the f_z/f_{ac} ratio and actual field geometry inside the trap.

In previous studies [9], [10], the beam was emitted continuously and thus the ac electric field inside the quadrupole caused defocusing of the beam and deflection of electrons toward the quadrupole electrodes (a quadrupole voltage ranges usually from 400–900 V in a frequency range of 0.3–3 kHz). It resulted in a presence of a significant density of the secondary electrons with a broad energy spectrum. Moreover, the relative density and the energy spectrum of these electrons (so-called background electrons) were unknown functions of the beam setting and energy. For this reason, the electron beam as well as the quadrupole power supply have been provided with a sampling electronics. The electron beam is switched on only inside the time window when the quadrupole voltage is pulled down to zero. According to the test, switching off the (primarily sinusoidal) quadrupole voltage up to 1/10 of a period does not measurably change the frequency of particle oscillations, and thus the calculated Q/m of the particle remains unchanged.

III. Particles Used for a Study

Monodisperse melamine resin particles [12] are polymer microspheres that are manufactured by hydrothermal acid-catalyzed polycondensation of methylol melamines in the temperature range 70–100 °C. According to cataloque values, MF particles have following properties:

- high monodispersity and uniformity with a spherical shape;
- hydrophilic surface;
- mass density of 1510 kg/m^3.

For our long-time study, we used particles (according to catalogue values) with diameters of 2.35±0.04 μm ($m \sim 1.0 \times 10^{-14}$ kg) and 9.78±0.13 μm ($m \sim 7.4 \times 10^{-13}$ kg). Their electron microscope images are presented in Fig. 2.

IV. Determination of Particle Parameters

The information about Q/m is important but insufficient for the description of charging process. Even in the case when well-defined samples are studied, the measurements of the grain mass and size are important. Dust samples often tend to create clusters or a fragment of a grain can be caught in the quadrupole. Moreover, parameters of some samples can evolve with the time as we would like to demonstrate in this paper.

For determination of grain size, a discharging process of a strongly positively charged grain was used. In this case, the beam ions cannot reach the particle surface due to the electrostatic repulsion. However, secondary electrons are produced on the quadrupole electrodes and cause the discharging of the particle. The particle's surface potential decreases, and when it

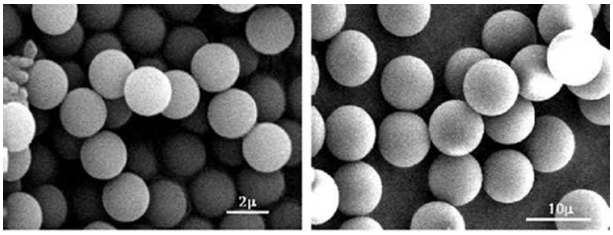

Fig. 2. MF particle photos taken by electron microscope: (a) $D = 2.35$ μm and (b) $D = 9.78$ μm. Length bars are not calibrated.

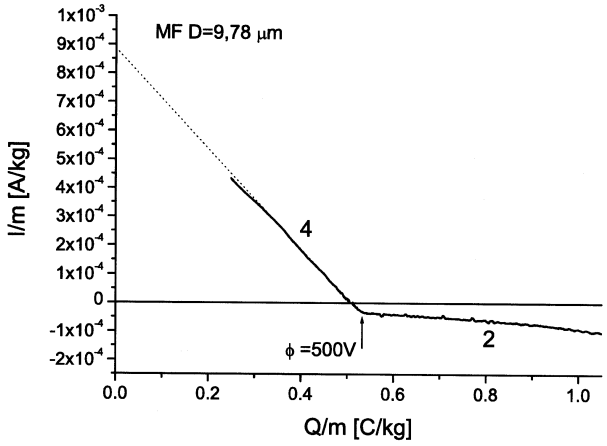

Fig. 3. Determination of specific capacitance C of the grain.

reaches a value at which the beam ions just come to the particle surface, the discharging current of secondary electrons compensates the ion current and the discharging slows down suddenly. The corresponding surface potential ϕ can be calculated from the energy E_i of the primary ions: $\phi = E_i/e_0$ where e_0 is the elementary charge. The knowledge of these values allows us to determine the particle radius from

$$r = \sqrt{\frac{3\varepsilon_0 \phi}{\rho} \cdot \frac{m}{Q}} \tag{2}$$

where ρ means the particle mass density and ε_0 is the dielectric constant of vacuum.

This process is presented in Fig. 3; the curve was obtained in several steps.

1) The grain was charged to the specific charge of Q/m of ~ 1 C/kg by the 5-keV ion beam.
2) The beam energy was stepwise decreased to 500 eV. Since ions of this energy cannot reach the grain due to its high potential, the grain is discharged by background electron current I_{back} and the temporal change of the specific charge was recorded until the specific charge reached its equilibrium value corresponding to 500 eV of the beam energy.
3) The beam energy was switched to ~ 200 eV and the grain was discharged to ~ 0.2 C/kg.
4) The beam energy was again switched to 500 eV and the temporal change of the grain charge was recorded.

5) First derivatives of the records (2) and (4) representing the current on the grain are plotted in Fig. 3 as a function of the grain charge.

The curve in Fig. 3 thus consists of two parts denoted as 2 and 4, according to the above description. The first of them corresponds to the background current and the second to the sum of the background and the beam currents. Their intersection shows a point where the grain potential is equal to the beam energy (500 eV). This point allows us to determine the proportionality constant between the grain specific charge and its surface potential, the specific capacitance C.

The nondestructive mass determination of the particle is based on the observation of stepwise changes in Q/m attributed to particle charging in steps of integral numbers of the elementary charge [13]. If the parameters V_{ac} and f_{ac} of the quadrupole voltage are constant during the observation, the relative change of particle frequency oscillations f_z is equal to the relative change of the Q/m ratio, according to (1).[1] In the case of micron-sized particles charged to an equilibrium surface potential about of 10 V, the relative frequency change is of the order of 10^{-4}, as can be seen in Fig. 4.

The key problem of this measurement is a suitable source of units of charged particles. In our experiment, the ion gun with switched off filament has been used. It was found that the natural ionization in the gun ionization chamber causes the charging of the investigated particle by several units of elementary charge per day. Ion gun voltages have been switched on for a few seconds in a period of $\sim$30 min. This caused a stepwise change of the particle charge. Corresponding averaged temporal dependence of the particle oscillation frequency f_z is presented in Fig. 4(a). The heights of frequency steps have been estimated and the elementary step of particle oscillation frequency Δf_z has been determined [Fig. 4(b)] by a linear regression. The particle charge can be found from

$$Q = \frac{e_0 \cdot f_z}{\Delta f_z} \tag{3}$$

and the mass of the particle is given as

$$m = \frac{e_0 \cdot f_z}{\Delta f_z} \frac{1}{\frac{Q}{m}} \tag{4}$$

where f_z and Q/m are known from the experiment.

V. Variations of MF Grain Parameters

The two methods described allow us apparently to determine the mass and diameter for any spherical grain. However, the first method cannot be applied in our setup to a small grain; whereas, the method of elementary charge provides good results for small grains only.

The experiments with emission properties of dust grains require well-defined parameters. For this reason, we have chosen MF dust simulants which have a perfect sphericity and well-defined diameter. However, in a course of three months of continuous measurements, we have observed a systematic change

[1]That is true only for small changes because of the nonlinearity of the correction function c in (1).

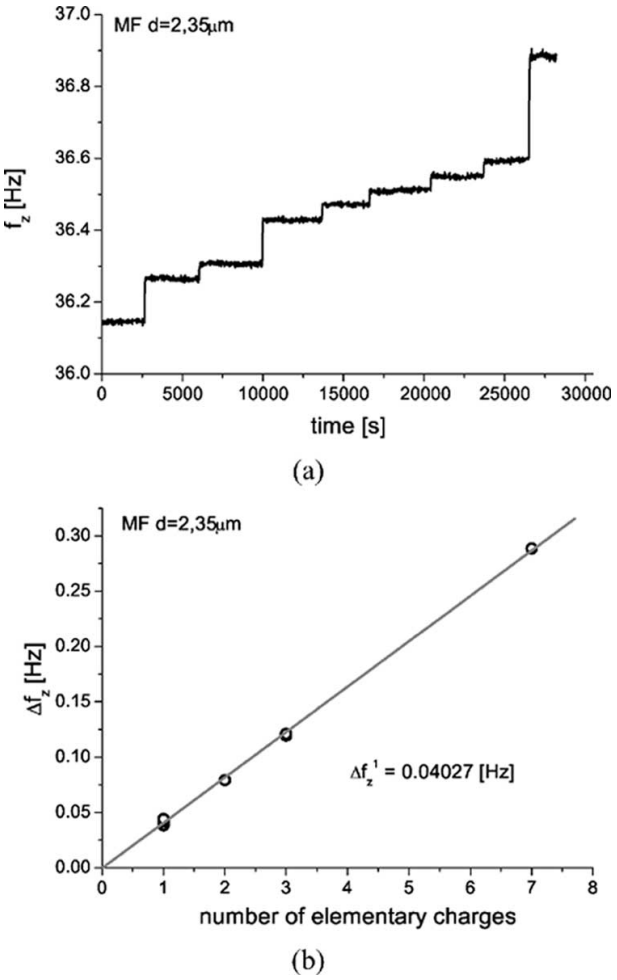

Fig. 4. Determination of the grain mass by the elementary charge method: (a) frequency jumps and (b) linear regression of these jumps.

of proportionality constant between the charge-to-mass ratio and grain surface potential determined by the method described above. This proportionality constant is hereafter denoted as C for briefness. The changes of C are demonstrated in Fig. 5 for 10 μm MF grains. The figure shows the measurements carried out on $\sim$50 different grains. We would like to point out that the precision of our measurements of C is better than $\pm 3 \times 10^{-4}$. This value was determined from 15 measurements of the same grain in the course of three days using different ion gun energies.

From the analysis in Fig. 5, it follows that the initial spread of C is about $\pm 4\%$, and it conserves for the whole time of measurements. The manufacturer [12] declares a precision of the diameter determination of ± 0.13 μm and the photo from the electron microscope (Fig. 2) confirms this value.

Assuming that the mass density of all grains is the same, the uncertainty of the diameter is able to explain the aforementioned spread. The $\pm 4\%$ limit is shown by two thin lines in Fig. 5. The most significant change of a mean value of C occurred at day 39 when the grains were baked out for 6 h at 240 °C. The average value of C changed by $\sim 8\%$ during this baking. Before and after

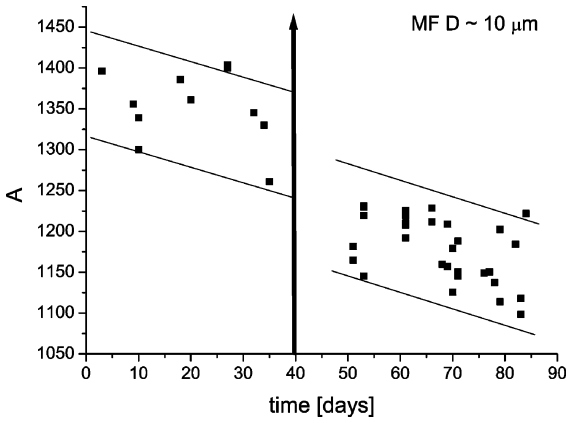

Fig. 5. Long-time statistics of proportionality constant C ($\sim 10\mu$m grain). Arrow denotes the time of baking.

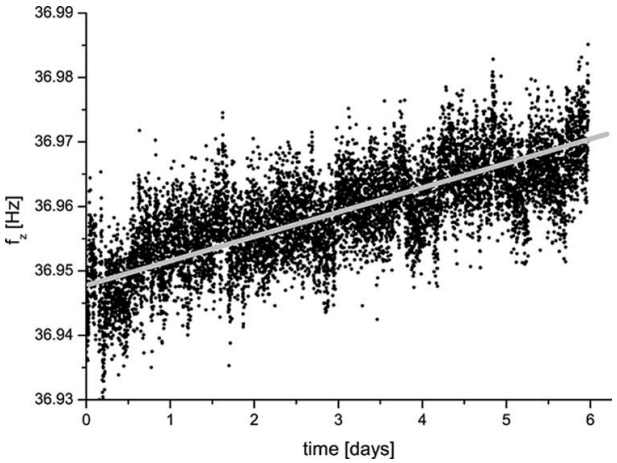

Fig. 6. Demonstration of time evolution of the grain mass.

baking, C decreases very slowly. A slope of the decreasing will be discussed later.

The interpretation of these results is not straightforward. We can probably assume that grains conserve their spherical shape. The decrease of the ratio C can be simply attributed to a decrease of the grain mass ($C = \phi \cdot m/Q$), if grains do not change diameters. On the other hand, C can be interpreted as a specific capacitance and thus

$$C \sim R^2 \cdot \rho \tag{5}$$

where ρ stands for the mass density. This simple expression reveals that the ratio C is more sensitive to a change of the grain radius than to a change of the mass density.

Unfortunately, measurements of the grain mass cannot be carried out on the same grain with sufficient accuracy, as we pointed out in the previous section. Therefore, we measured the change of the mass of a single 2.35-μm grain from the same material as it is presented in Fig. 6. The measurement started about 12 h after beginning of the pumping and lasted about five days. We have recorded the measurements of Q/m continuously but the noise exhibits daily variations connected with surrounding activities as can be seen in the figure. The linear increase of the frequency can be attributed to a decrease of the grain mass because the whole rise is smaller than that corresponding to one elementary charge ($\sim$0.04 Hz, see Fig. 4). Grain masses determined at the beginning and end of measurements show the mass change $\sim$0.015% per day.

The speed of the mass losses was recalculated into units used in Fig. 5 and determines the slope of thin lines bounding experimental points. As can be seen from the plot, the determined mass losses together with the uncertainty of the grain diameters can fully explain the observed behavior of the ratio C.

VI. Conclusion

We have demonstrated that our experimental facility is able to measure relative changes of the dust grain mass of the order of $\sim 10^{-4}$. These measurements were used for a description of the time-evolution of MF grain parameters. We have found that 2.35 μm grains placed into a vacuum vessel gradually evaporate with a speed of $\sim 1.2\times 10^{-18}$ kg/day. Such speed can explain the behavior of the charge-to-mass ratio observed on $\sim$10 μm grains.

A baking of the grains in vacuum at $\sim$240 °C causes a relative decrease of the grain mass by $\sim$10%. We think that the rate of mass change speed of the nonheated dust simulant is probably negligible for most laboratory experiments because the mass decreasing cannot reach the limits given by the uncertainty of the grain diameter in a reasonable time. However, this change can be of considerable interest in experiments where grains can be heated (or stored in vacuum for a very long time). The total mass loss during the time interval in Fig. 6 was $\sim 5\times 10^{-18}$ kg. Since the grains were exposed to air, we can expect a monolayer of water adsorbed on the surface. Such a monolayer weighs about 2.4×10^{-20} kg, only. According to the manufacturer, this difference can be attributed most probably to water originally bounded in the bulk material. We expect that the adsorbed layer desorbed prior our experiment starting, i.e., in the course of the first 12 h of pumping.

Acknowledgment

The authors would like to thank to Dr. E. Stoffels and Dr. W. Stoffels who kindly provided the investigated MF grains. Furthermore, the authors express thanks to Prof. D. Vítek for useful comments.

References

[1] D. A. Mendis, "Physics of dusty plasmas: An historical overview," *Adv. Dusty Plasmas*, pp. 3–19, 1997.

[2] A. Piel and A. Melzer, "Dynamical processes in complex plasmas," *Plasma Phys. Contr. Fusion*, vol. 44, pp. R1–R26, Jan. 2002.

[3] G. E. Morfill *et al.*, "A review of liquid and crystalline plasmas — New physical states of matter?," *Plasma Phys. Contr. Fusion*, vol. 44, pp. B263–B277, Dec. 2002.

[4] A. P. Nefedov *et al.*, "PKE-Nefedov: Plasma crystal experiment on the international space station," *New J. Phys.*, vol. 5, pp. 33.1–33.10, Apr. 2003.

[5] G. E. Morfill *et al.*, "Complex plasmas under microgravity conditions: First results from PKE-Nefedov," in *Proc. Dusty Plasmas in the New Millenium, Third Int. Conf. Physics Dusty Plasmas*, vol. 649, Durban, 2002, pp. 91–109.

[6] P. Roca i Cabarrocas *et al.*, "Plasma grown particles: From injected gases to nanoparticles and nanomaterials, from injected particles to dust clouds in the PKE experiment," in *Proc. Dusty Plasmas in the New Millenium, Third Int. Conf. Physics Dusty Plasmas*, vol. 649, Durban, 2002, pp. 45–52.
[7] G. V. Paeva, W. W. Stoffels, R. P. Dahiya, E. Stoffels, and M. W. Kroesen, "Voids in dust clouds suspended in the plasma sheath," in *Proc. Dusty Plasmas in the New Millenium, Third Int. Conf. Physics Dusty Plasmas*, vol. 649, Durban, 2002, pp. 188–191.
[8] A. A. Samarian and O. Vaulina, "Dust vortex in complex plasma," in *Proc. Dusty Plasmas in the New Millenium, Third Int. Conf. Physics Dusty Plasmas*, Durban, 2002, pp. 406–409.
[9] I. Čermák, E. Grün, and J. Švestka, "New results in studies of electric charging of dust particles," *Adv. Space Res.*, vol. 15, pp. (10)59–(10)64, 1995.
[10] P. Žilavý, Z. Sternovský, I. Čermák, Z. Němeček, and J. Šafránková, "Surface potential of small particles charged by the medium-energy electron beam," *Vacuum*, vol. 50, no. 1–2, pp. 139–142, June 1998.
[11] Z. Sternovský, P. Žilavý, Z. Němeček, and J. Šafránková, "Charging of small solid bodies: Laboratory simulation," in *Proc. ICPP 25th EPS Conf. Contr. Fusion Plasma Physics*, vol. 22C, 1998, pp. 2549–2552.
[12] [Online]. Available: www.microparticles.de
[13] P. Žilavý, Z. Němeček, and J. Šafránková, "Size and density determination of a spherical particle in the dust charging experiment," in *WDS'99 Proc. Contributed Papers*, 1999, pp. 252–257.

Jiří Pavlů was born in 1977 in Pardubice, Czech Republic. He received the M.S. degree from Charles University, Prague, Czech Republic, in 2001, and is currently working toward the Ph.D. degree there.

At present, he works in the Space Physics Laboratory, Department of Electronics and Vacuum Physics, Faculty of Mathematics and Physics, Charles University. His research interests include the laboratory investigation of elementary charging processes on dust grains.

Andriy Velyhan was born in 1976 in Uzhgorod, Ukraine. He received the M.S. degree in physics in 1999 from Uzhgorod State University, Uzhgorod, Ukraine, and he is currently working toward the Ph.D. degree at Charles University, Prague, Czech Republic.

His research interests include space and dusty plasmas and laboratory investigations of charging processes of dust grains. His speciality is the physics of solid state.

Ivana Richterová was born in 1979 in Český Brod, Czech Republic. She is working toward the M.S. degree at Charles University, Prague, Czech Republic, with diploma thesis "Emission Properties of Dust Particles."

Zdeněk Němeček was born in 1947 in Prague, Czech Republic. He received the M.S., Ph.D., and Dr.Sc. degrees from Charles University, Prague, Czech Republic, in 1971, 1982, and 1996, respectively.

Since 1971, he has held several positions in the Faculty of Mathematics and Physics, Charles University, where he is currently Vice Dean of the Faculty. His research interests include dealing with the solar wind interaction with the Earth's magnetosphere and the laboratory simulation of plasma processes.

Jana Šafránková was born in 1947 in Teplice, Czech Republic. She received the M.S., Ph.D., and Dr.Sc. degrees from Charles University, Prague, Czech Republic, in 1972, 1982, and 1996, respectively.

Since 1971, she has held several positions in the Faculty of Mathematics and Physics, Charles University, where she is currently Deputy Director of the Department of Electronics and Vacuum Physics and the Head of Space Physics Laboratory. Her recent research interests include the magnetospheric physics and laboratory simulation of elementary processes in dusty plasmas.

Ivo Čermák was born in 1966 in Velké Meziříčí, Czech Republic. He received the M.S. degree from Charles University, Prague, Czech Republic, in 1989 and the Ph.D. degree at the Rurecht-Karls University, Heidelberg, Germany, in 1994.

In the period 1994 to 1999, he worked as a Postdoctoral Researcher at MPI Heidelberg. Since 1999, he has held a position of Scientific Assistant at the University of Technology, Chemnitz, Germany. His research interests include collision processes in ion traps, charge state, and dynamics of cosmic dust.

Peter Žilavý was born in 1971 in Košice, Slovak Republic. He received the M.S. and Ph.D. degrees from Charles University, Prague, Czech Republic in 1996 and 2001, respectively.

At present, he works as a Scientist at the Department of Physics Education, Faculty of Mathematics and Physics, Charles University. His research interests include laboratory and computer simulations of the elementary processes in dusty plasmas.

B. Beránek et al. [2012]

Beránek, M., Čermák, I., Němeček, Z., Šafránková, J., Jeřáb, M., Pavlů, J., Linear trap with three orthogonal quadrupole fields for dust charging experiments. *Rev. Sci. Instrum.* 83 (11): 115109, 2012.

Linear trap with three orthogonal quadrupole fields for dust charging experiments

Martin Beránek,[1] Ivo Čermák,[2] Zdeněk Němeček,[1] Jana Šafránková,[1]
Martin Jeřáb,[1] and Jiří Pavlů[1]
[1]*Charles University, Faculty of Mathematics and Physics, Prague, Czech Republic*
[2]*CGC Instruments, Chemnitz, Germany*

(Received 25 July 2012; accepted 24 October 2012; published online 27 November 2012)

Investigations of charging processes on a single dust grain under controlled conditions in laboratory experiments are the unique way to understand the behavior of dust grains in complex plasma (in space, in laboratory, or in technological applications). An electrodynamic trap is often utilized for both holding a single grain and continuously measuring its charge-to-mass ratio. We propose a modified design of the linear quadrupole trap with the electrodes split into two parts; each of them being supplied by a designated source. The paper presents basic calculations and the results of the trap prototype tests. These tests have confirmed our expectations and have shown that the suggested solution is fully applicable for the dust charging experiments. The uncertainty of determination of the dust grain charge does not exceed 10^{-3}. The main advantages of the suggested design in comparison with other traps used for dust investigations can be summarized as: The trap (i) is more opened, thus it is suitable for a simultaneous application of the ion and electron beams and UV source; (ii) facilitates investigations of dust grains in a broader range of parameters; and (iii) allows the grain to move along the axis in a controlled way. © *2012 American Institute of Physics*. [http://dx.doi.org/10.1063/1.4766955]

I. INTRODUCTION

After its invention in the 1950s, an electrodynamic quadrupole trap (generally referred to as Paul trap[1]) and/or its different modifications quickly proved to be an extremely powerful tool for the experimental investigation of a wide range of phenomena. Various designs of traps are applied in formation of ion Coulomb crystals, in quantum computations, for application in optical frequency metrology, ion mass spectrometry, or high-resolution optical and microwave spectroscopy and many others.

Although originally developed for ion spectroscopy,[2] the method of trapping charged particles with time-varying electric fields is not restricted to atomic or molecular ions but is used equally to charged microparticles. It has been successfully employed to investigate single micron-sized grains.[3] Using this technique, photoemission experiments with the UV radiation[4,5] and rotation and alignment of dust grains by the radiation pressure[6] have been performed. A similar set-up was used in laboratory experiments where micron-sized grains bombarded by keV electrons were stored and a size dependence (observed by Svestka, Cermak, and Grün[7] and qualitatively explained by Chow, Mendis, and Rosenberg[8]) was investigated. An electrodynamic quadrupole inside an ultrahigh vacuum chamber was applied by Cermak, Grün, and Švestka[9] to trap grains of micron and submicron sizes which were charged by electron and ion beams of energies up to 5 keV.

In recent years, a 3D quadrupole trap[10–12] operating under ultrahigh vacuum conditions (10^{-7} Pa) was used for investigations of different charging processes on single grains from various materials. The experiments focused on secondary and ion or electron field emissions and on grain sputtering were reported.[13–19] Also Grimm *et al.*[20] studied the charging of dust particles in a high vacuum quadrupole trap, however, the grains were exposed to soft X rays in this case.

In the paper, we propose a linear quadrupole trap based on the ion trap technique for investigations of dust grains in wide ranges of their parameters. Our modified version of a trap uses each rod divided into two parts and split into two isolated cylinders. The paper discusses different requirements on both ion and dust traps, presents basic equations governing the motion of the grain within the trap and analyzes possible errors. We also describe the trap realization, its properties, and its experimental verification based on its first prototype.

II. DIFFERENCES BETWEEN ION AND DUST TRAPS

Although the problems of trapping a single charged dust grain or an ensemble of ions are similar in principle, there are important differences that should be taken into account in the trap design. Let us list the expected ranges of parameters of the investigated grains:

- Grain dimensions: 0.1–100 μm
- Grain mass: 10^{-18}–10^{-9} kg
- Specific charge: $\pm(10^{-3}$–$10^{2})$ C/kg
- Rate of specific charge changes: up to 10 C/(kg s)

As it can be seen from this list, the trap for the dust charging experiment should enable a stable grain trapping in much broader ranges of parameters than the ion trap. Another important difference is that the ion trap is used for trapping of a limited number of ion species that differ only slightly in their specific charges and these specific charges are known. Moreover, the fact that the ion outside a given range of

specific charges will leave the trap can often help to purify the trap content. By contrast, the dust trap should allow measuring the grain specific charge and provide the stable trapping even under fast changes of this charge by several orders of magnitude.

The known specific charges of ions can be used for calibration of a trap. However, the dust trap cannot be calibrated in this way and the only possibility for absolute measurements is to rely on calculations. Such calculations are difficult even for a very simple geometry, thus it is important to keep the trap design close to that used in calculations.

III. PROBLEMS OF DUST PARTICLE TRAPS

The charge of the trapped micron and submicron grains can be determined either by the additional dc field [as demonstrated e.g., by Ref. 21] or by measuring the frequency of the grain oscillations (so-called the secular frequency) [e.g., Refs. 9 and 11]. The latter technique is more precise and reliable if the grain oscillatory motion does not depend on the oscillation amplitude and/or on the grain location within the trap. It means that the force holding the grain inside the trap (confining force) should be proportional to its displacement or, in other words, the corresponding potential should be parabolic. Thus, the only non-zero term of the expansion of the electric field inside the trap should be the quadrupole (harmonic) term and higher multipole (anharmonic) terms should be suppressed in a sufficiently large volume of the trap.

Since the gravitational forces acting on a weakly charged grain significantly exceed the confining force that is proportional to square of the grain charge in quadrupole traps, the gravity should be compensated by an additional dc voltage. However, the electric force is proportional to the grain charge and fast variations of the grain charge lead to a corresponding change of the location of the investigated grain with respect to the trap center. As noted above, the confining force depends on the grain charge and its variations lead to the changes of the oscillation amplitude. Many dust charging experiments[6] use an interaction of the trapped grains with the surrounding gas for the damping of grain oscillations. However, a simulation of the conditions in the interplanetary space requires ultrahigh-vacuum conditions and another method of control of the oscillation amplitude is required.

The damping force should be in anti-phase with the grain motion, thus the grain position should be continuously recorded and this signal used in the feedback loop. In order to reach a sufficient accuracy of the damping system, the amplitude of the grain motion would be approximately 1 mm. Since the maximum size of the trap is limited by the applied RF voltage (≈up to several kV), the amplitude of grain oscillations is approximately 1/10 of the trap inner radius. Cermak, Grün, and Švestka[9] suggested using auxiliary electrodes for this purpose but their application leads to increase of a content of higher multipole terms inside the trap, thus a solution that uses the trap electrodes for the damping voltages would be preferred.

To ensure a homogeneous illumination of the trapped grain with particle beams, their cross-sections should be larger than the expected amplitude of motion. Consequently, only a small portion of the beam particles will interact with the investigated grain and the rest of particles should leave the trap without any interaction with its electrodes because photoelectrons and/or secondary electrons generated due to such interaction would spoil the measurements. This is the major problem of traps that use the rotationally symmetric design [e.g., Refs. 6, 7, 9 and 21].

IV. SUGGESTED SOLUTION OF A LINEAR TRAP

From these limitations it follows that the trap based on a linear quadrupole[22] would be a possible solution because it can be designed as open as possible and provides free path for particle and photon beams along its major axis and two planes among trap rods. However, a standard linear four-rod trap can confine the grain along the trap axis rather than just in a single point of the coordinate space.

Several modifications were proposed for the grain confinement along the quadrupole main axis. Some authors suggested to split each quadrupole rod into two[23] or three[24,25] parts allowing a dc voltage to be applied to the eight end-electrode pieces. Another possibility is to use auxiliary dc electrodes[26] that produce the confining electric field. Such trap variations are often used in quantum computations[27] and in investigations of large ion Coulomb crystals.[28,29]

An analysis of these trap configurations[26] has shown that splitting of the electrodes into three parts and an application of the dc confining voltage on the end parts of rods substantially increases the anharmonic terms of the trap field. This problem can be partly compensated by a combination of RF and dc voltages on these parts of electrodes [e.g., Ref. 26]. Since the peculiarities of the dust charging experiment require an addition of the dumping signals to the voltages supplying the electrodes, this solution leads to 12 high-voltage broadband RF amplifiers. On the other hand, the solution with additional dc electrodes does not spoil the quadrupole field within a reasonable volume around the trap center but it requires an application of large voltages. Reaching typical values of confining force achieved in our present quadrupole trap would require ≈50 kV of the dc voltage and the damping signals would be added to this voltage. Pedregosa *et al.*[26] suggested a modification of the shape of the dc electrodes that leads to decrease of this voltage but such version enhances the anharmonic terms of the quadrupole field.

Moreover, the confining dc electric field would affect the trajectory of low-energy ion and electron beams used for the grain charging. In the case of the ac electric fields, the beams can be switched-on for a short period around the zero voltage but the dc voltage would be switched-off when the particle beams are in operation. A periodic switching of the high-voltages would cause problems of sensitive detection electronics because relatively large electrodes would serve as effective antennas.

Last but not least, the dc confinement depends on the sign of the trapped grain charge. This is not critical for ion traps, however, the charge sign of the dust grain can change even in course of the experiment and one of our aims is investigation of this process.

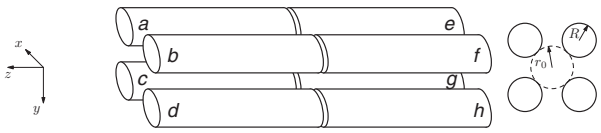

FIG. 1. The geometry and dimensions of the trap. The origin of coordinates is situated in the center of the trap.

A. The electric field in the trap

We propose to use the classical (four-rod) linear quadrupole and to split each electrode into two parts with a small insulating gap in between. The main idea of the trap is based on a superposition of three ac quadrupole fields. The design of such solution is shown in Fig. 1. The figure shows the trap geometry and defines the coordinate system used in our calculations. The parts of rods are labeled with a, b, …, h. Figure 2 schematically demonstrates the voltages providing three quadrupole fields. If we neglect the insulating gap, the voltages $\pm V_z$ shown in the left part of the figure will create the quadrupole field in the plane $z = 0$ because this is a standard linear quadrupole. The middle and right panels show the potentials creating the quadrupole fields in planes $x = 0$ and $y = 0$, respectively. We would like to note that we expect the same frequency and zero phase shift of both V_z and V_{xy}. The voltage applied onto the particular electrode is a sum of partial voltages shown in Fig. 2. It means that the half-rods will be supplied by

$$\begin{aligned}
V_a &= -V_z + V_{xy} - V_{xy} = -V_z,\\
V_b &= +V_z - V_{xy} - V_{xy} = +V_z - 2V_{xy},\\
V_c &= +V_z + V_{xy} + V_{xy} = +V_z + 2V_{xy},\\
V_d &= -V_z - V_{xy} + V_{xy} = -V_z,\\
V_e &= -V_z - V_{xy} + V_{xy} = -V_z,\\
V_f &= +V_z + V_{xy} + V_{xy} = +V_z + 2V_{xy},\\
V_g &= +V_z - V_{xy} - V_{xy} = +V_z - 2V_{xy},\\
V_h &= -V_z + V_{xy} - V_{xy} = -V_z.
\end{aligned} \tag{1}$$

The simplified view suggests that only three different HV supplies (amplifiers) can be used. This is true for the grain confinement but additional requirements such as a compensation of the gravity force or damping of the grain oscillation amplitude lead to a requirement of a dedicated supply for each half-rod.

The voltage supplying the trap maintains the central symmetry (the voltage on the electrodes and the potential inside the trap do not change if we invert the coordinates). The lowest multipole term that such field can form is the quadrupole term. The electric potential φ inside the trap is a result of superposition of three partial potentials referred hereafter as φ_x, φ_y, and φ_z. The potential φ_z is generated by an alternating voltage of amplitude V_z applied to the rods according to Fig. 2. The resulting electric field does not change the sign if we invert direction of the z axis but changes the sign if the direction of any of remaining two axes is inverted. Therefore, the only possible quadrupole term is proportional to xy. Introducing the geometrical factor λ_z and neglecting the higher multipole terms, we can write the equation,

$$\varphi_z = \lambda_z V_z \cdot \frac{xy}{r_0^2} \cdot \cos \omega t, \tag{2}$$

where r_0 is the radius of the inner void cylinder (see Fig. 1, right) and ω is the angular frequency of the applied voltage. Note that the quadrupole term does not depend explicitly on the rod radius R in this approximation. The exact solution of the potential inside the trap[30] shows that the parameter λ_z weakly depends on the ratio R/r_0 that determines the content of higher multipole terms. These terms lead to an anharmonic motion of the trapped grain but, according to Douglas *et al.*[31], they are suppressed for the R/r_0 ratio around 1.1.

Analogously, we take advantage of the symmetry of other components of the potential (see Fig. 2). The geometrical factor for both of them is the same and we define $\lambda_{xy} = \lambda_x = \lambda_y$. The both fields are formed by the voltage of amplitude V_{xy}. The respective equations are

$$\varphi_x = \lambda_{xy} V_{xy} \cdot \frac{yz}{r_0^2} \cdot \cos \omega t, \tag{3}$$

$$\varphi_y = \lambda_{xy} V_{xy} \cdot \frac{xz}{r_0^2} \cdot \cos \omega t. \tag{4}$$

The amplitude of the electric potential can be written as $\varphi_0(r) = (\varphi_x, \varphi_y, \varphi_z)_{t=0}$ and the corresponding amplitude of the electric field as $E_0(r) = \nabla\varphi_0(r)$. Using the amplitude of the electric field, we can define the effective mechanical potential (i.e., the potential of the virtual field affecting the motion of the charged grain inside the electric field of sufficient frequency) according to Gerlich:[32]

$$u_{\text{eff}}(\mathbf{r}) = \frac{Q^2}{4m\omega^2} \cdot |\mathbf{E}_0(\mathbf{r})|^2, \tag{5}$$

where Q and m are the charge and mass of the trapped grain, respectively.

B. Secular frequency

The superposition of the potentials given by Eqs. (2)–(4) forms the effective potential with a minimum in the center of the trap. Free oscillations of the grain inside the trap can be

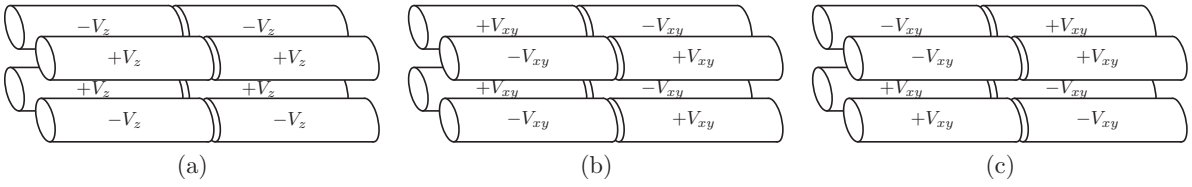

FIG. 2. Sketch of the voltages on electrodes forming the electric potentials φ_z, φ_y, and φ_x, respectively. The voltage applied on a particular segment of the rod is a sum of partial voltages shown in the figure.

thus described by eigenvectors and eigenvalues of the operator, $-\nabla u_{\text{eff}}$ (the operator of the force induced by the effective potential acting on the trapped grain). The equation of this operator can be simply obtained by the substitution of (2)–(4) into (5).

$$\begin{aligned}(-\nabla u_{\text{eff}})\begin{pmatrix}x\\y\\z\end{pmatrix} &= -\frac{Q^2}{4m\omega^2}\cdot\nabla|\mathbf{E}_0(\mathbf{r})|^2\\ &= -\frac{Q^2}{4m\omega^2}\cdot\nabla|\nabla\varphi_0(\mathbf{r})|^2\\ &= -\frac{Q^2}{4m\omega^2 r_0^4}\cdot\nabla|(\lambda_{xy}V_{xy}z+\lambda_z V_z y,\lambda_{xy}V_{xy}z\\ &\quad+\lambda_z V_z x,\lambda_{xy}V_{xy}(x+y))|^2. \qquad (6)\end{aligned}$$

We define the ratio of components of the electric field:

$$C=\frac{\lambda_{xy}V_{xy}}{\lambda_z V_z} \qquad (7)$$

and apply this relation to the previous expression:

$$\begin{aligned}&(-\nabla u_{\text{eff}})\begin{pmatrix}x\\y\\z\end{pmatrix}\\ &\quad=-\frac{Q^2\lambda_z^2V_z^2}{4m\omega^2r_0^4}\cdot\nabla|(Cz+y,Cz+x,C(x+y))|^2\\ &\quad=-\frac{Q^2\lambda_z^2V_z^2}{2m\omega^2r_0^4}\cdot\begin{pmatrix}C^2+1 & C^2 & C\\ C^2 & C^2+1 & C\\ C & C & 2C^2\end{pmatrix}\cdot\begin{pmatrix}x\\y\\z\end{pmatrix}. \qquad (8)\end{aligned}$$

We can rotate the coordinate system in such a way that the matrix representation of the operator will be diagonal. We get a new coordinate system (x', y', z') rotating by $\pi/4$ around the z axis and then rotating by θ around the x' axis. The exact value of θ depends on C as it is depicted in Fig. 3. The transformation matrix from the coordinates in a system (x, y, z) to the coordinates in the system (x', y', z') is

$$\begin{pmatrix}1 & 0 & 0\\ 0 & \cos\theta & -\sin\theta\\ 0 & \sin\theta & \cos\theta\end{pmatrix}\cdot\begin{pmatrix}1/\sqrt{2} & -1/\sqrt{2} & 0\\ 1/\sqrt{2} & 1/\sqrt{2} & 0\\ 0 & 0 & 1\end{pmatrix}, \qquad (9)$$

where

$$\cos\theta=\sqrt{\frac{1}{2}-\frac{1}{2\sqrt{8C^2+1}}}. \qquad (10)$$

Since the operator $-\nabla u_{\text{eff}}$ is purely diagonal in the new coordinate system, its eigenvectors (thus the principal directions of oscillations) are the base vectors of the new coordinate system:

$$(-\nabla u_{\text{eff}})=-\frac{Q^2\lambda_z^2V_z^2}{4m\omega^2r_0^4}\cdot\begin{pmatrix}2 & 0 & 0\\ 0 & 4C^2+1-\sqrt{8C^2+1} & 0\\ 0 & 0 & 4C^2+1+\sqrt{8C^2+1}\end{pmatrix}. \qquad (11)$$

The eigenvalues, α_i, of this operator determine the frequency of oscillations of the grain along the respective axis (secular frequency), Ω_i:

$$\Omega_i=\sqrt{-\frac{\alpha_i}{m}}=\frac{Q}{m}\cdot\frac{\lambda_z V_z}{2\omega r_0^2}\cdot\begin{Bmatrix}\sqrt{2} & \text{for } i=1,\\ \sqrt{4C^2+1-\sqrt{8C^2+1}} & \text{for } i=2,\\ \sqrt{4C^2+1+\sqrt{8C^2+1}} & \text{for } i=3.\end{Bmatrix}. \qquad (12)$$

The factor λ_z is easy to compute because it is a geometrical factor of an ordinal quadrupole consisting of four cylindrical rods. We slightly modified our design from the optimal ratio of a rod diameter and rod spacing and used 0.8 instead of 1.1 to get a more open trap. Beránek *et al.*[30] have shown that such deviation does not significantly affect the trap characteristics and the value of the geometrical factor of this particular trap geometry is

$$\lambda_z=1.95. \qquad (13)$$

On the other hand, the determination of the second geometrical factor, λ_{xy}, is difficult because it belongs to the component of the field generated by the voltage between the two parts of a single rod; solving such field is a three-dimensional problem.

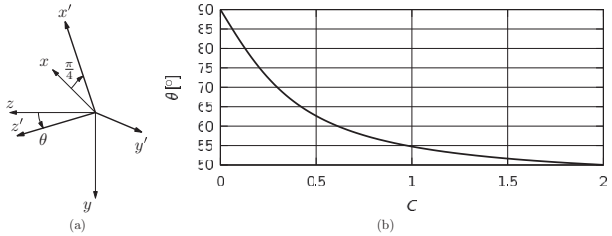

FIG. 3. Transformation of the coordinate system.

To make the calculations easier, we introduce symbols for general electric potentials, Φ_x and Φ_y, induced by the voltages according to Fig. 2 (center and right). We do not limit the calculations to the quadrupole term only but we assume a basic symmetry reflecting the symmetry of voltage supplies. It can be expressed by following identities:

$$\Phi_x(x, y, z) = \Phi_x(-x, y, z) = -\Phi_x(x, -y, z) = -\Phi_x(x, y, -z), \quad (14)$$

$$\Phi_y(x, y, z) = -\Phi_y(-x, y, z) = \Phi_y(x, -y, z) = -\Phi_y(x, y, -z), \quad (15)$$

$$\Phi_x(x, y, z) = \Phi_y(y, x, z). \quad (16)$$

Both $\Phi_x(x, y, z)$ and $\Phi_y(x, y, z)$ are even functions of variable z, therefore they are equal to zero in the whole plane $z = 0$ together with partial derivatives, $\partial/\partial x$ and $\partial/\partial y$. A sum of Φ_x and Φ_y is zero in the plane $x = -y$ that follows directly from equations above and the same is true for the partial derivative $\partial/\partial z$ in this plane. In the intersection of both planes (i.e., along the line $x = -y, z = 0$), there is the zero sum of potentials $\Phi_x + \Phi_y$ and the zero electric field generated by such potential. Thus, the oscillations along this line (i.e., the axis $\mathbf{x}'$) are independent of an actual amplitude and form of the electric field induced by the voltage V_{xy}. The only remaining field is the standard electric field of the linear quadrupole generated by the voltage of V_z.

While not important for measurements of a charge-to-mass ratio, the shapes and magnitudes of Φ_x and Φ_y electric fields are principal for the trap design. We have solved this three-dimensional problem using the Laplace solver of the SIMION® software[33] for dimensions of the trap used in our prototype. The results of numerical calculations have been fitted by spherical harmonics. The most significant terms of the fit are as follows:

$$\Phi_x(x, y, z) = \left(1.70\,\frac{yz}{r_0^2} - 1.26\,\frac{4xz^3 - 3x^3z - 3y^2xz}{r_0^4} - 0.47\,\frac{x^3z - 3y^2xz}{r_0^4}\right) \cdot V_{xy}\cos\omega t. \quad (17)$$

A formula for the potential Φ_y is same but with x and y interchanged. The grain should move in the region where the distance from the trap center is less than $0.1r_0$, therefore the original assumption of the quadrupole field can be considered to be valid with a sufficient accuracy based on the numerical results.

According to Eq. (17), we can express the coefficient C as a function of the ratio of voltages:

$$\lambda_{xy} = 1.70 \quad \Rightarrow \quad C = 0.87 \cdot V_{xy}/V_z. \quad (18)$$

Nevertheless, we would like to note that the first eigenvalue of operator Eq. (11) does not depend on C and thus the determination of the grain charge from Ω_1 would not depend on V_{xy}.

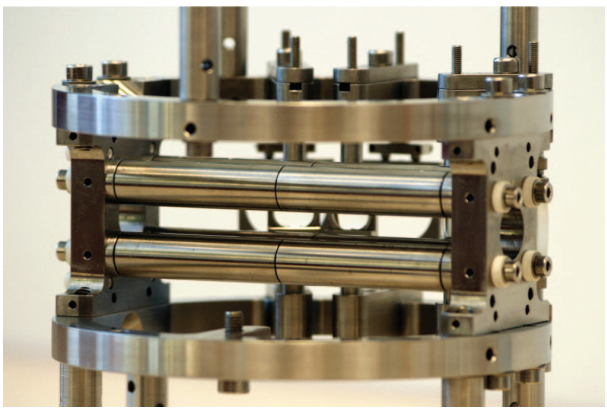

FIG. 4. The photo of the mechanical set-up of the new trap with holders.

V. EXPERIMENTAL VALIDATION

This section describes briefly a prototype of the trap that was built with motivation to check the theoretical considerations given above and analyzes the results of the prototype tests.

The trap is formed from four cylindrically shaped electrodes, each of them being split into two isolated cylinders of equal length on the common axis. The dimensions of the trap are as follows: the radius of each of four rods, R, is 6 mm, the rods are positioned around an inner empty cylinder of radius $r_0 = 7.5$ mm. The total length of the trap is 90 mm and the gaps dividing the rods are 0.5 mm wide. A photo of the assembled trap is shown in Fig. 4.

A. Experimental set-up

The trap was mounted inside a vacuum chamber that can be pumped down to ultrahigh vacuum ($<10^{-5}$ Pa). For validation, spherical SiO_2 grains 3–8 μm in diameter were used for several reasons: (1) the electron microscope revealed their almost perfectly spherical shape; (2) we have already investigated these grains and thus we know that they do not tend to form clusters; and (3) according to preliminary calculations, this diameter fits well to frequency and amplitude ranges of HV amplifiers used for the tests.

We dropped the grains into the powered trap from a dispenser and charged them during their fall by the electron beam until one of them had been trapped. The charge-to-mass ratio of the grain was of the order of 10^{-2} C/kg. The oscillations of the trapped grain were damped by a buffer gas (helium) and then the chamber was pumped down again. A trapped grain is irradiated by an red diode laser modulated by 10 kHz. The laser light scattered by the grain is collected by a simple lens system, and the magnified grain image is projected onto the entrance fiber optics of an image intensifier. The intensifier output is optically coupled to a PIN diode serving as a position sensitive detector. Signals from the PIN diode are amplified by narrow band and lock-in amplifiers prior to the coordinates of the light spot are determined.[10,11,34] The system provides electrical signals that are proportional to the grain current position in two axes. Processing of these signals al-

lows us to estimate the grain oscillation frequency and amplitude. The frequency of the vertical projection is then used for a determination of the grain specific charge. Both vertical and horizontal projections of the oscillations are used for production of signals for the amplitude stabilization. The electronic systems for detection of the motion and damping are similar to those used in another dust charging experiments [for more apparatus details, see Refs. 11 and 34].

All electrodes of the trap were powered by synchronous signals generated by a single tunable RF generator. The signals for each rod consisted of this RF signal amplified by an appropriate factor and summed with the signals for the gravity compensation and for damping of grain oscillations. Finally, these signals were amplified 500 times by eight independent linear high voltage amplifiers. Consequently, we can arbitrary change the V_{xy}/V_z ratio during the measurement.

B. Verification of the trap operation

We measured all three secular frequencies of a single grain at various settings of the trap supply (voltage and frequency). We plotted the ratio of these frequencies (Fig. 5) and fitted the theoretical curve given by Eq. (12). As it can be seen from the figure, the measured frequency ratios (points) follow their predictions, small disagreements are not systematic and they can be attributed to the noise of the detection system.

We recorded the motion of the grain by a video camera oriented roughly in the direction of the x axis (diverted 17° toward the z axis). The trap supply was set in such a way that $C = 0.914$ and three principal modes of oscillations observed by the camera are shown in Fig. 6. The expected directions of the grain oscillations in a particular mode according to the theory presented above are indicated by the arrows. Due to a symmetry of the trap, the oscillations along the x' direction are driven by the "ordinary" field of the linear quadrupole, φ_z, and the frequency should not be affected by the remaining components of the electric field. We can compute the charge-to-mass ratio of the grain from the angular frequency, Ω_1 of

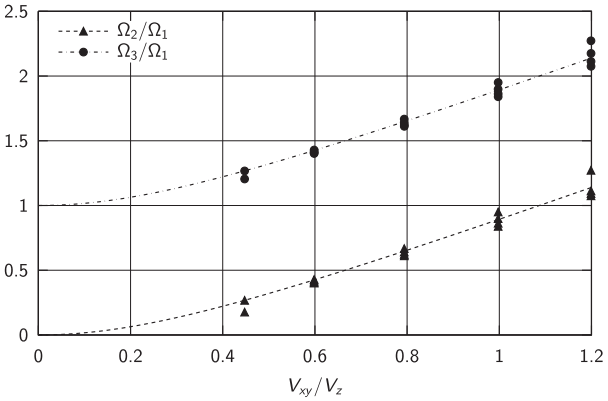

FIG. 5. The ratio of measured frequencies of three modes of oscillations at various settings of the trap. The curves are computed according to the theory shown above, coefficient λ_{xy} is determined by least squares fit.

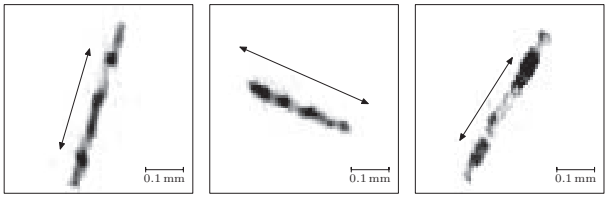

FIG. 6. The principal modes of oscillations inside the trap observed by the video camera (from left to right: Ω_1, Ω_2, Ω_3). Note that the camera was tilted with respect to quadrupole axes. The ratio of voltages was such that $C = 0.914$.

the oscillations along this axis:

$$\frac{Q}{m} = \frac{\sqrt{2}r_0^2}{\lambda_z} \cdot \frac{\Omega_1 \omega}{V_z}. \tag{19}$$

Equation (19) is based on an approximation of the effective potential which is not exact. There is a necessary assumption that the supply voltage frequency is much larger than the secular frequency. Therefore, the error decreases with a decreasing ratio of the secular frequency to the supply voltage frequency.

The precise solution of the motion in an alternating quadrupole field employs the Mathieu's differential equation. Solving this equation, we can obtain an additional factor correcting the result of Eq. (19). This factor can be expressed by an infinite sum but we can limit ourself to first two terms and express the correction factor, K as[34]

$$K = \frac{1}{\sqrt{1 + \left(1.8 \cdot \frac{\Omega_1}{\omega}\right)^2}}, \tag{20}$$

where Ω_1 is the angular frequency of the oscillations of the grain and ω is the angular frequency of the voltage supplying the trap.

We measured the secular frequency of the same grain keeping a constant charge-to-mass ratio under various values of the frequency of the supply voltage (therefore, varying the Ω_1/ω ratio). Figure 7 shows the relative change of the computed charge-to-mass ratio of the grain without and with the correction. We can conclude that the correction according to

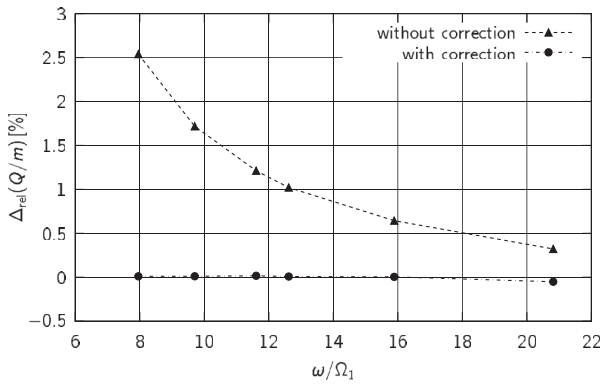

FIG. 7. A change of the measured charge-to-mass ratio at various values of the ratio of the supply voltage and secular frequencies. The correction term (20) almost makes the effect of the low ω/Ω_1 ratio negligible.

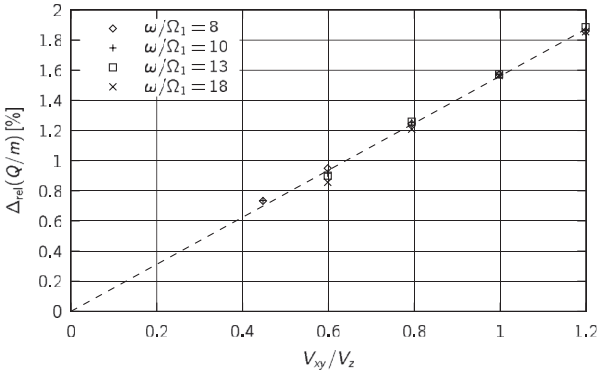

FIG. 8. A change of the measured charge-to-mass ratio, Q/m at various values of the ratio of V_{xy} and V_z. The determined Q/m is almost independent on the ratio of the secular and supply frequencies and obeys a linear dependence.

Eq. (20) provides the charge-to-mass ratio almost independent of the frequency applied on the quadrupole.

As a next step, we measured the change of the secular frequency, Ω_1 while varying the voltage V_{xy}. As we mentioned above, there should be no change of the grain oscillation frequency because the electric field inside the trap is symmetric (see Eq. (11)). However, the calculations neglect the gap between half-rods and the manufacturing of the prototype can introduce some asymmetries.

The measured data show a linear dependence of the relative error of the Q/m ratio on the V_{xy}/V_z ratio (see Fig. 8). One would intuitively expect that a correct value of Q/m is that for $V_{xy} = 0$ but we are not able to measure the secular frequency when the voltage V_{xy} is too low because the grain would not be safely trapped. As it can be seen in Fig. 8, the linear fit is an appropriate description of the dependence of measured Q/m on V_{xy}/V_z, thus it can be easily corrected. Nevertheless, we did an additional modeling in order to find the most probable source of this error.

We simulated few possible inaccuracies of the trap geometry and computed the electric field under such assumptions. We have found that the mechanical design of the trap is sensitive to misalignment in the z direction. While a change of the width of the insulation gap between two parts of each half-rod has a negligible effect, the longitudinal shift of the whole gap is important. The measured dependence of Q/m on V_{xy}/V_z matches the assumed effect of the shift of a single rod by approximately 0.15 mm. It is difficult to eliminate such error because the gaps should be open and no insulators can be used to fix their positions and widths. Nevertheless, the relative errors analyzed in Figs. 7 and 8 are of the order of 10^{-2} and suggested compensations would decrease these errors by an order of magnitude.

The determination of the absolute values of the grain specific charge relies on the calculations that use the trap dimensions, amplitude of the voltage on quadrupole electrodes and its frequency as an input. Thus, the resulting error is a function of the errors of all these parameters. Among them, the determination/stabilization of the amplitude of the high voltage (often kV) in a broad range of frequencies would be probably the major contributor to the resulting error of the specific charge determination. Moreover, the calculations assume the harmonic potential inside a sufficiently large volume of the trap. The anharmonic components of this potential would cause the change of the oscillation frequency with its amplitude and/or an increase of the oscillation amplitude with time. We have changed the oscillation amplitude between 0.1 and 1 mm and did not observe measurable change of the grain frequency. We did not find any recordable change of the oscillation amplitude in course of several minutes with an electrical damping switched off. We believe that it means a contribution of higher multipole terms is negligible.

VI. SUMMARY

We propose a novel design of the electrodynamic trap geometry that allows us to catch and hold a charged grain inside the trap and to measure its charge-to-mass ratio. It is possible to control and damp oscillations of the grain by small auxiliary voltages applied on the rods of the trap. Including the suggested corrections, a relative error of the order of 10^{-3} over a broad range of operational settings can be reached.

Computed charge-to-mass ratio is inversely proportional to the supply voltage, thus the relative error of the voltage contributes to the total error. Taking into account that this voltage is in the kV range, we suppose that the uncertainty of the voltage amplitude will be a major source of the errors, especially when operating over a broad range of frequencies.

As we expected, the proposed geometry is much more open than the trap with hyperbolic electrodes. Its configuration allows the trapped grain to oscillate in the almost purely quadratic effective potential even at a relatively large distance from the trap center.

The trap can be used in a wide range of values of the V_{xy}/V_z ratio. It is even possible to switch-off V_{xy} completely and to let the grain to leave the trap along the axis in a controlled way. This feature could be utilized in the experiments where another measurements on a particular grain prior to or after its investigation in the quadrupole trap are needed.

ACKNOWLEDGMENTS

This work was supported partly by the Research plan MSM 0021620860 financed by the Ministry of Education of the Czech Republic, partly supported by the Czech Grant Agency under Contract Nos. 202/08/0063 and 209/11/1412, and in part funded by the Grant Agency of Charles University (GAUK 171410).

[1]W. Paul, Rev. Mod. Phys. **62**, 531 (1990).
[2]W. Paul and H. Steinwedel, "Apparatus for separating charged particles of different specific charges," German patent 944,900 (1956).
[3]R. Wuerker, H. Shelton, and R. Langmuir, J. Appl. Phys. **30**, 342 (1959).
[4]M. Abbas, P. Craven, J. Spann, E. West, J. Pratico, D. Tankosic, and C. Venturini, Phys. Scr. **T98**, 99 (2002).
[5]M. Abbas, P. Craven, J. Spann, W. Witherow, E. West, D. Gallagher, M. Adrian, G. Fishman, D. Tankosic, A. LeClair, R. Sheldon, and E. Thomas, J. Geophys. Res. **108**, 1229, doi:10.1029/2002JA009744 (2003).
[6]M. Abbas, P. Craven, J. Spann, D. Tankosic, A. LeClair, D. Gallagher, E. West, J. Weingartner, W. Witherow, and A. Tielens, Astrophys. J. **614**, 781 (2004).

[7]J. Svestka, I. Cermak, and E. Grün, Adv. Space Res. **13**, 199 (1993).
[8]V. Chow, D. Mendis, and M. Rosenberg, IEEE Trans. Plasma Sci. **22**, 179 (1994).
[9]I. Cermak, E. Grün, and J. Švestka, Adv. Sp. Res. **15**, 59 (1995).
[10]P. Žilavý, Z. Sternovský, I. Čermák, Z. Němeček, and J. Šafránková, Vacuum **50**, 139 (1998).
[11]J. Pavlů, A. Velyhan, I. Richterová, Z. Němeček, J. Šafránková, I. Čermák, and P. Žilavý, IEEE Trans. Plasma Sci. **32**, 704 (2004).
[12]J. Pavlů, I. Richterová, Z. Němeček, J. Šafránková, and I. Čermák, Faraday Discuss. **137**, 139 (2008).
[13]J. Pavlů, J. Šafránková, Z. Němeček, and I. Richterová, Contrib. Plasma Phys. **49**, 169 (2009).
[14]I. Richterová, M. Beránek, J. Pavlů, Z. Němeček, and J. Šafránková, Phys. Rev. B **81**, 075406 (2010).
[15]I. Richterova, Z. Nemecek, J. Pavlů, M. Beranek, and J. Safrankova, Icarus **212**, 367 (2011).
[16]M. Jerab, I. Richterova, J. Pavlů, J. Safrankova, and Z. Nemecek, IEEE Trans. Plasma Sci. **35**, 292 (2007).
[17]M. Jerab, J. Vaverka, M. Vysinka, Z. Nemecek, and J. Safrankova, IEEE Trans. Plasma Sci. **38**, 798 (2010).
[18]Z. Nemecek, J. Pavlů, J. Safrankova, M. Beranek, I. Richterova, J. Vaverka, and I. Mann, Astrophys. J. **738**, 14 (2011).
[19]I. Mann, A. Pellinen-Wannberg, E. Murad, O. Popova, N. Meyer-Vernet, M. Rosenberg, T. Mukai, A. Czechowski, S. Mukai, J. Safrankova, and Z. Nemecek, Space Sci. Rev. **161**, 1 (2011).
[20]M. Grimm, B. Langer, S. Schlemmer, T. Lischke, U. Becker, W. Widdra, D. Gerlich, R. Flesch, and E. Rühl, Phys. Rev. Lett. **96**, 066801 (2006).
[21]J. Spann, M. Abbas, C. Venturini, and R. Comfort, Phys. Scr. **T89**, 149 (2001).
[22]J. D. Prestage, G. J. Dick, and L. Maleki, J. Appl. Phys. **66**, 1013 (1989).
[23]M. G. Raizen, J. M. Gilligan, J. C. Bergquist, W. M. Itano, and D. J. Wineland, Phys. Rev. A **45**, 6493 (1992).
[24]M. Drewsen and A. Brøner, Phys. Rev. A **62**, 045401 (2000).
[25]M. Drewsen, I. S. Jensen, N. Kjærgaard, J. Lindballe, A. Mortensen, K. Mølhave, and D. Voigt, J. Phys. B **36**, 525 (2003).
[26]J. Pedregosa, C. Champenois, M. Houssin, and M. Knoop, Int. J. Mass Spectrom. **290**, 100 (2010).
[27]J. I. Cirac and P. Zoller, Phys. Rev. Lett. **74**, 4091 (1995).
[28]M. Drewsen, C. Brodersen, L. Hornekær, J. S. Hangst, and J. P. Schiffer, Phys. Rev. Lett. **81**, 2878 (1998).
[29]P. Herskind, A. Dantan, M. Langkilde-Lauesen, A. Mortensen, J. Sørensen, and M. Drewsen, Appl. Phys. B: Lasers Opt. **93**, 373 (2008).
[30]M. Beránek, I. Čermák, M. Jeřáb, J. Pavlů, Z. Němeček, and J. Šafránková, in *WDS'07 Proceedings of Contributed Papers: Part II – Physics of Plasmas and Ionized Media*, edited by J. Šafránková, and J. Pavlů (Matfyzpress, Prague, 2007), pp. 111–118.
[31]D. J. Douglas, T. A. Glebova, N. V. Konenkov, and M. Y. Sudakov, J. Tech. Phys. **44**, 1215 (1999).
[32]D. Gerlich, "Inhomogeneous RF fields: A versatile tool for the study of processes with slow ions," in *Advances in Chemical Physics: State-Selected and State-To-State Ion-Molecule Reaction Dynamics, Part 1. Experiment*, Advances in Chemical Physics, Vol. 82, edited by C.-Y. Ng, M. Baer, I. Prigogine, and S. A. Rice (Wiley, 1992), pp. 1–176.
[33]See http://simion.com. for detailed description of the software package.
[34]I. Čermák, "Laboruntersuchung elektrischer Aufladung kleiner Staubteilchen," Ph.D. dissertation (Naturwissenschaftlich-Mathematischen Gesamtfakultät, Ruprecht-Karls-Universität, Heidelberg, 1994).

C. Nouzák et al. [2016]

Nouzák, L., Richterová, I., Pavlů, J., Němeček, Z., Šafránková, J., Investigations of photoemission from lunar dust simulant. *IEEE Trans. Plasma Sci.* 44 (2): in print, 2016.

Investigations of Photoemission From Lunar Dust Simulant

Libor Nouzák, Ivana Richterová, Jiří Pavlů, Zdeněk Němeček, and Jana Šafránková

***Abstract*— The surface of the Moon is covered by a layer of dust grains. On the sunlit side, the photoemission dominates other charging processes and the work function of grains determines the maximum energy of the originated photoelectrons and, consequently, the grain surface potential. We present laboratory measurements of the work function on a single micrometer-sized lunar dust simulant captured in an electrodynamic trap and irradiated by UV photons. The first results indicate that the work function of lunar dust simulant Minnesota Lunar Simulant grains exceeds 5 eV. We suggest that a slight difference between the work functions determined for two grains is probably caused by the shape effect. The photoelectron yield in the energy range of about 20 eV (58 nm) estimated from the measurements is around 0.05 and it is in good agreement with the previous results.**

***Index Terms*— Dusty plasmas, electron emission, particle charging, photoemission.**

I. Introduction

THE SURFACE of the Moon is composed of rocks and lunar regolith, formed during a long period of meteoroid impacts [1]. The lunar regolith, a fragmental layer of broken, melted, or otherwise altered debris from the original bedrock, consists of grains less than 1 cm in size [1]. Regolith thickness on the *maria* is typically a few meters [2], [3], but in older highland regions, it can reach 10–15 m. The lunar soil is a subcentimeter fraction of the lunar regolith. It is cohesive, dark to light gray, very fine-grained, loose, and clastic material primarily derived from mechanical disintegration of rocks. The finest composite of the lunar soil material is often called lunar dust [4], [5]. As a consequence of mechanical crashing, lunar dust grains have sharp edges [6], [7].

The sharp gradient in a UV flux from the Sun across the solar terminator (the boundary between day and night sides of the Moon) may generate clouds of electrostatically charged dust. This dust can be set into a motion across the Moon as the terminator moves. The Surveyor and Apollo missions discovered some phenomena (horizon glow [8] and streamers [5]) above the lunar surface probably caused by a light scattered off electrostatically charged dust clouds at the terminator region [9]–[11]. Unexplained glows were even noted by ground-based observations [12], [13]. However, Horányi *et al*. [14] recently reported *in situ* lunar dust observations along the orbit of the Lunar Atmosphere and Dust Environment Explorer mission. They found no evidence of the lunar dust at high altitudes that could account for the lunar horizon glow or streamers.

The irradiated lunar surface is positively charged as a consequence of the photoemission current [15], [16]. On the dayside, an equilibrium charge is established when the electric potential (+4 V, [15]) of the charged surface prevents further photoelectrons to escape. All other charging currents are small and they are balanced by a portion of photoelectrons with energies above the surface potential. The number of photoelectrons as well as their energy depends on the work function of the dust grain material, but the direct measurements of this parameter is difficult for insulators [17] and especially for small irregular samples.

Sternovsky *et al*. [18] determined the work function of a lunar (Johnson Space Center (simulant) (JSC-1)) regolith simulant using contact charging of dust falling on substrates from different materials. The contact charging with oxidized metal surfaces was found to be independent on the work function. The effective work functions of the lunar analog determined by extrapolation were 5.8 and 5.6 eV for two different samples. Abbas *et al*. [19] investigated the photoemission yield from lunar dust samples brought by the Apollo and Luna missions. They found that this yield is a rising function of the grain size with a tendency for a saturation at largest investigated grains. However, the saturated value was an order of magnitude larger than that reported for bulk materials with a similar composition.

A determination of the work function from *in situ* measurements would be desirable, but it is probably impossible because we can observe only an equilibrium state that results from the charging by different processes. Nevertheless, we can investigate these charging processes separately on a single dust grain in laboratory conditions [20] or using numerical simulations [21].

In this paper, we introduce laboratory measurements of the photoemission from lunar dust simulant Minnesota Lunar Simulant (MLS-1) [22] samples of micrometer sizes. A single grain is captured in a linear electrodynamic trap of a special design [23] and irradiated by a UV source that can operate with a variety of gases (He, Ne, Ar, etc.). In measurements, we determine the grain size, its surface potential, and the work function using a time evolution of charging/discharging processes. The first results indicate that the work function of the lunar dust simulant is above 5 eV, very similar to the work function of glass grains [20]. The estimation of the

Manuscript received July 31, 2015; revised October 7, 2015; accepted October 11, 2015. This work was supported in part by the Czech Science Foundation under Grant GP13/25185P and Grant P209/11/1412 and in part by the Grant Agency of Charles University under Grant 1410213.

The authors are with the Faculty of Mathematics and Physics, Charles University in Prague, Prague 121 16, Czech Republic (e-mail: libor.nouzak@mff.cuni.cz; ivana.richterova@mff.cuni.cz; jiri.pavlu@mff.cuni.cz; zdenek.nemecek@mff.cuni.cz; jana.safrankova@mff.cuni.cz).

Color versions of one or more of the figures in this paper are available online at http://ieeexplore.ieee.org.

Digital Object Identifier 10.1109/TPS.2015.2493885

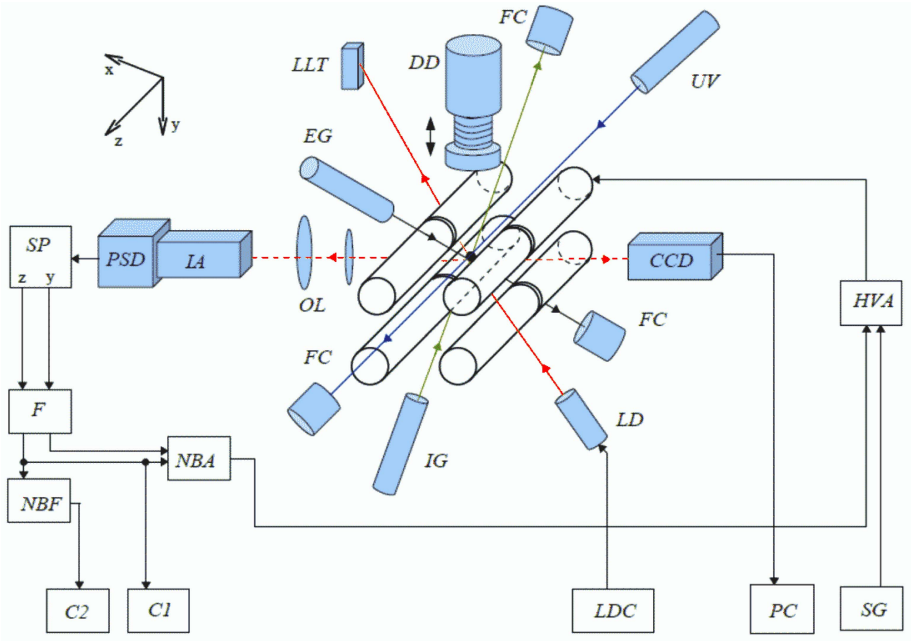

Fig. 1. Experimental setup—electrodynamic trap (FC—Faraday cup, EG—electron gun, IG—ion gun, UV—UV source, DD—dust dropper, IA—image amplifier, PSD—position sensitive detector, PC—personal computer, HVA—high voltage amplifier, OL—optical lenses, LLT—laser light trap, SP—signal processor, F—filter, NBF—narrowband filter, NBA—narrowband amplifier, C1 and C2—counters, LD—laser diode, LDC—LD control, SG—signal generator, CCD—charge-coupled device camera).

photoemission yield of one of the investigated grains provides a value of 0.05 for the ≈58-nm UV line.

II. Experimental Setup

The experimental setup is based on a linear electrodynamic trap (in the center of Fig. 1). The charged dust grain is caught in an effective potential that is formed by three-independent RF fields, all of them having dominant quadrupole terms [23]. The trap consists of four rods, each of them being divided into two parts and the rod parts are supplied by eight high voltage amplifiers. A harmonic signal with a time window for shooting charged particles is provided by a programmable signal generator. A grain is shaken out from a dust dropper, and the falling grain is charged by one of particle sources to be caught in the effective potential of the trap. Three particle sources can be used: 1) an electron gun; 2) an ion gun; and 3) a differentially pumped UV lamp (UV). The currents from particular sources are stabilized by a feedback loop and measured by the gridless Faraday cups (FCs). The measurements of the UV effects rely on the stability of the used UV source.

The measurements are based on a determination of the frequency of the grain oscillation within the trap. We use a synchronous optical detection of a light scattered by the grain. The light beam from a laser diode modulated by a controller (LDC) interacts with the levitating grain and a part of the scattered light is concentrated by a lens system (OL) onto an image amplifier and a position sensitive detector (PSD) that converts an optical signal to the electrical signal for a signal processor. The processor unit provides the position signal of the grain image that is used for damping/stabilization of dust grain oscillations. The signal from the PSD is amplified by a narrowband filter and its frequency f_x is measured by a frequency counter (C2). The charge-to-mass ratio of the grain is determined from its oscillation frequency, f_x

$$\frac{Q}{m} = \frac{4\pi^2\sqrt{2}f_x f_{\mathrm{AC}} r_0^2}{\lambda_z V_z} \tag{1}$$

where f_{AC} and V_z are the frequency and amplitude of the trap supply, and r_0 and λ_z are geometric parameters of the trap (see [23] for details). The Q/m evolution is recorded during the measurements.

III. Measurement Technique

The charge-to-mass ratio of the grain (Q/m) is directly proportional to its surface potential (ϕ) [24] through the grain specific capacitance C_m (the ratio of the grain capacitance and mass). This capacitance can be easily calculated for spherical grains, but an electron microscope photo (not shown) of an MLS-1 lunar simulant has shown that the grains are not spherical; they exhibit sharp edges and thus their specific capacitance is unknown.

In the case of photoemission charging by a monochromatic light with an energy of $h\nu$, the maximum attainable surface potential $\phi_{\max}$ of the dust grain would meet the equation

$$\phi_{\max} = \frac{1}{e}(h\nu - W) \tag{2}$$

where W is the work function of the grain, and its determination would be straightforward when C_m is known. In laboratory conditions, the situation is more complex for several reasons.

TABLE I
EMISSION LINES OF He, Ar, AND Ne GASES IDENTIFIED FROM Q/m VALUES OF TWO MLS-1 GRAINS OF DIFFERENT SIZES

Emission line	Excitation energy (eV)	Wavelength (nm)	$Q/m_{4.7\,\mu\mathrm{m}}$ (C/kg)	$Q/m_{4.0\,\mu\mathrm{m}}$ (C/kg)
Ar I	15.43	80.35	0.02 ± 0.0018	0.028 ± 0.0021
Ar II	17.13	72.38	0.0228 ± 0.0005	0.0332 ± 0.0013
Ar II	17.26	71.83	0.0256 ± 0.0007	0.0339 ± 0.0007
Ar II	18.44	67.23	0.0278 ± 0.0064	0.0358 ± 0.0008
Ar II	23.87	51.94	0.0368 ± 0.0011	0.0387 ± 0.001
Ar II	25.26	49.08	0.04 ± 0.0014	0.0559 ± 0.0054
He I	21.22	58.43	0.0316 ± 0.0045	0.0445 ± 0.0039
He I	23.08	53.72	0.0361 ± 0.0014	0.0507 ± 0.0052
He II	40.8	30.93	0.0703 ± 0.0038	0.0971 ± 0.0039
Ne I	16.67	74.38		0.0316 ± 0.0018
Ne I	16.85	73.58		0.0329 ± 0.0023
Ne I	20.14	61.96		0.0411 ± 0.0114
Ne II	26.82	46.26		0.0606 ± 0.0198
Ne II	30.45	40.72		0.069 ± 0.0054
Ne II	34.21	36.25		0.0801 ± 0.0124

1) We use a differentially pumped capillary discharge UV source [25] that can operate with a variety of gases (He, Ne, Ar, etc.), but investigations can be complicated by a presence of several emission lines in the discharge of each working gas. When no discharging background current is present, the maximum attainable surface potential $\phi_{\max}$ will be given by the emission line with the highest excitation energy.
2) A part of a UV light from the source or a possible reflected UV from surrounding surfaces can interact with walls of the vacuum vessel or with rods of the trap and produce background photoelectrons. Some of them can reach the grain and decrease its surface potential, and thus, the maximum surface potential of the grain will be lower than that given by (2).

On the other hand, if an emission line with the higher energy is present in the discharge and its intensity is sufficient, the surface potential can exceed the value given by (2). In such cases, the equilibrium grain potential is given by a balance of the photocurrent and the discharging background current.

The used UV source can operate in two modes differing by a pressure of the working gas and discharge current. In the mode denoted I (II), it predominantly emits lines with energies just below the first (second) ionization potential, but all other lines are emitted as well albeit with the depressed intensity. Table I shows the energies and corresponding wave lengths of lines that we were able to identify and that were used for the determination of the grain work function. We should note that these lines only partly correspond to a list of most intensive lines provided by the UV source manufacturer. The last two columns of Table I show the specific charges of two investigated grains, and a method of their estimation will be discussed later.

To overcome these difficulties, we have developed a method of a work function determination that uses two or more UV emission lines and employs the so-called current–voltage (I–V) plot technique [26]. Since I–V plots are a key technique for the determination of the work function, we briefly describe this method.

Let us assume that the grain is charged to a surface potential higher than that given by (2) when the UV source is switched ON. UV produces background electrons that discharge the grain and its potential starts to decrease. When the grain potential reaches the value of $\phi_{\max}$ corresponding to (2), the photoelectrons become to leave the grain and to reduce the discharging current.

The discharging current can be obtained as a derivative of the measured $Q/m(t)$ temporal profile

$$\frac{d}{dt}\left(\frac{Q}{m}\right) = \frac{I}{m}. \tag{3}$$

The plot I/m versus Q/m is called the I–V plot because Q/m is proportional to the grain potential. In this simple scenario, I/m consists of two components: 1) the background current I_{back}/m and 2) the photoemission current I_{photo}/m. One can expect that the dependence of both these components on Q/m can be approximated by straight lines in a vicinity of $\phi_{\max}$ [27]. Since I_{photo}/m is equal to zero above $\phi_{\max}$, the plot of the total current would exhibit a knee at Q/m corresponding to $\phi_{\max}$. The position of this knee can be determined from a bilinear fit of the I–V plot. This one point would be sufficient for a determination of the work function in an ideal case of a monochromatic light, but two or more points are needed in a real experiment.

IV. ESTIMATION OF THE WORK FUNCTION

The computation of the work function from measurements on a grain illuminated by the nonmonochromatic light is based on evaluation of records of charging/discharging characteristics. The key point is a relation between the grain potential and its specific charge. To simplify this task, we use the fact that the secondary electron emission under the bombardment by the 1-keV electron beam will charge the grain to $\approx$7 V of the surface potential [24], and the corresponding Q/m can be used for a rough estimation of the grain capacitance. The full measuring sequence for one dust grain is shown in Fig. 2 and a procedure is described in its captions. As it can be seen in Fig. 2, we applied three gases in order to identify a sufficient amount of lines and to decrease the error of the work function determination. The whole measurements proceed a long time because a rate of the Q/m determination is about 1 Hz, and the charging/discharging curves should be well sampled for computation of their derivatives.

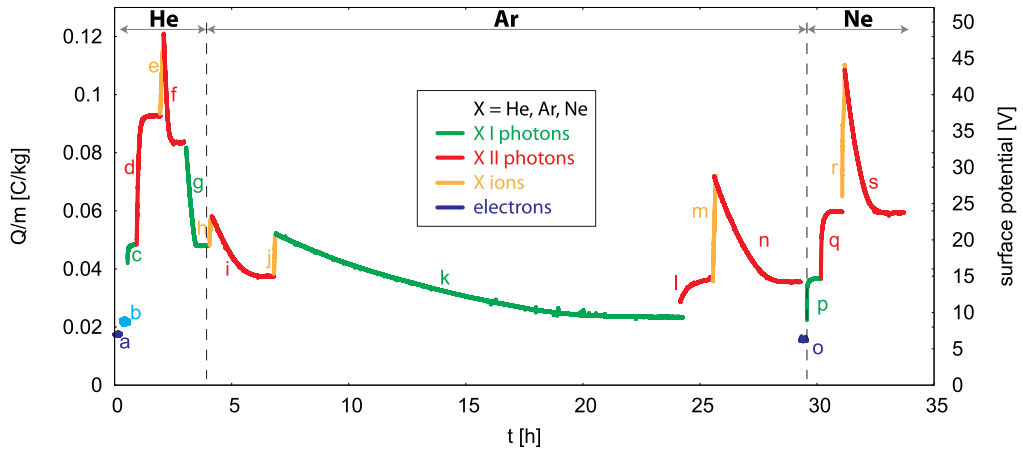

Fig. 2. Time evolution of the photoemission charging of the grain with a size of ≈4.0 μm. Charging/discharging procedure from left to right: (a) charging by 1-keV electrons, (b) charging by 1-keV electrons and He I photons, (c) charging by He I photons, (d) charging by He II photons, (e) charging by 1-keV He ions, (f) discharging by He II photoelectrons from the background, (g) discharging by He I photoelectrons from the background, (h) charging by 1-keV Ar ions, (i) discharging by Ar II photoelectrons from the background, (j) charging by 1-keV Ar ions, (k) discharging by Ar I photoelectrons from the background, (l) charging by Ar II photoelectrons, (m) charging by 1-keV Ar ions, (n) discharging by Ar II photoelectrons from the background, (o) discharging by 1-keV electrons, (p) charging by Ne I photoelectrons, (q) charging by Ne II photoelectrons, (r) charging by 1-keV Ne ions, and (s) discharging by Ne II photoelectrons from the background.

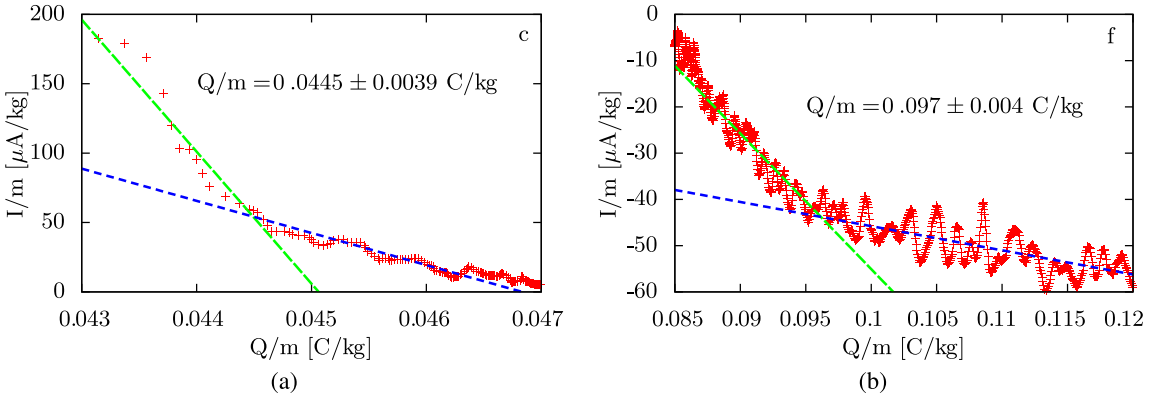

Fig. 3. Examples of I–V plots. (a) I–V characteristics recorded during the grain charging by He I lines [Fig. 2(c)]. (b) I–V characteristics that represent discharging of the grain by emission lines of He II groups [Fig. 2(f)].

Another reason for slow changes of the grain charge is that the precise determination of Q/m requires the grain oscillating around the trap center, thus the DC potential compensating a gravity should be simultaneously adjusted [24]. Fast changes of Q/m usually lead to grain loss and the experiment should start from the beginning. Nevertheless, we were able to measure the full sequence for one grain and the sequence limited to He and Ar emission lines for the second one.

We applied the I–V plot technique on all parts of the profile corresponding to the charging or discharging of the grain by the UV source with a special attention to the Q/m regions surrounding expected knees caused by the emission lines. According to theory, we would be able to identify plenty of lines (e.g., http://www.nist.gov/), but the Q/m data are noisy and the derivative increases the noise further. For this reason, we were able to find only the most intensive lines as it can be seen in Table I.

Fig. 3 presents two examples of I–V plots. First of them [Fig. 3(a)] was recorded during grain charging by He I lines [Fig. 2(c)], the second one [Fig. 3(b)] belongs to discharging of the grain charged by energetic ions to a surface potential exceeding the energies of He II groups of emission lines [Fig. 2(f)]. The ratio of Q/m corresponding to the intersection of two linear fits was recalculated to the grain potential using the grain specific capacitance that was determined in two steps. The first rough estimation was based on an assumption that the grain bombarded by 1-keV electrons is charged to 7 V. The value was later adjusted to achieve the best agreement between the distribution of measured surface potentials and possible energies of the UV lines.

The results of above described procedures applied on two grains from the Lunar Highlands Type lunar regolith simulant are shown in Fig. 4. The position of points on the horizontal axis is given by the energy of a particular emission line, and the vertical axis is marked in units of the grain specific charge. The error bars show propagated uncertainties of the linear fits to I–V plots; the thin line is a linear fit to depicted points that reflect the mentioned uncertainties. Under

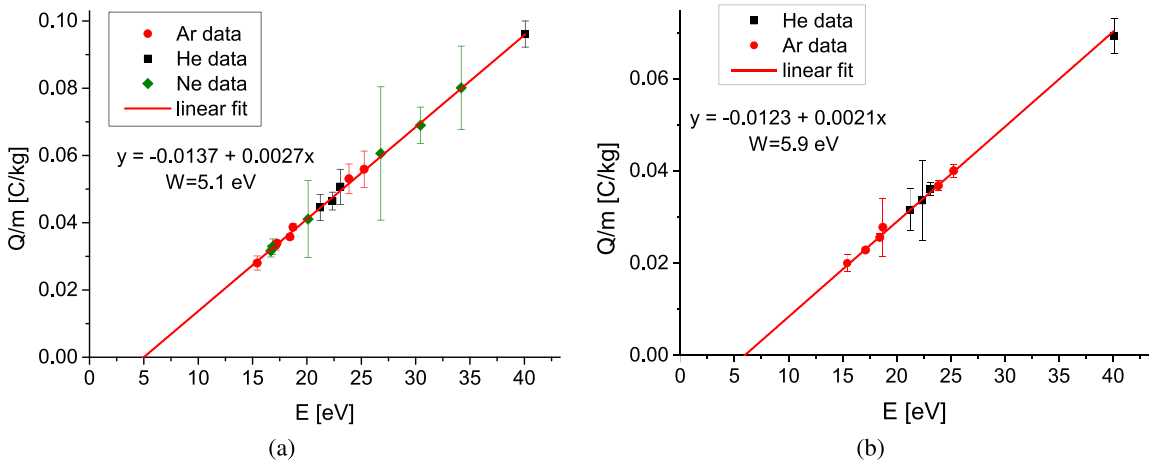

Fig. 4. Estimated work functions of two grains of different sizes using I–V plots. The grains used with an effective diameter of (a) 4 and (b) 4.7 μm.

assumptions that the potentials are given by (3) for each of identified UV lines, the points would lie on a straight line that intersects the horizontal axis at the energy equal to the grain work function. The investigated grains slightly differ by their dimensions and/or shapes. This fact can be described by their effective diameters calculated from the specific capacitance assuming a spherical shape. This effective diameter is 4 μm for the grain in Fig. 4(a) and 4.7 μm for that in Fig. 4(b). We should point out that it does not necessarily mean that the second grain is larger; as we mentioned, the difference can be caused by the different shapes of a particular grain.

The calculated values ($W_{4.7\ \mu\mathrm{m}} = (5.9 \pm 0.3)$ eV and $W_{4.0\ \mu\mathrm{m}} = (5.1 \pm 0.7)$ eV, respectively) of the grain work function are in a full accordance with the value of $W \approx 5.8$ eV obtained in [18] for the JSC-1 lunar regolith simulant by the contact charging method. We should note here that the work function of the glass grain [20] was determined as $W = (4.7 \pm 1.5)$ eV under the same conditions, also in agreements with the values obtained in [28] and [29] for the bulk material. According to the theories in [30] and [31], the work function would depend on the curvature of the surface, but this effect would be negligible for grains with a radius in the micrometer range but it would be seen for nanometer-sized grains. On the other hand, sharp edges that can be expected on the grain surface can lead to decrease of the measured work function. This means that the work function would be different for different parts of the grain surface, and this effect could be responsible for difficulties with a determination of breaks in I–V plots like those in Fig. 3.

V. Photoemission Yield

Estimates of background and photoemission currents belonging to particular emission lines of our UV source demonstrated in Fig. 3 could be used for the determination of the photoemission yield defined as a ratio of numbers of incoming photons and emitted electrons. The number of photons falling on the grain was determined from the total photoemission current measured by the FC with stainless steel collector under assumptions that the yield of this material for the most intensive He I emission line (21.2 eV) is ≈0.12 [32].

The diameter of the UV beam was estimated from the geometries of the source and experimental setup. The grain was expected to levitate in the center of the beam with the Gaussian intensity profile. The grain cross section was considered to be circular with an effective diameter determined from the grain specific capacitance. Under these assumptions, the photoemission yield η of the first grain (with a effective diameter of 4 μm) is

$$\eta_{\mathrm{dust}}(21.2\ \mathrm{eV}) = 0.05. \tag{4}$$

This value is in good agreement with measurements on a powdered sample of the lunar dust (48% of glass and 18% of Al_2O_3), $\eta(21.2\ \mathrm{eV}) = 0.02$ [33], and a silica solar cell covered by an indium oxide layer, $\eta(21.2\ \mathrm{eV}) = 0.07$ [32]. However, Feuerbacher *et al.* [33] point out that the measurement of the photoelectron yield on powdered sample might result in yields that are too low; the yield of an isolated particle can be significantly larger [34].

A value estimated by our procedure is similar to that found in [19] for the dust grains of micrometer diameters. However, we should note that the shape of grains investigated in our and their experiments were irregular, and thus a value of the yield would depend on the way used for a determination of the grain surface. We are using the effective diameter, and we believe that is a good approximation because it rises with an elongation of the grain and the same does the grain surface. Nevertheless, the grain shape is the most important source of the uncertainty of the yield determination.

VI. Conclusion

The main goal of this paper is to describe a procedure that allows a reliable determination of the work function of a single dust grain and its dependence on the grain material and on the energy of UV photons. The results of this preliminary study can be summarized as follows.

1) We observed time evolutions of the photoemission charging of two lunar dust simulant (MLS-1) grains illuminated by a UV discharge lamp emitting He I, He II, Ar I, Ar II, Ne I, and Ne II photons.

2) We calculated I–V plots and we identified several emission lines in He, Ar, and Ne discharges from the changes of charging/discharging currents.
3) We associated these lines with grain surface potentials (using corresponding Q/m ratio) and extrapolating them to zero grain potentials, we estimated work functions of the lunar simulant material.
4) The work functions of the lunar simulant grains were found to be $W_{4.7\ \mu\mathrm{m}} = (5.9 \pm 0.3)$ eV and $W_{4.0\ \mu\mathrm{m}} = (5.1 \pm 0.7)$ eV. We suggest that the difference of work functions can be connected with the effects of the grain shape.
5) We have determined the photoemission yield of the lunar dust MLS-1 material as $\approx$0.05 for 21.2-eV photons.

The effects of the grain shape on a value of the determined yield as well as on the determined work function will be subjects of consecutive studies.

ACKNOWLEDGMENT

The authors would like to thank Prof. D. Vítek for his useful suggestions and comments.

REFERENCES

[1] G. Heiken, D. Vaniman, and B. M. French, Eds., *Lunar Sourcebook: A User's Guide to the Moon*. Cambridge, U.K.: Cambridge Univ. Press, 1991.
[2] Y. Langevin and J. R. Arnold, "The evolution of the lunar regolith," *Annu. Rev. Earth Planet. Sci.*, vol. 5, no. 1, pp. 449–489, 1977.
[3] S. R. Taylor, *Planetary Science: A Lunar Perspective*. Houston, TX, USA: Lunar and Planetary Institute, 1982.
[4] D. S. McKay *et al.*, "The lunar regolith," in *Lunar Sourcebook: A User's Guide to the Moon*, G. Heiken, D. Vaniman, and B. French, Eds. Cambridge, U.K.: Cambridge Univ. Press, 1991, pp. 285–386.
[5] T. J. Stubbs, R. R. Vondrak, and W. M. Farrell, "A dynamic fountain model for lunar dust," *Adv. Space Res.*, vol. 37, no. 1, pp. 59–66, 2006.
[6] H. Heywood, "Particle size and shape distribution for lunar fines sample 12057,72," in *Proc. Lunar Sci. Conf.*, vol. 2. 1971, pp. 1989–2001.
[7] W. D. Carrier, G. R. Olhoeft, and W. Mendell, "Physical properties of the lunar surface," in *Lunar Sourcebook: A User's Guide to the Moon*, G. Heiken, D. Vaniman, and B. French, Eds. Cambridge, U.K.: Cambridge Univ. Press, 1991, pp. 475–594.
[8] D. A. Glenar, T. J. Stubbs, J. E. McCoy, and R. R. Vondrak, "A reanalysis of the Apollo light scattering observations, and implications for lunar exospheric dust," *Planet. Space Sci.*, vol. 59, pp. 1695–1707, Nov. 2011.
[9] J. E. McCoy and D. R. Criswell, "Evidence for a high altitude distribution of lunar dust," in *Proc. Lunar Sci. Conf.*, vol. 5. 1974, pp. 2991–3005. [Online]. Available: http://adsabs.harvard.edu/abs/1974LPSC....5.2991M
[10] D. R. Criswell, "Horizon-glow and the motion of lunar dust," in *Photon and Particle Interactions With Surfaces in Space* (Astrophysics and Space Science Library), vol. 37, R. J. L. Grard, Ed. Noordwijk, The Netherlands: Springer-Verlag, 1973, pp. 545–556.
[11] H. A. Zook and J. E. McCoy, "Large scale lunar horizon glow and a high altitude lunar dust exosphere," *Geophys. Res. Lett.*, vol. 18, no. 11, pp. 2117–2120, 1991.
[12] W. S. Cameron, "Manifestations and possible sources of lunar transient phenomena (LTP)," *Moon*, vol. 14, no. 1, pp. 187–199, Sep. 1975.
[13] W. S. Cameron, "Lunar transient phenomena catalog," NASA Goddard Spaceflight Center, Greenbelt, MD, USA, Tech. Rep. NSSDC/WDC-A-R&S v. 7803, Jul. 1978.
[14] M. Horányi *et al.*, "A permanent, asymmetric dust cloud around the Moon," *Nature*, vol. 522, no. 7556, pp. 324–326, 2015.
[15] R. H. Manka, "Plasma and potential at the lunar surface," in *Photon and Particle Interactions With Surfaces in Space* (Astrophysics and Space Science Library), vol. 37, R. J. L. Grard, Ed. Noordwijk, The Netherlands, Springer-Verlag, 1973, pp. 347–361.
[16] R. F. Willis, M. Anderegg, B. Feuerbacher, and B. Fitton, "Photoemission and secondary electron emission from lunar surface material," in *Photon and Particle Interactions With Surfaces in Space* (Astrophysics and Space Science Library), vol. 37, R. J. L. Grard, Ed. Noordwijk, The Netherlands: Springer-Verlag, 1973, pp. 389–401.
[17] A. A. Sickafoose, J. E. Colwell, M. Horányi, and S. Robertson, "Experimental investigations on photoelectric and triboelectric charging of dust," *J. Geophys. Res.*, vol. 106, no. A5, pp. 8343–8356, 2001.
[18] Z. Sternovsky, S. Robertson, A. Sickafoose, J. Colwell, and M. Horányi, "Contact charging of lunar and Martian dust simulants," *J. Geophys. Res. (Planets)*, vol. 107, no. E11, pp. 15-1–15-8, Nov. 2002.
[19] M. M. Abbas, D. Tankosic, P. D. Craven, J. F. Spann, A. LeClair, and E. A. West, "Lunar dust charging by photoelectric emissions," *Planet. Space Sci.*, vol. 55, nos. 7–8, pp. 953–965, 2007.
[20] L. Nouzák, I. Richterová, J. Pavlů, Z. Němeček, and J. Šafránková, "Investigations of the photoemission from glass dust grains," in *WDS'14 Proc. Contrib. Papers—Phys.*, Prague, Czech Republic, 2014, pp. 361–370.
[21] J. Vaverka, I. Richterová, J. Pavlů, J. Šafránková, and Z. Němeček, "Lunar surface and dust grain potentials during the Earth's magnetosphere crossing," *J. Geophys. Res.*, to be published.
[22] E. Hill, M. J. Mellin, B. Deane, Y. Liu, and L. A. Taylor, "Apollo sample 70051 and high- and low-Ti lunar soil simulants MLS-1A and JSC-1A: Implications for future lunar exploration," *J. Geophys. Res.*, vol. 112, no. E2, 2007, Art. ID E02006.
[23] M. Beránek, I. Čermák, Z. Němeček, J. Šafránková, M. Jeřáb, and J. Pavlů, "Linear trap with three orthogonal quadrupole fields for dust charging experiments," *Rev. Sci. Instrum.*, vol. 83, no. 11, p. 115109, 2012.
[24] J. Pavlů, I. Richterová, Z. Němeček, J. Šafránková, and I. Čermák, "Interaction between single dust grains and ions or electrons: Laboratory measurements and their consequences for the dust dynamics," *Faraday Discuss.*, vol. 137, pp. 139–155, 2008.
[25] *SPECS UV-Source UVS 10/35, User Manual*, SPECS Surf. Nano Anal. GmbH, Berlin, Germany, 2009.
[26] I. Čermák, E. Grün, and J. Švestka, "New results in studies of electric charging of dust particles," *Adv. Space Res.*, vol. 15, no. 10, pp. 59–64, May 1995.
[27] P. Žilavý, Z. Sternovský, I. Čermák, Z. Němeček, and J. Šafránková, "Surface potential of small particles charged by the medium-energy electron beam," *Vacuum*, vol. 50, no. 1–2, pp. 139–142, 1998.
[28] H. Kitabayashi and H. Fujii, "Charging of insulating glass caused by contact with plates," *IEEJ Trans. Fundam. Mater.*, vol. 125, no. 2, pp. 179–184, 2005.
[29] S. Okamura, T. Iwao, M. Yumoto, H. Miyake, and K. Nitta, "Measurement of photoelectron emission using vacuum ultraviolet ray irradiation," in *Proc. AIP Conf.*, vol. 1087. Jan. 2009, pp. 544–549.
[30] L. E. Brus, "A simple model for the ionization potential, electron affinity, and aqueous redox potentials of small semiconductor crystallites," *J. Chem. Phys.*, vol. 79, no. 11, pp. 5566–5571, 1983.
[31] G. Makov, A. Nitzan, and L. E. Brus, "On the ionization potential of small metal and dielectric particles," *J. Chem. Phys.*, vol. 88, no. 8, pp. 5076–5085, 1988.
[32] B. Feuerbacher and B. Fitton, "Experimental investigation of photoemission from satellite surface materials," *J. Appl. Phys.*, vol. 43, no. 4, pp. 1563–1572, 1972.
[33] B. Feuerbacher, M. Anderegg, B. Fitton, L. D. Laude, R. F. Willis, and R. J. L. Grard, "Photoemission from lunar surface fines and the lunar photoelectron sheath," in *Proc. 3rd Lunar Sci. Conf.*, vol. 3. 1972, pp. 2655–2663.
[34] J. C. Weingartner and B. T. Draine, "Photoelectric emission from interstellar dust: Grain charging and gas heating," *Astrophys. J. Suppl. Ser.*, vol. 134, no. 2, p. 263, 2001.

Libor Nouzák was born in Česká Lípa, Czech Republic, in 1988. He received the M.S. degree from Charles University in Prague, Prague, Czech Republic, in 2012, where he is currently pursuing the Ph.D. degree with the Space Physics Laboratory.

His current research interests include the laboratory simulation of elementary processes in dusty plasmas, namely, photoemission.

Ivana Richterová was born in Český Brod, Czech Republic, in 1979. She received the M.S. and Ph.D. degrees from Charles University in Prague, Prague, Czech Republic, in 2003 and 2012, respectively.

She is currently a Senior Assistant with the Space Physics Laboratory, Department of Surface and Plasma Science, Faculty of Mathematics and Physics, Charles University in Prague. Her research is devoted to the laboratory investigation and modeling of elementary charging processes on dust grains.

Jiří Pavlů was born in Pardubice, Czech Republic, in 1977. He received the M.S. and Ph.D. degrees from Charles University in Prague, Prague, Czech Republic, in 2001 and 2005, respectively.

He is currently a Senior Assistant with the Space Physics Laboratory, Department of Surface and Plasma Science, Faculty of Mathematics and Physics, Charles University in Prague. His current research interests include the laboratory investigations of elementary processes on dust grains induced by electron, ion, and photon irradiations.

Zdeněk Němeček was born in Prague, Czech Republic, in 1947. He received the M.S., Ph.D., and D.Sc. degrees from Charles University in Prague, Prague, in 1971, 1982, and 1996, respectively.

He has held several leading positions with the Faculty of Mathematics and Physics, Charles University in Prague, since 1971. His current research interests include the solar wind interaction with the Earth's magnetosphere and the laboratory simulations of plasma processes.

Jana Šafránková was born in Teplice, Czech Republic, in 1947. She received the M.S., Ph.D., and D.Sc. degrees from Charles University in Prague, Prague, Czech Republic, in 1972, 1982, and 1996, respectively.

She has held several positions with the Faculty of Mathematics and Physics; she is currently the Head of the Space Physics Laboratory. Her current research interests include the solar wind and laboratory simulations of elementary processes in dusty plasmas.

D. Pavlů et al. [2009]

Pavlů, J., Šafránková, Němeček, Z., Richterová, I., Dust charging in space-related laboratory experiments: A review focused on secondary emission. *Contrib. Plasma Phys.* 49 (3): 169–186, 2009.

Contrib. Plasma Phys. **49**, No. 3, 169 – 186 (2009) / **DOI** 10.1002/ctpp.200910019

Dust Charging in Space-related Laboratory Experiments: A Review Focused on Secondary Emission

J. Pavlů*, **J. Šafránková, Z. Němeček,** and **I. Richterová**

Charles University, Faculty of Mathematics and Physics, Department of Surface and Plasma Science, V Holešovičkách 2, 180 00 Prague, Czech Republic

Received 23 December 2008, accepted 18 February 2009
Published online 20 April 2009

Key words Electron impact, secondary emission, dust charging, dusty plasmas.
PACS 52.27.Lw, 79.20.Hx, 95.30.Wi

A role of dust in the space environment is of increasing interest in the recent years. Also the fast development of fusion devices with magnetic confinement brought new issues in the plasma-surface interaction. While there is a number of dusty plasma reviews, the present paper surveys experimental results connected with charging of dust grains under well-defined laboratory conditions for both space and industrial applications. The main purpose of these experiments is to study particular charging/discharging processes preferably on space-related (i.e., all sorts of glass and other oxides) as well as on elemental materials (carbon, nickel, gold). Single micrometer-sized spherical grains or grain's clusters stored in vacuum are exposed to electron and ion beams. Among several charging processes, the secondary emission is discussed in broad details because this process plays a prominent role everywhen a portion of energetic electrons is present in the medium surrounding a particular grain.

1 Introduction

Different types of plasmas contaminated with fine (nanometer- to micrometer-sized) charged dust grains usually referred to as dusty plasmas (and more recently as complex plasmas) occur in a wide variety of environments both cosmic and terrestrial. Dust is an almost ubiquitous component of the cosmic plasma (e.g., planetary and cometary magnetospheres, the heliosphere, the interstellar medium, supernova shells, etc); however, it also occurs in laboratory plasmas (e.g., plasmas applied in industrial material and microelectronic processing, plasmas in fusion devices, etc). While their spatial dimensions and temporal scales differ by tens of orders of magnitude, the basic physical processes in these two diverse environments are common. In recent times, the recognition of this fact has led to a connection of the space and laboratory plasma communities and the industrial plasma community working in this field.

Since dust particles are one of the main elements of interest in the solar system (e.g., Earth, Jovian and Saturnian systems) and in the interstellar medium, there is a number of missions (e.g., ROSETTA, Cassini) that provide or will provide investigations of the properties and global dynamics of charged dust grains (e.g., [1–6]). As an example, SEM studies of the craters on the Al foil during a passage of the Stardust satellite through the comet Wild 2 coma have shown evidence of dust particle impacts of a wide range of sizes from a few tens of nanometers to nearly 60 micrometers in diameter. Many of the large impact features were caused by dense silicate grains, accompanied by smaller quantities of diverse silicate and sulfide compositions [7, 8]. Furthermore, it is anticipated that future rocket campaigns in northern Scandinavia will provide more information regarding the mesospheric dust (e.g., [9–11]), while experiments on the International Space Station determine the dusty plasma behavior under microgravity conditions (e.g., [12, 13]).

On the other hand, dusty (complex) plasmas are fully or partially ionized low-temperature gases comprising neutral gas molecules, electrons, ions, and massive charged sub-micron- and micron-sized dust grains [14]. The

*Corresponding author: e-mail: jiri.pavlu@mff.cuni.cz; Phone: +00 420 221 912 226.

interaction of the dust with the ambient plasma (and UV radiation, if present) leads to dust charging with consequences for both the dust and plasma (e.g., [15–19]). The grain charging depends on the physical and electrical properties of the grains, on the nature of their interaction with the surrounding radiation and plasma fields, and on the relative velocity. The most important contributions come from fluxes of electrons and ions, from the UV-radiation induced photoemission and from secondary emission of electrons. The surface potential of a dust grain is established by a balance between various charging currents and resulting surface potentials can range from about ≈ -10 kV in planetary magnetospheres [20] to some ≈ 10 V in an interplanetary space (e.g., [21]) depending on size, material, and charging history of grains [21–23]. It appears that the dust grain charging is a significant physical process in both space and laboratory experiments.

It is usually expected that dust grains act as a sink for plasma electrons or ions (e.g., [24]) but dust can also act as a source of electrons, and occasionally of ions as well, in numerous ways [25, 26]. The processes inside grains addressed as a source of electrons include secondary electron emission through a primary electron impact, secondary electron emission by an ion impact (there are two distinct processes—a high-energy ion can penetrate the grain and excite material electrons that escape as secondaries, while a lower energy ion can recombine with an electron near the surface emitting a photon which, in turn, can release a (photo) electron), photoelectric emission, thermionic emission, electric field emission, radio activity, exo-electron emission (due to deformation and fracture of crystals leading to rapture of chemical bonds), balloelectric effect (charging of droplets and electron emission during mechanical disruption in liquid sprays) [27]. Besides these direct processes, there are further indirect ways by which dust can lead to the production of electrons and ions. For example, charge separation due to contact or triboelectric charge transfer between dust grains or droplets can lead to large ambipolar electric fields that cause electrical breakdown (e.g., volcanic eruptions and thunderstorms).

With regard to other charging processes, a significant attention has been paid to grain charging by secondary electron emission due to the impact of energetic electrons. The secondary electron yield (i.e., the number of secondary electrons emitted by the grain per incident electron) increases with an energy to a maximum (that could be greater than unity for certain materials) and then decreases, leading to the so-called "Sternglass" formula [28] that is still widely applied. The shape of the yield curve can lead to multiple roots of the currentvoltage curve (e.g., [29]), and thus grains in a plasma can acquire charges of opposite polarities during transient variations of temperature. This effect has been subsequently discussed by several authors (e.g., [22, 30]) and has been also established in the laboratory (e.g., [31]).

Chow et al. [32] have shown that grains of various sizes can achieve opposite polarities through an electron impact, with the smaller grains being positive and the larger ones being negative. This is due to the fact that when the grain size is comparable to the penetration depth of the primary electrons, the secondary electron emission yield increases sharply. Evidence for such a bipolar distribution of a grain charge, with positively charged small grains and negatively charged larger grains, is presented in the experimental studies of the grain growth (e.g., [33, 34]). Chow et al. [35] explained the observations of the latter authors using a combination of the aforementioned grain size effect of the secondary electron yield and electron depletion in the sheath above the negatively biased electrode where the grain growth occurs. However, as we will discuss later in the paper, the interpretation of these effects neglected the scattering of primary electrons inside grains that leads to increasing importance of backscattered electrons for the charging process.

The theory and models of a single dust grain charging and dynamics are well developed for environments that vary from hot plasma in fusion devices through planetary atmospheres to tenuous plasmas in the interstellar space. However, calculations based on these theories rely on material properties derived from large planar samples. On the other hand, laboratory investigations of individual grains in equilibrium state that can provide their electrical parameters are less common, perhaps due to the difficulty of such experiments. Nevertheless, several laboratory experiments have been focused on different aspects of grain charging. Suszcynsky et al. [36] measured secondary electron yields from ammonia and methanol ices as a function of the electron beam energy in the energy range of $2 - 30$ keV and summarized that secondary electron yields are at the low end of the range for insulators. Barkan et al. [16] studied charging of micron-sized dust grains dispersed into a fully ionized, magnetized plasma and found that the charge on a dust grain in a dense dust cloud can be substantially reduced with respect to the charge on an isolated grain. Walch et al. [17, 37] measured the charge on small grains of different non-conducting materials in a plasma containing both thermal and suprathermal electrons. Sickafoose et al. [38] studied the photoemission and triboelectric charging of single dust grains levitating upon the metal surface. They have

shown that triboelectric charging may be the dominant charging process for silicate planetary regolith analogs and thus it will play an important role in the subsequent behavior of dust grains released from planetary surfaces.

A new technique developed in the 1950s for ion spectroscopy [39], generally referred to as a quadrupole trap, has been successfully employed for the investigation of single micron-sized grains [40]. Using this technique, photoemission experiments with the UV radiation [41, 42], secondary electron emission experiments (e.g., [43]), and rotation and alignment of dust grains by the radiation [44] have been performed. A similar technique was used in laboratory experiments where micron-sized grains bombarded by keV electrons were stored and a size dependence (observed by Švestka et al. [45] and qualitatively explained by Chow et al. [46]) was identified.

In Čermák et al. [47], an electrodynamic quadrupole inside an ultra-high vacuum chamber was applied to trap grains of micron and submicron sizes which were charged by electron and ion beams of energies up to 5 keV. The authors developed a new method for determination of the dust grain size, surface potential, and electric field strength, and they measured the effects of electron and ion beam energies on the dust surface potential. They obtained energy spectrum of emitted secondary electrons and estimated the yield of the secondary electron emission. In the last ten years, their experimental set-up was further gradually extended and used to study different kinds of charging processes in idealized laboratory conditions.

In this paper, we present a survey of experimental investigations of the grain charge and associated potential carried out on both conductive and non-conductive materials. In our experimental apparatus, we can and did study various charging process, nevertheless, we have chosen only the processes connected with the secondary electron emission for this overview.

2 Short description of experimental facility

Details of the experimental setup are provided in a series of papers by Čermák [48], Žilavý et al. [49], Čermák et al. [50], and Pavlů et al. [51], thus we will only shortly repeat the basic principles here. As we already noted, the apparatus is based on trapping of a single dust grain in the electrodynamic quadrupole and on its influencing by mono-energetic ion and/or electron beams (both beams work in the range of 100 eV–10 keV). The electrodynamic quadrupole (a 3D quadrupole trap with modified hyperbolic electrodes) together with the dust reservoir are placed inside an ultra-high vacuum chamber (pressure in the chamber is about 10^{-6} Pa). The quadrupole is supplied symmetrically, thus there is zero potential in the middle of the trap. Note that a stability of the supplied voltages is significant for our application [52] similarly to the linear quadrupole often used for ion mass spectrometry. From the quadrupole theory it follows that the vertical electrodes should be supplied by the same voltage. However, we are using two different amplifiers for them in order to apply a damping voltage and dc voltage for the compensation of the gravity force.

A trapped grain is irradiated by a 635 nm diode laser and the laser light is modulated by 10 kHz for a reduction of noise. The laser light scattered by the grain is collected by a simple lens system, and the magnified grain image is projected onto the entrance fiber optic of an image intensifier. The output of the image intensifier is directly coupled to a PIN diode serving as a 2D coordinate detector. Signals from the PIN diode are amplified by narrow band, lock-in amplifier prior to the coordinates of the light spot are calculated. These coordinates are used to control the motion of the grain by a damping system. The grain oscillation frequency can be determined by a frequency counter or by Fourier analysis.

After several simplifications, theoretical considerations lead to the relation between the grain oscillation frequency and its charge-to-mass ratio (specific charge, Q/m):

$$\frac{|Q|}{m} \cong \frac{2\pi^2 r_0^2}{|\lambda_u|}\frac{f F_u}{V_{ef}} \tag{1}$$

where $V_{ef} = V_{AC}/\sqrt{2}$ is the RMS value of the AC voltage on the quadrupole electrodes, V_{AC} is its amplitude, $f = \omega/2\pi$ is the frequency of the applied AC voltage, $F_u = \Omega_u/2\pi$ is the secular frequency (frequency of the grain motion) in the u direction, r_0 denotes the inner radius of the quadrupole ring electrode, and λ_u is the weight factor of the electric field in the u direction. This simplified expression can be used for computation of the grain specific charge, Q/m if $f \geq 10\, F_u$.

The grain oscillation frequency is the only measurable quantity and we have developed several techniques to determine the grain size, mass, charge, capacitance, and other parameters [50, 51]. For estimation of the grain

size, a discharging process of a strongly positively charged grain is used; the grain is charged by energetic ions to an equilibrium surface potential and then the ion energy is decreased. In this case, the beam ions cannot reach the grain surface due to the electrostatic repulsion, nevertheless, secondary electrons are produced on the quadrupole electrodes and cause the discharging of the grain. The grain surface potential decreases, and when it reaches a value at which the beam ions just come to the grain surface, the discharging current of secondary electrons is partially compensated by the ion current and the discharging slows down suddenly. The corresponding surface potential, ϕ can be calculated from the energy of the primary ions: $\phi = E_i/e_0$ where e_0 is the elementary charge. The knowledge of its value allows us to calculate the grain radius, R from

$$R = \sqrt{\frac{3\varepsilon_0\phi}{\rho} \cdot \frac{m}{Q}} \tag{2}$$

where ρ means the grain mass density and ε_0 is the dielectric constant of vacuum.

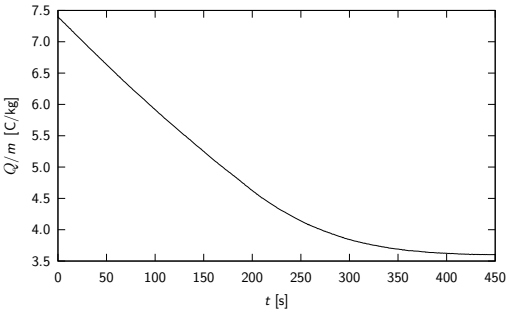

Fig. 1 Demonstration of the determination of a grain diameter by a discharging process.

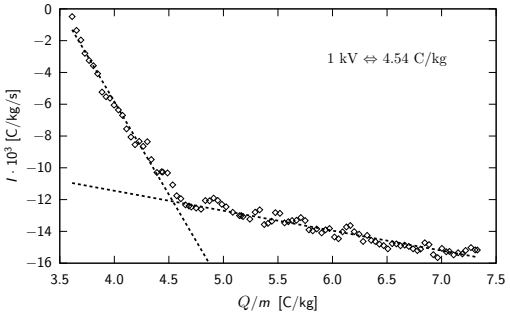

Fig. 2 Current-voltage characteristics for estimation of the proportionality constant between Q/m and ϕ.

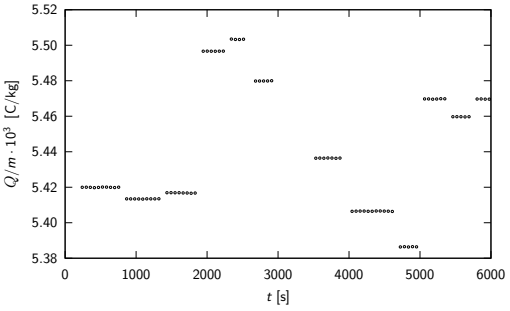

Fig. 3 Demonstration of the grain mass determination by the elementary charge method—frequency jumps.

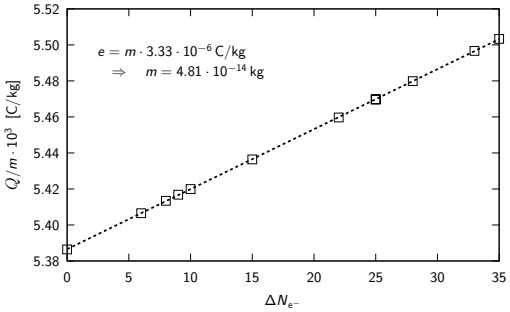

Fig. 4 An example of a linear regression of frequency jumps.

The process of the determination of R is schematically shown in Fig.1. A glassy carbon grain was chosen for demonstration. The figure shows a temporal evolution of the specific charge, Q/m during the discharging of the grain charged by the Ar^+ beam to a surface potential above 1000 V. Since the aforementioned change of the discharging current can be hardly found in this plot, Fig. 2 shows the derivative of temporal changes of the grain charge (a current-voltage characteristics). The slowly decreasing part of this characteristics represents the background current and the steeper part belongs to a sum of both background and ion beam currents. Note that both currents are a linear function of the grain charge. Intersection shows a point where the grain potential is equal to the beam energy. This point allows us to determine the proportionality constant between the grain specific charge, Q/m and its surface potential, ϕ, i.e., the specific capacitance, C/m. Our computation provides the grain radius $R = 1.96$ μm for the grain shown in Figs. 1 and 2.

The nondestructive determination of the grain mass is based on the observation of stepwise changes in the Q/m ratio that can be attributed to grain charging in steps of integral numbers of the elementary charge [53]. If

the parameters V_{AC} and f of the quadrupole voltage are constant during the measurement, the relative change of grain secular frequency F_u is nearly equal to the relative change of the Q/m ratio. In the case of micron-sized grains charged to an equilibrium surface potential of about 10 V, the relative frequency change is of the order of 10^{-4}. The mass, m of the grain is then given as

$$m = \frac{e_0 F_u}{\Delta F_u} \cdot \frac{m}{Q} \tag{3}$$

where F_u and Q/m are known from the experiment. Fig. 3 displays stepwise changes of the grain oscillation frequency in time, and Fig. 4 shows a linear regression of corresponding frequency step changes of the grain charge caused by one or several elementary charges. Note the excellent stability of the experiment that allows a precise determination of the grain mass ($m = 4.81 \cdot 10^{-14}$ kg in the case in Figs. 3 and 4).

3 Secondary electron emission

Primary electrons impacting the sample surface interact with a bulk material and lose an energy in many types of collisions that often result in excitation of material electrons and some of them can leave the surface after then. These electrons, so-called true secondary electrons, have typical energies of a few electronvolts. As we noted in the case of large planar samples the energetic dependence of the secondary emission yield, $\delta(E)$ defined as the mean number of secondary electrons per one primary electron can be described by the Sternglass universal curve [28, 54] that was later extended toward higher primary energies by [55]. This curve exhibits a maximum at a few tenths of kiloelectronvolts and decreases to zero at very high and low beam energies. Its parameters, the maximum yield, δ_{max} and the corresponding energy, E_{max}, depend only on a sample material at a certain incident angle. In collisions inside the target, primary electrons change their directions and thus they may be backscattered from the material before losing the whole energy. The backscattered yield, η increases with the material density and the atomic number up to ≈ 0.5 for the normal incident angle. It grows only slowly with the beam energy above a few hundreds of electronvolts. Thus, the total secondary yield, σ ($\sigma = \delta + \eta$) and δ vary in a similar way with the beam energy [56]. In the case of grains, the energy dependence of a total secondary yield of dust grains does not fully follow the universal curve that was suggested for large samples. The yield is enhanced due to a surface curvature that results in a variation of the incident angle along the grain surface because σ (and both constituents) increases with the incident angle [57].

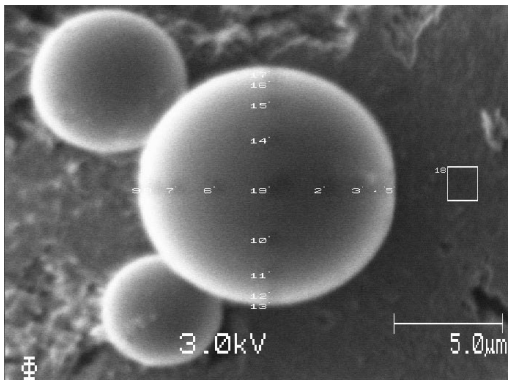

Fig. 5 A SEM image of the studied 12 μm carbon grain as obtained by SAM650. Measuring points and an area representing the substrate are sketched. (Adopted from [59].)

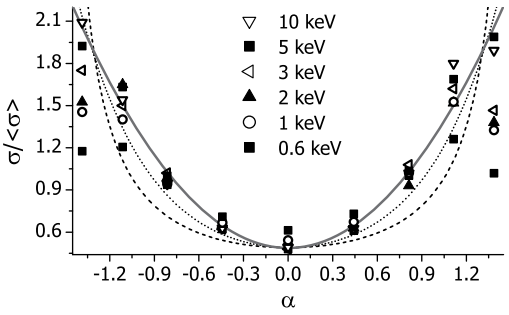

Fig. 6 The relative secondary electron yield as a function of an incident angle for different beam energies and empirical profiles: $\sec\alpha$ (dotted), $\exp(const \cdot (1 - \cos\alpha))$ (dashed), and $a_0 + a_2\alpha^2$ (solid). The quadratic fit parameters are: $a_0 = 0.49$ and $a_2 = 0.824$. (Adopted from [59].)

The dependence of the secondary emission yield on the incident angle was measured and fitted by different analytical expressions or simulated [58]. Since this function is of a principal importance for investigations of highly curved dust grains, Richterová et al. [59] used the SEM technique for its determination. Fig. 5 shows

a SEM image of the investigated 12 μm carbon spherical sample. The secondary emission yield was measured at several points in two perpendicular directions starting from the sample center. The distances between two measuring points were adjusted to achieve equidistant points on the angular scale. Note that an incidence angle of the beam is $\alpha = \arcsin(X/R)$ where X is the distance of the spot from the grain center and R is the grain diameter. The locations of measuring spots are shown in Fig. 5. The diameter of the electron beam was ≈ 30 nm and the energy was tuned in the range of $0.6 - 10$ keV.

Measurements of a local secondary electron yield as a function of the incidence angle are summarized in Fig. 6 for several electron beam energies. Since the yield was measured at 4 points with the same incident angle, the averages are plotted in the figure. The outermost points ($\alpha = \pm 1.4$) stand only 100 nm from the grain edge and they are very sensitive to all drifts. The measured yields represent an arbitrary value between those of grain and graphite substrate, thus we did not consider them for fitting. Despite the widely accepted curves [56, 57], a quadratic growth of the yield with the angle of incidence describes our data better. The same parabola ($\sigma/\langle\sigma\rangle(\alpha) = 0.49 + 0.824\alpha^2$) fits well all profiles for beam energies ranging from 1 keV. The profile measured for 600 eV seems to be a little flatter but we assume that the difficulties with the focussing of the primary beam lead to apparent flattening of the profile at this energy, thus we use the same parabola for all beam energies in further estimations.

Since the whole grain surface is illuminated by the parallel electron beam in our further experiments, the described angular dependence leads to an enhancement of the yield measured on the spherical grain with respect to planar samples by a factor of ≈ 1.3.

3.1 Secondary electron emission from dust grains

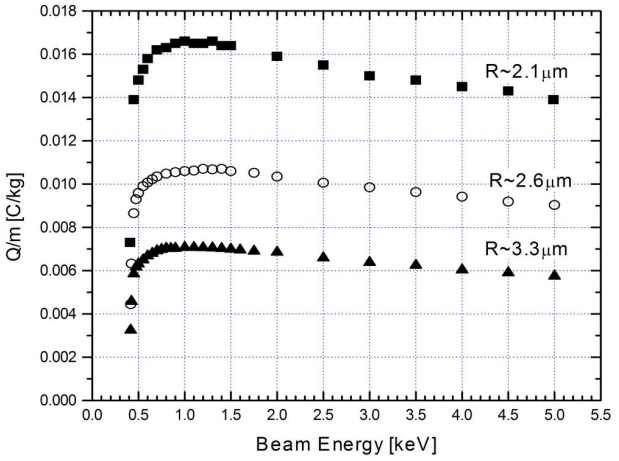

Fig. 7 The Q/m ratio as a function of the beam energy for three glass grains with different sizes in the micrometer range. (Reprinted from [49], ©(1998), with permission from Elsevier.)

As an example, basic measurements of the dust grain charging are shown in Fig. 7. The figure presents the equilibrium Q/m ratio for three grains of different diameters. All grains were measured at the same conditions (quadrupole voltage, primary electron current, pressure). None of the grains had been modified by an ion bombardment before the measurement. In Fig. 7, the measured curves are roughly self-similar, the scaling factor being inversely proportional to the square of the grain diameter. As it was discussed, it can be easily shown that

$$\frac{Q}{m} = \frac{C}{m}\phi = \frac{3\varepsilon_0}{\rho R^2}\phi \tag{4}$$

where C is the grain capacitance, ϕ is the surface potential of the grain, ρ is its mass density, ε_0 is the dielectric constant of vacuum, and R is the radius of the spherical grain. This indicates that it is the surface potential of the grain that determines the particle charging. If we suppose the secondary emission as a principal mechanism of the grain charging, we would expect the correspondence between the yield of the secondary emission and

the Q/m ratio. This is true, however, only qualitatively. The decrease of the Q/m ratio with the beam energy for the energies above 1500 eV is in agreement with the decreasing yield of the secondary electron emission in this energy range. On the other hand, a steep fall-off of the Q/m ratio occurs at 400 eV for all three grains. We suppose that this effect is caused by the secondary electrons emitted from the quadrupole electrodes and the chamber walls. Our suggestion is consistent with the fact that the energetic threshold is independent on the grain size (Fig. 7). In order to depress this effect, we have introduced the electron beam and quadrupole voltage sampling [49] into our setup and all results in this paper (except those in Fig. 7) use this technique. Nevertheless, a portion of background electrons generated by the beam scattering at the entrance orifice or by ionization of the residual gas in a vacuum chamber is still present and captured by the positively charged grain.

3.2 Secondary electron emission from clusters

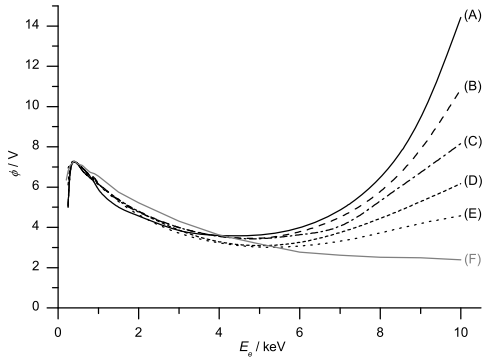

Fig. 8 Equilibrium surface potentials of clusters consisted of different numbers of grains (A: single grain, B: 3-grains cluster, C: 5-grains cluster, D: cluster of about 34 grains, E: cluster of more then 110 grains, F: the glass grain of a diameter of about 3.6 μm). (Adopted from [60] – Reproduced by permission of The Royal Society of Chemistry.)

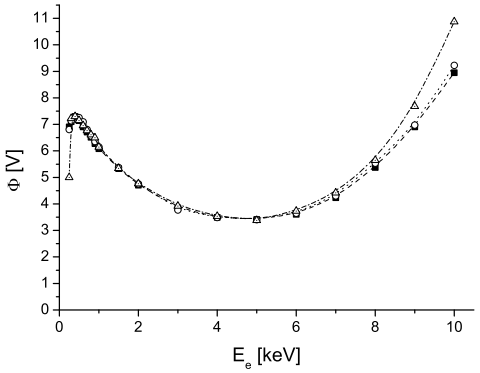

Fig. 9 Equilibrium surface potentials of one cluster consisted of 4 grains with different mutual configurations. (Reprinted with permission from AIP Conference Proceedings [61]. ©2002, American Institute of Physics.)

The finding that the equilibrium dust grain charge is determined by its surface potential was established by measurements on spherical grains but it can be used for grains of arbitrary shapes as an useful tool for interpretation of the experimental data. We have applied this assumption on investigations of clusters composed of different numbers of 1.2 μm SiO_2 spheres. In Fig. 8, we plotted examples of the surface potential measurements as a function of the beam energy; the curves differ by the number of grains in the particular cluster. Let us start with the uppermost curve (A) that belongs to a single grain. The grain surface potential rises with the beam energy up to about 400 eV and then it falls down as can be expected taking into account the "Sternglass" formula [28] for the secondary emission yield. However, when the beam energy exceeds 5 keV, the grain potential begins to rise with the increasing beam energy. A similar effect was observed by Švestka et al. [45] and theoretically treated by Chow et al. [32, 46]. They attributed it to the emission of secondary electrons from the opposite side of the dust grain that is not illuminated by the electron beam and, consequently, to the increase of the yield of the true secondary electrons. This hypothesis seems to be confirmed by the behavior of larger clusters. One can clearly see that, whereas initial parts of all curves in Fig. 8 are nearly the same, the slopes of high-energy tails decrease with a number of spheres in the cluster by a systematic manner. The exception from this rule will be discussed later.

The equilibrium potential of the grain or cluster is determined by a balance of incoming and outgoing electrons. If the beam energy is sufficiently low, the electrons are emitted only from an illuminated part of the cluster and the curves roughly follow the dependence found for planar surfaces. If the emission from the "back side" of a particular grain becomes important, the surface potential is a decreasing function of the number of grains in the cluster. We suggest that it is caused by a shielding of secondary electrons by other grains in the cluster because secondary electrons escaping "inside" the cluster are captured by another surface. It is interesting to note that,

even for a relatively high number of grains in the cluster, the charging characteristics differ from those measured for compact grains of a similar equivalent diameter. The second lowest curve in Fig. 8 (E) was measured for one cluster consisted of ≈ 110 grains. Its mass corresponds to a ≈ 5 μm sphere on which the effect of enhanced emission would not be observed [62] (compare with curve (F) belonging to larger single grain). We assume that the grains on the flank surfaces of a cluster which are not shielded are responsible for the enhanced cluster potential at high beam energies.

A better view on the effect of a cluster geometry on charging characteristics provides Fig. 9 where equilibrium surface potentials of clusters containing 4 grains are plotted as a function of the primary electron beam energy. As Pavlů et al. [61] noted, the different slopes of high-energy tails are caused by different spatial adjustment of the grains in a particular cluster and, consequently, by a different degree of shielding.

The previous figures show that dust grain charging exhibits rather complicated features. Fortunately, this system is rather simple and can be treated theoretically. The equilibrium grain potential is given by the balance of two currents: The beam current, I_B depends only on the beam energy, E_B and grain surface potential, ϕ:

$$I_B = I_{0B} \cdot \left(1 + \frac{e\phi}{E_B}\right) \tag{5}$$

and the secondary emission current, I_S depends on the actual beam current, secondary emission yield, σ and spectrum of secondary electrons, $f(E)$:

$$I_S = I_B \cdot \sigma(E_B) \cdot \int_{\phi}^{\infty} f(E)dE \tag{6}$$

The Sternglass approximation for $\sigma(E_B)$ can be used only for large grains because the assumptions of this approximation are not valid for the grain sizes comparable with the penetration depth of primary beam electrons. The second problem of this phenomenological approach it that the form of the energy spectrum of secondary electrons is generally unknown and can depend on the primary beam energy, grain diameter and its material, and on other factors. We will discuss these two constituents of the secondary emission current in the next section.

4 Model of secondary emission for spherical grains

Theoretical treatments of secondary electron emission have been based on many different approaches. The emission has been described by the elementary theories, e.g., by Salow [63], Baroody [64], Bruining [65]. A complex approach to the problem of electron-induced secondary electron emission can be found in Sternglass [28]. Later, Kanaya and Kawakatsu [66] and Kanaya et al. [67] have modified these results by using a Lindhard power potential to describe secondary emission from both metals and insulators. On the other hand, simulation studies of secondary emission have been based mainly on a Monte Carlo electron trajectory simulation and become important along with progress in electron probe microanalysis, electron spectroscopy, and microscopy (e.g., [68–70]) where the target influenced by the electron beam is studied. A series of the papers by Ding et al. [71–73] precises a Monte Carlo simulation model of electron interaction with solid that includes cascade secondary electron production. The model is based on Mott's elastic scattering cross-sections [74] and Penn's dielectric function approach [75] to electron inelastic scattering. The dependence of the secondary electron yield on the primary energy and the energy distribution of backscattered electrons have been obtained [71]. The authors noted a good agreement with experimental data for 19 different metals. In [76], an examination of the secondary yield as a function of primary energies and atomic numbers for the 44 elements is made. An analytical model of the dependence of secondary electron emission on the primary electron energy for application to polymers was referred by Cazaux [77].

Nevertheless, the majority of those and other models were prepared for the planar targets. For spherical dust grains, the secondary electrons are not limited to the point of incidence of primary electrons but may exit from all points of the grain surface, thus, as we already noted, the secondary emission yield is higher than that determined by these models. To this topic, theoretical considerations of the secondary emission from submicrometer oil drops of spherical shapes were done by Ziemann et al. [78]. They achieved a good matching with their experiment up to 250 eV of the primary energy. Chow et al. [32] developed a model of secondary emission from spherical bodies where the authors assume that the primary electron current density is conserved inside the grain, primary electrons

move straight inside the grain, the production rate of secondary electrons is proportional to the energy loss of primary electrons, and the escaping probability of secondary electrons decreases exponentially with a distance to the surface. They added the Whiddington law for energy losses along their path in the grain and computed the yield of secondary emission (similarly as in [79]). Their computation assumes that the primary electrons move along straight lines inside the grain but the secondary electrons can proceed toward the surface in any direction. Since their model did not reproduce the Svestka et al. [45] experimental data, Chow et al. [46] published an improved model. The new model provided the curve of the yield of secondary emission with several maxima (connected more with numerical approach then with physical base). Varying the constants of the model, the authors were able to fit the data but they should use different sets of constants for low- and high-energy regions.

A simple numerical model of secondary emission from small dust grains developed by Richterová et al. [80] has revealed the importance of backscattered electrons to the setting of the equilibrium surface potential, especially in a high-energy range of primary energies. Since the model assumptions were very simplified, the authors have revisited it in order to include more complex principles of the electron-solid interaction using a well-tested Monte Carlo technique developed for scanning electron microscopy [81].

A detailed description of the model is given in Richterová et al. [82], here we outline only shortly its principles. The hybrid Monte Carlo technique is used to monitor the path of primary electrons. In accord with Joy [81], the authors expect that the primary electron is scattered inside the material mainly by elastic collisions that are described by the Mott and Massey cross-sections [74] computed by Czyzewski et al. [83]. All possible energy losses of the primary electron are averaged into a collision-independent continuous energy loss along its path; the loss rate is taken in accordance with the modified Bethe stopping power equation [84]. If a primary electron is scattered towards the surface before being completely slowed down, it leaves the grain.

The whole energy lost by a primary electron is converted into the excitations of material electrons. The number of excited electrons is given by the mean excitation energy. Excited electrons reach the grain surface in a distance X with a probability $P(X) \sim \exp(-X/\Lambda)$, where Λ is the mean diffusion path. The secondary emission yield is calculated by integration of this probability around 4π of the spatial angle. A random energy, in accord with the chosen energy distribution, is given to each true secondary electron at the surface. If this energy is sufficient to overcome the grain surface potential (calculated from the actual grain charge and capacitance) the electron escapes and the grain charge increases.

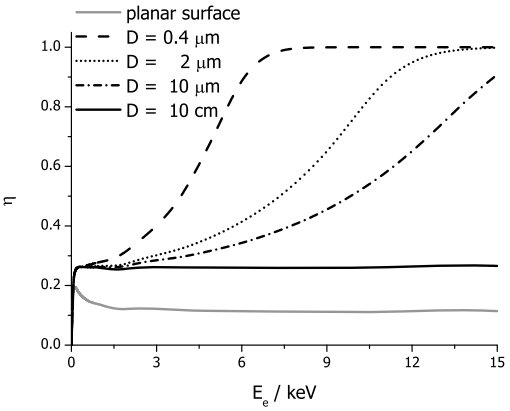

Fig. 10 Modeled backscattered yields of glass spherical grains of different diameters and their comparison with a planar surface. A model input value is: $\rho = 2.2$ gcm^{-3}. (Adopted from [85]. ©2007 IEEE.)

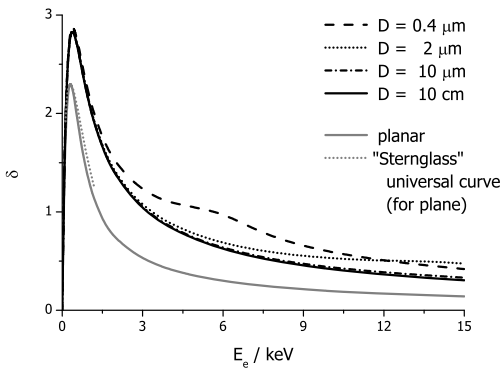

Fig. 11 Modeled yields of secondary electron emission for glass spherical grains of different diameters as a function of the primary energy. Model input values are: $\rho = 2.2$ gcm^{-3}, $\delta_{max} = 2.4$, $E_{max} = 300$ eV. The plot compares profiles for different grain sizes with profiles obtained by the model for a planar geometry and with a Sternglass universal curve. (Adapted from [85]. Modified with permission - © 2007 IEEE.)

The model contains only three free parameters: the mean excitation energy, ε (i.e., the mean energy that is necessary for excitation of an electron), the mean diffusion path, Λ and the energy distribution of the true

secondary electrons. These quantities strongly depend on the inner grain state, i.e., micro-porosity, admixtures, structure faults, etc., thus they should be determined by a fit to the experimental data. The model assumptions are not limited by the shape of studied objects, nevertheless, a spherical symmetry simplifies computation.

4.1 Electron emission yield

As an example, the modeled backscattered and secondary emission yields, respectively, and the equilibrium grain surface potential for several glass spheres of different diameters as a function of the electron beam energy are plotted in Figs. 10–12. In Fig. 10, where backscattered emission yields are plotted, one can note that the effect of the surface curvature is apparent even for a very large grain but in the range of micrometers, nearly all primary electrons leave the grain if the primary beam energy is large enough. This suggests that a low portion of the negative charge of primary electrons is deposited in small grains. The effects connected to a finite grain size on the yield of true secondary electrons may be observable for diameters below micrometer (see Fig. 11). The decrease of the grain diameter leads to the increase of the secondary emission yield for primary energies above 3 keV. The bump on its profile calculated for the 0.4-μm grain (at a primary beam energy in the range of 4–6 keV) is connected to the fact that the penetration depth of the primary electrons is comparable with a grain size; thus, the amount of energy deposited near the surface increases. Nevertheless, even if this effect is taken into account, the secondary emission yield increase due to the finite grain size does not exceed $\approx 20\%$ in the investigated ranges of sizes and primary energies.

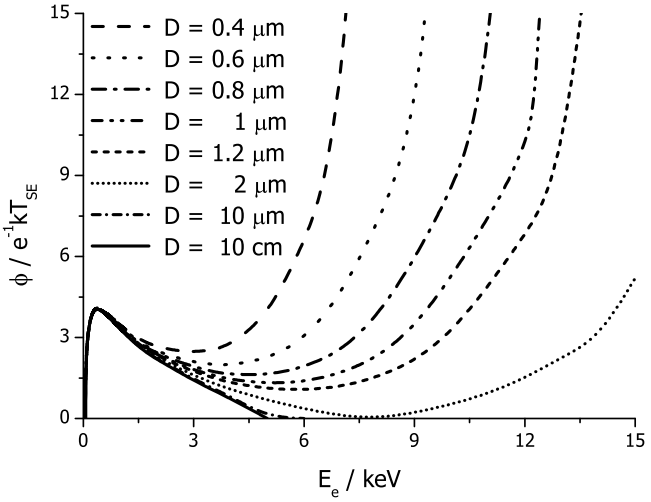

Fig. 12 Computed equilibrium surface potentials of glass spherical grains of different diameters. Model input values are the same as in the previous figure. In the model, the Maxwell distribution is used. (Adopted from [85]. ©2007 IEEE.)

The profiles in Figs. 10 and 11 result from the model but they cannot be compared directly with measurements, thus we have calculated the charge accumulated in the grain. Since this charge is relatively small, the resulting surface potentials do not exceed 20–30 V. Thus, we can expect that primary electrons scattered inside the grain reaching the surface have sufficient energy and they can escape from the grain. On the other hand, the energies of true secondary electrons are generally low and their energy distribution should be taken into account. We attribute to each electron at the surface random energy in accord with the chosen energy distribution. When this energy is sufficient to overcome the grain surface potential (calculated from the accumulated charge and grain capacitance), the electron escapes, and the grain charge is increased. According to Velyhan et al. [86], we are using the Maxwellian energy distribution for our calculations. The resulting profiles of equilibrium surface potentials as a function of the beam energy are shown in Fig. 12 for several diameters of glass grains. The low-energy parts of all curves are identical because neither η nor δ depend on the grain diameter at low primary-beam energies. The shape of this part of the curves is determined by the energetic dependence of the secondary emission yield and can be used for estimation of parameters ε and Λ. On the other hand, high-energy parts strongly depend on the grain size. This effect is connected with an increasing number of backscattered primary electrons from smaller grains (compare Figs. 10–12). When η approaches unity, the grain is charged positively by outgoing secondary electrons because primary electrons do not compensate this charge and the potential of

the grain rises. Note that the curve calculated for the 1.2μm grain very well, even quantitatively, reproduces the surface potential profile of a single grain from Fig. 8.

4.2 Spectrum of secondary electrons

Similarly to the secondary emission yield, the spectrum of secondary electrons is composed of two parts—spectrum of backscattered primary electrons $F_B(E)$, and spectrum of true secondary electrons, $F_S(E)$. The model discussed in the previous section [82] provides a realistic spectrum of backscattered electrons but there is no theory describing the spectrum of true secondary electrons until present. Many authors use the Maxwellian distribution with temperature of several eV (e.g., [56]) but Draine and Salpeter [55] and Grard et al. [87] suggested a little different forms of this distribution.

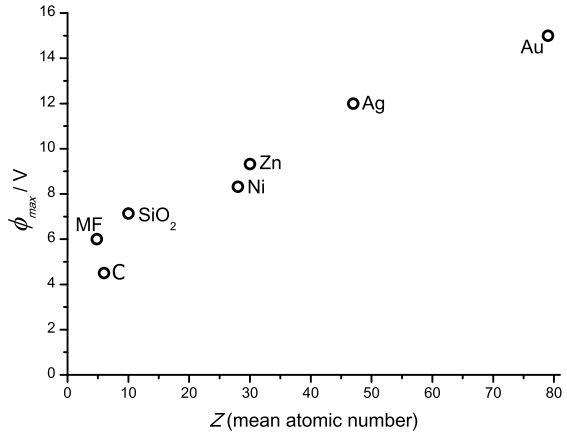

Fig. 13 The surface potential at the maximum of the secondary emission yield plotted as a function of the mean atomic number of the grain material. (Adapted from [60] – Reproduced by permission of The Royal Society of Chemistry.)

Since the shape of the distribution is connected with the equilibrium potential of the grain bombarded by the electron beam, we can use measured potential as a function of the beam energy and equations (3) and (4) and determine an appropriate spectrum by the fit. This approach was applied in [86] and later in [88]. In order to decrease the number of free model parameters, a possible change of the spectrum with the beam energy could not be considered. They found that the shape of spectrum depends on the material, being a more Maxwellian-like for insulators and resembling the Draine and Salpeter distribution for metals. This result was confirmed by a comparison of the measured equilibrium surface potential with that provided by the model [82]. Richterová et al. [88] examined the validity of the model and computed the contribution of the secondary electrons to the surface potential profile measured on gold and glass grains. Although the matching was not perfect, the authors concluded that the spectrum of electrons emitted from gold grains exhibits a large portion of energetic electrons (above 10 eV), and thus it resembles the Draine and Salpeter distribution, whereas the Maxwellian one is more appropriate for glass grains.

Rather small differences between energetic spectra of secondary electrons result in large differences in the grain equilibrium potential as can be seen in Fig. 13 where the surface potential at the maximum of the secondary emission yield is plotted as a function of the mean atomic number of the grain material (MF stands for melamine-formaldehyde resin [51]). One can note that this parameter orders the potentials rather well. Pavlů et al. [60] suggested that it is probably connected with an influence of the scattering of primary electrons on the formation of the spectrum of secondary electrons.

Richterová et al. [59, 89, 90] used scanning electron microscope (SEM) technique for direct measurements of secondary electron spectra from gold and carbon samples (note here that direct measurements of the spectra from insulated samples are impossible due to their charging). They found for gold that the shape of the spectra depends on the energy of primary electrons (Fig. 14) and that this dependence disappears after sputtering of several atomic layers with the Ar^+ beam. This suggests that the spectrum can be influenced by impurities that are always present on the grain surface.

5 Influence of surface layers

It is well known that surface properties differ from those of the bulk material and this fact is even more pronounced in the case of small dust grains. When investigating surface properties, the samples are often cleaned by an ion bombardment and, on the other hand, the grain immersed into a plasma is bombarded by ions [91]. For this reason, we have carried out several experiments with motivation to find how the surface layers influence the secondary emission process.

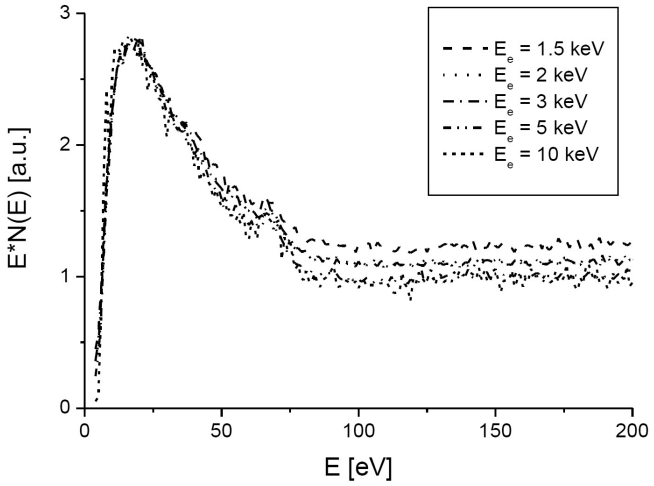

Fig. 14 A sequence of secondary emission spectra for several primary beam energies in the range of 1–10 keV before the Ar^+ treatment (the curves are normalized to the peak value). (Adopted from [89].)

Fig. 14 shows that a surface layer can influence the spectrum of secondary electrons and, consequently, the grain potential [89]. However, the layer of surface impurities was not defined in this case. Thus, we have used MF (melamine-formaldehyde resin) 2.35 μm spheres covered with $\approx$ 20 nm of the Ni layer and adapted the model of the secondary emission [82] (see section 4) and analyzed the effects of the layer thickness [92]. It was found that the secondary emission yield increases with the thickness of the layer until a saturation is reached. This fact suggested that secondary electrons excited below the layer have only a very low probability to escape through it and their portion decreases with increasing layer thickness. The calculations of the surface potential matched the experimental data as can be seen in Fig. 16. The figure compares data and model calculations for a pure MF grain and for the grain covered with 20 nm of Ni. We should note that the layer changes charging properties not only quantitatively but also qualitatively. For beam energies between 4 and 8 keV, the pure MF grain will be charged negatively, whereas the covered grain is positive in the whole energy range.

A systematic investigation of the influence of ion bombardment on surface layers was carried out by Žilavý et al. [93]. They trapped the Ni covered MF grain and repeated measurements of equilibrium surface potentials as a function of the energy of the primary electron beam. Particular measurements were separated by several hours of the grain bombardment with energetic Ar ions (Fig. 17). The results are summarized in Fig. 18 that shows the maximum of the surface potential as a function of the dose of Ar ions applied onto the grain surface. After application of a very low dose, the surface potential exhibits a small enhancement (point 3 in the figure). This can be explained by the removal of impurities from the Ni surface, in agreement with Fig. 13. We would like to point out that this effect is always observed for metallic grains because the layer of oxides and/or impurities exhibits generally lower surface potentials (Fig. 13).

After further ion bombardment, the surface potential fell down to the value earlier found for a pure MF grain (see Fig. 16) that is shown by a horizontal line in Fig. 18. According to the sputtering model of Pavlů et al. [94], the applied dose is about one tenth of that needed for the removal of the equivalent layer from the Ni grain. On the other hand, Ni and MF are very different materials and there is no information on adhesion of the Ni layer and one can expect that the layer was removed and that the potential drop will stop at this value. However, a new dose of Ar^+ further decreased the surface potential to a value that is on a lower limit of our detection possibilities. Our explanation of this effect is based on implantation of the Ar^+ into the grain surface that results in change of both elemental composition and structure of the surface. Further investigations of Žilavý et al. [93] have shown that

this implantation changes the profile of the secondary emission yield as well as the energy spectrum of emitted electrons.

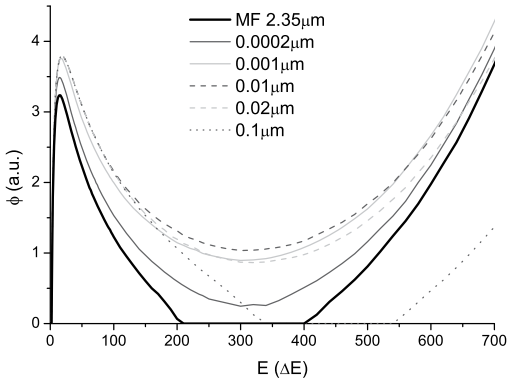

Fig. 15 The surface potential, ϕ as a function of the primary electron energy. The curves are parametrized by the layer thickness. The heavy line represents the pure MF grain. (Reprinted from [92], ©(2006), with permission from Elsevier.)

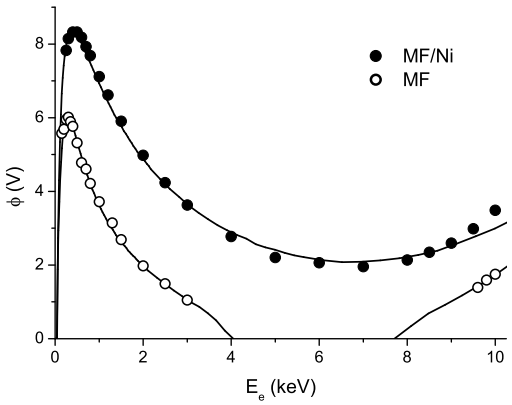

Fig. 16 A comparison of the model result and experimental data for pure MF and Ni covered MF grains. The lines represent model results, the dots show experimental data. (Reprinted from [92], ©(2006), with permission from Elsevier.)

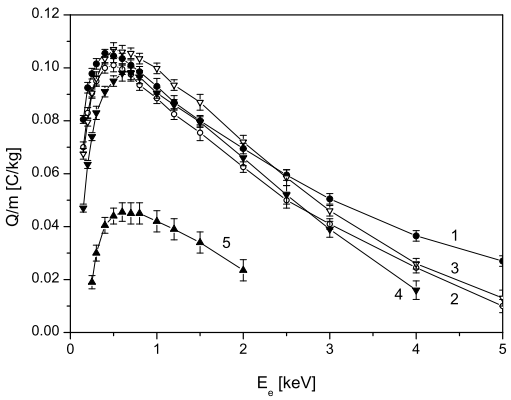

Fig. 17 The evolution of the equilibrium characteristics for the MF/Ni grain influenced by 5 keV Ar^+. The curves 1–5 correspond to an increasing dose of Ar^+: 1—without bombardment; 2—after one hour of 1 keV Ar^+ bombardment with the current density of $\approx 1 \times 10^{-5}$ A/m^2; 3—after one hour of 5 keV Ar^+ (the same current density); 4—after one hour of 5 keV Ar^+ with 5 times larger current density; 5—after 6 hours of 5 keV Ar^+ with 10 times larger current density. (Adopted from [93]. With kind permission from Springer Science+Business Media: [93], Figure 2.)

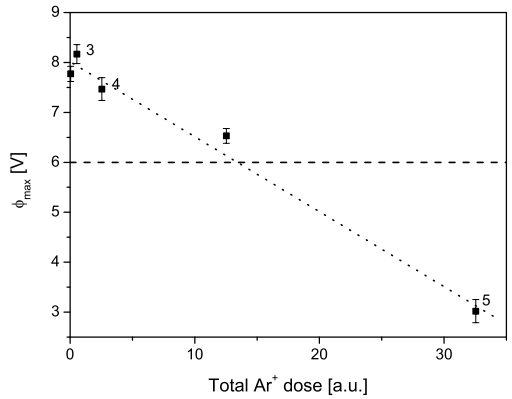

Fig. 18 The dependence of the equilibrium surface potential maximum on the dose of Ar ions. The numbered points correspond to the curves in Fig. 17. The horizontal line shows the surface potential of a pure MF and the dotted line presents a trend of all points. (With kind permission from Springer Science+Business Media: [93], Figure 3.)

A series of measurements of ion beam effects on the grains of different materials (e.g., [23, 95–97]) has shown that the changes of surface properties due to the ion bombardment are common and should be taken into account even for such materials as gold or carbon.

6 Influence of the electric field

Until present, we have discussed the secondary emission from grains that were charged only slightly and the electric field at their surface was weak. We will show that a strong electric field can modify the emission process substantially. A large positive potential of the grain prevents escaping of electrons and thus the current of secondary electrons falls to zero. On the other hand, a large negative electric field at the grain surface modifies electronic structure of the surface states and can led to change of the secondary emission yield through increase of the escape probability of excited electrons.

Charging of grains to negative potentials is possible for many materials in a limited range of diameters (Fig. 16 is an example of it) for which the secondary emission yield in a range of primary energies falls below unity. Applying a beam of such energy, the grain charges negatively because number of primary electrons stored inside the grain exceeds that of outgoing secondary electrons. The negative potential of the grain decelerates primary electrons and it leads to setting of a state when the secondary emission yield is equal to unity. This point on the profile of the secondary emission yield is often called the cross-over point and its position on the energy scale can serve as a measure of the secondary emission yield [99]. Beránek et al. [98] made systematic investigation on carbon grains and found that the crossover energy, E_{C2} increases linearly with the electric field at the grain surface (Fig. 19). This suggests an increase of the secondary emission yield by a factor of 1.5. A further investigation revealed that this factor is a function of the beam energy in the charged dust frame. The other effect of a prolonged bombardment of the grain with energetic electrons for several hours was the significant decrease of the crossover potential (compare in Fig. 19).

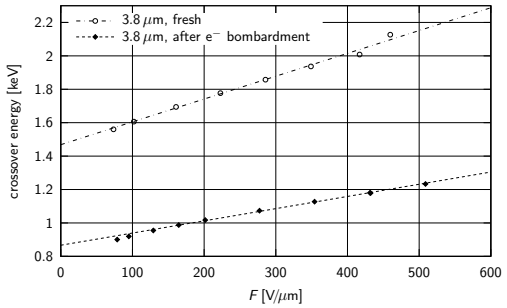

Fig. 19 The crossover energy, E_{C2} as a function of the surface electric field prior to and after the electron treatment of the grain. (Adopted from [98] with kind permission of The European Physical Journal (EPJ).)

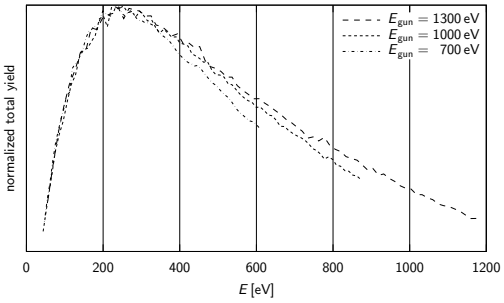

Fig. 20 The normalized total yield (with respect to σ_{max}) as a function of the incident energy for three electron beam energies. (Adopted from [98] with kind permission of The European Physical Journal (EPJ).)

The effect of the electron treatment is probably connected with an overall decrease of the secondary emission yield due to the electron-stimulated desorption [100]. As noted above, such effect was reported for example by Dennison et al. [101] for technical Al samples. Similar observations are referred in [102] where the authors presented discrepancies of the secondary electron yield between technical materials and pure metals (cleaned by 300° bake-out and an argon glow discharge). The authors observed a decrease of secondary electron yield after surface treatment. They explained it by a presence of insulating layers (e.g., oxides and adsorbed water) that significantly enhance the emissivity of metal surfaces and thus, various treatments involving a modification of the surface by ion bombardment can reduce the secondary electron yield of such materials.

We believe that we observed a similar effect because we noted a slow relaxation of the crossover potential towards the values prior to the treatment with a characteristic time of several tens of hours. This slow recovery suggests that not only absorption of a surface layer but some chemical reactions [103] are required to return σ to the values prior to the intensive electron irradiation.

The observed changes of the crossover energy can be caused either by an overall increase of σ or by a broadening of the peak on the $\sigma(E)$ profile. To resolve between these two possibilities, we measured this profile for several electron beam energies. The profiles in Fig. 20 are normalized with respect to σ_{max}. These preliminary results suggest that a broadening of the σ_{max} peak with the increase of the surface electric field takes place. We should note that this conclusion does not follow directly from Fig. 20 because the surface field continuously

changes along the measured profile and the profiles measured with the electron beam with higher energies were observed with a large charge (and a larger surface field) on the grain. Nevertheless, a possible change of the shape of the σ_{max} profile with the electric field is surprising because it implies a declination of this profile from the universal curve [28]. It should be noted that carbon exhibits a very low secondary emission yield ($\sigma_{max} \approx 0.6$), thus the cleaning of its surface leads to the decrease of the electric field. A similar effect (i.e., decrease of the crossover potential) was found after the ion bombardment, as we mentioned. Since the applied dose of Ar ions was very small, this decrease would be probably attributed to the cleaning of the surface rather than to changes of the structure of surface layers that we have discussed in section 5.

7 Concluding remarks

From a broad spectrum of processes that lead to the dust charging due to dust interaction with a surrounding plasma, the present paper deals only with electron emission induced by impacts of energetic electrons. Nevertheless, even such limited survey has brought much more questions than answers, many of them being connected with fundamental problems of the present physics of condensed matter. Main problems that this survey identified and that need further experimental and/or theoretical investigations can be briefly summarized as follows:

- Mechanism that leads to formation of a particular shape of the energy distribution of true secondary electrons, a possible role of the elastic scattering in this process.
- The cause(s) of changes of emission properties of the dust grain affected by energetic ions (surface roughness, changes of the surface elemental composition, reformation of crystalline structure at the grain surface).
- The connection of the secondary emission yield with the work function and electronic structure of a particular material.
- Sources of the enhancement of the secondary emission yield due to large electric field—backscattered primary or true secondary electrons.

On the other hand, a number of problems was successfully solved or elucidated in course of the last decade. The behavior of primary electrons inside the dust grain is well described by the model [82, 88] and their spectra (when leaving the grain) can be computed for different materials [85,92]. We know that the grain surface potential established by secondary emission depends neither on the work function nor on the secondary emission yield but rises with the mean atomic number of the grain material [60]. The dependence of the secondary emission yield on the electric field suggests that this field is not only fully screened by the surface electrons and penetrates deeper inside the conducting grains [98]. Nevertheless, we are still only on a half way to understanding of the interaction of dust grains with electron beams and even closer to the beginning of a full description of the dust interaction with plasmas.

Acknowledgements The presented work was partly supported by the Research plan MSM 0021620860 that is financed by the Ministry of Education of the Czech Republic, partly supported by the Czech Grant Agency under Contracts 202/08/P066 and 202/08/0063.

References

[1] R. Srama et al., Space Sci. Rev. **114**(1–4), 465–518 (2004).
[2] R. Srama, S. Kempf, G. Moragas-Klostermeyer, S. Helfert, T. J. Ahrens, N. Altobelli, S. Auer, U. Beckmann, J. G. Bradley, M. Burton, V. V. Dikarev, T. Economou, H. Fechtig, S. F. Green, M. Grande, O. Havnes, J. K. Hillier, M. Horanyi, E. Igenbergs, E. K. Jessberger, T. V. Johnson, H. Krueger, G. Matt, N. McBride, A. Mocker, P. Lamy, D. Linkert, G. Linkert, F. Lura, J. A. M. McDonnell, D. Moehlmann, G. E. Morfill, F. Postberg, M. Roy, G. H. Schwehm, F. Spahn, J. Svestka, V. Tschernjawski, A. J. Tuzzolino, R. Waesch, and E. Gruen, Planet. Space. Sci. **54**(9–10), 967–987 (2006).
[3] N. Altobelli, E. Grün, and M. Landgraf, Astron. Astrophys. **448**(1), 243–252 (2006).
[4] N. Altobelli, V. Dikarev, S. Kempf, R. Srama, S. Helfert, G. Moragas-Klostermeyer, M. Roy, and E. Grün, J. Geophys. Res. **112**(A07) (2007).

[5] F. Spahn, K. U. Thiessenhusen, J. E. Colwell, R. Srama, and E. Grün, J. Geophys. Res. **104**(E10), 24111–24120 (1999).
[6] F. Spahn, N. Albers, M. Sremcevic, and C. Thornton, Europhys. Lett. **67**(4), 545–551 (2004).
[7] F. Hörz et al., Science **314**(5806), 1716–1719 (2006).
[8] A. T. Kearsley, J. Borg, G. A. Graham, M. J. Burchell, M. J. Cole, H. Leroux, J. C. Bridges, F. Hoerz, P. J. Wozniakiewicz, P. A. Bland, J. P. Bradley, Z. R. Dai, N. Teslich, T. See, P. Hoppe, P. R. Heck, J. Huth, F. J. Stadermann, C. Floss, K. Marhas, T. Stephan, and J. Leitner, Meteorit. Planet. Sci. **43**(1-2), 41–73 (2008).
[9] C. La Hoz and O. Havnes, J. Geophys. Res. **113**(D19) (2008).
[10] O. Havnes and L. I. Naesheim, Ann. Geophys. **25**(3), 623–637 (2007).
[11] S. Robertson and Z. Sternovsky, IEEE Trans. Plasma Sci. **35**(2), 314–322 (2007).
[12] M. Kretschmer, H. Hofner, M. Thoma, M. Fink, S. Ratynskaia, G. Morfill, K. Tarantik, V. Fortov, O. Petrov, A. Usachev, A. Zobnin, and Y. Gerasimov, 'PK-4' – Laser-driven shear flow in a DC discharge complex plasma, in: New Vistas in Physics of Dusty Plasmas, edited by L. Boufendi, M. Mikikian, and P. K. Shukla, AIP Conference Proceedings Vol. 799 (American Institute of Physics, Melville, New York, 2005), pp. 235–238.
[13] H. M. Thomas, G. E. Morfill, V. E. Fortov, A. V. Ivlev, V. I. Molotkov, A. M. Lipaev, T. Hagl, H. Rothermel, S. A. Khrapak, R. K. Suetterlin, M. Rubin-Zuzic, O. F. Petrov, V. I. Tokarev, and S. K. Krikalev, New J. Phys. **10**(3) (2008).
[14] P. K. Shukla, Phys. Plasmas **8**(5), 1791–1803 (2001).
[15] E. Whipple, T. Northrop, and D. Mendis, J. Geophys. Res. **90**(A8), 7405–7413 (1985).
[16] A. Barkan, N. D'Angelo, and R. Merlino, Phys. Rev. Lett. **73**(23), 3093–3096 (1994).
[17] B. Walch, M. Hornyi, and S. Robertson, Phys. Rev. Lett. **75**(5), 838–841 (1995).
[18] M. Rosenberg and D. Mendis, IEEE Trans. Plasma Sci. **23**(2), 177–179 (1995).
[19] A. Sickafoose, J. Colwell, M. Horanyi, S. Robertson, and B. Walch, Photoelectric charging of dust particles, in: Frontiers in Dusty Plasmas, edited by Y. Nakamura, T. Yokota, and P. Shukla (Elsevier Science, Sara Burgerhartstraat 25, Po Box 211, 1000 Ae Amsterdam, Netherlands, 2000), pp. 367–372.
[20] H. Kimura and I. Mann, Astrophys. J. **499**(1), 454–462 (1998).
[21] E. C. Whipple, Rep. Prog. Phys. **44**(11), 1197–1250 (1981).
[22] N. Meyer-Vernet, Astron. Astrophys. **105**(1), 98–106 (1982).
[23] A. Velyhan, P. Žilavý, J. Pavlů, J. Šafránková, and Z. Němeček, Vacuum **76**(4), 447–455 (2004).
[24] H. Kersten, H. Deutsch, and G. M. W. Kroesen, Int. J. Mass Spectrom. **233**(1-3), 51–60 (2004).
[25] M. Sodha and S. Guha, Adv. Plasma Phys. **4**, 219–309 (1971).
[26] D. Mendis, M. Rosenberg, and V. Chow, Ionization equilibria in dusty plasma environments, in: Physics of Dusty Plasmas — Seventh Workshop, edited by Horanyi, M. and Robertson, S. and Walch, B., AIP Conference Proceedings Vol. 446 (Amer. Inst. Physics, 1998), pp. 1–11, 7th Workshop on the Physics of Dusty Plasmas, Boulder, CO, April, 1998.
[27] D. A. Mendis, Plasma Sources Sci. T. **11**(3A), A219–A228 (2002).
[28] E. Sternglass, Theory of secondary electron emission under electron bombardment, Scientific Paper 6-94410-2-P9, Westinghouse Research Laboratories, Pittsburgh 35, July 1957.
[29] E. C. Whipple, The equilibrium electrical potential of a body in the upper atmosphere and in interplanetary space, Publ. X615-65-296, NASA-GSFC, 1965.
[30] M. Horanyi and C. Goertz, Astrophys. J. **361**(1, Part 1), 155–161 (1990).
[31] B. Walch, M. Horanyi, and S. Robertson, Electrostatic charging of lunar dust, in: Physics of Dusty Plasmas — Seventh Workshop, edited by Horanyi, M. and Robertson, S. and Walch, B., AIP Conference Proceedings Vol. 446 (Amer. Inst. Physics, 1998), pp. 271–275, 7th Workshop on the Physics of Dusty Plasmas, Boulder, CO, April, 1998.
[32] V. Chow, D. Mendis, and M. Rosenberg, J. Geophys. Res. **98**(17), 19065–19076 (1993).
[33] Y. Watanabe, Plasma Phys. Contr. F. **39**(5A), A59–A72 (1997).
[34] M. Shiratani, H. Kawasaki, T. Fukuzawa, T. Yoshioka, Y. Ueda, S. Singh, and Y. Watanabe, J. Appl. Phys. **79**(1), 104–109 (1996).
[35] V. W. Chow, D. A. Mendis, and M. Rosenberg, Plasma Phys. Contr. F. **42**(1), 21–27 (2000).
[36] D. M. Suszcynsky, J. E. Borovsky, and C. K. Goertz, J. Geophys. Res. **97**(E2), 2611–2619 (1992).
[37] B. Walch, M. Horanyi, and S. Robertson, IEEE Trans. Plasma Sci. **22**(2), 97–102 (1994).
[38] A. Sickafoose, J. Colwell, M. Hornyi, and S. Robertson, J. Geophys. Res. **106**(A5), 8343 (2001).
[39] W. Paul and H. Steinwedel, Apparatus for separating charged particles of different specific charges, Patent 944,900, German Patent, 1956.
[40] R. Wuerker, H. Shelton, and R. Langmuir, J. Appl. Phys. **30**(3), 342–349 (1959).
[41] M. Abbas, P. Craven, J. Spann, E. West, J. Pratico, D. Tankosic, and C. Venturini, Phys. Scr. **T89**, 99–103 (2002).
[42] M. Abbas, P. Craven, J. Spann, W. Witherow, E. West, D. Gallagher, M. Adrian, G. Fishman, D. Tankosic, A. LeClair, R. Sheldon, and E. Thomas, J. Geophys. Res. **108**(A6), 1229 (2003).
[43] J. Spann, M. Abbas, C. Venturini, and R. Comfort, Phys. Scr. **T89**, 149–153 (2001).
[44] M. Abbas, P. Craven, J. Spann, D. Tankosic, A. LeClair, D. Gallagher, E. West, J. Weingartner, W. Witherow, and A. Tielens, Astrophys. J. **614**(2), 781–795 (2004).

[45] J. Švestka, I. Čermák, and E. Grün, Adv. Sp. Res. **13**(10), 199–202 (1993).
[46] V. Chow, D. Mendis, and M. Rosenberg, IEEE Trans. Plasma Sci. **22**(2), 179–186 (1994).
[47] I. Čermák, E. Grün, and J. Švestka, Adv. Sp. Res. **15**(10), 59–64 (1995).
[48] I. Čermák, Laboruntersuchung elektrischer Aufladung kleiner Staubteilchen, PhD thesis, Naturwissenschaftlich-Mathematischen Gesamtfakultät, Ruprecht-Karls-Universität, Heidelberg, 1994.
[49] P. Žilavý, Z. Sternovský, I. Čermák, Z. Němeček, and J. Šafránková, Vacuum **50**(1–2), 139–142 (1998).
[50] I. Čermák, J. Pavlů, P. Žilavý, Z. Němeček, J. Šafránková, and I. Richterová, 3D electrodynamic quadrupole: A nondestructive analysis of single dust grains, in: WDS'04 Proceedings of Contributed Papers: Part II – Physics of Plasmas and Ionized Media, edited by J. Šafránková (Matfyzpress, Prague, 2004), pp. 279–286.
[51] J. Pavlů, A. Velyhan, I. Richterová, Z. Němeček, J. Šafránková, I. Čermák, and P. Žilavý, IEEE Trans. Plasma Sci. **32**(2), 704–708 (2004).
[52] P. Řepa, J. Tesař, T. Gronych, L. Peksa, and J. Wild, J. Mass Spectrom. **37**(12), 1287–1291 (2002).
[53] P. Žilavý, Z. Němeček, and J. Šafránková, Size and density determination of a spherical particle in the dust charging experiment, in: WDS'99 Proceedings of Contributed Papers: Part II – Physics of Plasmas and Ionized Media, edited by J. Šafránková (Matfyzpress, Prague, 1999), pp. 252–257.
[54] E. J. Sternglass, On the phenomenon of secondary electron emission from solids, Master's thesis, Cornell University, 1951.
[55] B. Draine and E. Salpeter, Astrophys. J. **231**(1), 77–94 (1979).
[56] I. M. Bronstein and B. S. Fraiman, Secondary Electron Emission (Nauka, Moskva, 1969), in Russian.
[57] O. Hachenberg and W. Brauer, Advances in electronics and electron physics **11**, 413–499 (1959).
[58] Q. Lu, Z. Zhou, L. Shi, and G. Zhao, Chin. Phys. **14**(7), 1465–1470 (2005).
[59] I. Richterová, D. Fujita, Z. Němeček, M. Beránek, and J. Šafránková, Secondary electron yield of glassy carbon dust grains, in: WDS'08 Proceedings of Contributed Papers: Part II – Physics of Plasmas and Ionized Media, edited by J. Šafránková and J. Pavlů (Matfyzpress, Prague, 2008), pp. 68–73.
[60] J. Pavlů, I. Richterová, Z. Němeček, J. Šafránková, and I. Čermák, Faraday Discuss. **137**, 139–155 (2008); http://dx.doi.org/10.1039/b702843a
[61] J. Pavlů, J. Šafránková, Z. Němeček, and A. Velyhan, Charging properties of dust grain clusters, in: Dusty Plasmas in the New Millennium, edited by R. Bharuthram, M. Hellberg, P. Shukla, and F. Verheest, AIP Conference Proceedings Vol. 649 (American Institute of Physics, Melville, New York, December 2002), pp. 382–385.
[62] Z. Němeček, J. Pavlů, J. Šafránková, I. Richterová, and I. Čermák, The secondary emission from small spherical grains, in: Dusty Plasmas in the New Millennium, edited by R. Bharuthram, M. Hellberg, P. Shukla, and F. Verheest, AIP Conference Proceedings Vol. 649 (American Institute of Physics, Melville, New York, December 2002), pp. 378–381.
[63] H. Salow, Phys. Z. **41**, 434 (1940).
[64] E. M. Baroody, Phys. Rev. **78**(8), 780–787 (1950).
[65] H. Bruining, Physics and Applications of Secondary Emission (Pergamon, London, 1954).
[66] K. Kanaya and H. Kawakatsu, J. Phys. D **5**(9), 1727–1742 (1972).
[67] K. Kanaya, S. Ono, and F. Ishigaki, J. Phys. D **11**(17), 2425–2437 (1978).
[68] D. C. Joy, J. Microsc. **147**(1), 51–64 (1987).
[69] R. Shimizu and Z. J. Ding, Rep. Prog. Phys. **55**(4), 487–531 (1992).
[70] A. Dubus, J. C. Dehaes, J. P. Ganachaud, A. Hafni, and M. Cailler, Phys. Rev. B **47**(17), 11056–11073 (1993).
[71] Z. J. Ding, X. D. Tang, and R. Shimizu, J. Appl. Phys. **89**(1), 718–726 (2001).
[72] Z. J. Ding, H. M. Li, X. D. Tang, and R. Shimizu, Appl. Phys. A-Mater. **78**(4), 585–587 (2004).
[73] Z. J. Ding, H. M. Li, K. Goto, Y. Z. Jiang, and R. Shimizu, J. Appl. Phys. **96**(8), 4598–4606 (2004).
[74] N. F. Mott and H. S. W. Massey, Theory of atomic collisions (Oxford University Press, New York, 1965).
[75] D. R. Penn, Phys. Rev. B **35**(2), 482–486 (1987).
[76] Y. Lin and D. Joy, Surf. Interface Anal. **37**(11), 895–900 (2005).
[77] J. Cazaux, J. Phys. D **38**(14), 2433–2441 (2005).
[78] P. Ziemann, P. Liu, D. Kittelson, and P. McMurry, J. Phys. Chem. **99**(14), 5126–5138 (1995).
[79] G. F. Dionne, Journal of Applied Physics **46**(8), 3347–3351 (1975).
[80] I. Richterová, Z. Němeček, J. Šafránková, and J. Pavlů, IEEE Trans. Plasma Sci. **32**(2), 617–622 (2004).
[81] D. Joy, Monte Carlo Modeling for Electron Microscopy and Microanalysis (Oxford University Press, New York, 1995).
[82] I. Richterová, J. Pavlů, Z. Němeček, and J. Šafránková, Phys. Rev. B **74**(23), 235430 (2006).
[83] Z. Czyżewski, D. O'Neill MacCallum, A. Romig, and D. C. Joy, J. Appl. Phys. **68**(7), 3066–3072 (1990).
[84] P. Hovington, D. Drouin, and R. Gauvin, Scanning **19**(1), 1–35 (1997).
[85] I. Richterová, Z. Němeček, J. Šafránková, J. Pavlů, and M. Beránek, IEEE Trans. Plasma Sci. **35**(2), 286–291 (2007).
[86] A. Velyhan, Z. Němeček, and J. Šafránková, Secondary electron emisson from small metallic grains, in: WDS'01 Proceedings of Contributed Papers: Part II — Physics of Plasmas and Ionized Media, edited by J. Šafránková (Matfyzpress, Prague, 2001), pp. 267–272.

[87] R. J. L. Grard, J. A. M. McDonnell, E. Grun, and K. I. Gringauz, Astron. Astrophys. **187**(1–2), 785–788 (1987).
[88] I. Richterová, J. Pavlů, Z. Němeček, and J. Šafránková, Eur. Phys. J. D **48**(3), 375–381 (2008).
[89] I. Richterová, D. Fujita, J. Pavlů, Z. Němeček, and J. Šafránková, Ar^+ treatment influence on secondary electron spectra from dust grains, in: XXVIII International Conference on Phenomena in Ionized Gases, edited by J. Schmidt, M. Šimek, S. Pekárek, and V. Prukner (Institute of Plasma Physics AS CR, v.v.i., Prague, 2007), pp. 2263–2266.
[90] I. Richterová et al., Eur. Phys. J. D **in preparation** (2009).
[91] I. Stefanović, J. Berndt, D. Marić, V. Šamara, M. Radmilović-Radjenović, Z. L. Petrović, E. Kovačević, and J. Winter, Phys. Rev. E **74**(2), 026406 (2006).
[92] I. Richterová, J. Pavlů, Z. Němeček, J. Šafránková, and P. Žilavý, Adv. Sp. Res. **38**(11), 2551–2557 (2006).
[93] P. Žilavý, I. Richterová, Z. Němeček, J. Šafránková, and J. Pavlů, Czech. J. Phys. **55**(10), 1283–1292 (2005).
[94] J. Pavlů, I. Richterová, Z. Němeček, J. Šafránková, and J. Wild, IEEE Trans. Plasma Sci. **35**(2), 297–302 (2007).
[95] J. Pavlů, A. Velyhan, I. Richterová, J. Šafránková, Z. Němeček, J. Wild, and M. Jeřáb, Vacuum **80**(6), 542–547 (2006).
[96] J. Pavlů, I. Richterová, Z. Němeček, and J. Šafránková, Adv. Sp. Res. **42**(1), 129–135 (2008).
[97] M. Jeřáb, I. Richterová, J. Pavlů, J. Šafránková, and Z. Němeček, IEEE Trans. Plasma Sci. **35**(2), 292–296 (2007).
[98] M. Beránek, I. Richterová, Z. Němeček, J. Pavlů, and J. Šafránková, Eur. Phys. J. D **in print** (2009).
[99] J. Pavlů, Z. Němeček, J. Šafránková, and I. Čermák, IEEE Trans. Plasma Sci. **32**(2), 607–612 (2004).
[100] V. Matolín, T. Gronych, and M. Gillet, Surf. Sci. **321**(1–2), L143–L148 (1994).
[101] J. Dennison, A. Sim, and C. Thomson, IEEE Trans. Plasma Sci. **34**(5), 2204–2218 (2006).
[102] V. Baglin, J. Bojko, O. Gröbner, B. Henrist, N. Hilleret, C. Scheuerlein, and M. Taborelli, The secondary electron yield of technical materials and its variation with surface treatments, in: EPAC 2000 Contributions to the Proceedings, edited by M. ReglerEPAC (JACoW, http://www.JACoW.org/, August 2000), pp. 217–221.
[103] F. Le Pimpec, R. Kirby, F. King, and M. Pivi, J. Vac. Sci. Technol. A **23**(6), 1610–1618 (2005).

E. Pavlů et al. [2008]

Pavlů, J., Richterová, I., Němeček, Z., Šafránková, J., Čermák, I., Interaction between single dust grains and ions or electrons: laboratory measurements and their consequences for the dust dynamics. *Faraday Discuss.* 137: 139–155, 2008.

Interaction between single dust grains and ions or electrons: laboratory measurements and their consequences for the dust dynamics

Jiří Pavlů,*[a] Ivana Richterová,[a] Zdeněk Němeček,[a] Jana Šafránková[a] and Ivo Čermák[b]

Received 23rd February 2007, Accepted 16th March 2007
First published as an Advance Article on the web 20th July 2007
DOI: 10.1039/b702843a

The present paper reviews our latest, and brings several new, results on charging of dust grains of various materials and sizes. Charging processes of dust in space and their influence on the dust dynamics are analyzed in laboratory simulations of secondary emission, field ion and electron emissions, and dust sputtering. Single micrometre-sized grains and grain clusters are stored in a hyperbolic quadrupole field under ultra-high vacuum conditions for long time periods. The charge state of the grain and its evolution are recorded while the grain is exposed to ion or electron beams of various energies and fluxes. The influence of the secondary electron emission on the charge state is measured and compared with a computer model. Limitations on the grain charge by the field electron and ion emission are considered next. The measurements allow analyzing field emission from conductive and dielectric grains. The existence of long-lived surface states on insulating materials, which are probably responsible for the anomalous behavior of field electron emission and the low threshold of the field ion emission, is indicated. The observation of sputtering by energetic ions showing a surprising anisotropic erosion of a conductive grain is analyzed. The sputtering and the field ion emission are discussed as possible sources of the so-called pick-up ions.

1. Introduction

The manifestations of dust in different parts of the solar system have been known and intensively studied for a long time, namely, cometary comae and their dusty tails, planetary rings, circumsolar dust rings, the interplanetary medium, interstellar molecular clouds, *etc*. In the context of interplanetary space, ''dust'' refers to particulate matter that does not manifest itself as isolated bodies but from some distance can be recognized as an ensemble of indistinguishable particles. The interplay between plasmas and charged dust grains has opened up a new research area: that of a dusty (or complex) plasma. Dusty plasmas are fully or partially ionized gases comprising neutral gas molecules, electrons, ions, and highly charged sub-micron- and micron-sized dust grains. There is a variety of mechanisms by which cosmic dust grains can be electrically charged: the capture of ambient

[a] *Charles University, Faculty of Mathematics and Physics, V Holešovičkách 2, 180 00, Prague, Czech Republic. E-mail: jiri.pavlu@mff.cuni.cz*
[b] *CGC Instruments, Hübschmannstr. 18, 09112, Chemnitz, Germany*

electrons and ions, Secondary Electron Emission (SEE) by energetic electron and ion impacts, photoemission due to short-wavelength electromagnetic radiation, field emission of electrons, triboelectric effects, and field evaporation of ions. Interplanetary and interstellar dust grains acquire a positive charge in the solar wind and can be strongly influenced by the Lorentz force as they pass through planetary magnetospheres. There, the charge on the grains changes rapidly when they pass through different plasma environments.[1]

In the case of interplanetary dust grains, the relevant charging processes are interactions with solar wind electrons and ions and photoemission by solar UV radiation. The flux of photoelectrons from a metal surface at 1 AU was estimated by Wyatt[2] to be equal to 2.5×10^{10} cm^{-2} s^{-1}. The photoelectron flux from silicate and graphite surfaces can be up to one order of magnitude lower; the same is expected for the flux from icy surfaces. On the other hand, mean ion and electron fluxes are of the order of 10^8 cm^{-2} s^{-1}. From these numbers it follows that charging of interplanetary dust grains is dominated by photoemission, which leads generally to positively charged particles with surface potentials of several volts. The value of the potential depends on the photoemission yield of the grain material, *e.g.*, silicate grains attain potentials of 2.5–5 V, which are practically constant in the grain size interval 0.1–10 μm.[3] Potentials of grains from conducting materials might be somewhat higher. In the case of very small grains with dimensions comparable to the wavelength of light, the photoemission yield can be enhanced by a factor of 2–3, which results in higher surface potentials.[4]

In dense plasma regions where the electron flux is dominant, the sign and value of the dust grain surface potential will be determined by the energy of the impinging electrons. Electron attachment dominates in the eV range but, at electron energies above about 10 eV, SEE becomes important and results in a reduction of the negative potential. At energies above a few hundred eV, the SEE yield becomes larger than unity which causes a sign change of the potential from negative to positive. Generally, the SEE yield reaches a maximum value σ_{max} at energies E_{max} between 300 and 2000 eV. At higher energies, the SEE yield becomes again lower than unity, resulting in negative surface potential.

However, as the size of the grains becomes comparable with the mean free path of the primary electrons and with the diffusion length of excited electrons, the SEE yield may be substantially enhanced. Thus, the charge of micrometer-sized grains can be either positive or negative and the charge sign depends on their shape, dimensions, and material.[5]

Ion impacts may also induce the emission of secondary electrons, however, with a much lower yield and thus this effect is negligible in most environments.

The total electric charge of dust grains might be limited by field evaporation, or by field emission. These processes become dominant at field strengths $> 3 \times 10^{10}$ V m^{-1} (positive charge) and $> 10^9$ V m^{-1} (negative charge), respectively. However, even at much lower field strength, electrostatic repulsive forces can destroy the grains (electrostatic fragmentation) when they become higher than the tensile strength of the material. The latter process is particularly important in case of fluffy grains that may have tensile strengths as low as about 10^3 Pa. For such a fluffy grain with a radius of 1 μm, electrostatic fragmentation can occur already at surface potentials as low as 10 V. The other process leading to material losses from dust grains is sputtering due to impact of energetic ions.

These processes are very important in space plasma environments. However, their investigation in conditions resembling those of outer space is rather difficult. Usually several processes act in accord. Also, ambient conditions change rapidly. We can only study charging processes in a highly idealized laboratory setting. In our experiment, we store a single (charged) dust grain in an electrodynamic trap. The grain can be exposed to electron and/or ion beams of a variable energy. We can measure grain diameter, mass, and charge as well as the currents flowing from and to the grain. Each charging process can thus be studied separately.

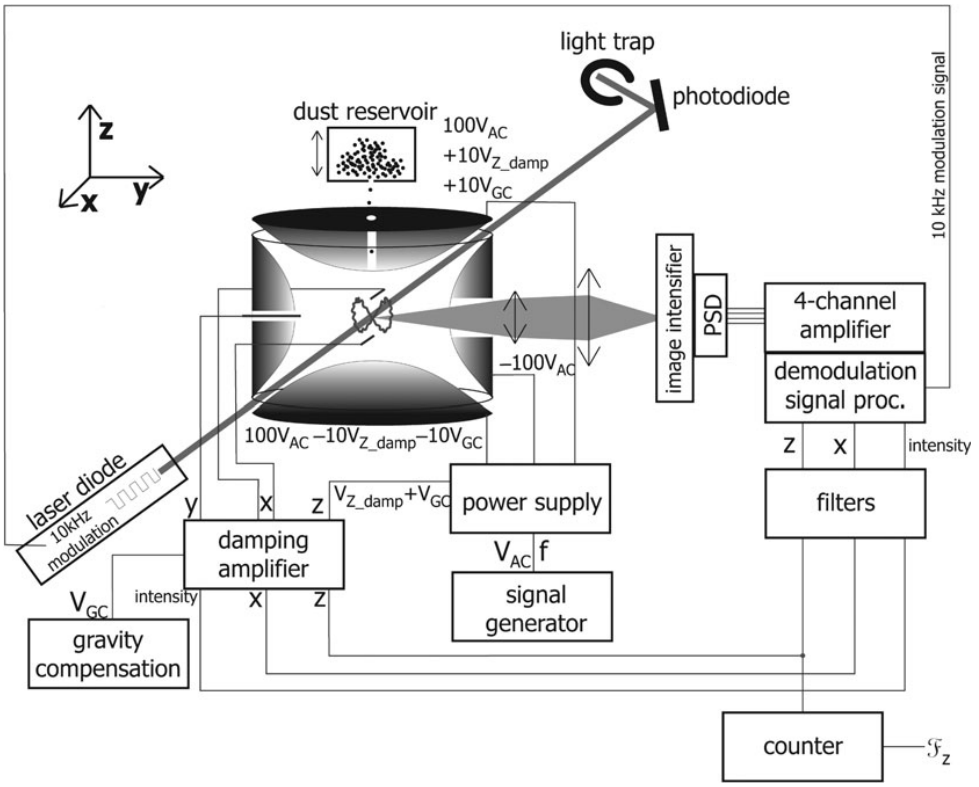

Fig. 1 Experimental setup. For details see text.

In this paper, we focus on electron-induced SEE, electron and ion field emissions, and sputtering of dust grains by energetic ions. By comparing these results with *in situ* observations, we provide a new view of the fundamental physical processes of dust in space.

2. Experimental

Details of the experimental setup are provided elsewhere,[6–9] thus, here we will only repeat the basic principles. The apparatus uses an electrodynamic quadrupole (a 3D quadrupole trap[10] with modified hyperbolic electrodes). As can be seen in Fig. 1, a grain trapped in the 3D quadrupole is irradiated by a 635 nm diode laser. The light scattered off the grain passes a small window in the ring electrode (electrically screened by a grid) and is magnified by a simple lens system. Since the intensity of the scattered light is rather low, an image intensifier is used to increase the detection sensitivity. The output of the image intensifier is directly coupled to a PIN diode serving as a 2D coordinate detector. The laser light is modulated at 10 kHz for a reduction of noise. The electrically amplified signal from the PIN diode is demodulated by the lock-in technique and the coordinates of the light spot are calculated. The grain oscillation frequency can be determined by a frequency counter or by Fourier analysis.

After several simplifications, theoretical considerations lead to the following relation between the grain oscillation frequency and its charge-to-mass ratio (specific charge, Q/m):

$$\frac{|Q|}{m} \cong \frac{2\pi^2 r_0^2}{|\lambda_u|}\frac{f F_u}{V_{\mathrm{ef}}}, \tag{1}$$

where

$V_{\mathrm{ef}} = V_{\mathrm{AC}}/\sqrt{2}$ is the RMS value of the AC voltage on the quadrupole electrodes, V_{AC} is its amplitude, $f = \omega/2\pi$ the frequency of the applied AC voltage, $F_u = \Omega_u/2\pi$ the frequency of the particle motion in the u direction, r_0 denotes the inner radius of

the quadrupole ring electrode, and λ_u is the weight factor of the electric field in the u direction.

This relation is based on the assumption of an adiabatic motion of the particle in the quadrupole field. This is valid for a sufficiently high-frequency ratio between the applied AC voltage and the particle oscillations. Further, the expression assumes an ideal quadrupole field. Any deviation from the ideal hyperbolic geometry manifests itself in a contribution of higher multipoles to the total field. The higher multipoles lead to an anharmonic potential, thus, the particle oscillation frequency becomes amplitude dependent. Since the deviation due to the anharmonicity increases with the oscillation amplitude, the amplitude must not exceed a certain value for a desired accuracy of the frequency determination. On the other hand, a reliable measurement of the oscillation frequency requires a sufficiently high oscillation amplitude. Therefore, to provide reproducible measurement conditions, the amplitude of the grain motion has to be stabilized.

The experiment was designed for operation under ultra-high vacuum conditions ($\approx 10^{-7}$ Pa or better). This is essential in order to reduce the interaction of the grain surface with molecules of the residual atmosphere. Interaction of the investigated grain with photons, electrons, or ions may lead to a substantial increase of its vibrational temperature, and thus, to an increase of the oscillation amplitude. Under ultra-high vacuum conditions, the collisional cooling of the grain by the residual gas is negligible and the grain can maintain this vibrational temperature for a very long time, or it can be even further heated by anharmonic effects. To control the vibrational temperature of a stored particle under any experimental conditions, we have developed an active control system. This system uses several auxiliary electrodes as well as the quadrupole electrodes themselves to produce an additional electric field along each coordinate. The electrodes are supplied by voltages derived from the coordinate signals. The coordinates of oscillating dust are monitored and the electric signal is used in an active feedback loop to control the amplitude of the dust motion. The damping signals are amplified and used to create auxiliary electric fields in the quadrupole that controls the grain oscillations.

The grain oscillation frequency is the only measurable quantity, and we have developed several techniques to determine the grain mass, charge, capacitance, and other parameters. The detailed description of these techniques can be found in Čermák *et al.*[8] and Pavlů *et al.*[9]

SEM images of the dust samples are shown in Fig. 2. Metallic grains are generally used as testing samples because their material properties are well known from previous studies, whereas SiO_2 and carbon are materials that can be frequently found in space. The ensemble of the used samples is complemented with grains from a Melamine Formaldehyde resin (hereafter MF) and with MF grains covered by a thin (≈ 20 nm) layer of nickel (hereafter MF/Ni). The dimensions of the SiO_2, MF, and MF/Ni samples are well defined, whereas the mass and the dimension of other grains have to be determined in the course of the experiment.

3. Secondary electron emission

Many papers on SEE from various materials have been published. Interest continues because of the important role that SEE plays in many fields of modern technology—insulator breakdown (damaging electronic devices), electron lithography, charging of spacecrafts and space dust grains exposed to cosmic radiation, and many others. As we noted above, secondary emission plays a prominent role when a portion of energetic (> 10 eV) electrons is present in the medium surrounding the grain.

One of the first theories published by Sternglass[11] describes experimental SEE from planar metal surfaces in the range of hundreds of eV to several keV. Primary electrons impacting the sample surface interact with the bulk material and lose their energy in many types of collisions. The energy losses often result in excitations of

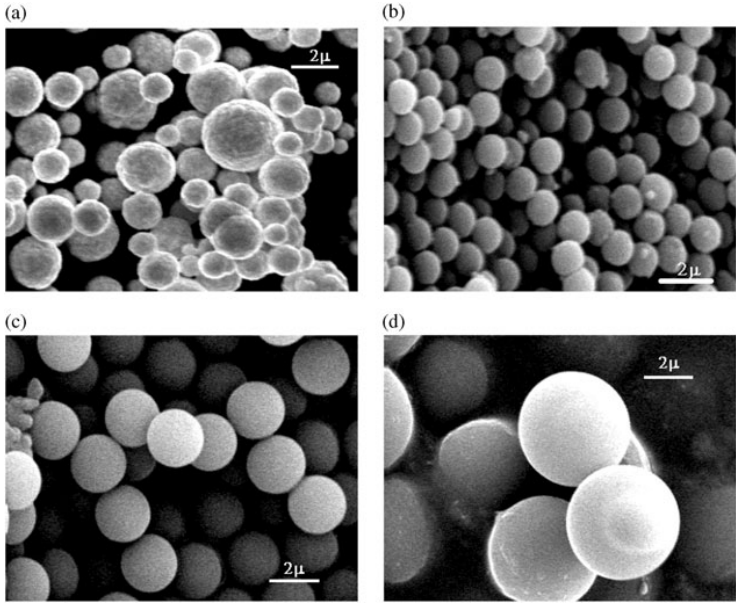

Fig. 2 Examples of grains—SEM photos: (a) gold grains, (b) monodispersed SiO_2 grains of 1.2 μm diameter, (c) precise-size MF grains of 2.35 μm diameter, (d) MF grains of 4.97 μm diameter.

material electrons and some of the excited electrons can leave the surface. These electrons, the so-called true Secondary Electrons (SE), have typical energies of a few eV. For large planar samples, the energy dependence of the SEE yield, $\delta(E)$, (defined as the mean number of SE per one primary electron) can be described by the Sternglass universal curve:[11]

$$\frac{\delta}{\delta_{\max}} = \frac{E}{E_{\max}} \exp\left(2 - 2\sqrt{\frac{E}{E_{\max}}}\right), \tag{2}$$

where $\delta_{\max}$ is the maximum SEE yield, and $E_{\max}$ is the corresponding primary electron energy. For real materials, the curve exhibits a maximum at energies in the range from several hundred eV to a few keV and decreases to zero at very high and low beam energies. Its parameters, the maximum yield, $\delta_{\max}$, and the corresponding energy, $E_{\max}$, depend only on the sample material at the incident angle. However, the validity of the universal curve is limited to $4E_{\max}$. In a later work, Draine and Salpeter[12] found a new approximation by fitting to experimental data; this approximation is valid to higher energies.

The primary electrons undergo scattering and may be re-emitted from the solid without a significant loss of their initial energy. The yield of backscattered electrons, η, increases with the material density and the atomic number up to ≈ 0.5 for a normal incident angle. It grows only slowly with the beam energy above a few hundreds of eV. Thus, the total SEE yield, $\sigma = \delta + \eta$, and the yield of true SE δ varies in a similar way with the beam energy.[13]

Srama *et al.*[4] noted that the process of SEE is very sensitive to the grain size and to the physical properties of the dust grains. At electron energies of >1 keV, the mean free path of electrons in a compact dust grain is >0.1 μm, therefore, electrons can penetrate through small grains and can also cause SEE from the exit side. However, using laboratory simulations and the SEE model, Richterová *et al.*[14] has shown that this effect has only negligible consequences for the grain charge.

The SEE yield increases with increasing angle of incidence of primary electrons by up to one order of magnitude over that seen from plane surfaces.[12] Our preliminary estimate of this for spherical grains and a parallel electron beam suggests an increase of the SEE yield by a factor of 1.2–2.

Theoretical studies of SEE are based mainly on Monte Carlo simulations of electron trajectories.[15–19] However, the majority of models was applied to planar metal or insulating targets and much less attention was paid to spherical samples. The finite grain size plays an important role when primary electrons are energetic enough to penetrate through the grain. Theoretical considerations of SEE from spherical sub-micrometre oil drops were carried by Ziemann *et al.*[20] He achieved a good match with experiment up to a primary energy of 250 eV. Chow *et al.*[21] developed a model of SEE from spherical bodies. Since that model did not reproduce experimental data,[22] Chow *et al.*[23] published an improved model. The new model provided the SEE yield with several maxima. By varying the parameters of the model, the authors were able to fit the data but they had to use different sets of constants for low- and high-energy regions. Richterová *et al.*[24] developed a simple Monte Carlo model of SEE from spherical dust grains. Although the model does provide a typical SEE yield curve and can roughly describe the observed energetic dependencies of the dust grain equilibrium charge, it has numerous non-measurable parameters. For this reason, Richterová *et al.*[14] prepared a new model based on more realistic assumptions. The results of the improved model can be briefly summarized as follows: (1) the scattering of primary electrons inside the grain is critical to understanding the SEE, (2) the grain charge is determined not only by the SEE yield—the energy distribution of SEs is equally important, (3) the increase of the surface potential with decreasing grain size is predominantly caused by the increasing number of backscattered primary electrons, not by true SEs. All these statements were demonstrated experimentally on spherical gold and glass grains.

SEs charge the dust grain positively; negative potentials can be reached only if the total SEE yield, σ is lower than unity. It is generally true for low beam energies (tens of eV) and, as we will show later, in the keV range for grain materials with a specific combination of true and backscattered SEE yields. These considerations are based on the assumption of compact spherical dust grains. In space, however, irregularly shaped grains can significantly change their properties. In order to demonstrate the effects of the grain surface structure and shape, we have carried out measurements of surface potentials of grain clusters composed of different numbers of ≈ 1.2 μm SiO_2 spheres. The clusters were exposed to an 0.1–10 keV electron beam, thus SEE was the dominant process for grain charging. The mass of each investigated cluster was determined by the method of elementary-charge steps[9] and the number of individual grains in the cluster was estimated from the total mass. These numbers are shown as parameters of surface potential profiles in Fig. 3. The shape of this profile for a single grain was discussed by Richterová *et al.*,[25] thus, we will concentrate on differences caused by the clustering.

Fig. 3 shows that, whereas the initial parts of all profiles are nearly identical, the slopes of the high-energy tails decrease with the number of spheres in the cluster in a systematic manner. The equilibrium potential of the grain or cluster is determined by a balance of incoming and outgoing electrons. If the beam energy is sufficiently low, the electrons are emitted only from the exposed part of the cluster and the curves roughly follow the dependence found for planar surfaces. If the emission from the "opposite side" of a particular grain becomes important, the surface potential is a decreasing function of the number of grains in the cluster. We suggest that it is caused by the shielding of the SEs as well as backscattered electrons by other grains in the cluster, because the SEs leaving the material "inside" the cluster are captured by another surface. It is interesting to note that, even for a relatively high number of grains in the cluster, the charging characteristics differ from those measured for compact grains of a similar equivalent diameter. The curve was measured for one cluster consisting of about 110 grains, thus, its mass corresponded to a 5 μm sphere, on which no comparable effect of enhanced emission at high energies could be observed. The lowest curve in Fig. 3 shows the surface potential profile measured on a 3.6 μm compact glass grain. The curve resembles the features measured on clusters

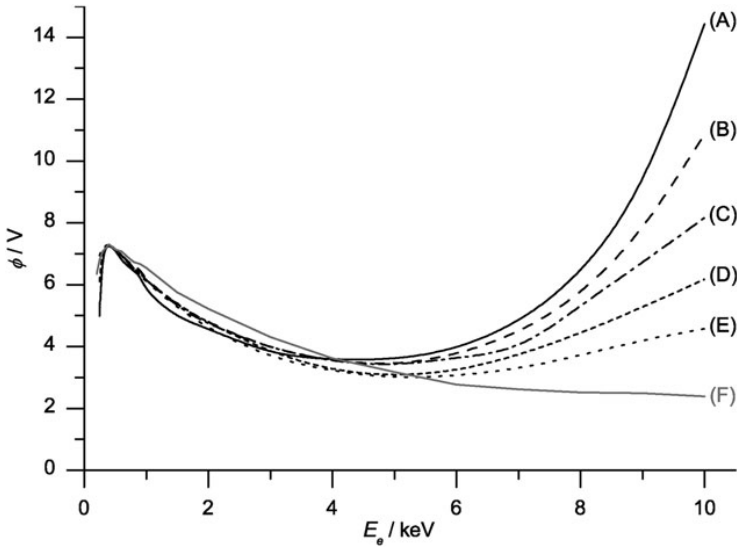

Fig. 3 Profiles of surface potential as a function of the primary electron beam energy measured for SiO_2 grains of 1.2 μm diameter and their clusters in comparison with a large glass grain. (A) Single grain, (B) cluster of three grains, (C) cluster of five grains, (D) cluster of about 34 grains, (E) cluster of more than 110 grains, (F) the glass grain of a diameter of about 3.6 μm.

in the low-energy range but the potentials follow the decreasing trend also at high energies. We assume that the grains on the edge of the cluster surface, which are not shielded, are responsible for the enhancement of the cluster potential at high beam energies.

This result can be applied to compact grains of an irregular shape. The surface potential of such grains will be determined by the part with the smallest characteristic dimension, thus, it would be significantly higher than that derived by a spherical approximation. As the cluster geometry in our experiment is unknown, we cannot reliably determine the tensile stress. However, the spherical approximation provides an upper limit of the order of 10 Nm^{-2}, *i.e.*, even below the value required for the destruction of fluffy aggregates. However, the tensile stress increases with decreasing diameter as the surface potential rises, and it could be sufficient to destroy clusters of nanoparticles.

It is generally expected that the surface potential of grains exposed to an electron beam would be a simple function of the SEE yield of a given material. In order to check this expectation, we have summarized the measurements of the equilibrium grain potential as a function of the electron beam energy carried out on grains of different diameters and materials in Fig. 4. The abscissa is divided into two regions: the high and the low energies. In the low-energy range, the profiles of the potential qualitatively follow the well known energy dependence of the SEE yield for planar samples because they rise with the beam energy until a maximum is reached. The beam energy corresponding to this maximum is several hundred eV. However, the SEE yield measured on planar samples would fall in the high-energy range since it is approximately equal to the yield of the backscattered electrons for highest energies. However, we could find even a rise of the grain potential in this energy range. These effects are connected to the finite size of the dust grain. They were broadly discussed in Richterová *et al.*[26] The computer simulation of Richterová *et al.*[14] showed without a doubt that for small dust grains, the size effects are predominantly caused by the increase of the yield of backscattered electrons. We would like to point out that the 3.7 μm carbon and the 2.35 μm MF grains, in the primary energy range from 3 to 7 keV, exhibit potentials lower than the detection limit of our setup. The use of a beam of energy between 4 and 6 keV would lead to negative grain potentials. Grains from all other investigated materials are charged positively in our energy range (0.1–10 keV).

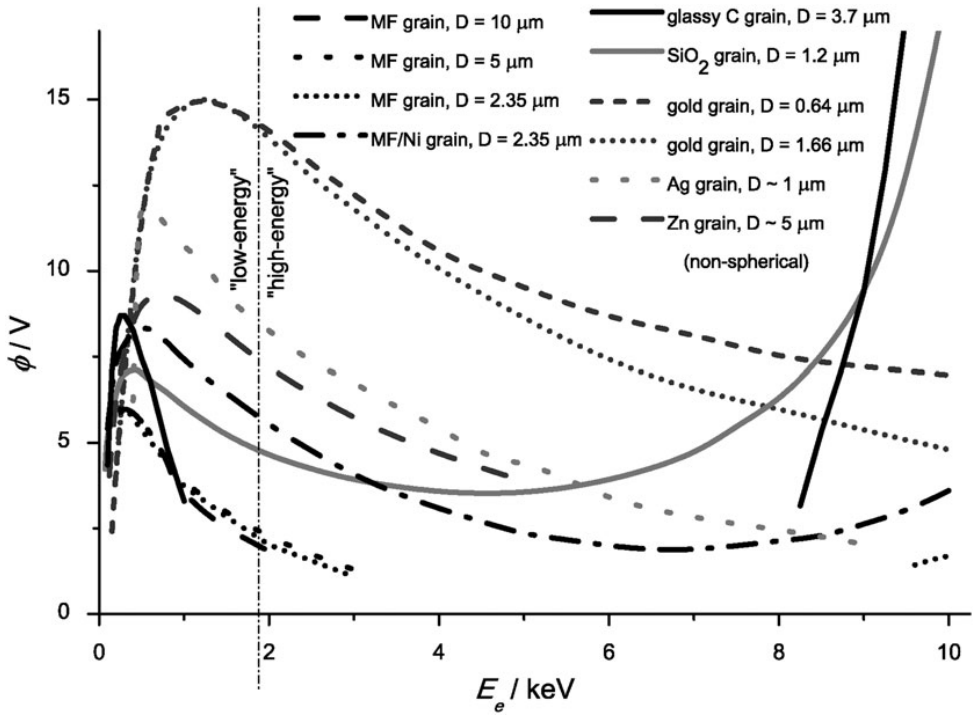

Fig. 4 Surface potential profiles as a function of the primary electron beam energy—comparison of various materials.

The quantitative interpretation of the low-energy part of the potential profiles is more difficult. One would expect that a larger SEE yield would result in a larger surface potential, but this is true only partially, as can be seen from Fig. 5. The surface potential at the SEE maximum, ϕ_{max} increases with σ_{max} (values from Bronstein[13] are used) for all depicted materials except SiO_2. SiO_2 has the largest SEE yield, but a rather small maximum potential ϕ_{max}. Taking into account that the equilibrium potential is reached when the current of primary electrons is balanced with the current of all true secondary and backscattered electrons with energy sufficient to overcome the grain potential, we can conclude that the principal difference between SiO_2 and other analyzed grains is in the energy spectrum of the

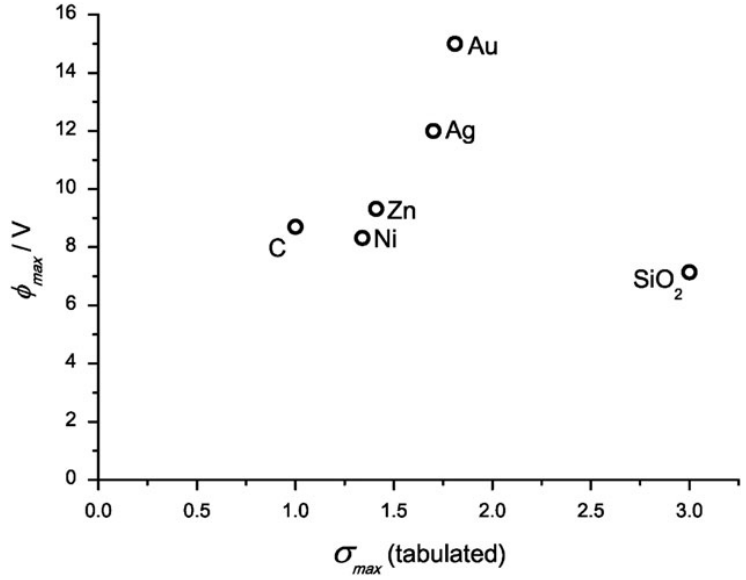

Fig. 5 Surface potential at the maximum of SEE as a function of the tabulated maximum total yield of SEE, σ.

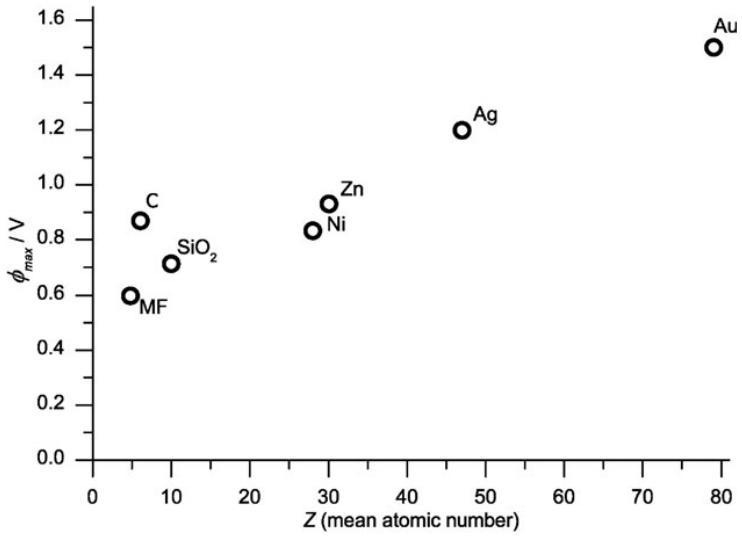

Fig. 6 Surface potential at the maximum of SEE as a function of atomic number, Z.

SEs. However, the reason for this difference is not clear. All materials in the first group are conductive elements, whereas SiO_2 is an insulator and a chemical compound. This problem can be elucidated with the data in Fig. 6, where the surface potentials are plotted as a function of the atomic number, A (the mean atomic number was used for compounds). This plot allows us to implement the measurements on MF that were not used in Fig. 5 because the SEE yield of MF is unknown. One can note that the atomic number sorts the data rather well. Since the atomic number influences predominantly the scattering of the electrons inside the grain, we can tentatively conclude that this scattering plays an important role in the formation of the energy spectrum of SEs. However, confirmation of this hypothesis requires precise measurements of the energy spectra of SEs in the eV range. This task, for single isolated microparticles, is a rather difficult experiment.

4. Field electron emission

Field emission of electrons from negatively charged dust grains occurs at high electric field strengths. This process was described in the 1950s for metals.[27] An explanation of this phenomenon is based on the inflection of the electron bands in the material, which enlarges the probability of electron tunneling from the surface to the vacuum level.

The field emission current is described by the Fowler–Nordheim equation:[27,28]

$$i \sim \frac{F^2}{\varphi t^2(F,\varphi)} \exp\left(\frac{\varphi^{\frac{3}{2}}}{F} v(F,\varphi)\right), \tag{3}$$

where F stands for the electric field strength, φ for the work function, and the variables t and v are weak functions of F and φ. If we plot the dependence of $\log i/F^2$ *vs.* $1/F$, the work function can be easily derived from the slope of this nearly linear plot:

$$\text{slope} = -2.96 \times 10^7 \varphi^{\frac{3}{2}} s(F,\varphi), \tag{4}$$

where the function s weakly depends on F and φ and varies in most cases within the range of 0.83–1, *i.e.*, its change is usually smaller than the scatter of the experimental points. All three functions s, t, and v are described by Good and Müller,[27] their values are tabulated.

Since measuring the work function of insulators is difficult, the Fowler–Nordheim plot could be used for this task. Eqn (3) was derived for metals but one can expect

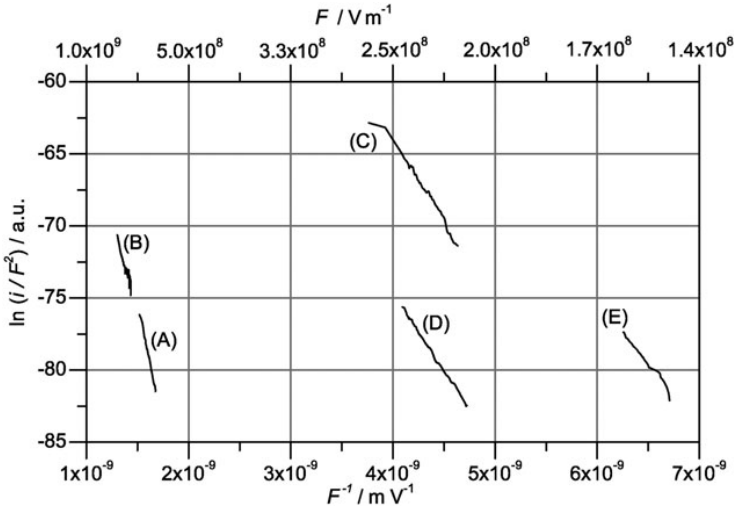

Fig. 7 Fowler–Nordheim plot of grain discharging due to a field electron emission for various materials. (A) Gold grain, $\varphi \approx 5.2$ eV, (B) MF grain (of a diameter of 4.97 μm), $\varphi \approx 4.6$ eV, (C) amorphous carbon grain, $\varphi \approx 2.5$ eV, (D) MF grain covered by a thin layer on nickel, $\varphi \approx 2.5$ eV, (E) SiO_2 grain, $\varphi \approx 2$ eV.

that a highly charged dust grain from any material has enough free electrons, thus, this method can be applied.

In order to observe the field emission current, the grain has to be charged to a sufficiently negative potential. As can be seen in Fig. 5, SEE tends to charge the grains positively. Negative surface potentials can be reached if the SEE yield is lower than unity. This is true at very low primary energies when electron attachment dominates (up to several tens of eV for insulators) and in the keV range for grains with a specific combination of the grain material and size (see below). Examples of such grains are carbon and MF particles in Fig. 5. We would like to point out that the application of high beam energies is further complicated by the enhancement of the SEE yield due to the large electric field at the grain surface.[29]

We have recorded field emission currents from several grains of different materials. The corresponding Fowler–Nordheim plots are shown in Fig. 7. These plots reveal several surprising facts: (1) The field emission current is able to fully compensate the primary beam current at field strengths as low as 1.5×10^8 V m^{-1} (the scale at the top edge of the figure), (2) the work functions that are given as parameters beside the curves vary in a broad range. Values for gold ($\varphi = 5.2$ eV) and MF ($\varphi = 4.6$ eV) roughly correspond to the expectations but those for MF/Ni, carbon, and SiO_2 are too low. However, values obtained on MF grains are questionable for several reasons described further below.

This effect was found by Pavlů *et al.*[30] for SiO_2 and attributed to the emission of electrons from surface states of SiO_2. However, such an explanation can be hardly applied to MF/Ni grains because the electrons are emitted from a metallic surface of the grain. If one would assume that the Ni layer on the grain surface is oxidized and insulating, the presence of surface states can be expected. The last sample exhibiting a small work function is amorphous carbon. Since the internal structure of carbon can vary from insulating diamond to conducting graphite and the exact structure of the samples is unknown, we can probably safely assume that the emission occurs from surface states with a low work function. Moreover, carbon is a highly reactive species that tends to saturate the dangling bonds at the material surface. In most cases, the bonds are saturated by hydrogen, however, other, more complicated chemical compounds can be chemisorbed, which can act as a source of the tentative surface states.

In contrast to the low work functions measured for the aforementioned samples, Fig. 7 shows measurements on an MF grain that exhibit a work function equal to 4.6 eV. This is in good agreement with the work functions of insulators found by

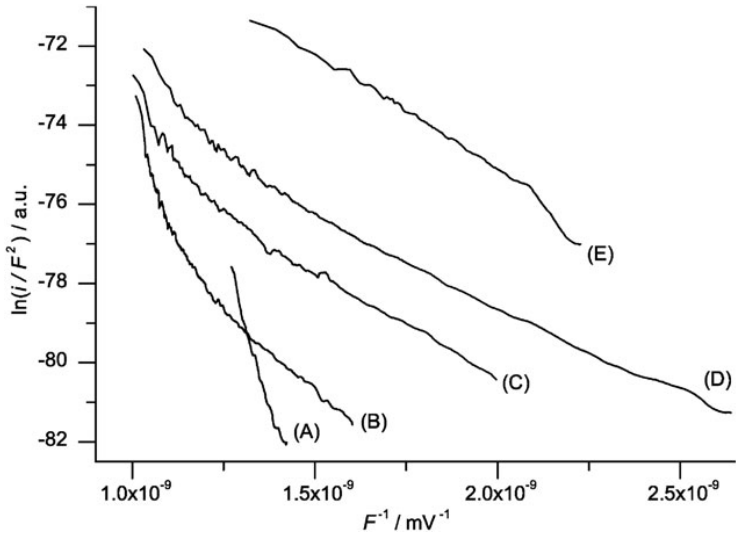

Fig. 8 Fowler–Nordheim plots of one MF grain. Characteristics were measured consecutively in the order from (A) to (E) using a 5 keV electron beam. Estimated work functions thus vary over 1.4–7.5 eV.

Sternovsky *et al.*[31] using triboelectric charging. The measurements on MF and SiO_2 were compared in Pavlů *et al.*[29] The authors suggest that the way of charging (*i.e.*, use either low- or high-energy electrons) is the reason for the substantial differences in the work functions of these materials.

As noted above, a negative grain charge can be achieved by applying either low- or high-energy electron beams. Whereas the eV electrons cannot modify the grain structure and can be captured in the surface states, the high-energy electrons penetrate deeper and their energy can destroy the electronic structure of the original insulating material with a clear band gap. In the experiments of Pavlů *et al.*,[29] SiO_2 samples were charged by a low-energy beam, whereas a 5 keV beam was used for MF grains. However, our new measurements on carbon samples charged by the 5 keV beam seem to contradict the above hypothesis. For this reason, we have repeated the measurements on MF grains and the results are plotted in Fig. 8. Different curves in this figure were measured on the same sample and they differ in the duration of bombarding (charging) the grain with 5 keV electrons. One can note a gradual evolution of the sample structure leading to a decrease of the work function from $\phi = 7.5$ eV to $\phi = 1.4$ eV. This suggests that the electron bombardment strongly affects the internal structure and that long-lived surface states are populated by the exposure to energetic electrons. Moreover, the measurements in a broader range of discharging currents clearly show that the Fowler–Nordheim theory cannot be applied to the MF samples, since the plots are strongly non-linear. This is probably caused by several effects: first, the surface states are discrete, thus, the description by the Fowler–Nordheim theory based on a band structure cannot be correct, and second, the finite lifetime of the surface states leads to their depopulation, thus, to a redistribution of the density of states.

Since such materials are relevant for investigations of interplanetary space, an explanation of the observed effects is desirable. Moreover, MF spheres are frequently used as calibration objects for their well defined diameters in electron microscopy and other experimental techniques. However, some of our measurements suggest a significant change in their dimensions during electron bombardment might be occurring.[32]

5. Field ion emission

Current understanding of field emission of ions from dust grains is based on experiments and theoretical considerations connected to field ion microscopy

(see, *e.g.*, review of Forbes[33] and references therein). The studies are based on the assumption of a sharp conductive tip biased by an external voltage source. The mechanism of field ion emission from an isolated particle, however, may be different since the strong electric field at the surface is a consequence of charge accumulated in the grain due to ion bombardment.

The emission of positive ions may be caused by three main processes: field desorption, field evaporation, and field ionization.[27,34] All these processes are based on tunneling of electrons from atoms situated above the sample surface into or toward the sample. The tunneling probability has a sharp maximum at a critical distance that is a function of the electric field strength. Consequently, the tunneling can occur only in a very thin layer above the dust grain. The three processes differ in the source of the atoms entering this layer. Atoms and molecules of the surrounding gas represent the source for the field ionization, whereas an ''internal'' source—atoms of the adsorbed gas or atoms of the grain material—acts in the field desorption and in the field evaporation, respectively. Since the adsorbed atoms are weakly bound in comparison with the bulk atoms, the field desorption should be the dominant process that releases the charge from positively charged dust grains in space or under experimental UHV conditions.

Field desorption proceeds in two phases. Adsorbed gas atoms leave the surface and are ionized at (or slightly beyond) a critical distance and are then pushed away by the repulsive electric force. The positive charge from the adsorbed atom leaves in the form of the ion; the released electron is attracted by the grain, and thus does not change the net charge. Pavlů *et al.*[35] and Jeřáb *et al.*[36] performed laboratory experiments where impacts of energetic ions led to a deposition of a positive charge onto a spherical grain. In these experiments, the accumulated charge is spontaneously released and the discharge is measurable when a certain value of the electric field at the grain surface is reached. This value was experimentally found to be on the order of 10^9 V m^{-1}, which is rather low, however, the field strength was determined under the assumption of spherical samples, thus, a local deformation of the sample surface could enhance the field by a factor of 3–5. By analyzing the plots of the discharge currents *vs.* the electric field strength, they found the field desorption to be the main discharging process. The authors suggested that the beam ions recombine at the grain surface and create a layer of atoms that then desorb during the discharging process.

In order to check this suggestion, we have carried out a series of measurements on one gold grain. The results are plotted in Fig. 9. In this experiment, the grain was exposed to a 5 keV ion beam for a time that is called ''time of treatment'' in the figure. After the beam was switched off, the discharge current was recorded together with the grain surface potential for several hours. The value of the discharge current at 1 kV surface potential is plotted on the ordinate. Although the spread of the experimental points is rather large, the plot shows a clear increase of the discharge current with the time of treatment. We would like to note that the uncertainty of the discharge current is principally due to the charge quantization—the measured current is rather small (number of elementary charges per second is used as the current unit in the figure) and the measurement time is limited by the rapid discharging at the origin.

The increase of the discharge current with the time of treatment is surprising because one would expect that grain charging is stopped at the point when the number of incoming and outgoing atoms are in equilibrium. Our experiments suggest that there is a mechanism that stores and gradually releases a portion of incoming ions.

Our tentative explanation is based on the implantation of beam ions into the grain material. However, this hypothesis must be checked further. Since the diffusion of the implanted ions toward the surface is probably a very slow process, it opens the question whether it can considerably contribute to the discharge current.

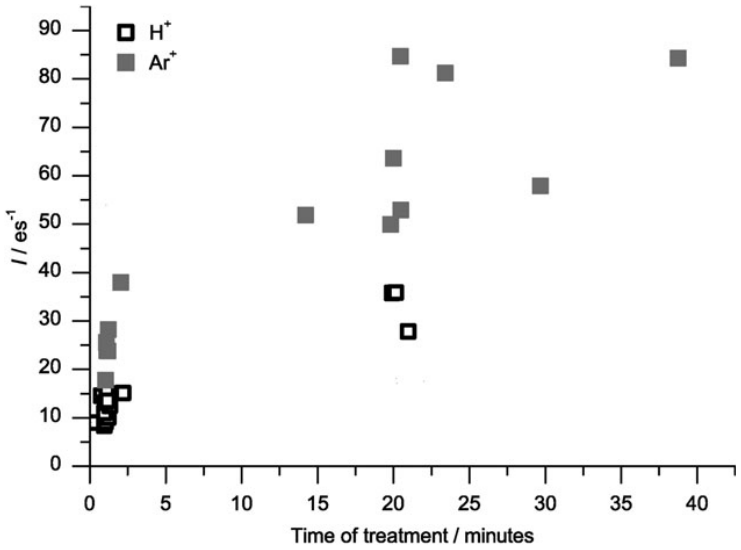

Fig. 9 Field ion emission currents from one gold grain after different treatment times, and for two ion species. Currents were measured at 1 kV of the grain surface potential. The full squares denote the Ar^+ bombardment, while the open circles show bombardment by H^+.

The implantation of solar wind ions and their subsequent release in the form of neutral atoms was suggested as a possible source of the so-called pick-up ions in the solar system (*e.g.*, Mann *et al.*[37]). Thus, the laboratory investigation of the rates of these processes is of great interest and will be followed up on in our future experiments.

6. Dust grain sputtering

Investigations of the sputtering rate require continuous monitoring of the grain mass evolution. By a precise measurement of the grain's oscillation frequency, we can determine the change in the specific charge Q/m induced by one elementary charge and, consequently, we can obtain the total charge and mass of the grain. Although the precision of the mass determination is better than 10^{-6}, the noise in the secular frequency restricts this measurement to weakly charged grains only, typically not larger than 10^5 elementary charges.

An alternative method is the determination of the grain's specific capacitance C/m that acts as a scaling constant between the specific charge and the surface potential:

$$\frac{Q}{m} = \frac{C}{m}\phi. \tag{5}$$

The specific capacitance C/m can be determined from the specific charge at a known surface potential, ϕ.[9] Assuming a spherical grain, $C = 4\pi\varepsilon_0 R$, the specific capacitance depends on the grain radius R and the mass density of its material only. From the known mass density, the grain radius, and consequently its mass, can be obtained.

In the experiment on grain sputtering, a spherical gold grain of an initial radius $R_0 = 0.57$ μm and a corresponding initial mass $m_0 = 1.48 \times 10^{-14}$ kg was used. The sputtering was initiated by an Ar^+ beam with an energy $E_0 = 5$ keV and a current density $i_p = 4 \times 10^{-4}$ Am^{-2}.

The primary experimental task is the investigation of the grain sputtering, but the beam ions charge the grain and the grain charge influences the energy and the flux of the beam ions impinging the grain. Without any other processes, the grain will charge up to the surface potential numerically equal to the energy of the beam ions (their effective energy, respectively) and the ion flux will drop to zero. However, as we have shown in the previous section, the grain charge is limited by the field ion

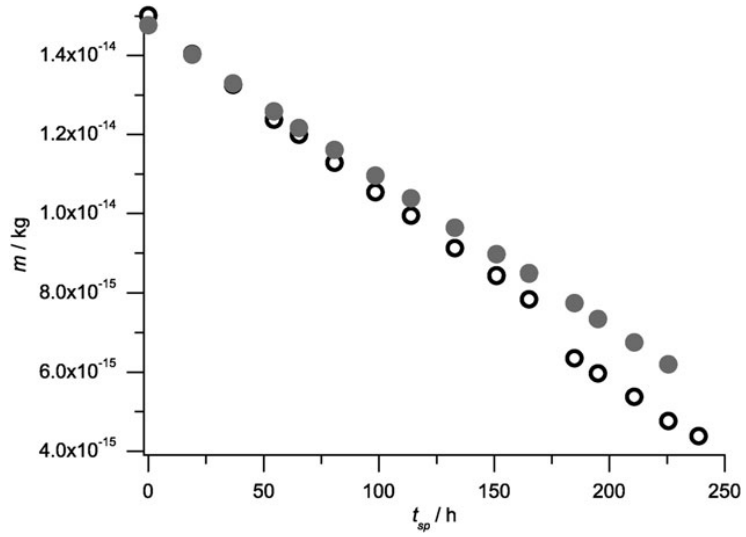

Fig. 10 Reduction of the grain mass in the course of ion bombardment. The full circles show the mass estimated by the elementary charge method; open circles stand for the mass estimated from the grain capacitance.

emission. Since the emission current increases rapidly with the electric field strength at the grain surface,[36] the grain's surface potential can be considered as constant for our experiment. We have obtained the value of the corresponding electric field: $F = 1.95 \times 10^9$ V m^{-1}. The constant surface field strength implies changes of the surface potential during the grain sputtering due to the changes of the grain diameter. Indeed, this potential was $\phi \approx 1.05$ kV at the beginning of the experiment and $\phi \approx 0.75$ kV at the end. The energy of the beam ions with respect to the grain surface thus changed from 3.95 to 4.25 keV. According to Behrisch,[38] the sputtering yield, Y, is roughly constant in this energy range with the following value: $Y \approx 5$. This value was determined for Ar^+ ions impacting perpendicular to a planar surface. The yield increases with decreasing incidence angle,[38] and we have estimated[39] that a factor of 1.2–2 should be considered for sputtering of spherical samples.

The temporal evolution of the mass of the treated Au grain with an initial radius of 0.568 μm is shown in Fig. 10. For direct mass measurements, we applied the two techniques mentioned above—the method of elementary charge steps and the calculation of the specific capacitance. Both methods lead to a sputtering yield of $Y \approx 20$, *i.e.*, four times larger than that for a planar uncharged surface. We suggest that this enhancement can be divided into two multiplicative parts. One part is attributed to the shape of the sample, the other part is probably caused by the presence of a strong electric field at the grain surface. This field is achieved by ion bombardment in the specific conditions of our experiment, however, very small grains in space ($\approx$20 nm), when sufficiently charged by photoemission, can reach similar field strengths. Moreover, we used a gold grain to be able to make comparison with known data, but the dust materials in space are insulators and the yield enhancement can be much larger due to the penetration of the electric field into the grain. These processes will be the subject of our further studies.

As can be seen in Fig. 10, the two methods of grain mass determination provide results that systematically differ. Since the method of the elementary charge steps does not require any additional assumption, we assume that it provides reliable mass estimates. The determination of the grain capacitance, however, is based on the known grain shape. Comparing the results of the two methods, the changes in the grain shape can be followed. The increasing difference between the measurements lets us conclude that the originally spherical grain shape is changed during the sputtering. The resulting shape is unknown, but the difference can be explained if an increase of the grain capacitance by a factor of 1.2 is assumed.[39] Such an increase corresponds to a change of the grain shape from a sphere to a rotational ellipsoid

Table 1 Rough approximation of sputtering times computed for micron-sized gold grain in different space locations for laboratory and space conditions (Earth orbit)

Conditions	Ion	1/2 mass	1/2 radius
Laboratory	Ar^+	190 hr	450 hr
Space (1 AU)	H^+	8×10^2 yr	2×10^3 yr
	He^{2+}	2×10^3 yr	5×10^3 yr
	Heavy ions	8×10^2 yr	2×10^3 yr

with an axis ratio of $\approx 1 : 2$. This result is surprising because one would expect that the sputtering, together with random rotation of the grains (in our experiment as well as in space), would result in well spherical grains. We suggest that the space charge of the ion beam interacts with the quadrupole term of the electric field of the grain, which can be described as a charged conductive rotational ellipsoid. Since the minimum potential energy of such a charged ellipsoid is reached if its axis is identical with the beam direction, the interaction leads to cancellation of any rotational motion and to orientation of the ellipsoid along the ion beam. As the surfaces parallel to the beam undergo a more rapid erosion, the sputtering causes a positive feedback. This leads to enlarging the axis ratio of the grain, thus to increasing the quadrupole term and, consequently, to a stronger orientation of the grains with respect to the ion beam.

In order to check the possible relevance of the measurements to interplanetary space, we have calculated[40] the sputtering times (Table 1) of a gold grain in typical solar wind conditions. At 1 AU, we assume that the solar wind has a velocity of 400 km s^{-1} and a number density of 10 cm^{-3}. In our estimates, we consider all solar wind ions as singly ionized atoms with an energy of 5 keV. However, Insepov *et al.*[41] show that the sputtering yield of multiply ionized ions can be much larger (by an order of magnitude). Indeed, all species (except protons) in the solar wind are in high ionization states. A typical mass composition of the solar wind was considered, however, the abundance of heavy ions can be significantly enhanced during coronal mass ejections, and these species are very effective for dust sputtering.

We would like to point out that the values in Table 1 are based on the tabulated values of the sputtering yield for gold corrected to the assumed spherical grain shape. The real times of the dust grain sputtering can therefore easily vary within an order of magnitude. Taking into account the observed orientation of conductive grains with respect to the direction of the bombarding ions and the consequently enhanced sputtering yield, we expect that our estimates represent the upper limit of the expected sputtering times.

Since the sputtering rate decreases with the square distance from the Sun, the lifetime of dust particles is expected to be rather short in the inner solar system and the sputtering can be, beside the ion field emission, the next important source of the pick-up ions.

7. Concluding remarks

The paper analyzes new results of dust grain charging under laboratory conditions and discusses the contribution of these simulations to processes in interplanetary space. A single spherical grain, trapped in ultra-high vacuum conditions for long time intervals, is exposed to ion and/or electron beams, and their mutual interactions are investigated. Several charging processes—secondary emission, field ion and electron emissions, and dust sputtering—are described in detail. For these simulations, micrometer-sized grains of various materials and different energies and fluxes of ion and electron beams were used. As a result, we can conclude:

1. The charge and corresponding potential of dust grains affected by the electron beam are determined by secondary emission. We have shown that the energy spectrum of secondary electrons plays an important role in this process and that scattering of electrons inside the grain influences the resulting spectrum of secondary electrons. However, confirmation of this hypothesis requires precise measurements of the SE electron spectra in the eV range.

2. Our study of field electron emission brings a few surprising facts to light—the field emission current is able to fully compensate the primary beam current at field strengths as low as 1.5×10^8 V m^{-1}, and the work functions of some materials (MF/Ni, amorphous C, and SiO_2) are too low. A tentative explanation based on the emission from surface states needs further detailed investigations.

3. We assume that the field desorption is the dominant process that releases the charge from positively charged dust grains in our simulations, thus, we have prepared long-term experiments where impacts of energetic ions led to a deposition of a positive charge onto a grain. An increase of the discharge current with the time of the grain exposure to a 5 keV ion beam was noted. Our tentative explanation of this observation is based on the implantation of beam ions into the grain material. However, this hypothesis should be further checked and the experimental results should be compared with a theoretical simulation.

4. Dust grain sputtering is an important process in space. Our simulations use Au spheres. We found that the sputtering yield can be significantly enhanced by the presence of a high electric field at the grain surface. Moreover, the shape of grains exposed to a collimated ion beam evolves from sphere to ellipsoid, and this change further enhances the sputtering yield. The consideration based on the mean abundance of heavy ions in the solar wind leads to a conclusion that these minor species can considerably contribute to the sputtering rate. However, a typical interplanetary dust is composed of insulators. The sputtering of such materials should be the subject of further studies, because the field-induced sputtering enhancement can be significantly larger due to penetration of the electric field into the grain.

Acknowledgements

The present work was financially supported by research plan MSM 0021620860, which is financed by the Ministry of Education of the Czech Republic.

References

1 J. E. Colwell, M. Horányi and E. Grün, in *Physics of Dusty Plasmas, Seventh Workshop of AIP Conference Proceedings*, ed. M. Horanyi, S. Robertson and B. Walch, American Institute of Physics, Melville, New York, 1998, vol. 446, pp. 299–306.
2 S. P. Wyatt, *Planet. Space Sci.*, 1969, **17**(2), 155–171.
3 P. L. Lamy, J. Lefevre, J. Millet and J. P. Lafon, in *IAU Colloq. 85. Properties and Interactions of Interplanetary Dust of ASSL*, ed. R. H. Giese and P. Lamy, 1985, vol. 119, pp. 335–339.
4 R. Srama, T. Ahrens, N. Altobelli, S. Auer, J. Bradley, M. Burton, V. Dikarev, T. Economou, H. Fechtig, M. Görlich, M. Grande, A. Graps, E. Grün, O. Havnes, S. Helfert, M. Horanyi, E. Igenbergs, E. Jessberger, T. Johnson, S. Kempf, A. Krivov, H. Krüger, A. Mocker-Ahlreep, G. Moragas-Klostermeyer, P. Lamy, M. Landgraf, D. Linkert, G. Linkert, F. Lura, J. McDonnell, D. Möhlmann, G. Morfill, M. Müller, M. Roy, G. Schäfer, G. Schlotzhauer, G. Schwehm, F. Spahn, M. Stübig, J. Švestka, V. Tschernjawski, A. Tuzzolino, R. Wäsch and H. Zook, *Space Sci. Rev.*, 2004, **114**, 465–518.
5 I. Richterová, J. Pavlů, Z. Němeček, J. Šafránková and P. Žilavý, *Adv. Space Res.*, 2006, **38**(11), 2551–2557.
6 I. Čermák *Laboruntersuchung elektrischer Aufladung kleiner Staubteilchen*, PhD thesis, Naturwissenschaftlich-Mathematischen Gesamtfakultät, Ruprecht-Karls-Universität, Heidelberg, 1994.
7 P. Žilavý, Z. Sternovský, I. Čermák, Z. Němeček and J. Šafránková, *Vacuum*, 1998, **50**(1–2), 139–142.

8 I. Čermák, J. Pavlů, P. Žilavý, Z. Němeček, J. Šafránková and I. Richterová, in *WDS'04 Proceedings of Contributed Papers Part II—Physics of Plasmas and Ionized Media*, ed. J. Šafránková, Matfyzpress, Prague, 2004, pp. 279–286.
9 J. Pavlů, A. Velyhan, I. Richterová, Z. Němeček, J. Šafránková, I. Čermák and P. Žilavý, *IEEE Trans. Plasma Sci.*, 2004, **32**(2), 704–708.
10 W. Paul and H. Steinwedel, *Apparatus for separating charged particles of different specific charges*, German Patent 944 900, Jun. 28, 1956. U.S. Patent 2 939 952, Jun. 7, 1960.
11 E. Sternglass, *Theory of secondary electron emission under electron bombardment*, Scientific Paper 6-94410-2-P9, Westinghouse Research Laboratories, Pittsburgh 35, 1957..
12 B. T. Draine and E. E. Salpeter, *Astrophys. J.*, 1979, **231**, 77–94.
13 I. M. Bronstein and B. S. Fraiman, *Secondary Electron Emission*, Nauka, Moskva, 1969.
14 I. Richterová, J. Pavlů, Z. Němeček and J. Šafránková, *Phys. Rev. B*, 2006, **74**(23), 235430.
15 D. C. Joy, *J. Microsc.*, 1987, **147**(1), 51–64.
16 R. Shimizu and Z.-J. Ding, *Rep. Prog. Phys.*, 1992, **55**(4), 487–531.
17 A. Dubus, J.-C. Dehaes, J.-P. Ganachaud, A. Hafni and M. Cailler, *Phys. Rev. B*, 1993, **47**, 11056–11073.
18 R. Renoud, F. Mady, C. Attard, J. Bigarré and J.-P. Ganachaud, *Phys. Status Solidi A*, 2004, **201**, 2119–2133.
19 J. Cazaux, *Nucl. Instrum. Methods Phys. Res., Sect. B*, 2006, **244**, 307–322.
20 P. Ziemann, P. Liu, D. Kittelson and P. McMurry, *J. Phys. Chem.*, 1995, **99**, 5126–5138.
21 V. Chow, D. Mendis and M. Rosenberg, *J. Geophys. Res., [Atmos.]*, 1993, **98**(17), 19065–19076.
22 J. Švestka, I. Čermák and E. Grün, *Adv. Space Res.*, 1993, **13**(10), 199–202.
23 V. Chow, D. Mendis and M. Rosenberg, *IEEE Trans. Plasma Sci.*, 1994, **22**(2), 179–186.
24 I. Richterová, Z. Němeček, J. Šafránková and J. Pavlů, *IEEE Trans. Plasma Sci.*, 2004, **32**(2), 617–622.
25 I. Richterová, J. Pavlů, Z. Němeček and J. Šafránková, *Adv. Space Res.*, 2007, submitted.
26 I. Richterová, Z. Němeček, J. Šafránková, J. Pavlů and M. Beránek, *IEEE Trans. Plasma Sci.*, 2007, **35**(2).
27 R. H. Good and E. W. Müller, in *Electron-Emission Gas Discharges I of Encyclopedia of Physics*, Springer-Verlag, 1988, vol. XXI ch. 2, pp. 176–231.
28 R. Fowler and L. Nordheim, *Proc. R. Soc. London, Ser. A*, 1928, **119**(781), 173–181.
29 J. Pavlů, Z. Němeček, J. Šafránková and I. Čermák, *IEEE Trans. Plasma Sci.*, 2004, **32**(2), 607–612.
30 J. Pavlů, Z. Němeček, J. Šafránková and I. Čermák, *Czech. J. Phys.*, 2003, **53**(2), 151–162.
31 Z. Sternovsky, S. Robertson, A. Sickafoose, J. Colwell and M. Horanyi, *J. Geophys. Res., [Atmos.]*, 2002, **107**(E11), 5105.
32 I. Richterová, J. Pavlů, Z. Němeček, J. Šafránková and M. Jeřáb, in *New Vistas in Physics of Dusty Plasmas of AIP Conference Proceedings*, ed. L. Boufendi, M. Mikikian and P. K. Shukla, American Institute of Physics, Melville, New York, 2005, vol. 799, pp. 395–398.
33 R. G. Forbes, *Ultramicroscopy*, 2003, **95**, 1–18.
34 R. Gomer, in *Field Emission and Field Ionization*, Harvard University Press, Cambridge, Massachusetts, Harvard monographs in applied science, 1961, vol. 9.
35 J. Pavlů, A. Velyhan, I. Richterová, J. Šafránková, Z. Němeček, J. Wild and M. Jeřáb, *Vacuum*, 2006, **80**(6), 542–547.
36 M. Jeřáb, I. Richterová, J. Pavlů, J. Šafránková and Z. Němeček, *IEEE Trans. Plasma Sci.*, 2007, **35**(2).
37 I. Mann, H. Kimura, D. A. Biesecker, B. T. Tsurutani, E. Grün, R. B. McKibben, J.-C. Liou, R. M. MacQueen, T. Mukai, M. Guhathakurta and P. Lamy, *Space Sci. Rev.*, 2004, **110**, 269–305.
38 R. Behrisch, *Sputtering by Particle Bombardment I, II*, Springer-Verlag, Berlin-Heidelberg-New York, 1981.
39 J. Pavlů and J. Wild, in *WDS'00 Proceedings of Contributed Papers: Part II—Physics of Plasmas and Ionized Media*, ed. J. Šafránková, Matfyzpress, Prague, 2000, pp. 238–242.
40 J. Pavlů, I. Richterová, Z. Němeček, J. Šafránková and J. Wild, *IEEE Trans. Plasma Sci.*, 2007, **35**(2).
41 Z. Insepov, J. P. Allain, A. Hassanein and M. Terasawa, *Nucl. Instrum. Methods Phys. Res., Sect. B*, 2006, **242**, 498–502.

F. Richterová et al. [2006]

Richterová, I., Pavlů, J., Němeček, Z., Šafránková, J., Model of secondary emission and its application on the charging of gold dust grains. *Phys. Rev. B* 74 (23): 235430, 2006.

Model of secondary emission and its application on the charging of gold dust grains

I. Richterová,* J. Pavlů,† Z. Němeček,‡ and J. Šafránková§
Charles University, Faculty of Mathematics and Physics, V Holešovičkách 2, 18000 Prague, Czech Republic
(Received 21 August 2006; published 19 December 2006)

We present a combined experimental and simulation study of the charging of the spherical gold samples by an electron beam in a 0.15–10 keV range of beam energies. Experiments on grains with diameters of the order of 10^{-6} m show that the charge (or surface potential) of grains levitating in a guadrupole trap is a function of both grain diameter and beam energy. Monte Carlo simulations reveal that an increase of the grain potential with the beam energy for a fixed diameter or a surface potential decrease with the grain diameter for a given beam energy are connected with changes of the relative number of backscattered primary electrons. The results of simulations are in a good quantitative agreement with previously published as well as our fresh experimental data.

DOI: 10.1103/PhysRevB.74.235430 PACS number(s): 79.20.Hx, 94.05.Bf, 52.27.Lw

I. INTRODUCTION

Comets, planetary rings, exposed dusty surfaces, and the zodiacal dust cloud are all examples of environments where dusty plasma effects establish the size and spatial distributions of small grains. Simultaneously, dust often influences the composition, density, and temperature of the surrounding plasma. The dynamics of charged dust grains can be surprisingly complex and fundamentally different from the well-understood limits of gravitationally dominated motions of neutral particles or the adiabatic motion of electrons and ions in electromagnetic fields that dominate gravity.

While the study of dust–plasma interactions is not new, early progress in the field was slow and uneven. However, it received a major boost in the 1980s with the Voyager spacecraft observations of peculiar features in the Saturnian ring system ("radial spokes") which could not be explained by gravitation alone and led to the development of the gravito-electrodynamic theory of dust dynamics. This theory scored another major success more recently in providing the only possible explanation of collimated high-speed beams of fine dust grains from Jupiter observed by the Ulysses and Galileo spacecraft.[1] At present, several space missions (e.g., Cassini, Rosetta, Helios) provide (or will provide) direct observations of dust grains in the interplanetary space and in the Jovian and Saturnian systems to investigate their physical, chemical, and dynamical properties.[2–6]

Immersed in a plasma, the grain is charged due to its interaction with radiative and plasma environment. The grain charging depends on the physical and electrical properties of the grains, on the nature of their interaction with the surrounding radiation and plasma fields, and on the relative velocity. The most important contributions come from a flux of electrons and ions, from the UV-radiation induced photoemission, and from secondary emission of electrons. The surface potential of a dust grain is established by a balance between various charging currents and resulting potentials can range from about −10 kV in planetary magnetospheres[7] to some 10 V in an interplanetary space[8] depending on size, shape, material, and charging history of grains.

The calculation of the acquired net charge is generally a difficult task mainly due to the complicated processes involved and because the knowledge of the adequate dusts properties (such as photoemission efficiency, secondary electron emission yield, etc.) is required. These properties are usually deduced from experimental measurements made on bulk materials or planar surfaces. However, the highly curved surface of small dust grains may considerably change the corresponding physical properties, thus these properties may be a function of the grain size and its shape.

The theory and models are well developed for environments that vary from dense planetary atmospheres to diffuse environments such as interplanetary space. However, experimental investigations of individual dust grains in equilibrium are less common, perhaps due to the difficulty of these experiments. Laboratory simulations were started at the beginning of the 1990s. For example, Suszcynsky *et al.*[9] measured secondary electron yields from ammonia and methanol ices as a function of the electron beam energy in the 2- to 30-keV energy range and summarized that secondary electron yields are on the low end of the range for insulators ($\approx$1–25). Spann *et al.*[10] dealt with secondary electron emission of dust grains levitating in the Paul trap in a very narrow range of attainable charges. Švestka *et al.*[11] measured the secondary electron emission profile of dust grains using an electron beam up to 20 keV. They achieved a positive charge even at high electron energies and they attributed this effect to an emission from the opposite side of the grain. Similar experiments were prepared on submicron oil and micron nonspherical metal grains by Ziemann *et al.*[12] and Velyhan *et al.*,[13] respectively. However, they used lower beam energies and thus they did not observe the surface potential growth at high beam energies.

II. SECONDARY ELECTRON EMISSION

Primary electrons (PEs) impacting the sample surface interact with a bulk material and they lose their energy in many types of collisions and it often results in excitations of material electrons. Some of the excited electrons can then leave the surface. These electrons, so-called true secondary electrons (SEs), have typically energies of a few electronvolts. For large planar samples, the energetic dependence of the secondary emission yield, δ (defined as the mean number of

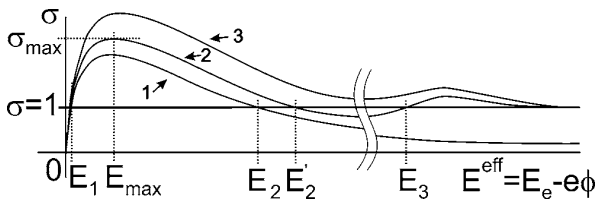

FIG. 1. Schematics of the total secondary emission yield as a function of the beam energy: (1) planar surface, (2) dust grain from the same material, and (3) dust grain from a material with a larger secondary emission yield.

SEs per one PE) can be described by the Sternglass universal curve.[14] This curve exhibits a maximum at a few tenths of kiloelectronvolts and decreases to zero at very high and low beam energies. Its parameters, the maximum yield δ_{max} and the corresponding energy E_{max} depend only on a sample material at a certain incident angle.

In collisions inside the target, PEs change their directions and thus they may be backscattered from the material before losing the whole energy. The backscattered yield η increases with the material density and the atomic number up to ≈ 0.5 for a normal incident angle. It grows only slowly with the beam energy above a few hundreds of electronvolts. Thus, the total secondary yield $\sigma = \delta + \eta$ and δ vary in a similar way with the beam energy.[15]

The energy dependence of a total secondary yield of dust grains does not fully follow the universal curve for large samples. It is enhanced due to a surface curvature that results in a variation of the incident angle along the grain surface because σ (and both constituents, δ as well as η) increases with an incident angle.[15] The secondary emission yield is enhanced by a factor of ≈ 1.3 for spherical grains. This enhancement does not change the profile of σ as a function of the primary energy in low- and mid-energy ranges. An energy dependence of σ and its variation with a sample shape is sketched in Fig. 1. The figure shows σ as a function of the primary energy for a planar surface (1) and for two dust grains (2) and (3). In a very low energy range, below an energy E_1, σ rises with the primary energy. Since $\sigma < 1$, all samples are charged negatively. This is a typical regime of the electron attachment. The rise of σ is terminated at E_{max}.

At higher energies ($E > E_{max}$), the PEs deposit their energy farther from the surface and σ decreases until it approaches unity (at E_2) for large samples. The sample is charged positively between E_1 and E_2, whereas a negative charge can be expected above E_2. On the other hand, depending on the grain size and material, the secondary emission yield can behave as it is shown by curves 2 or 3. The energy corresponding to $\sigma = 1$ can be shifted to higher energies (E_2') or even to infinity (curve 3) because the penetration depth of PEs increases with their energy and SEs leave the grain with a higher probability when the penetration depth of PEs becomes comparable with the grain size. This effect increases the value of σ and the decreasing trend of the profile reverses.

We would like to note that the rise of the total secondary emission yield at higher energies for small samples (curves 2 and 3) can be in principle caused by two factors: (1) by increase of the number of SEs due to emission from the "backside," this effect is well known as second-surface secondary electron emission from thin films, and/or (2) by increasing number of backscattered PEs. One of the aims of the present paper is to show that the second process is dominant for spherical samples.

At very high energies, the majority of PEs penetrate the grain without any energy loss and, thus, σ asymptotically approaches unity ($\delta \to 0$; $\eta \to 1$). Note that the grain behaving according to profile 2 will be charged negatively below E_1 and between E_2' and E_3, whereas grains following the profile 3 will be charged positively for all energies above E_1. The profiles like 3 were experimentally observed for glass samples[11,16] and profiles corresponding to curve 2 were reported by Richterová *et al.*[17] for grains from melamine-formaldehyde resin; all in micrometer range of sizes.

Theoretical treatments of secondary electron emission have been based on many different approaches. This emission has been described by the elementary theories of Salow,[18] Baroody,[19] and Bruining.[20] Kanaya and Kawakatsu[21] have modified these results by using a Lindhard power potential to describe SE emission from metals due to both primary and backscattered electrons (BEs), and Kanaya *et al.*[22] extended this approach to include insulators. A complex approach to the problem of electron-induced secondary electron emission can be found in Sternglass.[14] He found that the scattering of PEs inside the grain is principal for an explanation of the secondary emission. However, the validity of his already mentioned "universal curve" was limited to 4 E_{max}. Later, Draine and Salpeter[23] found a new approximation by fitting to experimental data and this approximation is valid to higher energies. A well-known and particularly useful theory for the emission of SEs from metals induced by energetic ions ($\geqslant$ a few megaelectronvolts) was proposed by Sternglass.[24] Suszcynsky *et al.*[9] modified this theory to predict the secondary electron yield from metals impacted by energetic (several kiloelectronvolts to about 200 keV) electrons. This modification accounts for the contribution of the BEs to the production of SEs based on knowledge of the BE energy distribution and the authors concluded that the modification is in reasonable agreement with the experimental data from gold targets in the 6–30-keV electron energy range.[25]

Simulation studies of secondary emission have been based mainly on a Monte Carlo electron trajectory simulation method which is a powerful tool for electron probe microanalysis, electron spectroscopy, and microscopy[26–28] where the target influenced by the electron beam is studied. These papers focus on various aspects of these phenomena (e.g., insulating target and internal fields,[29,30] insulating target and high and well-focused electron beams, respectively,[31–33] or electron-induced electron emission from inorganic insulators[34]).

A series of the papers by Ding *et al.*[35–37] precises a Monte Carlo simulation model of electron interactions with solids that includes cascade SE production. The model is based on the use of Mott's elastic scattering cross sections[38] and Penn's dielectric function approach[39] to electron inelastic scattering. The absolute primary energy dependence of the secondary yield and the energy distribution of SEs have been

obtained[37] and the authors noted a good agreement between the model and experimental data measured for clean Cu samples[40] in ultrahigh vacuum. Systematic investigations of SE generation and emission for 19 metals were published in Ding *et al.*[35] The calculated secondary yield curve for a primary beam energy ranging from 100 eV to 2 keV was found to correspond with experimental universal curve. The calculations indicated that the characteristic energy loss of PEs may result in a corresponding feature in the energy distribution of SEs.

Ding *et al.*[36] have used the model approach to calculate the full energy distribution of BEs from the elastic peak down to the true-secondary-electron peak. They compare calculated spectra and experimental data measured with a cylindrical mirror analyzer for primary beam energies ranging from 0.5 to 10 keV at normal incidence for the pure Au, Ag, and Cu polycrystalline samples. A reasonable agreement was reached for the backscattering background at primary energies in the kiloelectronvolt region.

As we noted above, the majority of models were applied on the planar metal or insulating targets but less papers deal with spherical samples. Theoretical considerations of the secondary emission from submicrometer oil drops of spherical shapes were done by Ziemann *et al.*[12] They achieved a good matching with their experiment up to 250 eV of the primary energy. Chow *et al.*[41] developed a model of secondary emission from spherical bodies. The authors assume that the primary electron current density is conserved inside the grain, PEs move straight inside the grain, the production rate of SEs is proportional to the energy loss of PEs, and the escaping probability of SEs decreases exponentially with a distance to the surface. They added the Whiddington law for energy losses along their path in the grain and computed the yield of secondary emission (similarly as in Dionne[42]). Their computation, in fact, assumes that the PEs move along straight lines inside the grain but the SEs can proceed toward the surface in any direction. Since their model did not reproduce the Švestka *et al.*[11] experimental data, Chow *et al.*[43] published an improved model. The new model provided the curve of the yield of secondary emission with several maxima. Varying the constants of the model, the authors were able to fit the data but they should use different sets of constants for low- and high-energy regions.

Richterová *et al.*[44] developed a simple Monte Carlo model of secondary emission from spherical dust grains. Although the model provides a typical secondary yield curve and can roughly describe observed energetic dependences of a dust grain equilibrium charge, it has numerous nonmeasurable parameters. Moreover, neither backscatter yield nor dependence on a sample material match the experimental data very well. Thus, we have prepared a new model based on more realistic assumptions and discuss the results in view of present knowledge of the electron–solid interaction as well as our fresh experimental data.

III. PREVIOUS MODEL FOR THE SPHERICAL GRAIN CHARGING

In Richterová *et al.*,[44] we have used the original Sternglass[14] approach and performed a computer Monte Carlo model of secondary emission from small bodies. The model follows individual trajectories of PEs inside the grain and, based on simple assumptions consistent with the Sternglass theory, calculates a probability of escaping of the excited electrons. The basic assumptions of the model were the following:

(1) The grain is spherical and consists of a continuous and homogeneous matter characterized by a few material constants and no detailed real atomic or electronic structures are included. This assumption means that grains are large enough. The model cannot be valid for small atomical/molecular clusters often present in the space. On the other hand, using the grain radius approaching infinity, the model can be used as a rough approximation of planar samples.

(2) PEs penetrate into a grain and undergo collisions with grain atoms and move along a straight line between collisions. The PE direction is altered after each collision according to a simple distribution like a cosine law (independently on the PE energy). The length of the primary electron path between two consecutive collisions, λ, is proportional to its current energy, $E{:}\lambda=\lambda_0\cdot(E/\Delta E)$, where λ_0 and ΔE are the material-dependent parameters of the model.

(3) One material electron is excited during each collision and then it behaves independently on the PE.

(4) A probability, $P=A\cdot\exp(-x/\Lambda)$, that the excited SE reaches a grain surface decreases exponentially with a distance from the surface x. Constant A normalizes the integral probability to be equal to 1/2 when the electron is on the surface of a grain with the infinite diameter. The mean free diffusion path of SEs, Λ, is expected to be of the order of a lattice constant for metals and much longer for insulators.[14] The resulting probability of the escape of excited electron is then calculated by integration of the probability around the whole grain surface.

(5) For an equilibrium grain potential modeling, the SE energy spectrum must be employed. In accord with the third assumption, we suppose that this spectrum does not vary with the beam energy. A random energy in accordance with a chosen distribution is generated for each SE and it escapes from the grain when this energy is larger than the actual grain potential.

Although the model provides relevant δ curve, a number of BEs remains independent on material and exceeded significantly experimental values as a consequence of the second assumption. Moreover, the model includes several free parameters $(\Delta E,\lambda_0,\Lambda)$ which can be determined by a fit of model results to the experimental data only. Nevertheless, the grain potential growth at the high-energy beam range was predicted. It was shown that this growth is caused by the η enhancement and not by the δ increase as suggested by Chow *et al.*[43] and Švestka *et al.*[11]

IV. NEW VERSION OF THE MODEL

The above discussion has shown that the scattering of PEs inside the grain is a principal factor for the grain charging due to secondary emission because it determines the number of BEs and coefficient η. For this reason, we have applied energy- and material-dependent cross sections often used in

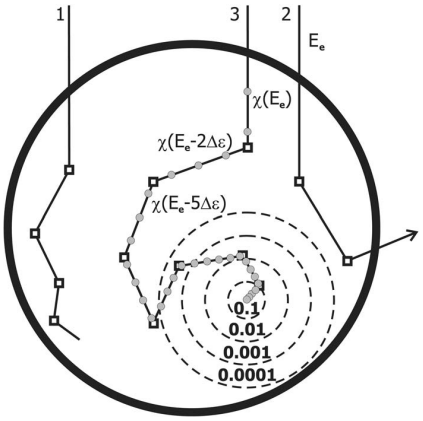

FIG. 2. A 2D demonstration of model assumptions.

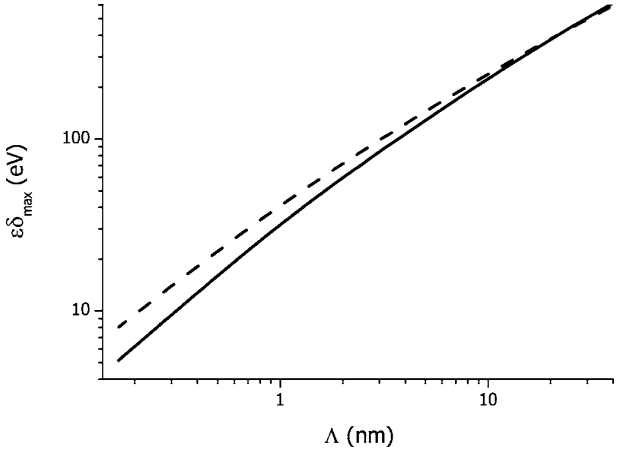

FIG. 3. $\epsilon\delta_{max}$ product as a function of the mean free diffusion path (see text for the full description)

modeling of the beam–solid interaction for an electron microscopy[40] into our new model. This application requires modification of aforementioned assumptions in the following way:

(1) Assumptions of (1), (4), and (5)—without modifications.

(2) For description of PE trajectories inside the matter, a single scattering model according to Hovington *et al.*[45] is used:

• A PE moves along straight lines between collisions. Since almost all non-negligible deflections are caused by elastic electron-atom collisions above several hundreds electronvolts,[46] Mott radial elastic cross sections,[38] namely values computed by Czyżewski *et al.*,[47] are employed. Since their computations were made for several energies between 20 eV and 30 keV only, we have used a cubic spline interpolation for intermediate values. Advantages of this approach (instead of any approximative function usually used[40]) are a better accuracy as well as a shorter computation time.

• All possible energy losses are averaged and thus each PE loses the energy continuously along its path according to the modified Bethe stopping power equation. This modified equation can be written as

$$\frac{dE}{ds} \sim \rho \frac{Z}{AE} \ln\left(\frac{1.166E}{J}\right),$$

where ρ is the sample mass density, Z and A are the atomic and neutron numbers, respectively, J is close to the mean ionization potential, ds is the path element, and E is the actual electron energy.[45]

(3) Whole deposited energy is converted to electron excitations. The number of excited electrons is related to the energy spent by the mean excitation energy ε. Excited material electrons behave independently on the collision type and/or on the PE energy or direction.

The principles of the model are illustrated in Fig. 2. Note that this is only a two-dimensional (2D) sketch but the model is 3D. PEs are scattered in elastic collisions (marked by squares) according to Mott's elastic scattering cross sections and their actual energy. Some of them are stopped in the grain (trajectory 1), while the others leave it (trajectory 2). Continuous energy losing given by the Bethe stopping power formula is realized by small discrete energy losses, $\Delta\varepsilon$, along the path (marked by circles) until the whole energy of the PE is spent. Material electrons are excited at these coordinates with a probability $\Delta\varepsilon/\varepsilon$ and the probability that they reach the surface decreases exponentially with the distance (demonstrated only for the last energy loss).

Only three free parameters—ε, Λ, and a SE spectrum—remain in our model and their influence on the model results will be examined in several following figures. However, we should note prior to the analysis that the mean ionization potential ε and the relative number of true secondary electrons δ are strongly coupled quantities. An increase of ε leads to a smaller number of ionizations along the PE path and thus to a decrease of δ. For this reason, their product $(\varepsilon\delta_{max})$ is plotted in the following figures. Taking into account that the experimental value of δ_{max} is close to unity for Au planar samples,[48] Fig. 3 shows that ε and Λ cannot be chosen independently in fitting to experimental data. On the other hand, one can see that the spherical grain exhibits several times larger δ_{max} than planar samples in any reasonable range of Λ. In order to further decrease the ranges of ε and Λ for a future fitting of model results to experiments, Fig. 4 shows how the product $\varepsilon\delta_{max}$ changes with a position of the maximum of secondary emission yield E_{max}. The dependences were obtained varying Λ as those in Fig. 3 and a linear relation was found.

V. EVALUATION OF THE MODEL

The model is developed for a study of the charging of dust grains. Since there is a lack of such data, we are comparing the model results with experiments on planar surfaces in this chapter. As we have shown above, the energy spectrum of BEs is of principal importance. Figure 5 shows such spectra for a planar Au sample bombarded by the electron beam of several energies. One can note that the spectra match experiments and/or previous models (compare with Fig. 1 in Ding *et al.*[36]).

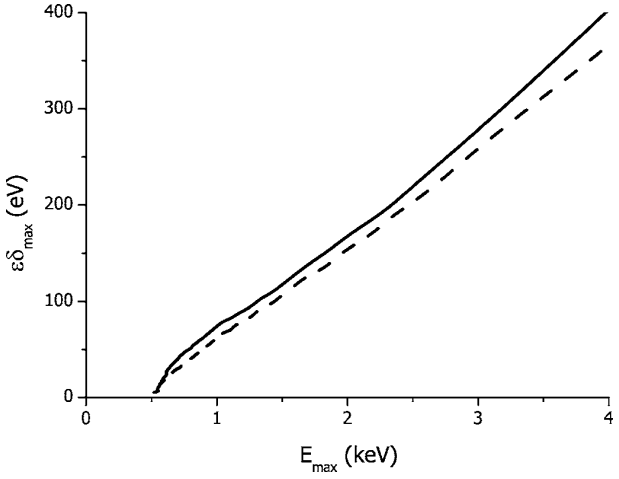

FIG. 4. $\epsilon\delta_{\max}$ product as a function of the energy corresponding to the maximum of secondary emission yield.

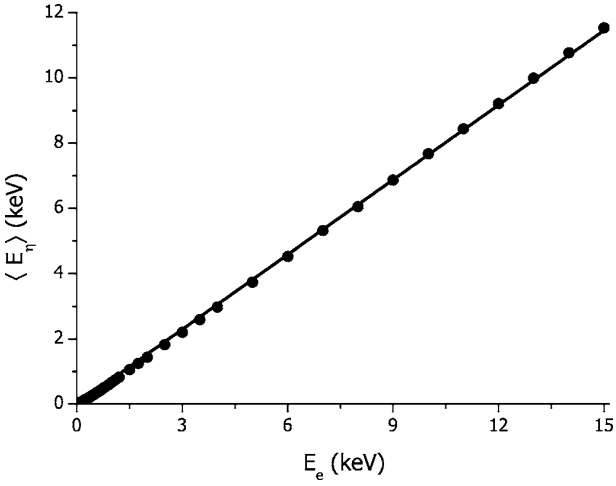

FIG. 6. Mean energy of backscattered electrons as a function of the beam energy.

BEs do not deposit their charge inside the target and thus, they do not contribute to the charging of the dust grains if their energy is high enough to overcome the grain potential. Figure 6 shows that the mean energy of BEs rises approximately linearly with the beam energy and the slope of a fit is ≈ 0.76. In other words, since η is roughly constant above 1 keV as we will show later, BEs carry out of the grain a constant fraction of the initial beam energy.

Summing all energy losses of PEs along the coordinate parallel with the beam axis, the distribution of beam energy losses in the sample can be obtained. Such data for several energies are plotted in Fig. 7 as a function of the depth beneath the sample surface x. A logarithmic scale has been chosen in order to show all curves in one figure. The position of the maximum of the energy losses increases with the beam energy E_e. The plot of this depth ($x_{\max}$) as a function of E_e in Fig. 8 reveals that this function can be approximated as $x_{\max}=k\cdot E^n$ where $n=3/2$ and $k=1$ in plot units. This function is not interesting for bulk targets influenced with primary energies above 1 keV because $x_{\max}$ is so large that the escaping probability of SEs from this depth is nearly zero. On the other hand, it can be important for dust grains (or thin films) when the grain size becomes comparable with $x_{\max}$.

Different assumptions and simplifications lead to different values of the exponent in the above equation. Its value ranges from 1 to 2 (if the scattering is neglected).[40] Sternglass[14] made a precise study of a secondary emission process that led to profiles of energy losses very similar to those in Fig. 7. On the contrary to many other authors, he supposed that the beam scattering is fundamental for the beam–solid interaction. He assumed that a non-negligible part of the PEs undergoes collisions which lead to a serious energy losses due to production of UV photons or Auger electrons. The re-absorbtion of these particles arises in a narrow peak of the distribution of beam energy losses close to the surface, and a peak position varies as a square root of an initial beam energy. Although the value of this exponent

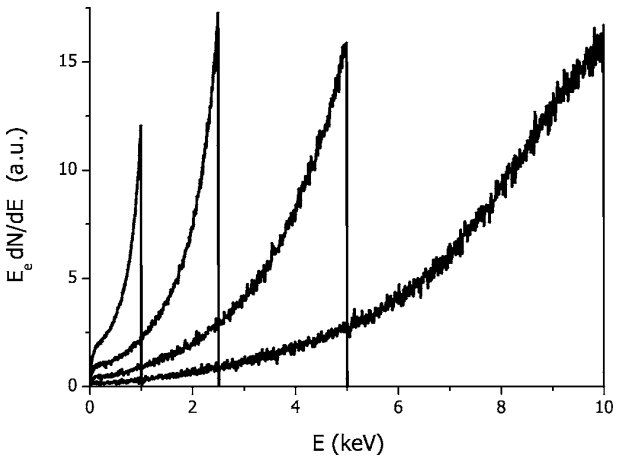

FIG. 5. Calculated spectra of backscattered electrons for several beam energies.

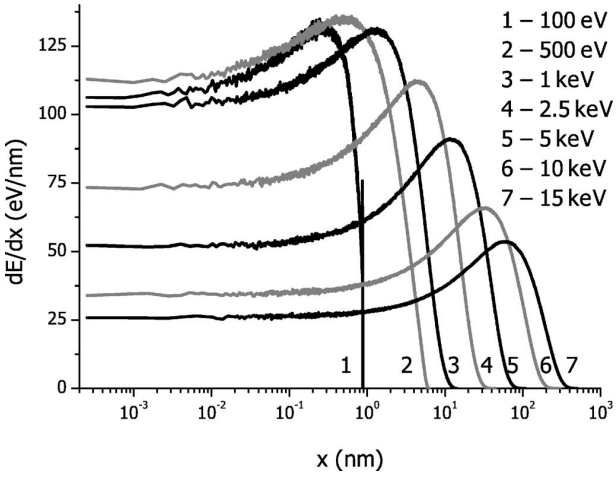

FIG. 7. Energy deposited per unit depth as a function of the distance from the planar sample surface for several beam energies.

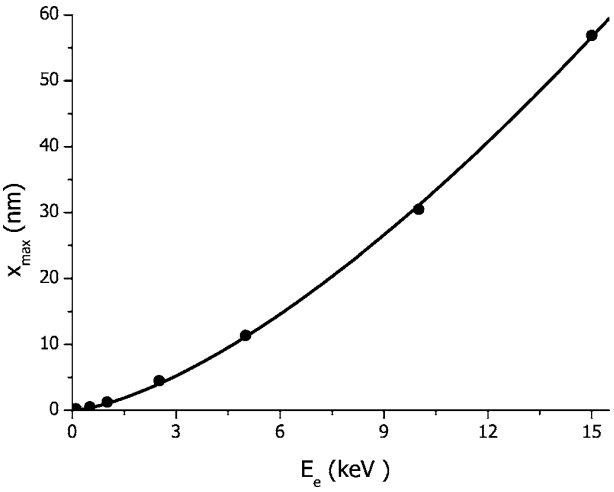

FIG. 8. Location of the maximum of energy deposition as a function of the beam energy.

would be very important for a decision among different models of the scattering inside the material, it cannot be measured and thus, we are leaving this point without comments.

VI. COMPARISON OF THE MODEL WITH EXPERIMENTAL DATA AND DISCUSSION

We have shown that our model describes details of secondary emission with a reasonable accuracy and thus, we can discuss effects connected with a finite size of dust grains. Figure 9 shows the secondary emission yield δ as a function of the beam energy for several diameters of spherical Au targets. The computed yield for a planar sample and "universal" curve[23] are given for the sake of reference. Taken into account the spread of the data used for a determination of this universal curve, we can consider the model results as

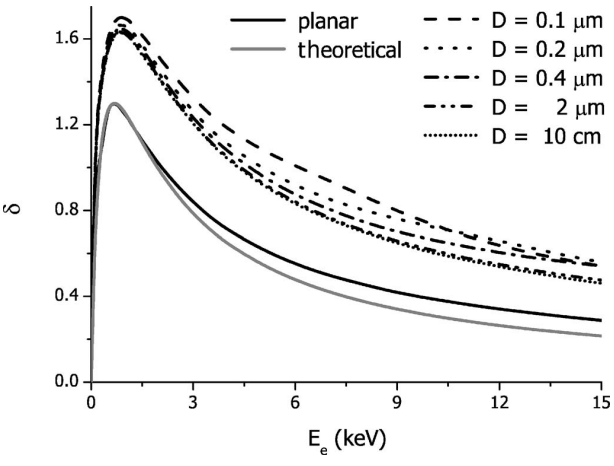

FIG. 9. Calculated energetic profiles of true secondary emission yield for the planar gold sample and several diameters of spherical samples. The universal curve of Draine and Salpeter[23] is given for reference.

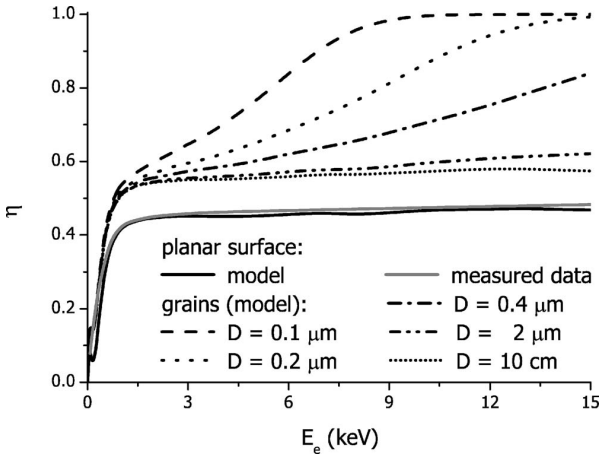

FIG. 10. Calculated energetic profiles of backscattered yield for planar gold sample and several diameters of spherical samples. Experimental data measured on a planar surface from Bronstein and Fraiman[15] are shown for comparison.

satisfactory. Moreover, the yield of true secondary electrons has only a small effect on resulting grain charge, as we will show later. On the other hand, our model neglects the production of x rays. A part of the produced photons leaves the grain and, thus, one can expect that δ provided by the model can be larger than experimental values especially at higher beam energies.

The principal rise of the yield δ is connected with the curvature of the grain surface but we did not find any difference in yields computed for 10 cm and 2 μm grains. A notable increase of the yield can be found for grain diameters below $\approx$1 μm. This increase is more pronounced at higher energies and can be probably attributed to the fact that a larger fraction of the primary energy is deposited near the surface as it follows from Fig. 7. Such effect would lead to a distinct maximum on secondary emission yield profile for thin films but, for spherical grains, it results only in a relatively small enhancement of δ for particular diameter in a certain range of energies (e.g., around 7 keV for the 0.1 μm grain).

The changes of the amount of true secondary electrons due to a finite size of the grain are of the order of several percent. On the other hand, the increase of the number of BEs is more distinct as it can be seen in Fig. 10. The calculated yield η for a planar sample matches exactly the experimental values taken from Bronstein and Fraiman.[15] The spherical surface of the grain leads to an increase of η from $\approx$0.45 to 0.55 in the high-energy range. The effects of finite grain dimensions start from a diameter of about 2 μm and η increases to nearly unity for smaller grains and high energies of PEs. Since the total secondary electron yield is a sum of δ and η, we can conclude that the rise of η represents a principal contribution to the increasing amount of electrons leaving small dust grains.

A comparison of analyzed effects with experimental data obtained on small grains is difficult because such observations are generally missing. The measurements on glass samples made by Švestka *et al.*[11] cannot be used for a quan-

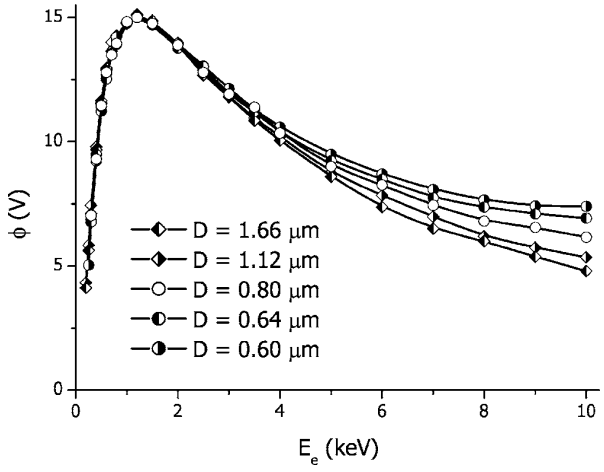

FIG. 11. Surface potential as a function of the beam energy as measured on several gold grains of different diameters.

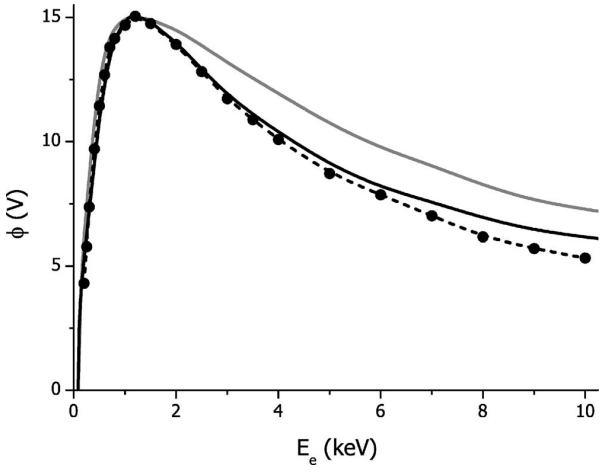

FIG. 12. Comparison of measured and calculated grain potentials. Grey (upper) curve uses Maxwell distribution, black (lower) curve uses Draine and Salpeter[23] distribution, and the experimental points are connected with the dashed line.

titative analysis because the composition of glass used for measurements is unknown. For this reason, we have carried out a series of measurements of charging characteristics on gold spherical grains. Details of the experiment are described elsewhere.[49–51] The experiment provides the grain potential as a function of the electron beam energy. Our experimental setup allows us to measure surface potentials of gold grains larger than ≈ 0.5 μm under primary energies in a range of 0.15–10 keV. Model calculations presented in Figs. 9 and 10 show that effects of the grain dimension would be small but observable. The measurements for five grains of different diameters are shown in Fig. 11. The profile roughly resembles an energetic dependence of the secondary emission yield (compare with Fig. 9) but the differences among grain potentials at larger energies (above ≈ 5 keV) cannot be explained this way. Nevertheless, Fig. 10 suggests that changes of the backscattered yield are responsible for a rise of the potential with a decreasing grain diameter.

A quantitative analysis of experimental data requires an assumption on the energy distribution of true secondary electrons (note that the spectrum of BEs is provided by the model). Although an energy spectrum of SEs is generally expected to be Maxwellian-like, Velyhan *et al.*[13] showed that the Draine-Salpeter distribution[23] seems to be more suitable for metallic grains.

Other two-model parameters (mean free diffusion path of SEs, Λ, and characteristic energy loss, ε) can be determined directly by a comparison of measured profiles with the results of computation in several steps:

- Since the maximum of $\phi(E_e)$ should correspond to the maximum of $\delta^*(E_e)$, the profiles of $\delta^*(E_e)$ were computed for different Λ. Among them, that peaking for the same E_e as measured profile $\phi(E_e)$ has been chosen ($\Lambda = 1.25$ nm).
- Knowledge of Λ allows us to find a value of the product $\varepsilon\delta_{\max}$ in Fig. 4 ($\varepsilon\delta_{\max} = 40.3$ eV).
- Since $\delta_{\max} = 1.3$ for a planar Au sample,[48] $\varepsilon = 31$ eV.

As a last step, the model was running with both aforementioned energy distributions of SEs and those potential profiles exhibiting the same values of maxima as measured data are plotted in Fig. 12.

The computations confirm the conclusion of Velyhan *et al.*[13] that the Draine-Salpeter distribution is more appropriate for metals because the Maxwellian distribution provides a much broader peak of the ϕ profile. On the other hand, there is no physical reason preferring a particular shape of distribution of SEs and thus, we cannot speculate if the difference between model and experimental results is connected with this distribution or with other simplifications used in the model. The distribution of SEs from dust grains can be measured in our experimental setup[52] and thus we plan to study it in detail.

VII. CONCLUSION

Our numerical and experimental investigations of the charging of dust grains illuminated by the electron beam have shown that a present version of the developed model describes very well basic features of measured profiles of the secondary electron yields for planar targets as well as the surface potential of small spherical grains. Consequently, we can conclude that the model includes principal processes leading to the emission of secondary electrons.

A further development of the model would include the x-ray production inside grains and excitation of secondary electrons this way. We think that these processes are responsible for an excess of the secondary emission yield in our calculations. A detailed experimental investigation of the energy distribution of true secondary electrons is necessary for a precise prediction of the grain potential.

ACKNOWLEDGMENTS

This work is a part of the research plan MSM 0021620834 that is financed by the Ministry of Education of the Czech Republic.

*Electronic address: ivana.richterova@mff.cuni.cz
†Electronic address: jiri.pavlu@mff.cuni.cz
‡Electronic address: zdenek.nemecek@mff.cuni.cz
§Electronic address: jana.safrankova@mff.cuni.cz

[1] M. Horanyi, Annu. Rev. Astron. Astrophys. **34**, 383 (1996).
[2] R. Srama, T. J. Ahrens, N. Altobelli, S. Auer, J. G. Bradley, M. Burton, V. V. Dikarev, T. Economou, H. Fechtig, M. Görlich *et al.*, Space Sci. Rev. **114**, 465 (2004).
[3] M. Horányi, T. W. Hartquist, O. Havnes, D. A. Mendis, and G. E. Morfill, Rev. Geophys. **42**, RG4002 (2004).
[4] N. Altobelli, E. Grün, and M. Landgraf, Astron. Astrophys. **448**, 243 (2006).
[5] F. Spahn, K.-U. Thiessenhusen, J. E. Colwell, R. Srama, and E. Grün, J. Geophys. Res. **104**, 24111 (1999).
[6] F. Spahn, J. Schmidt, N. Albers, M. Hörning, M. Makuch, M. Seiß, S. Kempf, R. Srama, V. Dikarev, S. Helfert *et al.*, Science **311**, 1416 (2006).
[7] H. Kimura and I. Mann, Astrophys. J. **499**, 454 (1998).
[8] E. C. Whipple, Rep. Prog. Phys. **44**, 1197 (1981).
[9] D. M. Suszcynsky, J. E. Borovsky, and C. K. Goertz, J. Geophys. Res., [Solid Earth] **97**, 2611 (1992).
[10] J. Spann, M. Abbas, C. Venturini, and R. Comfort, Phys. Scr., T **T89**, 149 (2001).
[11] J. Švestka, I. Čermák, and E. Grün, Adv. Space Res. **13**, 199 (1993).
[12] P. Ziemann, P. Liu, D. Kittelson, and P. McMurry, J. Phys. Chem. **99**, 5126 (1995).
[13] A. Velyhan, Z. Němeček, and J. Šafránková, in *WDS'01 Proceedings of Contributed Papers: Part II—Physics of Plasmas and Ionized Media*, edited by J. Šafránková (Matfyzpress, Prague, 2001), pp. 267–272.
[14] E. J. Sternglass, Master's thesis, Cornell University (1951).
[15] I. M. Bronstein and B. S. Fraiman, *Secondary Electron Emission* (Nauka, Moskva, 1969), in Russian.
[16] Z. Němeček, J. Pavlů, J. Šafránková, I. Richterová, and I. Čermák, in *Dusty Plasmas in the New Millennium*, edited by R. Bharuthram, M. Hellberg, P. Shukla, and F. Verheest, AIP Conf. Proc. No. 649 (AIP, Melville, New York, 2002), pp. 378–381.
[17] I. Richterová, J. Pavlů, Z. Němeček, J. Šafránková, and M. Jeřáb, in *New Vistas in Physics of Dusty Plasmas*, edited by L. Boufendi, M. Mikikian, and P. K. Shukla, AIP Conf. Proc. No. 799 (AIP, Melville, New York, 2005), pp. 395–398.
[18] H. Salow, Phys. Z. **41**, 434 (1940).
[19] E. M. Baroody, Phys. Rev. **78**, 780 (1950).
[20] H. Bruining, *Physics and Applications of Secondary Emission* (Pergamon, London, 1954).
[21] K. Kanaya and H. Kawakatsu, J. Phys. D **5**, 1727 (1972).
[22] K. Kanaya, S. Ono, and F. Ishigaki, J. Phys. D **11**, 2425 (1978).
[23] B. Draine and E. Salpeter, Astrophys. J. **231**, 77 (1979).
[24] E. Sternglass, Scientific Paper 6-94410-2-P9, Westinghouse Research Laboratories, Pittsburgh 35 (1957).
[25] D. M. Suszcynsky and J. E. Borovsky, Phys. Rev. A **45**, 6424 (1992).
[26] D. C. Joy, J. Microsc. **147**, 51 (1987).
[27] R. Shimizu and Z.-J. Ding, Rep. Prog. Phys. **55**, 487 (1992).
[28] A. Dubus, J.-C. Dehaes, J.-P. Ganachaud, A. Hafni, and M. Cailler, Phys. Rev. B **47**, 11056 (1993).
[29] J. P. Ganachaud, C. Attard, and R. Renoud, Phys. Status Solidi B **199**, 175 (1997).
[30] C. Attard and J. P. Ganachaud, Phys. Status Solidi B **199**, 455 (1997).
[31] R. Renoud, C. Attard, J.-P. Ganachaud, S. Bartholome, and A. Dubus, J. Phys.: Condens. Matter **10**, 5821 (1998).
[32] R. Renoud, F. Mady, and J.-P. Ganachaud, J. Phys.: Condens. Matter **14**, 231 (2002).
[33] R. Renoud, F. Mady, C. Attard, J. Bigarré, and J.-P. Ganachaud, Phys. Status Solidi A **201**, 2119 (2004).
[34] J. Cazaux, Nucl. Instrum. Methods Phys. Res. B **244**, 307 (2006).
[35] Z. J. Ding, X. D. Tang, and R. Shimizu, J. Appl. Phys. **89**, 718 (2001).
[36] Z. J. Ding, H. M. Li, K. Goto, Y. Z. Jiang, and R. Shimizu, J. Appl. Phys. **96**, 4598 (2004).
[37] Z. J. Ding, H. M. Li, X. D. Tang, and R. Shimizu, Appl. Phys. A: Mater. Sci. Process. **78**, 585 (2004).
[38] N. F. Mott and H. S. W. Massey, *Theory of Atomic Collisions* (Oxford University Press, New York, 1965).
[39] D. R. Penn, Phys. Rev. B **35**, 482 (1987).
[40] D. Joy, *Monte Carlo Modeling for Electron Microscopy and Microanalysis* (Oxford University Press, New York, 1995).
[41] V. Chow, D. Mendis, and M. Rosenberg, J. Geophys. Res., [Space Phys.] **98**, 19065 (1993).
[42] G. F. Dionne, J. Appl. Phys. **46**, 3347 (1975).
[43] V. Chow, D. Mendis, and M. Rosenberg, IEEE Trans. Plasma Sci. **22**, 179 (1994).
[44] I. Richterová, Z. Němeček, J. Šafránková, and J. Pavlů, IEEE Trans. Plasma Sci. **32**, 617 (2004).
[45] P. Hovington, D. Drouin, and R. Gauvin, Scanning **19**, 1 (1997).
[46] R. F. Egerton, *Electron Energy-loss Spectroscopy in the Electron Microscope* (Plenum, New York, 1996).
[47] Z. Czyżewski, D. O'Neill MacCallum, A. Romig, and D. C. Joy, J. Appl. Phys. **68**, 3066 (1990).
[48] H. Seiler, J. Appl. Phys. **54**, R1 (1983).
[49] I. Čermák, E. Grün, and J. Švestka, Adv. Space Res. **15**, 59 (1995).
[50] P. Žilavý, Z. Sternovský, I. Čermák, Z. Němeček, and J. Šafránková, Vacuum **50**, 139 (1998).
[51] J. Pavlů, A. Velyhan, I. Richterová, Z. Němeček, J. Šafránková, I. Čermák, and P. Žilavý, IEEE Trans. Plasma Sci. **32**, 704 (2004).
[52] P. Žilavý, I. Richterová, Z. Němeček, J. Šafránková, and J. Pavlů, Czech. J. Phys. **55**, 1283 (2005).

G. Richterová et al. [2012]

Richterová, I., Němeček, Z., Beránek, M., Šafránková, J., Pavlů, J., Secondary emission from non-spherical dust grains with rough surfaces: Application to lunar dust. *Astrophys. J.* 761 (2): 108, 2012.

The Astrophysical Journal, 761:108 (5pp), 2012 December 20 doi:10.1088/0004-637X/761/2/108

SECONDARY EMISSION FROM NON-SPHERICAL DUST GRAINS WITH ROUGH SURFACES: APPLICATION TO LUNAR DUST

I. Richterová, Z. Němeček, M. Beránek, J. Šafránková, and J. Pavlů
Charles University, Faculty of Mathematics and Physics, Prague, Czech Republic
Received 2012 August 21; accepted 2012 October 24; published 2012 December 3

ABSTRACT

Electrons impinging on a target can release secondary electrons and/or they can be scattered out of the target. It is well established that the number of escaping electrons per primary electron depends on the target composition and dimensions, the energy, and incidence angle of the primary electrons, but there are suggestions that the target's shape and surface roughness also influence the secondary emission. We present a further modification of the model of secondary electron emission from dust grains which is applied to non-spherical grains and grains with defined surface roughness. It is shown that the non-spherical grains give rise to a larger secondary electron yield, whereas the surface roughness leads to a decrease in the yield. Moreover, these effects can be distinguished: the shape effect is prominent for high primary energies, whereas the surface roughness predominantly affects the yield at the low-energy range. The calculations use the Lunar Highlands Type NU-LHT-2M simulant as a grain material and the results are compared with previously published laboratory and in situ measurements.

Key words: dust, extinction – methods: numerical – Moon

1. INTRODUCTION

Many papers on secondary electron emission from various materials have been published to date because this emission is an important factor in different fields of modern technology, e.g., electron lithography and imaging, powering of spacecraft, the study of space dust grains exposed to cosmic radiation, and many others. Secondary emission becomes prominent when an amount of energetic (>10 eV) electrons is present in the medium surrounding an object.

Theoretical studies and models of secondary electron emission are often based on Monte Carlo simulations of electron trajectories (Joy 1987; Shimizu & Ding 1992; Dubus et al. 1993; Renoud et al. 2004). Nevertheless, the majority of models have been applied to planar metal or insulating targets and less attention has been paid to dust grains. However, the finite grain size plays an important role when primary electrons are energetic enough to penetrate such objects. A description of secondary emission from finite spherical samples from different materials can be found for example in Richterová et al. (2010), but investigations of real samples show that they are often far from ideal because they can be rough and/or non-spherical in shape.

Experimental values of secondary emission yields determined from large planar samples of various materials can differ by a factor of two probably due to differing experimental conditions and sample qualities. An excellent laboratory data set under 10^{-7}–10^{-9} Torr was compiled by Bronstein & Fraiman (1969), and it was recently revised by El Gomati et al. (2008) and Walker et al. (2008) for both scattered and secondary yields, respectively. These papers also deal with the influence of surface adsorbates and oxide layers on the secondary yield but, unfortunately, the surface coarseness was not reported.

On the other hand, several papers have been devoted to secondary emission from rough surfaces, mainly motivated to reduce the secondary emission from surfaces bombarded by energetic particles in particle colliders (Pivi et al. 2008) or in high-power microwave devices (Watts et al. 2011). Although the surface roughness is not quantified in the latter paper, the former deals with surface deformations with dimensions of the order of millimeters and the walls of these deformations are treated as being ideally smooth. Nevertheless, the authors of both papers noted a decrease in the secondary emission yield for rough surfaces.

Halekas et al. (2009) reported the first in situ measurements of secondary electron emission efficiency of a lunar regolith. They found that the secondary emission yield from this material is a factor of ≈3 lower than that measured under laboratory conditions (Willis et al. 1973; Horányi et al. 1998; Němeček et al. 2011). The authors discussed the discrepancy between their observations and laboratory measurements and concluded that it might result from the roughness and irregular shape of the lunar regolith, which likely affect the escape of secondary electrons from the surface.

Following models designed for scanning electron microscopy (e.g., Li et al. 2008; Hovington et al. 1997a, 1997b), we have developed a numerical model of secondary emission from spherical objects suitable for various materials including metals (Richterová et al. 2006a), insulators (Richterová et al. 2007; Němeček et al. 2011), and complex compounds (Richterová et al. 2006b; Mann et al. 2011). These papers give many examples of excellent agreement of model results with laboratory measurements on spherical samples; the deviations are of the order of single units percent. However, the agreement between model calculations and laboratory measurements was much worse when the sample shape could not be approximated by a sphere with sufficient accuracy, and the deviations were attributed to the effect of unspecified shape. A very preliminary calculation in Richterová et al. (2011a) compared secondary emission yields of a sphere and a cube from the Lunar Highlands Type NU-LHT-2M (LHT) simulant. The comparison revealed a larger secondary emission yield for a cube but the effect was notable only in the keV range of primary energies. In order to elucidate these effects of surface form and quality, we adjust our model to non-spherical grains with different surface roughness and discuss the influence of these parameters on the secondary emission characteristics of the grains.

2. MODEL OUTLINE

The model of Richterová et al. (2006a) provides the charge accumulated in the grain as a function of the primary beam energy (which is directly measurable) as well as the energetic

dependence of the secondary and backscattered yields. The model was successfully verified in laboratory experiments by charging of gold and glass dust grains. However, further investigations revealed a small disagreement between model predictions and experiments for light materials like carbon; thus, Richterová et al. (2010) suggested several model corrections. We briefly review the model approach that is applied to calculations presented in this paper.

The model follows trajectories of primary electrons inside the spherical grain of a given composition. The primary electrons are scattered by collisions with the grain atoms and the deflection angle is generated according to energy-dependent Mott differential cross-sections (Mott & Massey 1965). Note that these cross-sections are calculated in two dimensions and provide only the total deflection angle. Since the model is three dimensional, we use this angle as a polar angle and generate the azimuthal angle in a random way.

In the case of compounds (e.g., LHT), we do not compute a new weighted differential cross-section; instead, a random number is generated to decide which particular species causes the electron deflection at each collision. Integrating the radial cross-section over a whole space angle, we can obtain the total cross-section, $\sigma_T(E)$, where σ_T decreases monotonically with energy and can be easily interpolated via cubic splines.

A path length between two subsequent collisions, $\lambda(E)$, is generated according to $\sigma_T(E)$. The energy of the primary electrons decreases continuously along their path. Since a corresponding change of $\sigma_T(E)$ between two subsequent collisions can often be neglected, the mean-free forceless path, $\lambda(E)$, was used in Richterová et al. (2006a, 2007). When a σ_T increase along the electron path is not omitted, electrons travel a shorter distance than that given by the mean-free path, $\lambda(E)$. This effect is potentially important for samples containing light species and, thus, Richterová et al. (2011b) suggested a model correction that was applied to ice grains. The present calculations follow this approach.

To determine the traveling path of primary electrons, we use the modified Bethe stopping power formula (Joy & Luo 1989). The effective number of atomic electrons and the effective mean ionization potential are calculated using the Hovington et al. (1997a) procedure.

In contrast to primary electrons, the diffusion of secondary electrons inside the target is treated statistically using an exponential decay of the escape probability with distance from the surface. All elemental processes incorporated in the model, cross-section data sources, and a calibration of material constants to the experimental data can be found in Joy & Luo (1989) and references therein.

Continuous monitoring of each primary electron allows us to investigate size and shape effects connected with micron and submicron dust grains. Since we neglect possible quantum effects, grains should have at least 10,000 particles, i.e., be larger than about 10 nm.

Approximations used in the model limit the validity of both the secondary (δ) and scattered (η) yields down to about 50 eV of the primary energy. Nevertheless, their sum (the sign of the grain net current) can be determined reliably up to 15 eV. At lower energies, the secondary emission process is dominated by a surface plasmon decay that is omitted in our model.

3. NON-SPHERICAL GRAINS

The model yields can serve as the input for computations of the dust grain charge for arbitrary surrounding plasma parameters. However, the model has been applied for large planes and spherical grains until now because the model routines use a spherical symmetry which simplifies the calculations. As noted above, different disagreements between observations and model calculations are often attributed to effects of shape and/or surface roughness of the investigated samples; thus, we have modified the model routines; trajectories of primary electrons inside the grain are monitored in a 3D Cartesian coordinate system. The calculations become time-consuming; nevertheless, this procedure allows us to calculate the secondary emission yields from objects of arbitrary shape.

The dependence of the yield of the secondary emission $\delta(E)$ on the primary energy, E, is often described by the so-called Sternglass universal formula (Sternglass 1957):

$$\frac{\delta}{\delta_{max}} = \frac{E}{E_{max}} \exp\left(2 - 2\sqrt{\frac{E}{E_{max}}}\right) \quad (1)$$

for $E \leqslant 4E_{max}$. This formula uses δ_{max} (maximum of the secondary emission yield) and E_{max} (primary energy corresponding to this maximum). These parameters are expected to be a function of the target material only. Note that several different descriptions of $\delta(E)$ have been suggested (e.g., Draine & Salpeter 1979) but almost all of them use the same or similar parameters. For this reason, we will demonstrate the model results using these parameters.

Equation (1) assumes the monoenergetic electron beam directed along the normal to a planar target. The secondary emission yield depends on the incidence angle of the primary beam being larger for larger angles; thus, an application of Equation (1) to a large spherical sample affected by a parallel beam requires a correction factor. The same factor can be applied for the case of bombardment of a planar target with isotropic electrons of a given energy. Draine & Salpeter (1979) have shown that this factor is equal to 2 if an angular dependence described by $\cos^{-1}\theta$ is assumed. The value of δ_{max}^{eff} (i.e., $\delta_{max}^{eff} = 2\delta_{max}$) is used for estimations of dust grain charging (e.g., Horányi et al. 1998; Halekas et al. 2009). On the other hand, Bronstein & Fraiman (1969) argued that the value of this factor depends on the target material. Model results of Richterová et al. (2007) revealed a value of $\approx$1.3 for glass spheres and one can expect that this value would be close to that for lunar dust. On the other hand, our calculations directly provide the value of the yield for the dust grain bombarded by isotropic electrons of a given energy and thus we do not distinguish between δ_{max}^{eff} and δ_{max}.

The other parameter important for the charging of dust grains is the average fraction of primary electrons scattered out of the target. For planar surfaces and a primary beam parallel to the surface normal, the scattered yield rises with the primary energy up to several hundred eV and exhibits a saturation for higher energies. The saturated level rises from $\approx$0.1 to 0.5 with the mean atomic number of the target (Bronstein & Fraiman 1969).

Both the scattered and secondary electrons contribute to the charging of the dust grains. For a description of charging by secondary emission, an effective charging yield, $\delta^* = \delta/(1-\eta)$ is more appropriate because it is roughly proportional to the surface potential that the dust grain would reach under bombardment by electrons of a particular energy if all other charging currents could be neglected. This condition is fulfilled in many laboratory experiments (Mann et al. 2011).

As already noted, our previous calculations (Richterová et al. 2007, 2010) were performed for spherical objects that can

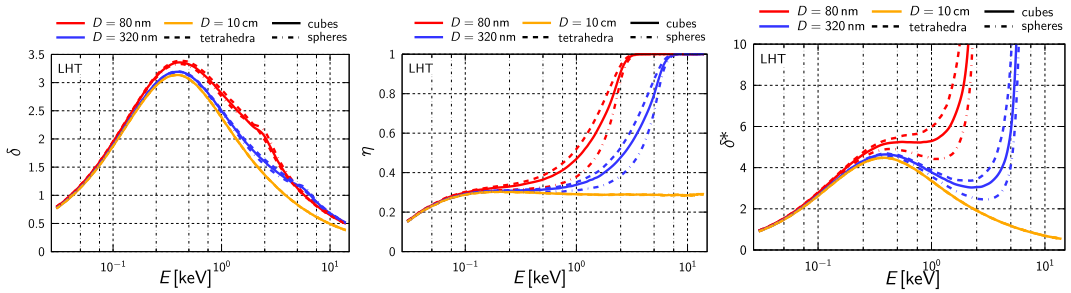

Figure 1. Demonstration of the grain shape effect. The left panel shows the secondary yield, δ; the middle panel the scattered yield, η; and the right panel shows the effective charging yield, δ^*, as a function of the primary energy for different shapes (spheres: dash–dotted; cubes: full; tetrahedrons: dashed).

be described by one parameter (diameter) for a given mass composition. However, the problem of arbitrarily-shaped grains with a rough surface is multidimensional. For this reason, we limit demonstrations of the present model results to cubes and tetrahedrons of different dimensions with smooth surfaces and, conversely, to cubes of a given mass with different surface roughnesses. As the dust grain material, we have chosen the LHT simulant.

4. SHAPE EFFECTS

Figure 1 demonstrates the effects of different grain shapes on a particular yield. The left panel shows δ, the middle panel presents η, and the right panel demonstrates the effective charging yield, δ^*, all as a function of the primary energy for LHT spheres (dot–dashed lines), cubes (full lines), and tetrahedrons (dashed lines). The dimensions of these objects retain their volume (mass), and they correspond to LHT spheres with 80 nm (red) and 320 nm (blue) diameters. The large cube (10 cm) is shown by the yellow line for comparison. The calculations assume an isotropic illumination of the grain with primary electrons of a given energy.

From Figure 1 it follows that the replacement of a sphere with a cube (or pyramid) of the same mass does not change the profile of δ (left panel) substantially. On the other hand, the profiles of η (middle panel) are sensitive to the target shape preferentially at the high-energy range. The rise of η starts at lower energies but it is not so steep for cubes or pyramids. We can conclude that neither δ nor η is affected by grain shape or dimension in the low-energy (up to 200–300 eV) range. An examination of cuboids with different edge ratios (not shown) revealed that this is true until the shortest edge of a cuboid becomes comparable with the penetration depth of the primary electrons, but such an effect is known from earlier investigations of secondary emission from thin films (e.g., Bronstein & Fraiman 1969). This means that grains would be charged to the same potential if the energy of impinging electrons were sufficiently low, as experimentally proved by Němeček et al. (2011). However, the charging strongly depends on the dimensions at higher energies, as can be seen from profiles of the charging yield in the right panel of the figure. Such energies dominate in some regions of planetary magnetospheres or in fusion devices and the grains of different shapes would be charged to different surface potentials there. On the other hand, shape effects would be negligible in a great majority of applications where dust grains are immersed in a low-temperature plasma.

5. INFLUENCE OF SURFACE ROUGHNESS

We have prepared a simple description of the surface roughness which follows an approach used in critical dimension metrology (Li et al. 2008). An example of the modeled coarse surface is shown in Figure 2. The grain basic shape is cubic and its surface is triangulated by a regular mesh with step a. The height/depth, h, of the surface features at each point of the mesh is generated as a random number with normal distribution and standard deviation σ. When $|h| \geqslant 3\sigma$ is generated, we put $|h| = 3\sigma$. The mesh points closest to the edges of the basic cube are not affected. Since the distribution of h is symmetric around the original cube surface, this procedure roughly conserves the volume of the modified cube.

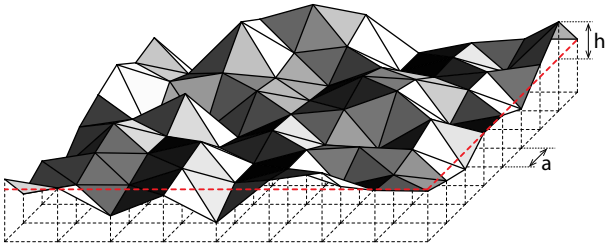

Figure 2. Example of the modeled coarse surface: a is the step of the mesh and h is the height/depth of surface coarseness measured from the original smooth surface.

Figure 3 presents the model results for an 8 μm cube in the same format as used in Figure 1. The left panel demonstrates that the surface roughness strongly influences the secondary electron yield at low energies (below 2 keV) of the primary electrons. Note that the curves are parameterized by quantities characterizing the surface roughness and that their values range from 1 to 20 nm. This means that such differences in the surface roughness can be recognized only by scanning tunneling or atomic force microscopy; they would look mirror-bright for white light.

The increased surface roughness generally leads to a decrease in the yield of secondary electrons and to a shift of its maximum toward higher energies. The yield decrease is caused by the capture of some electrons that had already left the surface by the neighboring "hillock." The same should be true for scattered electrons, and we can see a decrease in their yield in the middle panel. The increase in η for primary energies exceeding 2 keV does not depend on the surface parameters and is caused by the shape effect discussed in the previous section. Note that we have used an 8 μm cube for the demonstration because this dimension allows us to show both shape and surface roughness effects in one figure. These effects would be mixed for smaller grains, whereas the increase in η would occur at energies exceeding the investigated range for large grains.

For the sake of simplicity, Figure 3 presents examples of the rough surface with $a = \sigma$. Since the shapes of the δ profiles

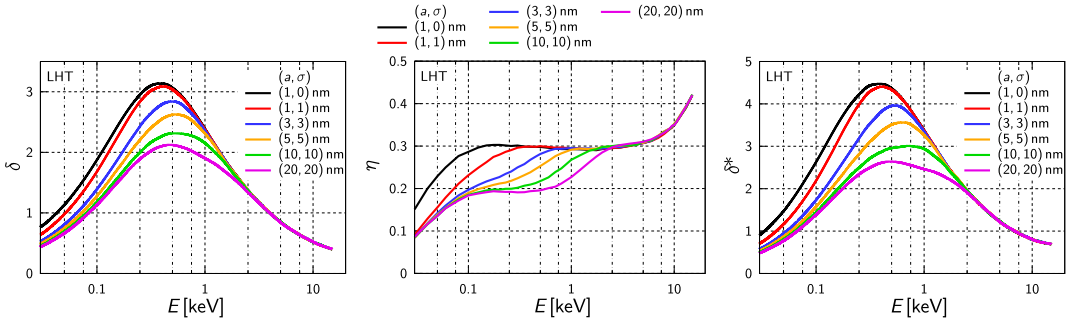

Figure 3. Demonstration of the surface roughness effect on the cube (in the same format as in Figure 1) for different a and σ values.

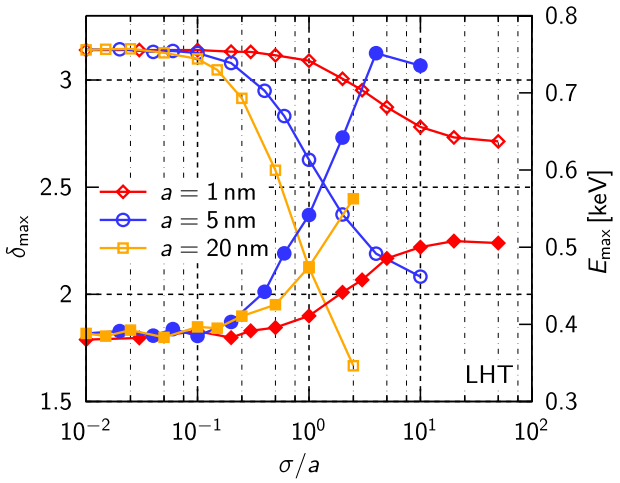

Figure 4. Dependence of δ_{max} (open symbols) and E_{max} (full symbols) as a function of the σ/a ratio.

are roughly self-similar, we can describe them by Equation (1) with the parameters δ_{max} and E_{max} depending on the σ/a ratio. These dependences are shown in Figure 4 where filled points stand for E_{max} and open symbols for δ_{max} for three values of the parameter a; they are distinguished by different colors. As can be seen in the figure, if the "height" of the hillocks on the surface does not exceed 10% of their base, secondary emission is not affected. Larger surface deformations lead to decreasing secondary emission yield, which can reach a factor of 2 and which is accompanied by a shift of E_{max} toward higher energies.

6. DISCUSSION AND CONCLUSION

We present model calculations that are primarily focused on applications in astrophysics. The first part of the paper deals with the influence of dust grain shape, and the results are relevant if these grains are immersed in a medium with a sufficiently high amount of energetic electrons. Such environments can be formed in many regions of space or in fusion devices. However, large temperatures in fusion devices would lead to intensive thermoemission (or even to grain evaporation) that would mask the effects of secondary emission.

By contrast, changes in secondary emission yield caused by surface roughness are relevant for all applications because they can be observed mainly in the low-energy range. Calculations were performed for a small cube but the method can be applied to objects with arbitrary shape and dimension, including large planar samples. The decrease in the secondary emission yield is remarkable even for surface roughness in the nanometer range. It can explain the deviations between values of the secondary emission yield published by different authors.

Calculations are demonstrated for a roughness with typical dimensions up to 20 nm because this is the range of the penetration depth of 1 keV electrons in different materials. If the roughness significantly exceeds the penetration depth, such a surface would instead be treated as a conglomerate of different bodies. This is the case for the Moon's surface in Halekas et al. (2009) and we will return to this topic below.

Probably the most appropriate experiment for a comparison with our model calculations is that of Horányi et al. (1998) when the authors compare two lunar dust simulants and samples of lunar soil collected by the *Apollo 17* mission. The measurement of the secondary emission yield used large monodisperse samples (≈30 μm) that were received by grinding larger pieces; thus, their shapes were irregular. Assuming that $E_{max} = 400$ eV, they found δ_{max}^{eff} in the range 3.1–3.4 for three investigated materials. Although the composition of LHT differs slightly from that of the materials investigated by Horányi et al. (1998), this narrow range allows us to compare their results with our calculations.

We have found (Figure 4) E_{max} varying between ≈370 and 720 eV and δ_{max} ($= \delta_{max}^{eff}$ in the notation of Horányi et al. 1998) between 1.8 and 3.2. Since they used large grains, the shape effects would be negligible in their range of primary energies (i.e., 10–100 eV) and the value of δ_{max} suggests relatively smooth surfaces that can be assumed if the used material exhibited a crystalline microstructure.

A comparison of our calculations with in situ observations of Halekas et al. (2009) is more difficult because their estimations of the secondary emission yield are based on distant observations of the secondary electrons escaping from a relatively large area of the highly charged lunar surface. A simple scaling of our results would provide a mean δ_{max} of about 1.5 or even lower but our calculations assume no electric field above the emitting surface. The vertical (perpendicular to the surface) component of the electric field would lead to a further δ_{max} increase, whereas the horizontal component resulting from the differential surface charging can turn already released electrons toward the surface, and thus it can further lower the electron current observed by spacecraft at large distances.

Summarizing the calculations of secondary emission yields of LHT grains with complex geometry and rough surface, we can conclude the following.

1. Not only the total grain mass and composition but also its shape can significantly affect the secondary emission yield.
2. Primary electrons start to penetrate micron and submicron non-spherical grains at lower energies than in the case of

equivalent spheres, but the rise of the scattered yield with the primary energy exhibits a more gradual slope.
3. The low-energy (i.e., below 200 eV) yields are the same for all grain geometries with smooth surfaces.
4. Rough surfaces scatter out a smaller number of primary electrons than smooth grains.
5. Both the height and width of the surface features are important for the determination of the resulting yields.
6. When the height-to-width ratio is higher than 0.1, the electrons become captured inside valleys and the resulting yield decreases.

Finally, we note that the grain shape and surface roughness are usually unknown and thus a direct comparison with experiments is difficult. On the other hand, the model provides limits on the uncertainty of the experimental data.

This work was supported partly by the research plan MSM 0021620860 financed by the Ministry of Education of the Czech Republic, and partly supported by the Czech Grant Agency under contracts 202/08/0063 and 209/11/1412.

REFERENCES

Bronstein, I. M., & Fraiman, B. S. 1969, Secondary Electron Emission (in Russian; Moskva: Nauka)
Draine, B., & Salpeter, E. 1979, ApJ, 231, 77
Dubus, A., Dehaes, J.-C., Ganachaud, J.-P., Hafni, A., & Cailler, M. 1993, Phys. Rev. B, 47, 11056
El Gomati, M. M., Walker, C. G. H., Assa'd, A. M. D., & Zadražil, M. 2008, Scanning, 30, 2
Halekas, J. S., Delory, G. T., Lin, R. P., Stubbs, T. J., & Farrell, W. M. 2009, Planet. Space Sci., 57, 78
Horányi, M., Walch, B., Robertson, S., & Alexander, D. 1998, J. Geophys. Res., 103, 8575
Hovington, P., Drouin, D., & Gauvin, R. 1997a, Scanning, 19, 1
Hovington, P., Drouin, D., Gauvin, R., Joy, D. C., & Evans, N. 1997b, Scanning, 19, 29
Joy, D. C. 1987, J. Microsc., 147, 51
Joy, D. C., & Luo, S. 1989, Scanning, 11, 176
Li, Y. G., Mao, S. F., Li, H. M., Xiao, S. M., & Ding, Z. J. 2008, J. Appl. Phys., 104, 064901
Mann, I., Pellinen-Wannberg, A., Murad, E., et al. 2011, Space Sci. Rev., 161, 1
Mott, N., & Massey, H. 1965, Theory of Atomic Collisions (New York: Oxford Univ. Press)
Němeček, Z., Pavlů, J., Šafránková, J., et al. 2011, ApJ, 738, 14
Pivi, M., King, F. K., Kirby, R. E., et al. 2008, J. Appl. Phys., 104, 104904
Renoud, R., Mady, F., Attard, C., Bigarré, J., & Ganachaud, J.-P. 2004, Phys. Status Solidi A, 201, 2119
Richterová, I., Beránek, M., Pavlů, J., Němeček, Z., & Šafránková, J. 2010, Phys. Rev. B, 81, 075406
Richterová, I., Němeček, Z., Beránek, M., Pavlů, J., & Šafránková, J. 2011a, in AIP Conf. Proc. 1397, Dusty/Complex Plasmas: Basic and Interdisciplinary Research (Melville, NY: AIP), 325
Richterová, I., Němeček, Z., Pavlů, J., Beránek, M., & Šafránková, J. 2011b, Icarus, 212, 367
Richterová, I., Němeček, Z., Šafránková, J., Pavlů, J., & Beránek, M. 2007, IEEE Trans. Plasma Sci., 35, 286
Richterová, I., Pavlů, J., Němeček, Z., & Šafránková, J. 2006a, Phys. Rev. B, 74, 235430
Richterová, I., Pavlů, J., Němeček, Z., Šafránková, J., & Žilavý, P. 2006b, Adv. Space Res., 38, 2551
Shimizu, R., & Ding, Z.-J. 1992, Rep. Prog. Phys., 55, 487
Sternglass, E. 1957, Theory of Secondary Electron Emission under Electron Bombardment, Scientific Paper 6-94410-2-P9, Westinghouse Research Laboratories, Pittsburgh 35
Walker, C. G. H., El Gomati, M. M., Assa'd, A. M. D., & Zadražil, M. 2008, Scanning, 30, 365
Watts, C., Gilmore, M., & Schamiloglu, E. 2011, IEEE Trans. Plasma Sci., 39, 836
Willis, R. F., Anderegg, M., Feuerbacher, B., & Fitton, B. 1973, in Astrophysics and Space Science Library, Vol. 37, Photon and Particle Interactions with Surfaces in Space, ed. R. J. L. Grard (Dordrecht: Reidel), 389

H. Richterová et al. [2016]

Richterová, I., Němeček, Z., Pavlů, J., Šafránková, J., Vaverka, J., Secondary emission from clusters composed of spherical grains. *IEEE Trans. Plasma Sci.* 44 (2): in print, 2016.

Secondary Emission From Clusters Composed of Spherical Grains

Ivana Richterová, Zdeněk Němeček, Jiří Pavlů, Jana Šafránková, and Jakub Vaverka

***Abstract*— Dust grains or their clusters can be frequently found in many space environments—interstellar clouds, atmospheres of planets, tails of comets, or planetary rings are only typical examples. Space dust grains are formed by various processes and their shapes are complex. These grains are exposed to electrons with different energies, and thus, they can acquire positive or negative charge during this interaction. We present a systematic study of well-defined systems—clusters consisting of different numbers of small spherical (1 μm) grains and such objects can be considered as examples of real irregularly shaped space grains. The charges acquired by investigated objects as well as their secondary emission yields are calculated using the secondary emission model. We have found that: 1) the charge and surface potential of clusters exposed to the electron beam are influenced by the number of grains and by their geometry within a particular cluster; 2) the model results are in an excellent agreement with the experiment; and 3) there is a large difference between charging of a cluster levitating in the free space and that attached to a planar surface. The calculation provides a reduction of the secondary electron emission yield of the surface covered by dust clusters by a factor of 1.5 with respect to the yield of a smooth surface.**

***Index Terms*— Dust charging, dusty plasmas, secondary electron emission.**

I. Introduction

DUST as a component of the universe plays an important role in the dynamics and chemistry of the interstellar and intergalactic medium and in the formation of stars and planets [1]. Many space missions such as Ulysses, Cassini, and Galileo [2]–[4] probed the composition, size distribution, and characteristics of interstellar and interplanetary dust grains that carried information on an origin and evolution of particular bodies and on environments where these grains originate. Dust grains in the interplanetary space are a subject of various charging processes [5]. Grains are exposed to solar ultraviolet (UV) and X-ray radiations that excite photoelectrons from the surface of the dust grain and, at the same time, electrons and ions of the solar wind and/or magnetospheric origin constitute negative and positive currents falling onto the grain. Moreover, in environments where high-energy electrons are present, the secondary electron emission becomes nonnegligible or even dominating charging process [6]–[8]. Each of the mentioned charging currents depends on the electrostatic potential of the grain surface with respect to the surrounding plasma.

Charging of space dust grains has been examined [7]–[12] but most of these works assumes a simple geometry of dust grains, usually a compact sphere. However, grains in the space are formed by processes like nucleation, condensation, coagulation, and destruction of larger bodies, and thus, the grains gain complex structures and shapes. The data and/or samples collected in the space have shown porous fluffy structures that can be frequently found among interplanetary dust grains, in cometary bodies, and maybe also among interstellar dust grains [13]–[15]. They can consist of many micrometer-sized aggregates with submicrometer-sized subunits [16]–[18].

The charging of aggregates of dust grains has been studied recently in both laboratory and astrophysical environments [19]–[21]. These results have shown that aggregates tend to acquire a more charge when compared with spherical grains of the same mass due to their porous/fluffy structure, and that the charge of aggregates has a significant effect on subsequent dust evolution. A detailed study characterizing the charge on aggregates based on structural characteristics such as the compactness factor was performed in [22] using a 3-D model that takes into account three different charging processes: 1) ion and electron currents; 2) secondary electron emission; and 3) UV radiation. They show that the equilibrium charge on aggregates can differ from spherical grains with the same mass but that the charge can be estimated for a given environment based on structural characteristics of the grain. The small particle effect typical of the secondary electron emission is also found to be important for determining the charge of micrometer-sized aggregates consisting of nanosized particles.

Pavlů *et al.* [23], [24] experimentally investigated SiO_2 spherical grains in various configurations of clusters consisting of different numbers of such grains. The systematic study led to a suggestion that the charge acquired by an investigated object (grain or cluster of grains) by the particle beam of a given energy depends not only on grain macroscopic characteristics but also on a configuration of the grains in a particular cluster.

In this paper, we use another approach, in which we calculate the charge and surface potential of clusters of different geometries by a well proven Monte Carlo model of the

Manuscript received August 28, 2015; revised November 9, 2015; accepted December 12, 2015. This work was supported by the Czech Science Foundation under Grant P209/11/1412 and Grant P209/13/25185P.

The authors are with the Faculty of Mathematics and Physics, Charles University in Prague, Prague 121 16, Czech Republic (e-mail: ivana.richterova@mff.cuni.cz; zdenek.nemecek@mff.cuni.cz; jiri.pavlu@mff.cuni.cz; jana.safrankova@mff.cuni.cz; jakubvaverka@gmail.com).

Color versions of one or more of the figures in this paper are available online at http://ieeexplore.ieee.org.

Digital Object Identifier 10.1109/TPS.2015.2509238

secondary electron emission [25], [26] and compare the numerical results with experimentally determined surface potentials of different cluster configurations. Our calculations confirmed Pavlů *et al.*'s [23], [24] suggestions that the secondary emission yield and its dependence on the primary electron energy differ from those determined for planar surfaces as well as for compact spherical grains. Further calculations revealed a significant difference between charging of the cluster levitating in the free space and the same cluster attached to a planar substrate. We are showing a reduction of the secondary electron emission yield of a surface due to dust cover, and we discuss this effect in view of *in situ* measurements of the potential of the lunar surface.

II. Model of the Secondary Electron Emission

The model of Richterová *et al.* [25], [26] calculates the charge accumulated in the grain as a function of the primary electron beam energy as well as the energetic dependence of the secondary and backscattered yields. Briefly, the model follows trajectories of primary electrons inside the spherical grain of a given composition described by known material constants. The primary electrons are scattered by collisions with the grain atoms, and the deflection angle is generated according to energy-dependent Mott differential cross sections [27]. Note that these cross sections are calculated in two dimensions and provide only the total deflection angle. Since the model is 3-D, we use this angle as a polar angle and generate the azimuthal angle as a random number in the range 0–2π. Continuous monitoring of each primary electron allows us to investigate size and shape effects reported for micrometer- and submicrometer-sized grains. Since we neglect possible quantum effects, grains should have at least 10 000 particles, i.e., be larger than about 10 nm. A summary of the model principles can be found in the Appendix. Approximations used in the model limit the validity of both the secondary (δ) and scattered (η) yields down to about 50 eV of the primary energy. Nevertheless, their sum (the grain net current) can be determined reliably up to 15 eV. At lower energies, the secondary emission process is dominated by a surface plasmon decay that is omitted in the model.

A number of secondary electrons leaving the positively charged surface is given by their energy distribution that is expected to be Maxwellian with the temperature of 3 eV that fits well the experimental data. The model expects the grain levitating in the space and bombarded by monoenergetic electrons from all directions. Note here that in the experimental apparatus, the grain is bombarded by a parallel beam but the grain rotates, thus these two situations can be considered as equivalent.

The model was already applied to nonspherical grains and grains with defined surface roughness in [28]. Their calculations used the Lunar Highlands Type NU-LHT-2M simulant as a grain material and revealed that nonsphericity of grains leads to a rise of the secondary electron emission yield, whereas the surface roughness causes its decrease. Moreover, these effects depend on the primary electron beam energy; the shape influence is prominent for high primary energies, whereas the surface roughness predominantly affects the yield at the low-energy range.

III. Model Results and Their Comparison With the Experiment

Pavlů *et al.* [24] presented investigations of charging of monodisperse silica spheres with 1 μm of diameter that tended to create clusters composed of different numbers of spheres. The clusters were bombarded by the electron beam of a tunable energy (in the range from 50 eV to 10 keV), and the charge-to-mass ratio versus beam energy profiles were determined. The ratios (for the same beam energy) differed by an order of magnitude, and this difference was attributed to variations of grain numbers in investigated clusters. Under assumptions that the peak of the grain surface potential at low energies ($\approx$400–500 eV) would be given by the energy distribution of secondary electrons that does not depend on the grain size or a number of the grains in the cluster, the secondary electron emission yield and the number of grains in the cluster were determined.

In order to check this hypothesis, we carry out numerical simulations on silica clusters composed of four grains with different topologies that were used in the mentioned experiment [24]. Fig. 1(a)–(c) presents the results of calculations as dependencies of the true secondary electron emission yield, backscattered yield, and cluster surface potential, respectively, on the energy of primary electrons. These profiles were calculated for a single sphere (red lines), for four spheres in a line (vivid orange lines), and for four spheres creating a compact cluster (blue lines). Fig. 1(a) shows that the maximum of the true secondary electron emission yield (δ) of clusters is lower than that of a single grain and it further decreases with increasing compactness of clusters. On the other hand, all profiles tend to be identical in the high-energy range.

By contrast, the difference between backscattered yields [η, Fig. 1(b)] of clusters with different configurations increases with the energy of primary electrons. The yield reaches unity for all clusters at about 14 keV of the primary energy. Although a difference among yields computed for both geometries seems to be small, it results in relatively large differences between cluster surface potentials shown in Fig. 1(c). However, it should be noted that the potentials are calculated assuming the Maxwellian distribution of secondary electrons. This assumption is valid for the true secondary electrons, but a portion of scattered primary electrons leaving the grain becomes comparable with the number of true secondary electrons at energies above $\approx$8 keV. Taking both populations together, the energy distribution of all electrons attempting to leave the grain has the Maxwellian core with a significantly enhanced tail. The distribution leads to large potentials, and the effect will be more pronounced for individual grains or their linear configuration. This enhancement of the grain potential was discussed, for example, in [24], and depends on the size of the grain, its material, and the beam energy. For a sample used in the present study, the calculated potentials up to $\approx$10 kV of primary energy are realistic, but the calculated values represent a lower limit of the potentials that would be measured.

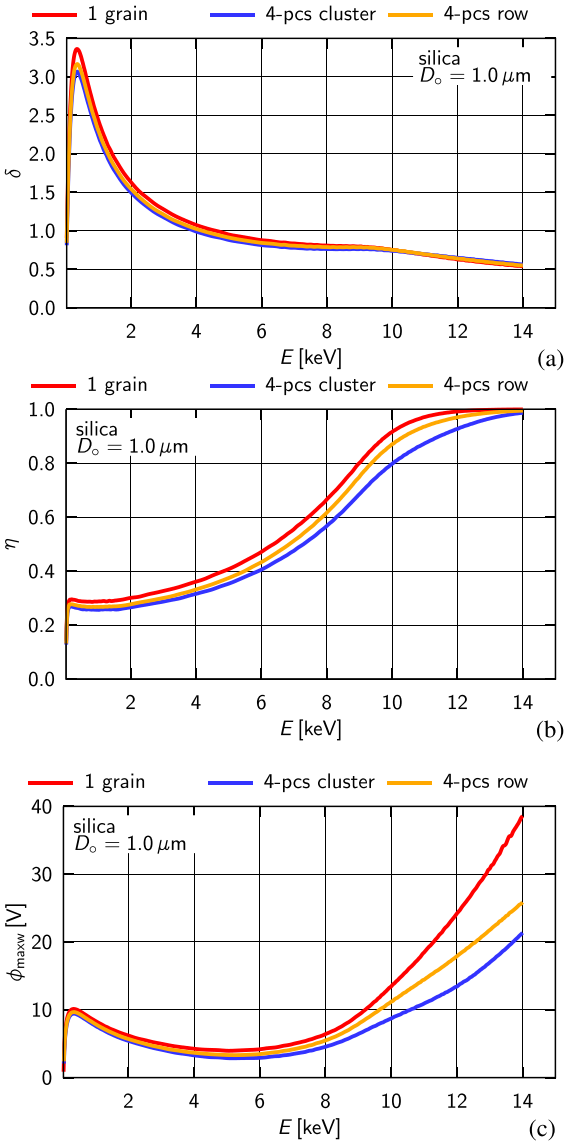

Fig. 1. Modeled (a) true and (b) backscattered secondary electron emission yields and (c) surface potentials for one grain (red line) and four grains in a line (vivid orange line), and in a compact configuration (blue line). The diameter of all grains is 1 μm.

The most interesting behavior can be observed in the range of small energies (hundreds of electronvolts). Although it is generally expected that the surface potential does not depend on a shape of the object, the model predicts about a 5% decrease of the potential maximum for the compact cluster with respect to the single sphere. We have checked this effect by computations of the potentials for clusters consisting of two and six spheres and found 3% and 8% of the potential decrease, respectively.

This effect requires a slight modification of results of the experimental analysis in [24]. The experiment provided a value of the grain charge, and the potential was calculated as a ratio between the charge and capacitance of the object. The capacitance of a simple grain was computed in the

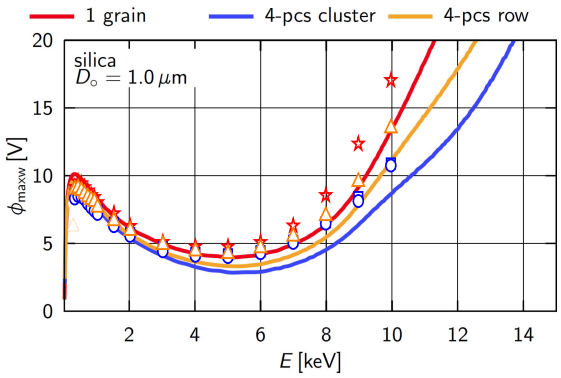

Fig. 2. Comparison of measured (different points) and modeled (lines) surface potentials for one grain (red stars and line), for four grains in a line (vivid orange triangles and line), and for four grains in a compact configuration (blue circles, rectangles, and line). The measured potentials were computed from the specific charge. Note that a detailed description of the experimental setup as well as the measurement procedure has been presented in [24] and [29]–[32].

spherical approximation but it could not be determined for clusters of unknown geometry. For this reason, the potentials of clusters were estimated under an assumption that a value of the potential in the low-energy range does not depend on the size or shape of the cluster and was set to be equal to the potential of the single grain. We used the results of modeling and renormalized the data for clusters. The resulting surface potential profiles for a configuration of clusters analyzed in Fig. 1 are shown in Fig. 2 by the points. For an easier comparison, the modeled potentials are added and plotted with the lines of corresponding colors.

One can see that the experimental and model data agree very well, even quantitatively. A detailed analysis shows a small difference in the high-energy range because, for example, the surface potential of a linear configuration of grains corresponds rather to that of a single grain in the model data. However, the model expected grains of 1-μm diameters, but the real grains can be smaller and about a 50-nm uncertainty in the size of grains can explain the observed variations. Another slight disagreement between calculations and experiment can be found in the middle-energy range (3–6 keV) because the experiment provides a slightly higher potential than the model, but this part of the potential profile strongly depends on the distribution of secondary electrons that is not purely Maxwellian [33] as we discussed above.

An illustration of the mechanisms of changes of the surface potential with a number of grains in the cluster in different energy ranges is shown in Fig. 3. The sketch shows three grains in a compact configuration but the discussion can be applied on other numbers of grains as well as on other geometries.

Low-energy (tens of electronvolts) electrons penetrate only into a very thin surface layer of the grains that are directly exposed to the beam electrons, they excite the electrons of the bulk material, and a part of them can escape as true secondary electrons. The primary electrons are either captured inside the grain or they are scattered back against the beam and do not affect other grains in the cluster. This situation is

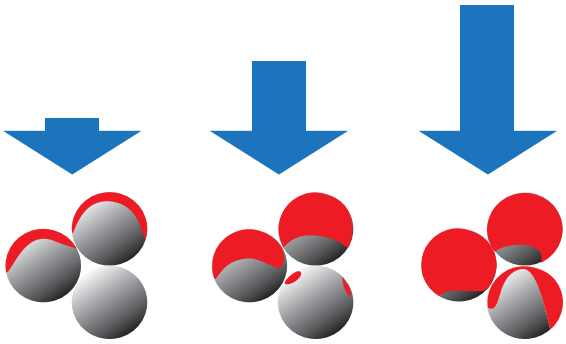

Fig. 3. Sketch of the interaction of the dust grain with the primary electron beam. The length of the arrows corresponds to a beam energy value (low energy—left part), the red color shows the grain area affected by the electron beam under corresponding energy, and the shadow color presents the shielding areas.

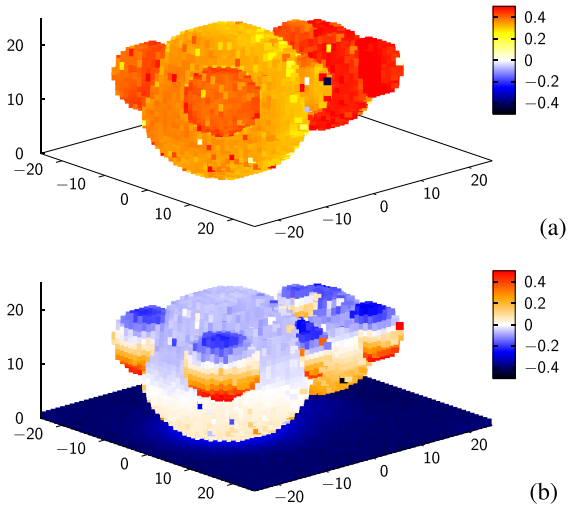

Fig. 4. (a) Surface charge density of the teddy-bear shaped cluster composed from size-different spherical (from 1 to 0.1 μm in diameter) grains levitating above the surface and bombarded by 10-keV electrons with a random distribution of directions. (b) Same cluster lying on the surface layer with the same material. Units of a color scale are $N_{\rm esc}/N_{\rm imp} - 1$, where $N_{\rm esc}$ is the number of escaping electrons and $N_{\rm imp}$ is the number of impinging electrons.

similar to a single grain, and thus, the potentials of a single grain and a cluster would be the same. An increasing energy of primary electrons (hundreds of eletronvolts) increases the volume of excited electrons within the grain, and a part of the backscattered primary electrons leaving one grain can impact other grains. The energies of these electrons are generally low, and thus, they do not contribute significantly to a number of true secondary electrons but they are captured within the cluster. It leads to a decrease of the backscattered yield in a comparison with the single grain. Since this decrease is larger than their contribution to the yield of true secondary electrons (note that a majority of the electrons emitted inside the cluster are captured by another grain), both the total yield and the grain potential decrease. This effect is responsible for the decrease of the potential maximum observed in the model.

A further rise of the primary energy sharply increases a number of backscattered primary electrons as well as their energy. The equilibrium potential of the cluster is given by the energy distribution of these electrons. Since a part of them leaving one grain is captured by another, the yield and surface potential are lower than those of a single grain.

Last but not least, we should stress out that the calculations of the grain charging expected the tightly contacted conducting grains despite their material. In the experiment, the grains are bombarded by an intensive beam of energetic electrons that excite the material electrons from valence to conducting bands and we think that this assumption (that in turn leads to a well-defined surface potential) is fully justified.

IV. Influence of the Surface

A very good agreement of model calculations with the experimental results allows us to investigate more complicated structures that could be closer to a real situation encountered in the free space (levitating clusters) or at the surfaces of larger bodies like the Moon (clusters creating a surface layer). Since a shape of the clusters can be arbitrary, we composed it from spheres of different diameters (the largest sphere of 1-μm diameter and the smallest sphere of 0.1-μm diameter). As a modeled cluster, we have chosen a large composition of grains that resembles a teddy bear. Such a shape can illustrate various features like shielding of different areas of the surface or a capture of electrons emitted from a part of the cluster by another part. The cluster composition corresponds to the Lunar Highlands Type NU-LHT-2M simulant. However, the assumption on the cluster conductivity that was used in previous calculations should be abandoned in simulations of the charging of clusters at or above the lunar surface because the expected primary electron number flux does not exceed 1 $\mu{\rm m}^{-2}{\rm s}^{-1}$, and it is clearly not enough to excite a sufficient number of bulk electrons.

Since the secondary emission yield depends on the surface curvature, each part of the cluster surface should be treated individually and the only connection between different parts is mediated by primary electrons that can enter the grain in a particular place but leave it at another place. The surface potential is not well defined under such conditions, and thus, a charge balance along the surface shown in Fig. 4 was computed for $\phi = 0$. The spatial axes are calibrated in hundreds of nanometers, and the color scales show the surface charge normalized to the charge of primary electrons impinging on a particular grain location. The units of the color scale are thus $(N_{\rm esc}/N_{\rm imp} - 1)$. This value is positive if a number of escaping electrons $N_{\rm esc}$ exceeds the number of impinging electrons $N_{\rm imp}$, and such a part of the surface will be charged positively.

The cluster levitating in the free space and bombarded by 10-keV electrons from all directions is shown in Fig. 4(a). As it could be expected for a small object in the free space, all parts of the cluster are charged positively regardless of their shape and the charge density increases with decreasing dimensions of the particular part of the cluster. Nevertheless, the shielding effects modify this simple estimation.

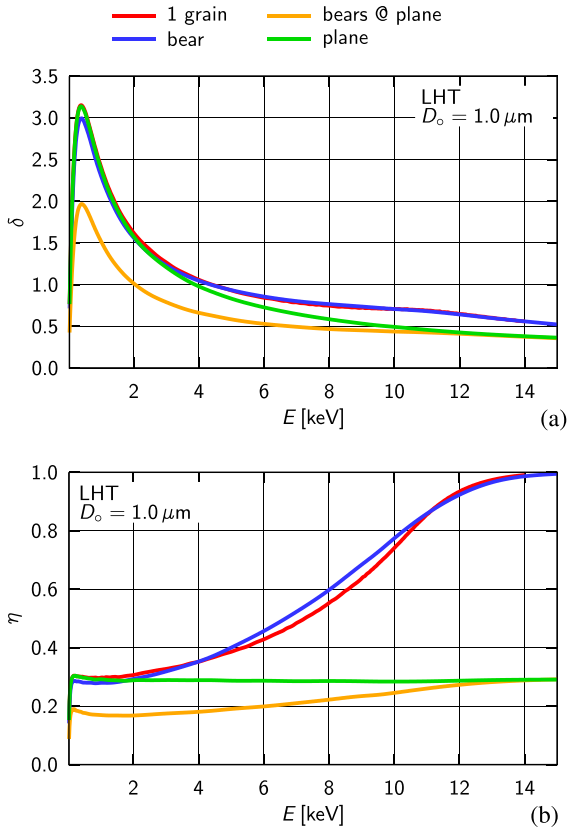

Fig. 5. Modeled (a) true and (b) backscattered secondary electron emission yields for teddy bear-shaped clusters in the free space (blue line) and lying on the surface (vivid orange line). The single grain (red line) and the planar surface (green line) are given for a comparison.

On the other hand, for clusters lying on the solid surface, the picture differs as it can be seen in Fig. 4(b). The panel shows one unit of the periodic mesh that is isotropically illuminated from the top half-space. It means that side parts of the cluster are partially shadowed by neighboring clusters. The areas with the blue color are acceptors of electrons, whereas the emission prevails at vivid orange or red parts of the cluster. One can note a large negative charge of the background plane that is caused by a very low escape probability of secondary electrons. The top part of the cluster is either without the charge or charged slightly negative. The reason is that 10-keV primary electrons penetrate deeply into clusters and the probability of escaping of excited electrons is small. This effect can be clearly seen on paws of the bear. They are illuminated mainly from the top, but their path prior to the first excitation is comparable to the diameter of paws. A majority of secondary electrons thus leave from the bottom part of paws and this part is charged positively. A similar effect can be seen on the bear head, but the bottom part of the body is about neutral because its diameter is larger and its charge is more influenced by secondary electrons from the underlying planar surface. Since we expect an insulating material and do not allow the transfer of a charge among different parts of the cluster, they will attain different potentials, which will in turn influence the trajectories of low-energy secondary electrons, and thus, the whole charging process becomes much more complicated and it cannot be modeled.

The purpose of Fig. 4 is to illustrate difficulties connected with an exact description of the charging of dust grain clusters on the scale of nanometers. Nevertheless, important parameters like the secondary electron emission yield can be obtained for such complex cluster. Fig. 5 presents the components of the secondary emission yield for the two cluster positions shown in Fig. 4. Fig. 5 compares true and scattered secondary emission yields with the values computed for a smooth plane and for a sphere levitating in the free space. This sphere is equal to the basic sphere in the cluster (1 μm).

The profiles of both yield components (δ and η) for a single sphere (red lines), levitating cluster (blue lines), and planar smooth surface (green lines) are nearly identical in the low- and middle-energy ranges (up to $\approx$3 keV), but the yields of the surface covered with clusters (vivid orange lines) are reduced by a factor of $\approx$1.5. This reduction factor decreases with the energy and the yields computed from the smooth surface and the surface covered by clusters become about equal for energies above 10 keV. However, the levitating cluster exhibits larger yields than all other investigated topologies in the full energy range.

The decrease of the yield of the dust covering the surface in a comparison with the smooth surface was already suggested in [34] when they explained the observations of electron energy spectra above the nightside lunar surface by the Lunar Prospector mission. However, the authors expected a reduction of the yield by a factor of 3, whereas our calculations lead to a factor lower than 2. Such a factor is insufficient for explanations of the observed negative surface potentials on the lunar nightside in the magnetosphere [35], and thus we will return to this point in further works.

V. Conclusion

The Monte Carlo model of the secondary electron emission applied on the clusters of four grains shows that a compact configuration of clusters would exhibit the lower secondary electron emission yield (both true and backscattered components) due to shielding of a part of emitted electrons by neighboring grains in the cluster. This confirms the Pavlů *et al.*'s [24] suggestion that clusters composed of identical dust grains are generally charged to lower potentials than a single grain, and their surface potential decreases with the number of grains in the cluster. Fig. 3 suggests that the surface potential of a compact cluster would be similar to a single grain with a diameter lower than but close to a convex envelope of the whole cluster regardless of the sizes of particular grains creating the cluster.

Calculations of charging of clusters from the Lunar Highlands Type NU-LHT-2M simulant attached to a surface revealed the reduction in both components of the secondary electron emission yield by a factor of $\approx$1.5 in a comparison with the planar surface composed of the same material. This reduction seems to be too small for explanations of the observed potentials of the lunar surface in the earth's magnetosphere.

APPENDIX
MODEL PRINCIPLES

As it was noted in Section II, the secondary electron emission model development was already described in [25], [26], and [28], but we are repeating its principles here for a better orientation. The model uses a Monte Carlo technique to trace trajectories of primary electrons inside the grain. The primary electron excites secondary electrons along its path but these electrons are treated in a probabilistic way. The physical principles included in the model of the secondary electron emission from small bodies can be briefly summed up as follows.

1) The grain material is characterized by constants like the atomic or nucleon numbers or the mass density (note that different crystalline forms of the same material can differ in their mass densities, e.g., diamond versus graphite). Since no detailed atomic or electronic structure is included, the modeled grain should consist of sufficient numbers of atoms.
2) For a description of trajectories of the primary electron inside the matter, a single scattering model according to [36] is used. A primary electron moves along straight lines between collisions. Since almost all nonnegligible deflections are caused by elastic electron–atom collisions above several hundreds of electronvolts [37], Mott radial elastic cross sections [27], namely, the values computed in [38] are used.
3) Primary electron loses the energy continuously along its path according to the modified Bethe stopping power equation. This modified equation is calculated omitting inner electron shells that cannot participate in inelastic collisions at the lowest energies [26]

$$\frac{dE}{ds} \sim -\frac{\varrho}{N}\frac{A_{\text{eff}}(E)}{E}\ln\frac{1.166E}{J_{\text{eff}}(E)} \tag{1}$$

   where E is an actual electron energy, s is a traveled path, ϱ is a mass density, and N is a nucleon number. The effective number of atom electrons $A_{\text{eff}}(E)$ and the effective mean ionization potential $J_{\text{eff}}(E)$ can be derived from the energy loss function that represents a dielectric response of material to a passage of charged particles or electromagnetic radiation.
4) A whole deposited energy is spent to excitations of secondary electrons. These electrons are excited at the place where the energy loss reaches the mean excitation energy. Excited electrons then behave independently on the primary electron energy or the direction of its motion in the matter.
5) The probability that the excited electron reaches a grain surface decreases exponentially with a distance from the surface. The mean free diffusion path of these electrons is of the order of a lattice constant for metals and much longer for insulators. This is the only parameter that we determine by a comparison with experimental data. The resulting probability of the escape of excited electrons is then calculated by integration of the probability around a given part of the surface. This can be the whole surface for the determination of δ or η of the cluster but only a part of the surface for the description of the local charging effect like that in Fig. 4.
6) The secondary electron energy spectrum is key for a calculation of the equilibrium grain potential. We suppose that this spectrum does not depend on the beam energy, and thus, a random energy in accordance with a chosen distribution is generated for each secondary electron. This electron escapes from the grain when this energy is larger than the actual grain potential. The present calculations use the Maxwellian distribution parameterized by the temperature. This approach does not consider Auger electrons or backscattered primary electrons. These populations are very minor under standard conditions, but they can be important in the case of small grains bombarded by energetic electrons. These electrons can enhance the grain potential in laboratory conditions up to one half of the primary energy [24]. However, this effect can be seen in the experiments with monoenergetic electron beams but not in the space because the low-energy electrons from the ambient plasma would decrease this potential. For this reason, the potentials calculated with the Maxwellian distribution of secondary electrons are more realistic for space applications.

ACKNOWLEDGMENT

The authors would like to thank Prof. D. Vítek for a teddy bear inspiration.

REFERENCES

[1] A. P. Jones, "The lifecycle of interstellar dust," in *From Stardust to Planetesimals* (Astronomical Society of the Pacific Conference Series), vol. 122, Y. J. Pendleton and A. G. G. M. Tielens, Eds. San Francisco, CA, USA: Astronomical Society of the Pacific, 1997, p. 97–106.
[2] N. Altobelli *et al.*, "Cassini between Venus and Earth: Detection of interstellar dust," *J. Geophys. Res.*, vol. 108, no. A10, 2003, Art. ID 8032.
[3] H. Krüger *et al.*, "Three years of Ulysses dust data: 2005 to 2007," *Planetary Space Sci.*, vol. 58, pp. 951–964, Jun. 2010.
[4] H. Krüger *et al.*, "Galileo dust data from the jovian system: 2000 to 2003," *Planetary Space Sci.*, vol. 58, pp. 965–993, Jun. 2010.
[5] D. A. Mendis and M. Rosenberg, "Cosmic dusty plasma," *Annu. Rev. Astron. Astrophys.*, vol. 32, pp. 419–463, Sep. 1994.
[6] E. C. Whipple, "Potentials of surfaces in space," *Rep. Prog. Phys.*, vol. 44, no. 11, pp. 1197–1250, 1981.
[7] T. Mukai, "On the charge distribution of interplanetary grains," *Astron. Astrophys.*, vol. 99, pp. 1–6, Jun. 1981.
[8] H. Kimura and I. Mann, "The electric charging of interstellar dust in the solar system and consequences for its dynamics," *Astrophys. J.*, vol. 499, no. 1, pp. 454–462, May 1998.
[9] V. W. Chow, D. A. Mendis, and M. Rosenberg, "Role of grain size and particle velocity distribution in secondary electron emission in space plasmas," *J. Geophys. Res.*, vol. 98, no. A11, pp. 19065–19076, Nov. 1993.
[10] B. Feuerbacher, R. F. Willis, and B. Fitton, "Electrostatic potential of interstellar grains," *Astrophys. J.*, vol. 181, pp. 101–114, Apr. 1973.
[11] B. T. Draine and E. E. Salpeter, "On the physics of dust grains in hot gas," *Astrophys. J.*, vol. 231, no. 1, pp. 77–94, Jul. 1979.
[12] B. Walch, M. Horányi, and S. Robertson, "Charging of dust grains in plasma with energetic electrons," *Phys. Rev. Lett.*, vol. 75, pp. 838–841, Jul. 1995.
[13] A. P. Jones, "Modelling interstellar extinction—I. Porous grains," *Monthly Notices Roy. Astron. Soc.*, vol. 234, pp. 209–218, Sep. 1988.
[14] J. W. Woo, G. W. Clark, C. S. R. Day, F. Nagase, and T. Takeshima, "ASCA measurements of the grain-scattered X-ray halos of eclipsing massive X-ray binaries: VELA X-1 and Centaurus X-3," *Astrophys. J. Lett.*, vol. 436, pp. L5–L8, Nov. 1994.

[15] G. Wurm, H. Relke, and J. Dorschner, "Experimental study of light scattering by large dust aggregates consisting of micron-sized SiO_2 monospheres," *Astrophys. J.*, vol. 595, pp. 891–899, Oct. 2003.
[16] D. E. Brownlee, L. Pilachowski, E. Olszewski, and P. W. Hodge, "Analysis of interplanetary dust collections," in *Proc. Symp. Solid Particles Solar Syst.*, vol. 90. 1980, pp. 333–341.
[17] J. M. Greenberg and J. I. Hage, "From interstellar dust to comets—A unification of observational constraints," *Astrophys. J.*, vol. 361, pp. 260–274, Sep. 1990.
[18] Z. W. Hu and R. Winarski, "Unlocking the nanoscale fluffy structure in interplanetary dust with hard X-ray phase contrast nanotomography," in *Proc. 42nd Lunar Planetary Sci. Conf.*, vol. 42. Mar. 2011, p. 2662.
[19] R. Wiese, V. Sushkov, H. Kersten, V. R. Ikkurthi, R. Schneider, and R. Hippler, "Behavior of a porous particle in a radiofrequency plasma under pulsed argon ion beam bombardment," *New J. Phys.*, vol. 12, no. 3, p. 033036, Mar. 2010.
[20] S. Okuzumi, H. Tanaka, T. Takeuchi, and M.-A. Sakagami, "Electrostatic barrier against dust growth in protoplanetary disks. II. Measuring the size of the 'frozen' zone," *Astrophys. J.*, vol. 731, p. 96, Apr. 2011.
[21] M. Ilgner, "Grain charging in protoplanetary discs," *Astron. Astrophys.*, vol. 538, p. A124, Feb. 2012.
[22] Q. Ma, L. S. Matthews, V. Land, and T. W. Hyde, "Charging of aggregate grains in astrophysical environments," *Astrophys. J.*, vol. 763, no. 2, p. 77, 2013.
[23] J. Pavlů, J. Šafránková, Z. Němeček, and A. Velyhan, "Charging properties of dust grain clusters," in *Dusty Plasmas in the New Millennium* (AIP Conference Proceedings), vol. 649, R. Bharuthram, M. A. Hellberg, P. K. Shukla, and F. Verheest, Eds. Melville, NY, USA: AIP, 2002, pp. 382–385.
[24] J. Pavlů, I. Richterová, Z. Němeček, J. Šafránková, and I. Čermák, "Interaction between single dust grains and ions or electrons: Laboratory measurements and their consequences for the dust dynamics," *Faraday Discussions*, vol. 137, pp. 139–155, 2008.
[25] I. Richterová, J. Pavlů, Z. Němeček, and J. Šafránková, "Model of secondary emission and its application on the charging of gold dust grains," *Phys. Rev. B*, vol. 74, no. 23, p. 235430, 2006.
[26] I. Richterová, M. Beránek, J. Pavlů, Z. Němeček, and J. Šafránková, "Electrons scattered inside small dust grains of various materials," *Phys. Rev. B*, vol. 81, no. 7, p. 075406, 2010.
[27] N. F. Mott and H. S. W. Massey, *Theory of Atomic Collisions*. New York, NY, USA: Oxford Univ. Press, 1965.
[28] I. Richterová, Z. Němeček, M. Beránek, J. Šafránková, and J. Pavlů, "Secondary emission from non-spherical dust grains with rough surfaces: Application to lunar dust," *Astrophys. J.*, vol. 761, no. 2, p. 108, 2012.
[29] I. Čermák, "Laboruntersuchung elektrischer Aufladung kleiner Staubteilchen," Ph.D. dissertation, Naturwissenschaftlich-Mathematischen Gesamtfakultät, Ruprecht-Karls-Universität, Heidelberg, Germany, Nov. 1994.
[30] P. Žilavý, Z. Sternovský, I. Čermák, Z. Němeček, and J. Šafránková, "Surface potential of small particles charged by the medium-energy electron beam," *Vacuum*, vol. 50, nos. 1–2, pp. 139–142, 1998.
[31] J. Pavlů *et al.*, "Mass-loss rate for MF resin microspheres," *IEEE Trans. Plasma Sci.*, vol. 32, no. 2, pp. 704–708, Apr. 2004.
[32] Z. Němeček *et al.*, "Lunar dust grain charging by electron impact: Dependence of the surface potential on the grain size," *Astrophys. J.*, vol. 738, no. 1, p. 14, 2011.
[33] A. Velyhan, "Interaction of charged particle beams with dust grains," *Planetary Space Sci.*, vol. 56, no. 7, pp. 1054–1056, 2008.
[34] J. S. Halekas, G. T. Delory, R. P. Lin, T. J. Stubbs, and W. M. Farrell, "Lunar Prospector measurements of secondary electron emission from lunar regolith," *Planetary Space Sci.*, vol. 57, no. 1, pp. 78–82, Jan. 2009.
[35] J. Vaverka, I. Richterová, J. Pavlů, J. Šafránková, and Z. Němeček, "Lunar surface and dust grain potentials during the earth's magnetosphere crossing," *Astrophys. J.*, submitted.
[36] P. Hovington, D. Drouin, and R. Gauvin, "CASINO: A new Monte Carlo code in C language for electron beam interaction—Part I: Description of the program," *Scanning*, vol. 19, no. 1, pp. 1–14, Jan. 1997.
[37] R. F. Egerton, *Electron Energy-Loss Spectroscopy in the Electron Microscope*. New York, NY, USA: Springer, 1996.
[38] Z. Czyżewski, D. O. MacCallum, A. Romig, and D. C. Joy, "Calculations of Mott scattering cross section," *J. Appl. Phys.*, vol. 68, no. 7, pp. 3066–3072, Oct. 1990.

Ivana Richterová was born in Český Brod, Czech Republic, in 1979. She received the M.S. and Ph.D. degrees from Charles University in Prague, Prague, Czech Republic, in 2003 and 2012, respectively.

She is currently a Senior Assistant with the Space Physics Laboratory, Department of Surface and Plasma Science, Faculty of Mathematics and Physics, Charles University in Prague. Her research is devoted to the laboratory investigation and modeling of elementary charging processes on dust grains.

Zdeněk Němeček was born in Prague, Czech Republic, in 1947. He received the M.S., Ph.D., and D.Sc. degrees from Charles University in Prague, Prague, in 1971, 1982, and 1996, respectively.

He has held several leading positions with the Faculty of Mathematics and Physics, Charles University in Prague, since 1971. His current research interests include the solar wind interaction with the earth's magnetosphere and the laboratory simulations of plasma processes.

Jiří Pavlů was born in Pardubice, Czech Republic, in 1977. He received the M.S. and Ph.D. degrees from Charles University in Prague, Prague, Czech Republic, in 2001 and 2005, respectively.

He is currently a Senior Assistant with the Space Physics Laboratory, Department of Surface and Plasma Science, Faculty of Mathematics and Physics, Charles University in Prague. His current research interests include the laboratory investigations of elementary processes on dust grains induced by electron, ion, and photon irradiations.

Jana Šafránková was born in Teplice, Czech Republic, in 1947. She received the M.S., Ph.D., and D.Sc. degrees from Charles University in Prague, Prague, Czech Republic, in 1972, 1982, and 1996, respectively.

She has held several positions with the Faculty of Mathematics and Physics, Charles University in Prague, where she is currently the Head of the Space Physics Laboratory. Her current research interests include the solar wind and laboratory simulations of elementary processes in dusty plasmas.

Jakub Vaverka was born in Prague, Czech Republic, in 1983. He received the M.S. and Ph.D. degrees from Charles University in Prague, Prague, in 2008 and 2015, respectively.

He is currently a postdoctoral researcher with Umeå University, Sweden. His current research interests include the numerical and laboratory simulations of elementary processes in (dusty) plasmas.

I. Pavlů et al. [2007]

Pavlů, J., Richterová, I., Němeček, Z., Šafránková, J., Wild, J., The sputtering of dust grains: Aspects of experimental observations. *IEEE Trans. Plasma Sci.* 35 (2): 297–302, 2007.

The Sputtering of Dust Grains: Aspects of Experimental Observations

Jiří Pavlů, Ivana Richterová, Zdeněk Němeček, Jana Šafránková, and Jan Wild

***Abstract*—Dust grains are sputtered at every environment containing energetic ions (i.e., ions with energies of several kiloelectronvolts). In the laboratory, only the beam experiments would fulfill these conditions; however, in the space, ions of these energies can be found even in the solar wind. It was suggested that the sputtering is one of the most important destruction processes of micrometer-sized dust grains, and on the other hand, it would be a source of heavy species in the interplanetary medium. We simulate the space environment by trapping the dust grains in an electrodynamic quadrupole trap and by influencing them by the ion beam with a variable energy up to 5 keV. The grains are charged to high surface potentials, and thus, a strong electric field near the surface can affect the sputtering rate. The finite size and the small curvature radius of grains play an important role in the quantification of sputtering efficiency. We propose a simple sputtering model for spherical grains and compare its predictions with measurements. An interpretation of the preliminary results obtained on gold microspheres bombarded by argon ions indicates that not only the grain mass but also the grain shape is changing in the course of our experiment. We suggest that similar effects can occur in the space if the dust is exposed to collimated ion beams.**

***Index Terms*—Dust, ion bombardment, sputtering.**

I. Introduction

DUST GRAINS in the space undergo a number of processes induced by impinging particles—ions, electrons, and photons. The majority of them result in a grain charge due to the various processes including photoemission, electron/ion attachment, secondary emissions, emissions in high electric fields, etc. Bombarding particles are not only charging the grain, but their impacts can also lead to a destruction or, on the other hand, to a growth of the dust grains—both can also be a result of grain–grain collisions. Among the destruction processes of dust in the space, the sputtering by energetic particles is probably of the greatest importance. Not only sputtering by fast ions occurs in the space, but also photosputtering, electron induced sputtering and desorption, and chemical sputtering should be taken into account for particular cases [1]–[5].

It could be assumed that the most important destruction process for the dust in the solar system is the sputtering by ions of the solar wind. Because all solar-wind ions have the same velocities, the energy increases with their masses (e.g., $E_{\mathrm{H}^+} \approx 1$ keV, $E_{\mathrm{He}^{2+}} \approx 4$ keV, etc.). Depending on the energy and dust properties, the grains can reach high-positive surface potentials when exposed to the streams of ions only. On the other hand, the process of field ion emission limits the positive potentials of small grains (of micrometer and submicrometer sizes) [6]–[8].

The sputtering rate obviously decreases with the distance from the sun in the solar system, thus the conditions differ significantly at the Earth to that at the Saturn orbit. However, we will show that even the sputtering of dust in Saturn rings could be of a particular importance. The lost material of dust grains could serve as a source of the so-called "pickup ions." There is an evidence of pickup ions to be present nearly within the whole solar system [9], [10].

Small meteorites entering the Earth's atmosphere could also be a subject of sputtering. Radar echoes from Leonid meteors were recorded at altitudes up to 400 km [11]. The velocity of "standing" ionospheric ions in the dust (meteorite) frame of reference is high enough for an effective sputtering that results in observable radar echoes.

As can be seen from our short overview, the investigation of the dust sputtering is of great interest. We are taking advantage of our laboratory facilities (detail description can be found in [12]) which allow us to catch a single charged grain into an electrodynamic trap and to affect it by electron/ion beams with a tunable energy. We have chosen a gold spherical sample for our experiments, because the sputtering properties of Au are well known; thus, we can investigate the effects of a finite curvature radius of dust grains and an influence of the surface electric field on the sputtering yield.

II. Experimental Procedures

A. Setup

The experiment is performed under ultrahigh vacuum conditions (typically 10^{-7} Pa). The investigated grain is illuminated by a red laser light, and the charge-to-mass ratio Q/m of the grain is calculated from the secular frequency of the dust-grain oscillatory motion detected by an optical system

$$\frac{|Q|}{m} \approx \pi^2 r_0^2 \cdot \frac{f_{\mathrm{ac}} \cdot f_z}{V_{\mathrm{ac}}^{\mathrm{ef}}} \cdot c(f_z, f_{\mathrm{ac}}) \tag{1}$$

where r_0 is the inner radius of the ring quadrupole electrode, V_{ac} and f_{ac} are the amplitude and the frequency of the power supply, f_z is the grain oscillation (secular) frequency, and $c(f_z, f_{\mathrm{ac}})$ is the empirical correction for variable ratio $f_z : f_{\mathrm{ac}}$. For more details on the experiment, see also [8].

Manuscript received August 4, 2006; revised November 16, 2006. This work was supported in part by the Research Plan MSM 0021620834 that is financed by the Ministry of Education of the Czech Republic and in part by the Czech Grant Agency under Contract 202/04/0912.

The authors are with the Faculty of Mathematics and Physics, Charles University, V Holešovičkách 2, 180 00 Prague, Czech Republic.

Digital Object Identifier 10.1109/TPS.2007.891636

The only quantity we measure directly is the secular frequency and thus the Q/m ratio. However, we have developed methods that allow us to measure other important grain parameters: mass, charge, and capacitance of the grain [12], [13].

B. Estimations of Grain Mass, Charge, and Capacitance

The grain mass was determined by measurements of the change of Q/m caused by an increase of the grain charge due to an impact of one electron. Such measurements expect that the grain charge is of the order of 10^3 elementary charges. Since the grain charge is $\approx 10^5$ elementary charges during the sputtering experiment, the ion beam should be switched off, and the grain should be discharged to the aforementioned value by the electron beam. The grain is illuminated by an electron source providing about one electron per several minutes, and a temporal evolution of Q/m is recorded. The changes of Q/m corresponding to one elementary charge are used for the determination of the grain charge Q assuming that the change of a grain mass is negligible in such a case (i.e., $\Delta Q = e$ and $\Delta m = 0$). The mass is then computed from the measured Q/m and the estimated Q. A complete description of this method can be found in [12].

The precision of the mass estimation is limited by many factors like the precision of the quadrupole geometry, the distortion of the quadrupole voltage, etc., and thus, it is of the order of 10^{-2}. However, the relative error is better than 10^{-6}.

The important quantity is the surface potential of the dust grain ϕ. It could be calculated from

$$\frac{Q}{m} = \frac{C}{m} \cdot \phi \tag{2}$$

where C is the grain capacitance. Assuming a spherical shape, C will read as $C = 4\pi\epsilon_0 \cdot R$. However, the grain radius R should be considered as a variable in our sputtering experiment, thus we should apply an independent method for the surface-potential determination. We are using the following procedure: The grain is charged by the midenergy ion beam (1 keV). During the sputtering, its surface potential is close to 1 kV. Then, the beam energy is switched to 500 eV. The ions of such energy cannot reach the grain, but they produce electrons in the vacuum vessel due to the ionization of the residual gas and the secondary electron emission from the trap surfaces. These electrons are caught by the positive grain, and it leads to the slow discharging of the grain. When the grain potential decreases to 500 V, the beam ions can again reach the grain and the discharging vanishes, if the net current is zero. This point is usually not too distinct in records of a temporal evolution of the Q/m ratio, but it can be easily found by a differentiation of such record. At this point, the grain potential and the corresponding Q/m ratio are known, and the capacitance C can be calculated from (2).

C. Experimental Conditions

A spherical gold grain (the same as in [8]) of an initial radius of $R_0 = 0.57$ μm and the corresponding initial mass $m_0 = 1.48 \times 10^{-14}$ kg were used in this paper. The sputtering was done by the Ar^+ beam with the energy of $E_0 = 5$ keV and the current density of $i_p = 4 \times 10^{-4}$ Am^{-2} (Table I).

TABLE I
SUMMARY OF MODEL PARAMETERS USED FOR FITTING THE EXPERIMENTAL DATA DISPLAYED IN ALL FIGURES

parameter	symbol	value
sputtering yield (4 keV Ar^+, Au)	Y	5
geometrical enhancement	Λ_g	2
el. field enhancement	Λ_f	2
beam current density	i_p	4×10^{-4} Am^{-2}
grain radius	R_0	5.68×10^{-7} m
initial grain mass	m_0	1.48×10^{-14} kg
limiting electric field	F_{max}	1.95×10^9 Vm^{-1}

Our primary task is the investigation of the grain sputtering, but the beam ions charge the grain, and the grain charge influences the energy of ions impinging the grain. The grain charge is limited by field ion emission, and since the emission current increases roughly and exponentially with the electric field F at the grain surface [8], this field can be considered as a constant for our experiment. We have found a value of the electric field magnitude $F_{\max} = 1.95 \times 10^9$ V/m. This fact would lead to changes of the surface potential during the grain sputtering due to the changes of the grain diameter. Indeed, this potential was $\phi_{\max} \approx 1.05$ kV at the beginning of the experiment and $\phi_{\max} \approx 0.75$ kV at the end. The energy of the beam ions with respect to the grain surface was thus in the range 3.95–4.25 keV. According to [14], the sputtering yield Y is roughly constant in this energy range, and its value is about $Y \approx 5$. This value was determined for the Ar^+ ions with a normal impact to a planar surface. The yield increases with the decreasing incidence angle [14], and we have estimated [15] that a factor of 1.2–2 should be considered for the sputtering of spherical samples.

III. GRAIN SPUTTERING MODEL

By contrast to sputtering experiments carried out on large planar samples that are held at a constant potential, our experiment exhibits several differences that can be summed up as follows.

1) The grain surface potential reduces the energy of bombarding ions and evolves in the course of the grain sputtering.
2) The potential is stabilized by ion field emission at a level $\phi = F(i) \cdot R$, where $F(i)$ is the electric field strength producing the field emission current equal to the ion beam current.
3) The variations of the grain potential change the energy of impinging ions and the cross section of the grain. The sputtering yield of the grain is enhanced by a geometrical factor up to $\Lambda_{\rm g} = 2$ due to a varying incidence angle along the sample surface.
4) There is a question whether the yield is further enhanced by the electric field at the sample surface.

The experiment can provide directly the change of the mass of the sputtered sample, but this measurement requires stopping of sputtering. However, the Q/m ratio is measured throughout the sputtering, and thus, it is desirable to find a relationship between the temporal changes of Q/m and the variations of the grain mass. It would be very helpful for the evaluation of further experiments.

Linking up to our previous calculations [15], we continue the development of the sputtering model of the dust grains. The mass change under an ion bombardment could be written as

$$\frac{dm}{dt} = -M_{\mathrm{Au}} \cdot i_p \cdot Y \cdot \Lambda_{\mathrm{g}} \cdot \Lambda_{\mathrm{f}} \cdot \pi R(t)^2 \cdot \left(1 - \frac{e \cdot \phi_{\max}(t)}{E_0}\right) \tag{3}$$

where m and R are the grain mass and radius, E_0 and i_{p} are the energy and current density of primary ions, M_{Au} is the mass of a gold atom, $\phi_{\max}$ is the grain equilibrium surface potential as noted above, Y, Λ_{g}, and Λ_{f} are the sputtering yield and its enhancements due to a geometry (shape) and due to an intense electric field at the grain surface, respectively. The right part of the equation (starting with π) describes the grain cross section that depends on the grain potential.

Solving this ordinary differential equation using the following substitutions:

$$k = M_{\mathrm{Au}} \cdot i_p \cdot Y \cdot \Lambda_{\mathrm{g}} \cdot \Lambda_{\mathrm{f}} \cdot \pi \cdot \left(\frac{3}{4\pi\rho_{\mathrm{Au}}}\right)^{\frac{2}{3}} \tag{4}$$

$$p = \frac{F_{\max}}{E_0} \cdot \left(\frac{3}{4\pi\rho_{\mathrm{Au}}}\right)^{\frac{1}{3}} \tag{5}$$

leads to a formula describing the mass change

$$m(t) = \left(\frac{1 + \exp\left(\frac{kpt}{3}\right) \cdot \left(pm_0^{1/3} - 1\right)}{p}\right)^3 \tag{6}$$

where m_0 is the initial mass of the grain.

In a spherical approximation and assuming limiting potential due to the field ion emission, the charge of a grain is given by

$$Q(t) = 4\pi\epsilon_0 \cdot R(t) \cdot \phi_{\max} = 4\pi\epsilon_0 \cdot F_{\max} \cdot \left(\frac{3m(t)}{4\pi\rho}\right)^{2/3}. \tag{7}$$

Dividing the previous equation by $m(t)$, we get

$$Q/m(t) = 4\pi\epsilon_0 \cdot F_{\max} \cdot \left(\frac{3}{4\pi\rho}\right)^{\frac{2}{3}} \cdot m(t)^{\frac{-1}{3}}. \tag{8}$$

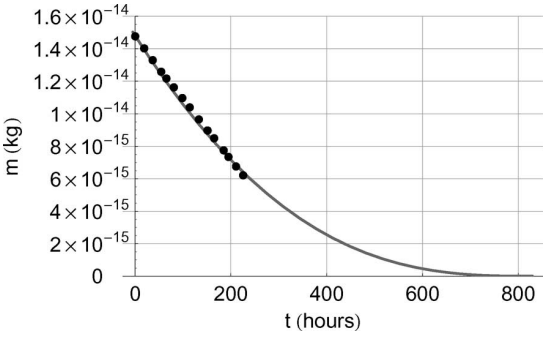

Fig. 1. Time evolution of the Au grain mass during Ar^+ ion bombardment and comparison of the model (solid line) and the experimental results (dots).

Using substitutions

$$a = (4\pi)^{\frac{1}{3}}\epsilon_0 \cdot F_{\max} \cdot \left(\frac{3}{\rho}\right)^{\frac{2}{3}} \cdot p \tag{9}$$

$$b = pm_0^{\frac{1}{3}} - 1 \tag{10}$$

$$c = \frac{1}{3}kp \tag{11}$$

and combining (6) and (8), a formula for the time evolution of the $Q/m(t)$ ratio is given as

$$Q/m(t) = \frac{a}{1 + b \cdot \exp(c \cdot t)}. \tag{12}$$

IV. Model Versus Experiment

Our simple sputtering model leads to (6) and (12), giving the time evolution of the grain mass and charge-to-mass ratio during the sputtering process. In our laboratory experiment, we could measure these two quantities; thus, using the experimental conditions and values mentioned above, we can compare the experimental data with the suggested model. In Fig. 1, the time evolution of the Au grain mass with an initial radius of 0.568 μm is shown (heavy dots correspond to the experimental points). The model curve (line) fits the experimental points very well when the enhancement factor $\Lambda = \Lambda_{\mathrm{g}} \cdot \Lambda_{\mathrm{f}}$ is set to 4. Taking into account that the enhancement due to a spherical shape is $\Lambda_{\mathrm{g}} \leq 2$ only, one can expect that the rest could be attributed to the influence of the strong electric field.

We have tried to compare the measurements of the time evolution of the Q/m ratio with (12), but the result was unsatisfactory (Fig. 3, dashed line). However, the mass of the grain was measured directly, whereas (12) was derived under the assumption of the spherical grain. Since we have measured the grain capacitance in the course of sputtering, we could check this assumption. Fig. 2 shows how the relative capacitance (normalized to the sphere of a given mass) evolves during the sputtering. The figure shows that the experiment started with a spherical grain, and the shape of this grain changed continuously due to the sputtering. We do not know the resulting shape, but the ratio $C/C_{\mathrm{sphere}} = 1.2$ corresponds to an ellipsoid of revolution with the ratio of axes 1 : 2. We have

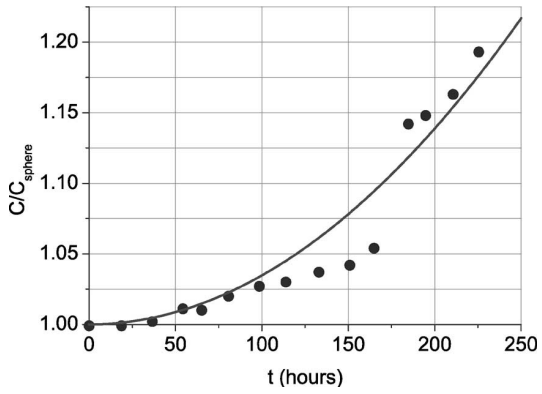

Fig. 2. Evolution of the relative capacitance in the course of our 250-h experiment. The dots represent experimental data; the solid line is a parabolic fit used for further calculations.

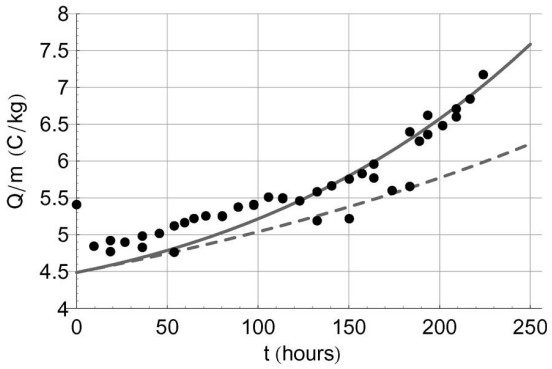

Fig. 3. Changes of the Q/m ratio in time. Experimental data (dots) compared with the uncorrected model (dashed line) and with the model corrected to a changing shape, i.e., changing capacitance (solid line).

fitted the measured temporal evolution of the capacitance by a parabola (see Fig. 2) and corrected the expression (7) for the grain charge accordingly. Expressions (8) and (12) were corrected in the same sense, i.e., right sides were multiplied by a quadratic fit of $C/C_{\mathrm{sphere}}(t)$ that is displayed in Fig. 2. After this correction, the agreement between the measured data and the calculations of Q/m is rather good as it can be seen in Fig. 3 (solid line).

V. Discussion

Direct measurements of the mass of the sputtered grain in Fig. 1 suggest that the sputtering yield of the gold grain bombarded by the 5-keV Ar^+ ions is enhanced by a factor of 4 with respect to the planar uncharged sample. We suggest that this enhancement can be divided into two multiplicative parts. One part is attributed to a shape of the investigated sample; the other part of this enhancement can be probably caused by the presence of the strong electric field at the surface of the charged grain. This field is limited by the ion field emission in specific conditions of our experiment, but such limitation would not act in the space because only very small grains ($\sim$20 nm) can be sufficiently charged by photoemission. Moreover, our experiment uses the gold grain for the sake of comparison with known data, but the materials in the space are insulators, and the yield enhancement can be much larger due to the penetration of the field into the grain. These processes will be the subject of a further study.

TABLE II
Typical Solar-Wind Ions and Their Sputtering Yields of Gold

ion species	solar wind abundance [16]	sputtering yield of 5 keV singly ionized ions [14]
H^+	95%	0.05
He^{2+}	4%	0.5
heavy ions: O^{n+}, Si^{n+}, Fe^{n+}, etc.	1%	5

In order to check the possible relevance of the measurements to the interplanetary space, we have calculated the sputtering time of the gold grain in typical solar-wind conditions. At 1 AU, we suppose the solar-wind velocity of $400\ \mathrm{km}\cdot\mathrm{s}^{-1}$ and the density of $10\ \mathrm{cm}^{-3}$. Table II gives the ion composition and sputtering yields for a calculation. The sputtering times at two places of the space are reviewed in Table III, but these results can be used as a first approximation only. In our calculations, all ions were taken as single ionized, with the energy of 5 keV, but Insepov *et al.* [17] show that the sputtering yield of multiple ionized ions can be much larger (an order of magnitude), and all species (except H) in the solar wind are in high ionization states. Moreover, a typical mass composition of the solar wind was considered [16], but the abundance of heavy ions can be significantly enhanced during coronal mass ejections, and these species are very effective in the dust sputtering.

We would like to point out that the values in Table III are based on the tabulated values of the sputtering yield for gold corrected to an assumed spherical shape. The real times of the dust-grain sputtering can thus vary within an order of magnitude. However, the structure of space dust grains would be probably less rigid, thus one would expect our calculations to be an upper limit of the expected sputtering times.

VI. Conclusion

We have measured the sputtering of a gold grain under an Ar^+ bombardment, and we can conclude that the observed data fit well with our simple sputtering model. The influence of the electric field on the sputtering rate probably needs a further investigation. We have found a factor of 2 for the electric field of about $10^9\ \mathrm{Vm}^{-1}$, but this value is based on the yield from [14]. However, the simulations made in [17] suggest that this yield could be larger. We partially prove that not only the size but also the shape of the sputtered grain could be changed. Our estimations show that the sputtering by the solar wind of micrometer-sized ($> 1\ \mu$m) grains is negligible in man-life horizon already at the Earth's orbit; nevertheless, in terms of space, the time constants of hundred years are short. Moreover, the sputtering rate decreases with the square of the distance from the sun, and thus, the lifetime of dust particles would be rather short near the sun, and their sputtering can be an important source of pickup ions [18].

TABLE III
COMPUTED SPUTTERING TIME OF A MICROMETER-SIZED GOLD GRAIN IN DIFFERENT SPACE LOCATIONS (ROUGH APPROXIMATION)

sputtering conditions	ion	1/2 mass	1/2 radius	"0" mass
laboratory	Ar^+	190 hours	450 hours	840 hours
at the Earth orbit	H^+	8×10^2 years	2×10^3 years	3×10^3 years
at the Earth orbit	He^{2+}	2×10^3 years	5×10^3 years	8×10^3 years
at the Earth orbit	heavy ions	8×10^2 years	2×10^3 years	3×10^3 years
at the Earth orbit	sum	3×10^2 years	8×10^2 years	1×10^3 years
at the Saturn orbit	H^+	8×10^4 years	2×10^5 years	3×10^5 years
at the Saturn orbit	He^{2+}	2×10^5 years	5×10^5 years	8×10^5 years
at the Saturn orbit	heavy ions	8×10^4 years	2×10^5 years	3×10^5 years
at the Saturn orbit	sum	3×10^4 years	8×10^4 years	1×10^5 years

REFERENCES

[1] B. T. Draine and E. E. Salpeter, "On the physics of dust grains in hot gas," *Astrophys. J.*, vol. 231, no. 1, pp. 77–94, Jul. 1979.

[2] ——, "Destruction mechanisms for interstellar dust," *Astrophys. J.*, vol. 231, no. 2, pp. 438–455, Jul. 1979.

[3] B. T. Draine, "On the chemisputtering of interstellar graphite grains," *Astrophys. J.*, vol. 230, no. 1, pp. 106–115, May 1979.

[4] ——, "Charging processes for interstellar dust," in *Evolution of Interstellar Dust and Related Topics*, A. Bonetti, J. M. Greenberg, and S. Aiello, Eds. Amsterdam, The Netherlands: North Holland, 1989, pp. 91–102.

[5] ——, "Destruction processes for interstellar dust," in *Evolution of Interstellar Dust and Related Topics*, A. Bonetti, J. M. Greenberg, and S. Aiello, Eds. Amsterdam, The Netherlands: North Holland, 1989, pp. 103–120.

[6] Z. Sternovsky, Z. Němeček, J. Šafránková, and A. Velyhan, "Ion field emission from micrometer-sized spherical glass grains," *IEEE Trans. Plasma Sci.*, vol. 29, no. 2, pp. 292–297, Apr. 2001.

[7] J. Pavlů, A. Velyhan, I. Richterová, J. Šafránková, Z. Němeček, J. Wild, and M. Jeřáb, "Ion beam effects on dust grains: 2. Influence of charging history," *Vacuum*, vol. 80, no. 6, pp. 542–547, Mar. 2006.

[8] M. Jeřáb, I. Richterová, J. Pavlů, J. Šafránková, and Z. Němeček, "Influence of charging conditions on dust grain's field ion emission," *IEEE Trans. Plasma Sci.*, vol. 35, no. 2, pp. 292–296, Apr. 2007.

[9] G. Gloeckler and J. Geiss, "Interstellar and inner source pickup ions observed with SWICS on ULYSSES," *Space Sci. Rev.*, vol. 86, no. 1–4, pp. 127–159, Jul. 1998.

[10] D. J. McComas, N. A. Schwadron, F. J. Crary, H. A. Elliott, D. T. Young, J. T. Gosling, M. F. Thomsen, E. Sittler, J.-J. Berthelier, K. Szego, and A. J. Coates, "The interstellar hydrogen shadow: Observations of interstellar pickup ions beyond Jupiter," *J. Geophys. Res.*, vol. 109, no. A18, p. A02104, Feb. 2004.

[11] N. Brosch, L. S. Schijvarg, M. Podolak, and M. R. Rosenkrantz, "Meteor observations from Israel," in *Proc. ESA SP-495: Meteoroids Conf.*, B. Warmbein, Ed, Nov. 2001, pp. 165–173.

[12] J. Pavlů, A. Velyhan, I. Richterová, Z. Němeček, J. Šafránková, I. Čermák, and P. Žilavý, "Mass-loss rate for MF resin microspheres," *IEEE Trans. Plasma Sci.*, vol. 32, no. 2, pp. 704–708, Apr. 2004.

[13] I. Čermák, E. Grün, and J. Švestka, "New results in studies of electric charging of dust particles," *Adv. Space Res.*, vol. 15, no. 10, pp. 59–64, May 1995.

[14] R. Behrisch, *Sputtering by Particle Bombardment I, II*. Berlin, Germany: Springer-Verlag, 1981.

[15] J. Pavlů and J. Wild, "Simulation of dust particle sputtering," in *Proc. WDS, Contributed Papers: Part II—Physics of Plasmas and Ionized Media*, J. Šafránková, Ed. Matfyzpress, 2000, pp. 238–242.

[16] L. Avanov, N. Borodkova, Z. Němeček, A. Omeltchenko, J. Šafránková, A. Skalski, Y. Yermolaev, and G. Zastenker, "Some features of solar-wind protons, alpha-particles and heavy-ions behavior: The Prognoz-7 and Prognoz-8 experimental results," *Czech. J. Phys.*, vol. 37, no. 6, pp. 759–774, 1987.

[17] Z. Insepov, J. P. Allain, A. Hassanein, and M. Terasawa, "Surface erosion by highly-charged ions," *Nucl. Instrum. Methods Phys. Res. B, Beam Interact. Mater. At.*, vol. 242, no. 1/2, pp. 498–502, Jan. 2006.

[18] I. Mann, H. Kimura, D. A. Biesecker, B. T. Tsurutani, E. Grün, R. B. McKibben, J.-C. Liou, R. M. MacQueen, T. Mukai, M. Guhathakurta, and P. Lamy, "Dust near the sun," *Space Sci. Rev.*, vol. 110, no. 3/4, pp. 269–305, Jan. 2004.

Jiří Pavlů was born in Pardubice, Czech Republic, in 1977. He received the Ph.D. degree from Charles University, Prague, Czech Republic, in 2005.

Currently, he is a Senior Assistant with the Space Physics Laboratory, Department of Surface and Plasma Science, Faculty of Mathematics and Physics, Charles University. His research interests include the laboratory investigations of elementary processes on dust grains induced by electron, ion, and photon irradiations.

Ivana Richterová was born in Český Brod, Czech Republic, in 1979. She received the M.S. degree from Charles University, Prague, Czech Republic, in 2003. She is currently working toward the Ph.D. degree at the Space Physics Laboratory, Department of Surface and Plasma Science, Faculty of Mathematics and Physics, Charles University. Her research is devoted to the laboratory investigation and modeling of elementary charging processes on dust grains.

Zdeněk Němeček was born in Prague, Czech Republic, in 1947. He received the M.S., Ph.D., and Dr.Sc. degrees from Charles University, Prague, in 1971, 1982, and 1996, respectively.

Since 1971, he has been holding several positions at the Faculty of Mathematics and Physics, Charles University, where he is currently Dean of the Faculty. His research interests include the solar-wind interaction with the Earth's magnetosphere and the laboratory simulations of plasma processes.

Jana Šafránková was born in Teplice, Czech Republic, in 1947. She received the M.S., Ph.D., and Dr.Sc. degrees from Charles University, Prague, Czech Republic, in 1972, 1982, and 1996, respectively.

Since 1972, she has been holding several positions at the Faculty of Mathematics and Physics, Charles University, where she is currently the Head of Space Physics Laboratory. Her recent research is focused on the magnetospheric physics and the laboratory simulations of elementary processes in dusty plasmas.

Jan Wild was born in Litoměřice, Czech Republic, in 1960. He received the M.S. and Ph.D. degrees from Charles University, Prague, Czech Republic, in 1984 and 1991, respectively.

Currently, he holds the position of Scientific Secretary at the Department of Surface and Plasma Science, Faculty of Mathematics and Physics, Charles University. His research interests include the pulsed laser deposition and the laboratory simulations of sputtering of dust grains.

J. Beránek et al. [2010]

Beránek, M., Vyšinka, M., Pavlů, J., Richterová, I., Němeček, Z., Šafránková, J., Dust as a gas carrier. *IEEE Trans. Plasma Sci.* 38 (4): 886–891, 2010.

Dust as a Gas Carrier

Martin Beránek, Marek Vyšinka, Jiří Pavlů, Ivana Richterová, Zdeněk Němeček, and Jana Šafránková

***Abstract*—Dust in space can collect particles from surrounding plasma and transport them over long distances. Release of the implanted particles can then change the mass composition in a particular place of the space. The depth of ion penetration into the dust body strongly depends on an initial mutual energy and differs with ion species as well as with the grain composition. The same holds for diffusion constant of implanted ions (already neutralized) exiting back to the free space. We have used our measurements of the release of Ar ions implanted into glassy carbon dust grains for determination of the diffusion coefficient. Our calculations provide the limits for the amount of gas that can be dissolved in the grain as well as its release rate. We discuss the influence of the dust sputtering and dust temperature on the aforementioned quantities.**

***Index Terms*—Dust charging, gas diffusion, interplanetary dust.**

I. Introduction

DUST as a common constituent of space as well as laboratory plasmas is bombarded by energetic ions (e.g., dust in the solar wind is exposed to H^+ of about 1 keV, He^{++} of about 4 keV, etc.). Ions not only modify and sputter the dust surface but also can penetrate into the material of the grain itself. Then, the diffusion starts to release atoms, and its rate depends on the diffusion coefficient that is generally an exponential function of temperature.

In the interplanetary space, the dissolved ions (already neutralized) could be transported in the dust safely across long distances due to a low temperature. Once the gas leaves the grain, it becomes usually ionized again quickly by solar UV or by charge exchange. The ions are picked up by the interplanetary magnetic field and carried outward with the solar wind as a distinct component of the solar wind called pick-up ions [1]. Pick-up ions are often considered to be produced by ionization of neutral interstellar gas that penetrates the solar system [2]. Dust interactions with the solar wind provide a further source that contributes to a different elemental composition of the pick-up ion population. Pick-up ions are clearly identifiable due to their distinctive charge state and velocity distribution [3]. Dust may contribute to the formation of pick-up ions through a number of processes: 1) sublimation of the grain material; 2) sputtering of the grain due to an ion bombardment; 3) by recycling of solar-wind particles into pick-up ions by adsorption and desorption; and 4) by release of the atoms that were previously implanted and stored in the grain.

It is known that the surface layers of lunar samples are doped with solar-wind particles. Banks [4] studied theoretically this effect for dust grains. Rajan *et al.* [5] reported large ^{4}He concentrations in collected micrometeorites (e.g., small interplanetary particles which enter the Earth's atmosphere without being melted by frictional heating), and the authors concluded that this helium comes from the implanted solar wind. Nier [6] performed experiments to determine the amount and isotopic composition of helium and neon found in individual interplanetary dust particles collected in the Earth's stratosphere in order to distinguish between particles of cometary and asteroidal origin. He found that the ^{4}He degassing pattern of the dust is comparable to that of the lunar samples. However, while implantation of heavier ions would also be expected, heavier elements have not been measured. Based on observations of solar-wind implantation, Fahr *et al.* [7] suggested that the implantation of solar-wind particles into the surface layer of dust can lead to subsequent desorption of neutrals. They predicted that, inside 0.5 AU (0.05 AU, respectively), the density of neutral hydrogen (helium, respectively) produced by this process exceeds that of the interstellar hydrogen (helium, respectively) found at these distances from the Sun. The amount of dust-generated neutral molecular hydrogen was calculated by Gruntman [8]. He considered the efficiency of various processes for conversion of the H_2 molecules to H_2^+ ions and their subsequent destruction. He concluded that a significant part of H_2^+ ions should survive and make unique molecular pick-up ions.

Vernazza *et al.* [9] analyzed the sources of reddening of asteroid surfaces. They concluded that implantation of solar-wind ions is the favorite mechanism causing reddening. Plainaki *et al.* [10] modeled space weathering processes that take place on the surfaces of near-Earth objects. Starukhina [11] studied deposition of solar-wind ions on the surface of Moon. She identified polar regions as possible repositories of gases related to the solar wind.

In the laboratory plasma, e.g., in tokamaks, dust can accommodate plasma ions—retention of tritium and deuterium being particularly important for safety reasons [12]. Yoshida *et al.* [13] studied the carbon–tungsten dust prepared by deuterium arc discharge and measured the desorption rate of heated samples. They concluded that the deuterium concentration in the carbon dust was estimated to be 0.2 of the atomic ratio (D/C) and even higher in carbon–tungsten grains, and they suggested to increase the temperature of the outer walls. Since the dust is charged, it moves and accelerates within the tokamak [14]. Rudakov *et al.* [15] examined a migration of dust in the DIII-D tokamak, and they gave an experimental evidence that a

Manuscript received July 10, 2009; revised October 29, 2009. First published January 19, 2010; current version published April 9, 2010. This work was supported in part by the Research plan MSM 0021620860 financed by the Ministry of Education of the Czech Republic, by the Czech Grant Agency under Contracts 202/08/P066 and 202/08/H057, and by the Grant Agency of Charles University (GAUK 146207).

The authors are with the Department of Surface and Plasma Science, Faculty of Mathematics and Physics, Charles University, 180 00 Prague, Czech Republic (e-mail: jiri.pavlu@mff.cuni.cz).

Digital Object Identifier 10.1109/TPS.2009.2038219

micrometer-sized carbon dust contained in a tokamak divertor can become highly mobile and reach the core plasma. However, a dust contribution to the core contamination is still unclear.

As a side effect of measurements of sputtering yields, it was also found recently [16] that carbon traps ions at the surface more efficiently than metallic materials, which may significantly bias mass loss measurements on samples that have been subjected to high irradiation doses (Xe^+ in this particular case).

Based on these observations, we can expect that the mass of the dust grain exposed to the ion bombardment can increase with time as the sputtering could be less efficient than trapping in some cases. These ions (now neutrals) can later diffuse within the grain and leave it when they reach the surface. In this paper, we focus on the observation of the diffusion and successive desorption of Ar ions in the micrometer-sized amorphous carbon sphere. The mass-change rate is evaluated and successfully modeled.

II. Experiment

The experiment has been performed on a single glassy carbon grain trapped inside the cylindrical quadrupole electrodynamic trap. The frequency of the grain oscillations inside the trap is proportional to the ratio of the grain charge and its mass [17], [18]. Special techniques described in [19] can be used for determination of the other parameters of the investigated grain. The optical detection of the motion of the grain and electrical damping of its oscillations allow us to perform measurement under UHV conditions $(10^{-7}$ Pa) and hold the grain in the trap for a long period (on the order of weeks) [17]–[19].

The analyzed spherical glassy carbon samples have been produced by HTW Hochtemperatur-Werkstoffe. The diameter of the grains lies between 1 and 5 μm. According to the specification of the manufacturer, grains are amorphous and isotropic with the mass density of 1500 kg/m^3. The specific resistance $(50\ \Omega \cdot \mu\text{m})$ is low enough to prevent the presence of electric field inside the grain.

The glassy carbon grain with a mass of $(6.27 \pm 0.01) \cdot 10^{-15}$ kg and a diameter of 1.93 μm has been trapped and treated with an Ar^+ beam for 8 h. The energy of impinging ions was 7 keV. The total current of ions has been approximately 35 000 particles per second, and the corresponding beam intensity is on the order of nanoamperes per square millimeter. This value was determined from the initial field ion emission current measured on another grain after switching the ion gun off.

The surface potential of the grain was held low enough to eliminate the ion field emission [20] using simultaneous electron bombardment. After the treatment, the grain was held in the trap for a few days, and its charge-to-mass ratio was continuously monitored. According to our previous observations [19], the charge of the trapped grain remains constant over days when there is neither field emission nor beams of charged particles. Because of the constant charge of the grain, we attributed the observed changes of specific charge to variations of the grain mass. Note that we can observe relative changes of the mass on the order of 10^{-4}. This long-term stability has been achieved subtracting the temperature drift.

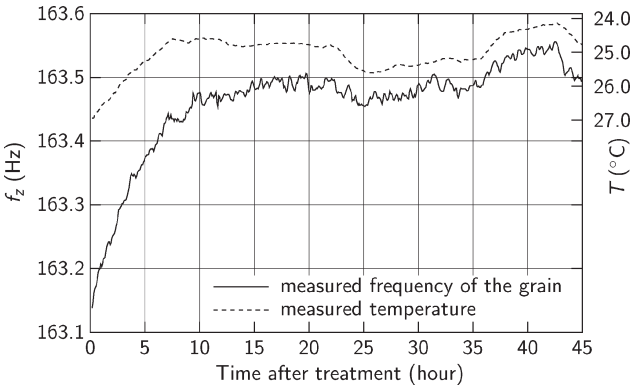

Fig. 1. Measured frequency of oscillations of the grain and the ambient temperature.

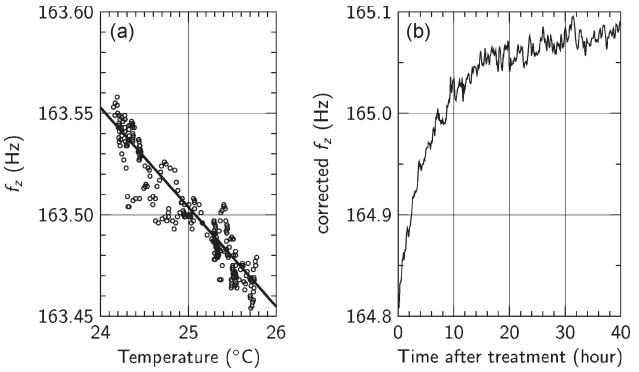

Fig. 2. (a) Correlation between the temperature and frequency after 25th hour. (b) Frequency of the grain corrected for the temperature drift.

A. Correction of the Temperature Drift

In our experiment, there are many devices and circuits that are potentially sensitive to the change of temperature. It is not possible to analyze each device independently; therefore, we found out an appropriate temperature correction experimentally through the following procedure: We have measured the frequency of the grain oscillation together with the ambient temperature (Fig. 1). Under the assumption that there is no measurable change in the charge-to-mass ratio after a sufficiently long time, we fit a linear dependence between the measured temperature and oscillation frequency starting at 25th hour after treatment [Fig. 2(a)], when the frequency copies the measured temperature (compare the lines in Fig. 1). Furthermore, we have applied this fit to correct the measured frequency in the full range of time [Fig. 2(b)]. We suggest that the remaining roughly exponential increase of the frequency (which is directly proportional to the charge-to-mass ratio) after the treatment is caused by deposited Ar atoms leaving the grain due to diffusion.

III. Diffusion Coefficient

We have utilized a simple model of diffusion to find a diffusion coefficient D. We neglect the surface effects and compute the diffusion inside the homogeneous grain. Since the

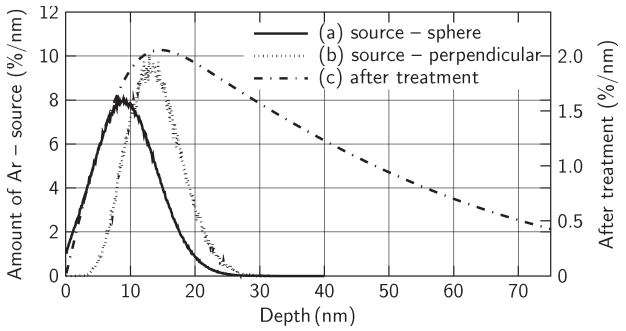

Fig. 3. [(a) and (b)] Probability of deposition of the 7-keV Ar ion in a given depth (left axis) and computed by the SRIM code [21]. (c) Distribution of Ar after 8 h of treatment (right axis). $D = 5 \cdot 10^{-16}$ cm^2/s and $N = 35\,000$ s^{-1}.

problem has a radial symmetry, the general equations of the diffusion can be written as

$$\frac{\partial \rho}{\partial t} = D \frac{1}{r} \cdot \frac{\partial^2}{\partial r^2}(r\rho) \tag{1}$$

$$J = -D \frac{\partial \rho}{\partial r} \tag{2}$$

where ρ is the mass density and J is the mass flux. The density of gas outside the spherical grain is set to zero in our model; therefore, the mass of argon leaving the grain of radius R due to the diffusion according to (2) is

$$\frac{dm}{dt} = 4\pi R^2 \cdot D \cdot \left.\frac{\partial \rho}{\partial r}\right|_{r=R}. \tag{3}$$

During the treatment, there is an additional source term representing the incoming argon ions. We have computed the distribution $f(x)\,dx$ of the impinging ions deposited in a given depth under the surface by the SRIM code [21], [22]. We suppose that the grain rotation in the trap is fast enough to distribute the incoming ions with a radial symmetry. The radial distribution of 7-keV Ar ions is shown in Fig. 3. The dotted line stands for the profile provided by the SRIM code that expects a perpendicular impact of ions. The full line considers the effect of varying incident angles over the sphere [23].

Having the total number of impinging ions per second, i.e., N, we can modify (1) in the following way:

$$\frac{\partial \rho}{\partial t} = D \frac{1}{r} \cdot \frac{\partial^2}{\partial r^2}(r\rho) + \frac{N m_{\mathrm{Ar}} f(R-r)}{4\pi r^2} \tag{4}$$

where R is radius of the grain and $m_{\mathrm{Ar}} = 6.64 \cdot 10^{-26}$ kg is the mass of the argon atom. $f(R-r)$ represents a source term shown in Fig. 3 (profile a). The analytic expression of the source term is unknown; nevertheless, we can solve the equations numerically.

We have modeled the conditions in our experiments, i.e., the 8-h-long treatment (4) and the subsequent diffusion without the source term (1). Distribution of argon just after the treatment is shown in Fig. 3 as the dashed-dotted line.

The results of our model for various values of diffusion coefficients have been compared to the measured data. We are not able to measure the change of mass during the treatment, but

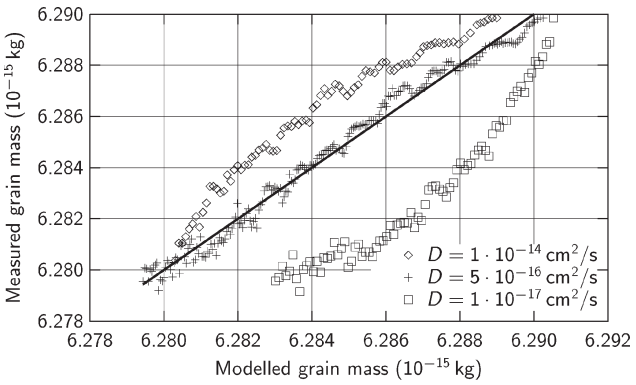

Fig. 4. Relation between the measured mass of the grain and the modeled mass at the same time after treatment for three diffusion coefficients.

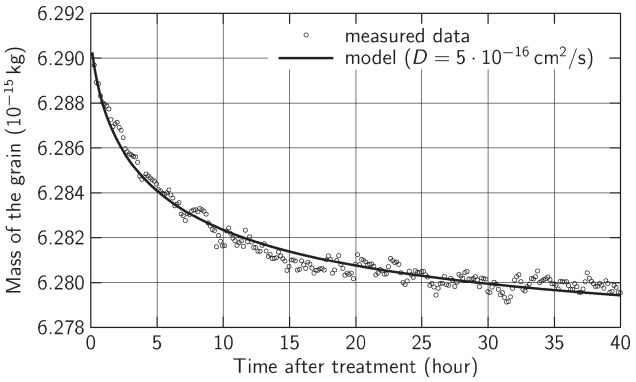

Fig. 5. Change of the grain mass in time. The parameters of the model ($D = 5 \cdot 10^{-16}$ cm^2/s, treatment: 8 h, incident current: 32 400 particles per second) are chosen according to the best fit in Fig. 4.

we compare the model and measured data in the period after the treatment. A modeled mass of the grain versus measured mass at the same time is shown in Fig. 4 for three values of D. The uncertainty of absolute values of the primary current and the final mass of the grain imply uncertainty of the linear scaling of the model result. Nevertheless, the relation is close to linear for the diffusion coefficient, $D = 5 \cdot 10^{-16}$ cm^2/s only, and the value of incident current, 32 400 particles per second, is in good agreement with the value estimated from other measurements. The value of diffusion coefficient will be used in further considerations. In order to demonstrate the agreement between measurement and model, the data from Fig. 4 are replotted in Fig. 5 that compares the computed and measured temporal changes of the grain mass.

IV. Amount of the Gas Dissolved

A. Stable Solution of Diffusion Equation

In our experiment, we have implanted more than 10^{-17} kg of argon into a single 2-μm glassy carbon grain. This is approximately 0.2% of the total mass. The majority of the gas is dissolved in a thin layer at the surface (see Fig. 3, curve c). The mass fraction of Ar in this layer was about 1%.

After a long treatment, the equilibrium state would be reached when the amount of gas inside the grain remains

constant over time. The diffusion equation without a source term (1) is valid for $(R - r)$ that is higher than the implantation depth, i.e., approximately 50 nm. This equation can be solved analytically. Angularly independent solution without singularity at the origin is a constant density. The particular value of this density depends on the boundary conditions which are set by the source term in the thin surface layer. The equilibrium density of gas inside the grain is constant in the majority of grain and decreases in the thin layer at the surface (note that, in equilibrium state, there cannot be any flux toward the center). The actual density and its decrease at the surface have been obtained numerically.

We numerically found the stable solution of (4)

$$\frac{d^2}{dr^2}\left(r\rho(r)\right) = -\frac{N m_{\mathrm{Ar}}}{D} \cdot \frac{f(R-r)}{4\pi r^2} \tag{5}$$

in the range of the implantation depth. The conservation of total mass of the gas inside the grain gives us the second boundary condition at the surface

$$\left.\frac{d\rho(r)}{dr}\right|_R = -\frac{N m_{\mathrm{Ar}}}{D} \frac{\int_0^R f(R-r)dr}{4\pi R^2}. \tag{6}$$

The solution of (5) and (6) depends on a spatial distribution of implanted ions and on the grain radius. The primary current and diffusion coefficient act as the multiplicative factor (N/D). The maximum total mass of argon dissolved $m_{\max}$ depends on the diameter of the grain approximately linearly in the case of fixed number of ions hitting the grain, N; in other words, the implanted mass is proportional to the volume of the grain in the case of the fixed ion flux I

$$m_{\max} = \alpha \cdot m_{\mathrm{Ar}} \cdot R \cdot \frac{N}{D} = \alpha \cdot m_{\mathrm{Ar}} \cdot \pi R^3 \cdot \frac{I}{D} \tag{7}$$

where R is the radius of the grain, N is the total number of impinging ions per second, D is the diffusion coefficient, and I is the flux of ions (particles per square meter per second). A coefficient α depends on the spatial distribution of implanted ions. An actual value for 7-keV Ar ions on glassy carbon sphere is $\alpha = 3.08 \cdot 10^{-7}$ cm. Note that (7) is not an analytical solution of (5) and (6) but the linear fit of the numerical results. The difference between numerically computed mass and fit (7) is approximately 0.5% at $R = 1$ μm and decreases for larger grains where the implantation depth becomes negligible compared to the grain radius.

When we put the parameters of the investigated 2-μm grain into (7), we get

$$m_{\max} = (1.97 \cdot 10^{-36}\ \mathrm{kg \cdot cm^2}) \cdot N/D = 1.38 \cdot 10^{-16}\ \mathrm{kg}. \tag{8}$$

B. Effect of the Sputtering

The grain sputtering and ion implantation act simultaneously, and rates of both processes are directly proportional to the number of impinging ions. However, the sputtering decreases the grain radius and, according to (7), limits the amount of gas that can be dissolved in the grain. The analysis has shown that

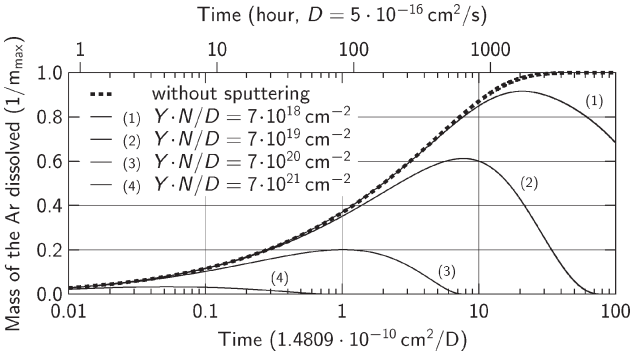

Fig. 6. Modeled increase of the mass of the 2-μm grain under the Ar^+ bombardment due to the dissolved gas and the sputtering of the material of the grain. The vertical axis is scaled with respect to the maximum amount of the gas (7); the scale of the horizontal axis is such that the unit value represents $1/e$ of total mass. The investigated grain is represented by the curve (2). Time in hours is shown for the conditions of our measurement.

the dependences of the mass of the dissolved gas on the time of the grain bombardment can be parameterized by a factor $Y \cdot N/D$, where Y stands for the sputtering yield. The results obtained for several values of $Y \cdot N/D$ are shown in Fig. 6. The dissolved mass is given as a fraction of $m_{\max}$, and the time is scaled by D; thus, the dashed line can be considered as a universal curve describing a temporal evolution of the implanted mass if the sputtering is neglected. The effect of the grain sputtering is demonstrated by profiles computed for different values of $Y \cdot N/D$.

Other parameters influencing the temporal evolution of the dissolved amount of the gas are the grain diameter. Since the dependence on the grain diameter is rather complicated and the computation is time consuming, Fig. 6 shows the results for the 2-μm grain. It allowed us to use other parameters from our experiment ($N = 35\,000$ s^{-1} and $D = 5 \cdot 10^{-16}$ cm^2/s) and to put the absolute time scale to the top of the panel. Since the sputtering yield for Ar^+ is about unity in the kiloelectronvolt range of energies [24], the line 2 describes the cumulated effect of sputtering, implantation, and diffusion under our experimental conditions.

V. Discussion

The presented numerical results use the value of the diffusion coefficient determined from the experiment. In order to relate this experiment to conditions in the space, we should estimate the dust grain temperature that cannot be directly measured. The temperature of the grain in the vacuum is determined by the radiation balance since the contribution of ion impact to the heating is several orders of magnitude lower. The grain is heated by background environment radiation ($T_{\mathrm{bg}} \approx 300$ K) and by the laser beam (635 nm, with an approximate beam intensity of 1.7 mW/mm^2). The incoming power is compensated by the grain thermal radiation.

We have utilized the MiePlot software [25], [26] to compute the spectral emissivity of the grain. The refractive index of the glassy carbon was set according to [27] and [28]. We integrated the product of emissivity and spectral intensity of a black body radiation over the range of wavelengths, and we

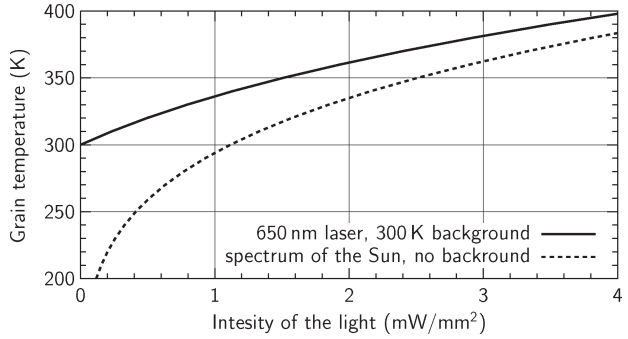

Fig. 7. Equilibrium temperature of glassy carbon grain (2 μm in diameter) illuminated (solid line) by the monochromatic 635-nm light and (dashed line) by the Sun light.

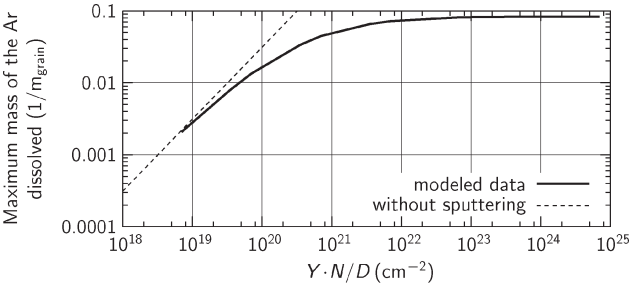

Fig. 8. Maximum amount of Ar dissolved in the 2-μm grain related to the original mass of the grain $m_{\rm grain}$. Both diffusion and sputtering have been taken into account.

scaled the result to the grain surface area. The result is the total radiated power at a given temperature. A power of the laser beam is multiplied by the emissivity factor ($\varepsilon_{635\ \rm nm} = 0.264$). Equilibrium temperature plotted versus laser intensity is shown in Fig. 7. We added a similar dependence for the solar spectrum ($\varepsilon_{\rm Sun} = 0.286$) without background (we neglect the 4-K space background radiation). The comparison of two profiles in this figure shows that the temperature of the grain in our experiment is similar to that expected near the Venus orbit.

An exponential dependence of the diffusion coefficient on the temperature means that this coefficient can differ by several orders of magnitude in different places of the space. The gas accumulated during a long time in the cold interstellar medium can then be quickly released near the Sun and change the mass composition of the pick-up ions.

The change of the diffusion coefficient with temperature influences strongly the amount of the gas that can be dissolved. Fig. 8 shows a computed maximum of the dissolved mass as a function of the N/D ratio for the sputtering yield, $Y = 1$. The dashed line neglects the grain sputtering, and it rises without limitations, whereas the full line exhibits a clear saturation that results from the fact that the grain is sputtered off earlier than the diffusion established an equilibrium density profile of the dissolved gas. However, we should point out that the results for large portions of the dissolved gas should be taken with care because our computation does not include structural changes of the grain that occur due to implantation of ions.

VI. Conclusion

We have presented the measurements of the diffusion of Ar atoms that were implanted into the amorphous carbon grain. This measurement was compared with theoretically obtained solutions of the diffusion equation. Our calculations show that the number of atoms that can be dissolved in a particular grain is directly proportional to its mass and inversely proportional to the diffusion coefficient of a given ion in the grain material. The time needed to reach this saturation level increases with the grain dimensions and decreases with the diffusion coefficient. Under our laboratory conditions, the maximum amount of the dissolved gas is as high as 2.2% of the grain mass, and this equilibrium density would be reached in ≈ 1000 h if the grain sputtering is neglected. On the other hand, the sputtering would completely destroy the grain in a comparable time. Since the diffusion coefficient strongly increases with temperature whereas the sputtering rate does not, the grain radiation budget should be taken into account in all considerations.

Acknowledgment

The authors would like to thank Prof. Vítek for endless discussions.

References

[1] I. Mann, H. Kimura, D. A. Biesecker, B. T. Tsurutani, E. Grün, R. B. McKibben, J.-C. Liou, R. M. MacQueen, T. Mukai, M. Guhathakurta, and P. Lamy, "Dust near the sun," *Space Sci. Rev.*, vol. 110, no. 3/4, pp. 269–305, Jan. 2004.

[2] I. Mann, "Interplanetary medium—A dusty plasma," *Adv. Space Res.*, vol. 41, no. 1, pp. 160–167, 2008.

[3] T. Minato, M. Köhler, H. Kimura, I. Mann, and T. Yamamoto, "Momentum transfer to interplanetary dust from the solar wind," *Astron. Astrophys.*, vol. 424, no. 2, pp. L13–L16, Sep. 2004.

[4] P. M. Banks, "Interplanetary hydrogen and helium from cosmic dust and the solar wind," *J. Geophys. Res.*, vol. 76, no. 19, pp. 4341–4348, Jan. 1971.

[5] R. S. Rajan, D. E. Brownlee, D. Tomandl, P. W. Hodge, H. Farrar, and R. A. Britten, "Detection of 4He in stratospheric particles gives evidence of extraterrestrial rigin," *Nature*, vol. 267, no. 5607, pp. 133–134, May 1977.

[6] A. O. Nier, "Helium and Neon in interplanetary dust particles," in *Analysis of Interplanetary Dust Particles*, vol. 310, E. Zolensky, T. L. Wilson, F. J. M. Rietmeijer, and G. J. Flynn, Eds. College Park, MD: AIP, 1994, ser. American Institute of Physics Conference Series, pp. 115–126.

[7] H. J. Fahr, H. W. Ripken, and G. Lay, "Plasma-dust interactions in the solar vicinity and their observational consequences," *Astron. Astrophys.*, vol. 102, no. 3, pp. 359–370, Oct. 1981.

[8] M. Gruntman, "H_2^+ pickup ions in the solar wind: Outgassing of interplanetary dust," *J. Geophys. Res.*, vol. 101, no. A7, pp. 15 555–15 568, Jul. 1996.

[9] P. Vernazza, R. P. Binzel, A. Rossi, M. Fulchignoni, and M. Birlan, "Solar wind as the origin of rapid reddening of asteroid surfaces," *Nature*, vol. 458, no. 7241, pp. 993–995, Apr. 2009.

[10] C. Plainaki, A. Milillo, S. Orsini, A. Mura, E. de Angelis, A. M. di Lellis, E. Dotto, S. Livi, V. Mangano, S. Massetti, and M. E. Palumbo, "Space weathering on near-Earth objects investigated by neutral-particle detection," *Planet. Space Sci.*, vol. 57, no. 3, pp. 384–392, Mar. 2009.

[11] L. V. Starukhina, "Polar regions of the moon as a potential repository of solar-wind-implanted gases," *Adv. Space Res.*, vol. 37, no. 1, pp. 50–58, 2006.

[12] G. Federici and C. Skinner, "Nuclear fusion research: Understanding plasma-surface interactions," in *Tritium Inventory in the Materials of the ITER Plasma-Facing Components*, vol. 78, *Chemical Physics*. Berlin, Germany: Springer-Verlag, Jan. 2006, ch. 12, pp. 287–317.

[13] H. Yoshida, M. Taniguchi, K. Yokoyama, Y. Yamauchi, Y. Hirohata, M. Akiba, and T. Hino, "Deuterium retention in carbon dust and

carbon–tungsten mixed dust prepared by deuterium arc discharge," *J. Nucl. Mater.*, vol. 329–333, pt. 1, pp. 790–794, Aug. 2004.
[14] P. Shukla and N. Tsintsadze, "Charged dust grain acceleration in tokamak edges," *Phys. Lett. A*, vol. 372, no. 12, pp. 2053–2055, Mar. 2008.
[15] D. Rudakov, W. West, C. Wong, N. Brooks, T. Evans, M. Fenstermacher, M. Groth, S. Krasheninnikov, C. Lasnier, A. McLean, A. Pigarov, W. Solomon, G. Antar, J. Boedo, R. Doerner, E. Hollmann, A. Hyatt, R. Moyer, and J. Watkins, "Migration of artificially introduced micron-size carbon dust in the DIII-D divertor," *J. Nucl. Mater.*, vol. 363–365, pp. 227–232, Jun. 2007.
[16] R. D. Kolasinski, J. E. Polk, D. Goebel, and L. K. Johnson, "Carbon sputtering yield measurements at grazing incidence," *Appl. Surf. Sci.*, vol. 254, no. 8, pp. 2506–2515, Feb. 2008.
[17] I. Čermák, "Laboruntersuchung elektrischer Aufladung kleiner Staubteilchen," Ph.D. dissertation, Naturwissenschaftlich-Mathematischen Gesamtfakultät, Ruprecht-Karls-Universität, Heidelberg, Germany, Nov. 1994.
[18] P. Žilavý, Z. Sternovský, I. Čermák, Z. Němeček, and J. Šafránková, "Surface potential of small particles charged by the medium-energy electron beam," *Vacuum*, vol. 50, no. 1/2, pp. 139–142, May/Jun. 1998.
[19] J. Pavlů, A. Velyhan, I. Richterová, Z. Němeček, J. Šafránková, I. Čermák, and P. Žilavý, "Mass-loss rate for MF resin microspheres," *IEEE Trans. Plasma Sci.*, vol. 32, no. 2, pp. 704–708, Apr. 2004.
[20] M. Jeřáb, I. Richterová, J. Pavlů, J. Šafránková, and Z. Němeček, "Influence of charging conditions on field ion emission from dust grains," *IEEE Trans. Plasma Sci.*, vol. 35, no. 2, pp. 292–296, Apr. 2007.
[21] J. F. Ziegler, J. P. Biersack, and M. D. Ziegler, *SRIM*, 2009. ver. 2008.04. [Online]. Available: http://www.srim.org
[22] J. F. Ziegler, J. P. Biersack, and M. D. Ziegler, *SRIM—The Stopping and Range of Ions in Matter*. Morrisville, NC: Lulu Press Co., 2008.
[23] M. Vyšinka, J. Vaverka, J. Pavlů, Z. Němeček, and J. Šafránková, "Depth profiles of ions implanted into spherical dust grains—A trim based model," in *Proc. Contrib. Papers, Part II—Phys. Plasmas Ionized Media WDS*, J. Šafránková and J. Pavlů, Eds., 2009, pp. 195–201.
[24] R. Behrisch and W. Eckstein, *Sputtering by Particle Bombardment*, vol. 110, R. Behrisch and W. Eckstein, Eds. Berlin, Germany: Springer-Verlag, 2007, ser. Topics in Applied Physics.
[25] P. Laven, "Effects of refractive index on glories," *Appl. Opt.*, vol. 47, no. 34, pp. H133–H142, Dec. 2008.
[26] P. Laven, *MiePlot*, 2009. v4. [Online]. Available: http://www.philiplaven.com/mieplot.htm
[27] C. Jager, H. Mutschke, and T. Henning, "Optical properties of carbonaceous dust analogues," *Astron. Astrophys.*, vol. 332, pp. 291–299, Apr. 1998.
[28] M. W. Williams and E. T. Arakawa, "Optical properties of glassy carbon from 0 to 82 eV," *J. Appl. Phys.*, vol. 43, no. 8, pp. 3460–3463, Aug. 1972.

Martin Beránek was born in Prague, Czech Republic, in 1983. He received the M.S. degree from Charles University, Prague, in 2007, where he is currently working toward the Ph.D. degree in the Department of Surface and Plasma Science, Faculty of Mathematics and Physics.

Marek Vyšinka was born in Brno, Czech Republic, in 1984. He received the M.S. degree from Charles University, Prague, Czech Republic, in 2008, where he is currently working toward the Ph.D. degree in the Department of Surface and Plasma Science, Faculty of Mathematics and Physics.

His recent research interest includes the laboratory simulation of elementary processes in dusty plasmas.

Jiří Pavlů was born in Pardubice, Czech Republic, in 1977. He received the M.S. and Ph.D. degrees from Charles University, Prague, Czech Republic, in 2001 and 2005, respectively.

Currently, he is a Senior Assistant with the Space Physics Laboratory, Department of Surface and Plasma Science, Faculty of Mathematics and Physics, Charles University. His research interests include the laboratory investigations of elementary processes on dust grains induced by electron, ion, and photon irradiations.

Ivana Richterová was born in Český Brod, Czech Republic, in 1979. She received the M.S. degree from Charles University, Prague, Czech Republic, in 2003, where she is currently working toward the Ph.D. degree in the Space Physics Laboratory, Department of Surface and Plasma Science, Faculty of Mathematics and Physics.

Her research is devoted to the laboratory investigation and modeling of elementary charging processes on dust grains.

Zdeněk Němeček was born in Prague, Czech Republic, in 1947. He received the M.S., Ph.D., and Dr.Sc. degrees from Charles University, Prague, in 1971, 1982, and 1996, respectively.

Since 1971, he has been holding several positions with the Faculty of Mathematics and Physics, Charles University, where he currently serves as the Dean. His research interests include the solar-wind interaction with the Earth's magnetosphere and the laboratory simulations of plasma processes.

Jana Šafránková was born in Teplice, Czech Republic, in 1947. She received the M.S., Ph.D., and Dr.Sc. degrees from Charles University, Prague, Czech Republic, in 1972, 1982, and 1996, respectively.

Since 1971, she has been holding several positions with the Faculty of Mathematics and Physics, Charles University, where she is currently the Director of the Department of Surface and Plasma Science and the Head of the Space Physics Laboratory. Her recent research interests include the magnetospheric physics and laboratory simulation of elementary processes in dusty plasmas.

K. Němeček et al. [2011]

Němeček, Z., Pavlů, J., Šafránková, J., Beránek, M., Richterová, I., Vaverka, J., Mann, I., Lunar dust grain charging by electron impact: Dependence of the surface potential on the grain size. *Astrophys. J.* 738 (1): 14, 2011.

The Astrophysical Journal, 738:14 (7pp), 2011 September 1 doi:10.1088/0004-637X/738/1/14

LUNAR DUST GRAIN CHARGING BY ELECTRON IMPACT: DEPENDENCE OF THE SURFACE POTENTIAL ON THE GRAIN SIZE

Z. Němeček[1], J. Pavlů[1], J. Šafránková[1], M. Beránek[1], I. Richterová[1], J. Vaverka[1], and I. Mann[2]
[1] Faculty of Mathematics and Physics, Charles University, Prague, Czech Republic
[2] Belgian Institute for Space Aeronomy, Brussels, Belgium
Received 2011 February 17; accepted 2011 June 5; published 2011 August 9

ABSTRACT

The secondary electron emission is believed to play an important role for the dust charging at and close to the lunar surface. However, our knowledge of emission properties of the dust results from model calculations and rather rare laboratory investigations. The present paper reports laboratory measurements of the surface potential on Lunar Highlands Type regolith simulants with sizes between 0.3 and 3 μm in an electron beam with energy below 700 eV. This investigation is focused on a low-energy part, i.e., $\leqslant$100 eV. We found that the equilibrium surface potential of this simulant does not depend on the grain size in our ranges of grain dimensions and the beam energies, however, it is a function of the primary electron beam energy. The measurements are confirmed by the results of the simulation model of the secondary emission from the spherical samples. Finally, we compare our results with those obtained in laboratory experiments as well as those inferred from in situ observations.

Key words: dust, extinction – planetary systems

1. INTRODUCTION

Photoelectron emission, sticking and recombination of plasma particles, secondary electron emission (SEE), thermionic and field ion and electron emissions electrically charge dust grains in space. Their charge depends on the UV flux, the size, shape, and structure of the grains, their velocity relative to the plasma, and the plasma temperature. Since photoelectron, secondary electron, and thermionic emissions vary with the material, the dust surface charge is also influenced by the dust composition. As a result of the dominating photoelectron emission caused by the solar radiation, dust grains in the interplanetary medium are usually positively charged and their charges correspond to surface potentials relative to infinity between 5 and 10 V (Mukai 1981; Whipple 1981). Differences among dust grains of various compositions occur for higher plasma temperatures where SEE becomes important (Kimura & Mann 1998). Moreover, the dust surface potential depends on the charging history of grains (Whipple 1981; Meyer-Vernet 1982; Velyhan et al. 2004).

In the space, grain charging by SEE due to the impact of energetic electrons is significant in environments where these high-energy electrons are present. In dense plasma regions where the electron flux is significant, the sign and value of the dust grain surface potential are determined by the energy of the impinging electrons. Electron attachment dominates in the eV range but, at electron energies above about 10 eV, SEE becomes important and causes a reduction of the negative potential. When the total SEE yield reaches the value larger than unity, the surface potential changes its sign from negative to positive values (Meyer-Vernet 1982; Horanyi & Goertz 1990). This effect has been demonstrated in laboratory experiments (Walch et al. 1998; Pavlů et al. 2009).

Richterová et al. (2007) have studied the profiles of equilibrium surface potentials at glass grains as a function of the beam energy over a wide range of diameters. The low-energy parts (below several hundreds of eV) of the profiles are identical because neither η (the backscattered yield defined as the mean number of backscattered electrons per one primary electron) nor δ (the secondary electron yield) depend on the grain diameter in this energy range. The shape of these parts of the curves is determined by the energetic dependence of the secondary emission yield and energy spectrum of secondary electrons. This approach was applied, for instance, to the charging of water ice grains in the Saturn magnetosphere, where Jurac et al. (1995) show that the surface potentials are not sensitive to the grain size as long as the grains are not much smaller than 0.1 μm.

On the other hand, high-energy parts strongly depend on the grain size. This effect is connected with an increasing number of backscattered primary electrons. When η approaches unity, the grain is charged positively by outgoing secondary electrons because primary electrons do not compensate this charge and the potential of the grain rises.

The lunar surface is composed of rocks and regolith, i.e., soil-like layer with the grain size from centimeters to submicron scales (e.g., Stubbs et al. 2006). The surface is exposed to solar ultraviolet (UV) and X-rays as well as solar and magnetospheric plasma and energetic particles (Halekas et al. 2009b). All these processes generate currents to the surface and can produce an escaping flux of secondary electrons. Each of these charging currents depends on the electrostatic potential of the surface with respect to the surrounding plasma. Due to high variability of these charging currents along the Moon orbit around the Earth, lunar surface potentials can vary over orders of magnitude (Halekas et al. 2005, 2007). On the sunlit hemisphere of the Moon, photoelectron currents usually prevail, and the surface charges to a small positive potential. On the night side, currents of energetic electrons tend to dominate, and the surface charges to a negative potential. However, SEE can complicate expectations providing an additional positive current source, and thus the nightside surface could even charge positive (Halekas et al. 2008). Evaluation of the Lunar Prospector (Halekas et al. 2009a) in situ measurements suggests that the secondary emission yield of the lunar regolith is by a factor $\approx$3 lower than the measured for samples in the laboratory. By contrast, Abbas et al. (2010) reported laboratory results of the charging of dust grains with dimensions of 0.2–13 μm selected from the Apollo 11 and 17 missions and exposed by the monoenergetic electron beam in the 10–200 eV energy range. The authors obtained much larger secondary emission yield than reported

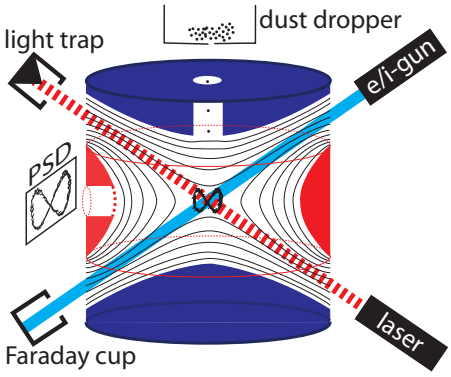

Figure 1. Principles of the experimental setup. The AC voltage is applied between blue and red rotationally symmetric hyperbolic electrodes; the thin black lines stand for its equipotentials. The grain oscillations are projected onto the position sensitive detector (PSD). Note that the frequency in the radial direction is twice large than in the axial direction due to the geometry of our trap.

from other laboratory investigations (e.g., Richterová et al. 2007).

The lunar regolith consists of dust grains of various sizes, and the distant spacecraft cannot resolve individual potentials but provides a mean value. As noted above, it is generally expected and proved by secondary emission models that the grain potential depends on the incident electron energy but not on the dimensions of individual grains. Consequently, the measured mean value would be about equal to the surface potentials of individual grains on or above the lunar surface. However, Abbas et al. (2010) estimations provide the equilibrium surface potential independent on the primary energy but rising with the grain size.

Uncertainties in secondary emission yield estimations may contribute to the poor accuracy of predictions from models, thus new laboratory measurements of the secondary emission from a lunar regolith under realistic charging conditions could solve this issue. For this reason, we studied changes of the surface potential of small grains (with sizes of 0.3–3 μm) in a narrow energy range (75 and 100 V) because it is a lower limit of our apparatus (and our electron beam source). We used Lunar Highlands Type (LHT) lunar stimulant, thus we can directly compare our results with measurements of other authors or with in situ observations.

2. EXPERIMENTAL SETUP

The heart of our measuring setup is schematically shown in Figure 1. Since details of our experiment can be found in Čermák (1994), Čermák et al. (1995), Žilavý et al. (1998), and Pavlů et al. (2004b, 2009), we will describe only the principal features for the present paper.

Our investigations are based on trapping a single dust grain in an electrodynamic quadrupole and its influencing by tunable monoenergetic ion and/or electron beams. The quadrupole is supplied with the symmetrical AC voltage (the voltage ranges usually from 400 to 900 V in a frequency range of 0.3–3 kHz), thus the zero potential is in the middle of the trap where the grain is levitating. Moreover, this configuration provides a straight line through the trap along which the AC potential is zero (Figure 1). Consequently, the energy of the beam firing along this line is not altered.

From the quadrupole theory it follows that the vertical electrodes should be supplied by the same voltage. However, we are using two different amplifiers for them in order to apply a symmetrical dumping voltage and symmetrical DC voltage for the compensation of the gravity force. These voltages are small (several volts) but they can deflect the electron beam. Moreover, the AC electric field perpendicular to the beam direction deflects this electron beam. For these reasons, both the electron gun and quadrupole power supply are equipped with a sampling electronics. The electron beam is switched on only inside the time window when the quadrupole voltage is pulled down to zero. According to the test, switching off the quadrupole voltage up to 1/10 of the period does not measurably change the frequency of grain oscillations (Žilavý et al. 1998; Pavlů et al. 2009).

A trapped grain is irradiated by a 635 nm diode laser modulated by 10 kHz. The light scattered by the grain passes a small window in the ring electrode (electrically screened by a grid) and is collected by a simple lens system. The magnified grain image is projected onto the entrance of an image intensifier and its output is optically coupled to a position sensitive detector. Signals from this coordinate detector are amplified by narrow band, and lock-in amplifiers prior to the coordinates of the light spot are calculated. These coordinates are used to control the grain motion by the damping system and to determine the grain oscillation frequency (in the axial direction in our particular case) by a counter or by Fourier analysis.

After several simplifications, theoretical considerations (Čermák 1994) lead to the following relation between the grain oscillation frequency and its charge-to-mass ratio (specific charge, Q/m):

$$\frac{|Q|}{m} = \pi^2 r_0^2 \cdot \frac{f_{\mathrm{AC}} \cdot f}{V_{\mathrm{eff}}} \cdot \frac{1}{\sqrt{1 + (1.8 f / f_{\mathrm{AC}})^2}}, \qquad (1)$$

where $V_{\mathrm{eff}} = V_{\mathrm{AC}}/\sqrt{2}$ is the rms value of the AC voltage on the quadrupole electrodes, V_{AC} is its amplitude, f_{AC} is the frequency of the applied AC voltage, f is the frequency of the grain oscillation in the axial direction, and r_0 denotes the inner radius of the quadrupole ring electrode ($r_0 = 10$ mm).

This relation is based on the assumption of an adiabatic motion of the grain in the quadrupole field. This is valid for a sufficiently high ratio between frequencies of the applied AC voltage and of grain oscillations. Further, the expression assumes an ideal quadrupole field. Any deviation from the ideal hyperbolic geometry results in a contribution of higher multipoles to the total field, the effective potential is non-harmonic and the grain oscillation frequency becomes amplitude dependent. Since the deviation from the quadrupole field increases with the oscillation amplitude, the amplitude must not exceed a certain value for a desired accuracy of the frequency determination. Therefore, a damping system keeps the oscillation amplitude constant at the reasonable level.

The experiment can be run in a broad range of pressures but special techniques were used to allow the operation under ultrahigh vacuum conditions (10^{-9} torr). This is essential in order to reduce the interaction of the grain surface with molecules of the residual atmosphere and to decrease the grain charging by products of ionization of the residual gas. Assuming the pressure of 10^{-9} torr, the mean free path of electrons is of the order of 10^6 cm. Since the ratio of the beam and grain cross-sections is similar, we can expect that the number of ionization events and the number of beam electrons striking

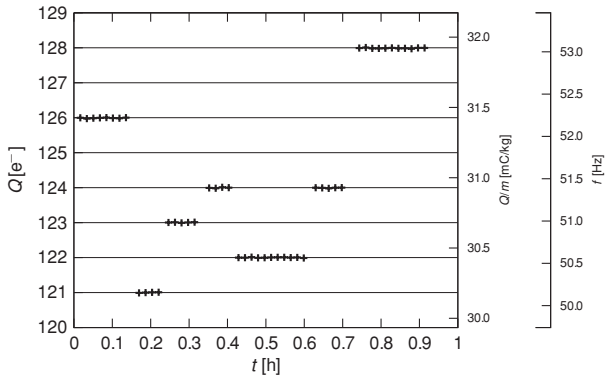

Figure 2. Determination of the grain mass by the elementary charge method. The grain mass calculated from frequency jumps is 6.44×10^{-16} kg.

the grain surface are also similar. The direction of motion of the ionization products is arbitrary and thus their contribution to the grain charging is negligible.

The grain oscillation frequency is the only measurable quantity, and we have developed several techniques to determine the grain mass, charge, capacitance, and surface potential. The detailed description of these techniques can be found in above-mentioned papers, thus we only briefly comment on them here.

The specific charge (charge-to-mass ratio) is determined from the grain oscillation frequency using Equation (1). The charge and mass are separated by a method analogous to the Millikan experiment (Žilavý et al. 1998). A procedure is as follows: the grain is charged by a small (up to several hundreds) number of electrons to be reliably trapped. Then, its charge is changed by a few electrons and the variances of its oscillation frequency together with the known elementary charge allow us to determine the grain mass. We used a low-energy electron beam with a minimum possible intensity, a duration of the sampling pulse ≈1 ms and with a repetition period of ≈6 minutes. Figure 2 shows an example of such measurements. There are three scales on the vertical axis—the measured oscillation frequency of the grain, f in the axial direction, the values of the Q/m ratio calculated according to Equation (1) (two right-hand scales), and the grain charge in units of the elementary charge (the left axis) that was obtained by the linear regression of the data that assigned the steps to the number of electrons (Žilavý et al. 1998; Pavlů et al. 2009). Note that the grain charge steps up and down because the yield of the secondary emission is close to unity for the chosen beam energy, thus impacts of individual electrons can result in both decreasing or increasing of the grain charge due to statistical nature of the emission process. The error of the mass determination depends on many factors but it does not exceed ≈1% under conditions discussed in the present paper.

The grain charge is connected with its surface potential via grain capacitance. To determine it, the grain is charged to a high positive potential by the beam of Ar^+ ions. Then, the energy of the beam is decreased and the beam Ar ions cannot impact the grain but they are scattered in the grain electric field and interact with the residual gas and quadrupole electrodes. These interactions produce low-energy electrons that are attracted by the positive grain, thus the grain is gradually discharged. After some time (≈2 hr), the grain potential becomes numerically equal to the beam energy and the current of beam electrons starts to compensate discharging current. Since both currents are

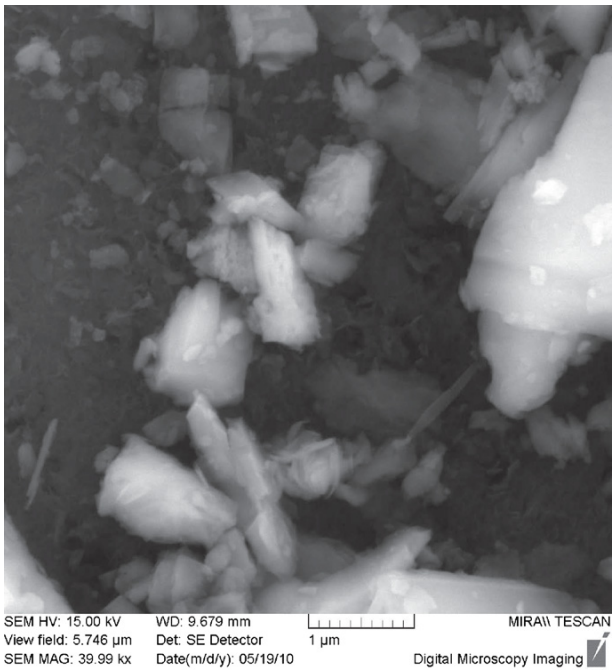

Figure 3. SEM photo of LHT analogs.

linear functions of the grain charge, the point where the beam energy becomes equal to the grain potential can be easily found in the plot of Q/m versus time. This point allows us to determine the proportionality constant between the grain specific charge, Q/m and its surface potential, ϕ, i.e., the specific capacitance, C/m. The error of this method is larger than that for the mass determination. We will provide error estimations for each measurement of a particular grain, however, this error is lower than 10% in general.

3. EXPERIMENTAL RESULTS

The measurements were carried out on LHT dust analogs. The dust sample was produced by grinding from larger pieces, thus the shapes of individual grains are irregular as it can be seen from the scanning electron micrograph (SEM) photo in Figure 3.

Each grain was investigated in several steps that guarantee the same charging conditions and history for each of them.

1. The fresh dust grain was released from the dust dropper and bombarded by the ≈300 eV electron beam when falling through the quadrupole center. This procedure results in a positive charge that allows us the grain trapping.
2. The grain mass (and charge) was determined as described in the previous section.
3. The grain was charged by the electron beam of a tunable energy, and the equilibrium charge-to-mass ratio was recorded for each energy step.
4. The Ar^+ ion bombardment was used for determination of the grain capacitance (see above).
5. Using the known mass and capacitance, the grain specific charge was recalculated into the surface potential.

Figure 4 shows an example of the dependence of the grain surface potential on the beam energy. The paper is focused on lowest energies, but we are showing the measurements up to

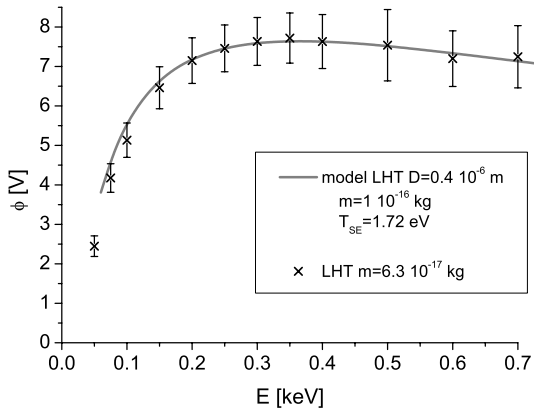

Figure 4. Dependence of the equilibrium surface potential on the energy of the primary electron beam. The crosses show the experimental data, and the full line presents the model prediction (Richterová et al. 2010).

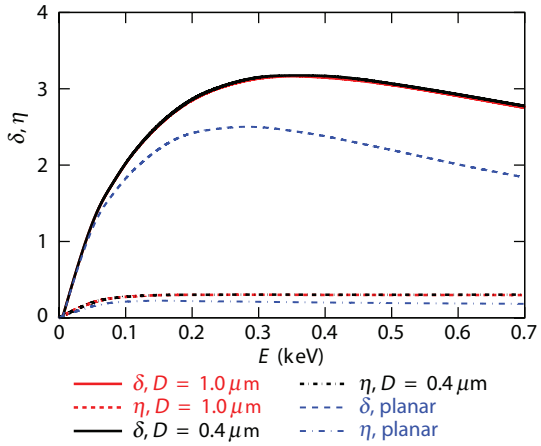

Figure 5. Modeled yields of the true, δ and backscattered, η secondary electrons for LHT spheres with 0.4 and 1 μm diameters. The dotted lines represent the same yields for a planar LHT sample.

700 eV. We are comparing experimental data with the results of the secondary emission model (Richterová et al. 2010). As it can be seen from the figure, the model describes the surface potential rather well at energies above 200 eV and slightly overestimated the potential at lower beam energies. Nevertheless, the differences between measured and modeled potentials stay within the range of measuring errors, thus the model prediction can be used as a support for interpretation of experimental data.

The electrons leaving the grain can be divided into two groups. The first of them, so-called backscattered electrons, consists of primary electrons that entered the grain, lost a part of their energy in the interaction with the grain atoms, and left the grain again. The ratio of numbers of these and all primary electrons is named the backscattered yield, η and cannot exceed unity. However, some electrons of the grain matter gain a sufficient energy to leave the grain in the interactions. Such electrons are called true secondary electrons and their yield, δ can vary in a broad range with the grain material, shape, and dimensions and with the primary electron beam.

The yield of the secondary emission cannot be measured directly but it can be considered as a scaling factor for the secondary emission model. Figure 5 shows the yield of the true

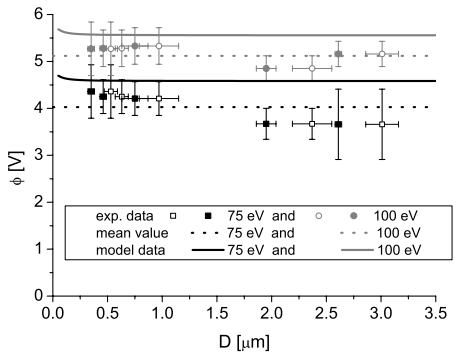

Figure 6. Dependencies of the equilibrium surface potential on grain sizes for two energies of the primary electron beam: 75 eV (squares) and 100 eV (circles). The open symbols stand for diameters determined from the grain capacitance, the filled symbols show the diameters estimated from the grain mass. The full lines show the results of the Richterová et al. (2010) model, and the dashed lines represent the mean values.

(δ) and backscattered (η) secondary electrons calculated for two LHT spheres (0.4 and 1 μm in diameter). For comparison, the calculations for a planar sample from the same material are shown as dotted lines in the figure. The corresponding profiles for two spheres cannot be distinguished in the figure, however, the differences between the planar sample and spheres are significant. This effect is known and is caused by an angular dependence of the secondary emission yield (Jurac et al. 1995; Richterová et al. 2010).

The experimental procedure described above is time consuming, thus we have a full set of measurements only for five grains of sufficiently different masses. The shape of a particular grain is unknown; we use the mass density given by the supplier—Zybek company (2900 kg m^{-3})—and calculate the grain effective diameter, D_m in a spherical approximation. This diameter can be compared with the value of D_C that was obtained from the grain capacitance; again in the spherical approximation. The measured mass, m, the capacitance, C, the diameters computed from these quantities, and their ratio, D_m/D_C, are given in Table 1 for all investigated grains. As it can be seen from the table, the D_m/D_C ratio varies in a broad range. Since the capacitance of the sphere is lower than the capacitance of any other object of the same volume (mass), the D_m/D_C ratio is close to unity for spherical objects, whereas deviation from unity suggests a more complicated shape.

The last two columns in Table 1 show the equilibrium potentials of grains measured under bombardment with the monoenergetic electron beam with the energy of 75 eV and 100 eV, respectively. Unfortunately, our present setup does not allow reliable measurements at lower energies.

The potentials from the table are plotted in Figure 6 as a function of the grain diameter. Since there are two different estimations of the grain diameter in Table 1, each measured point appears twice in Figure 6; at the positions corresponding to D_m and D_C. The dashed lines stand for the mean values of the measured potential for each energy. The full lines show the results of the Richterová et al. (2010) model. The model predicts a constant grain potential in the range from 0.2 to 3.5 μm of the grain diameter and a small rise of this potential for smaller grains. Taking into account the model prediction and the fact that a constant value fits to all measured data if the measuring error is considered, we can conclude that the surface potential is a rising function of the beam energy but it does not depend

Table 1
Details of Five Picked Grains

m (kg)	C (F)	D_m (μm)	D_C (μm)	D_m/D_C	ϕ_{75} (V)	ϕ_{100} (V)
$(6.4 \pm 1.1) \times 10^{-16}$	$(5.0 \pm 1.1) \times 10^{-17}$	0.75 ± 0.12	0.97 ± 0.18	0.8 ± 0.3	4.2 ± 0.4	5.3 ± 0.4
$(2.69 \pm 0.04) \times 10^{-14}$	$(1.68 \pm 0.08) \times 10^{-16}$	2.61 ± 0.03	3.01 ± 0.15	0.87 ± 0.05	3.7 ± 0.8	5.2 ± 0.3
$(1.12 \pm 0.05) \times 10^{-14}$	$(1.3 \pm 0.1) \times 10^{-16}$	1.95 ± 0.09	2.37 ± 0.18	0.82 ± 0.10	3.7 ± 0.3	4.9 ± 0.3
$(1.44 \pm 0.08) \times 10^{-16}$	$(3.5 \pm 0.3) \times 10^{-17}$	0.46 ± 0.03	0.63 ± 0.06	0.73 ± 0.12	4.3 ± 0.4	5.3 ± 0.4
$(6.6 \pm 0.5) \times 10^{-17}$	$(2.9 \pm 0.4) \times 10^{-17}$	0.35 ± 0.03	0.53 ± 0.06	0.66 ± 0.13	4.4 ± 0.6	5.3 ± 0.6

Notes. m is a measured mass of the grain, C is a measured capacitance, D_m and D_C are estimated effective diameters based on measured mass and capacitance, respectively, ϕ_{75} and ϕ_{100} are calculated equilibrium surface potentials of a particular grain under 75 eV and 100 eV electron bombardment, respectively. The errors represent three standard deviations.

on the grain mass in the investigated energy range. The slight decrease of the grain potential with the grain size for 75 V of the beam energy is in the range of measuring errors. Moreover, we can note that the equilibrium potential does not depend on the grain shape because the shape parameter, D_m/D_C varies over a broad range (Table 1).

4. DISCUSSION OF RESULTS

Our measurements show that the equilibrium potential of the grain illuminated by the low-energy (75–100 eV) parallel electron beam does not depend on the grain dimensions and shapes but that it is a rising function of the energy. This is consistent with our previous investigations of the secondary emission from dust grains of different materials (e.g., Richterová et al. 2004, 2006; Pavlů et al. 2008, 2009). These experimental investigations revealed that the effects of shape would be notable either for very small (tens of nanometers) grains or for grain dimensions in the micrometer range with energies exceeding $\approx$1 keV. The same conclusion follows from model calculations (Jurac et al. 1995; Richterová et al. 2010).

Fitting of our measurements to the model leads to the secondary emission yield $\delta \approx 2$ at 100 eV and $\delta \ll 1$ at 10 eV of the primary beam energies. As it can be seen in Figures 4 and 6, the model overestimates the potentials at the low primary energies. There can be two reasons for this overestimation: (1) the distribution of true secondary electrons is non-Maxwellian or (2) the real yield of secondary emission is lower than that given by the model in this range of energies.

Our estimations lead to the maximum of the secondary emission yield $\delta \approx 3.2$ (at about 350 eV) for a small dust grain. This is consistent with previous laboratory experiments but it is much larger than that follows from the Halekas et al. (2009a) analysis of in situ observations. We believe that the value of δ for a planar surface would be more appropriate to the interpretation of the data measured at larger distances from the lunar surface because it reflects partly the effects of a surface roughness. Nevertheless, this value is still larger than an integral value suggested by Halekas et al. (2009a).

On the other hand, Abbas et al. (2010) reported experimental investigations of the samples of the lunar dust and have shown the potential rising with the grain diameter but (as it can be deduced from the text) independent of the beam energy in similar ranges of the beam energies and grain dimensions and that a secondary emission yield varying from 3 to 5.4 at 10 eV of the primary energy.

The differences between our and Abbas et al. (2010) measurements are (1) we use the LHT lunar dust analog, whereas Abbas et al. (2010) investigated the real lunar dust; and (2) the measuring techniques are slightly different. Horányi et al. (1998) compared the secondary emission from two lunar dust stimulants (MLS-1 and JSC-1) and Apollo 17 soil sample in the energy range from 20 to 90 eV and they did not find any significant differences. Consequently, we do not expect that the difference between our and Abbas et al. (2010) results can be connected with different samples.

Let us discuss the energy balance of the secondary emission process. The primary electron is accelerated in the electric field of the charged grain and falls on the surface where it receives an additional energy equal to the work function of the grain material. The energy of the primary electron is then distributed among the electrons of the grain. Those electrons that gained the sufficient energy to overcome the surface barrier (represented by the work function) and grain surface potential leave the grain as secondary electrons. Figure 4 of Abbas et al. (2010) provides the following data: primary electron energy 10 eV, secondary emission yield 5.3, and surface potential 2.2 V. A typical work function of insulators can be considered as 5 eV (e.g., Sternovsky et al. 2001). The 10 eV electron is accelerated to 12.2 eV and receives additional 5 eV of the energy at the surface. The total energy is 17.2 eV. To leave the grain, a secondary electron should gain about 7.2 eV (it is a sum of the work function and the energy corresponding to the grain potential). Neglecting all energy losses, the secondary emission yield cannot exceed a value of $17.2/7.2 = 2.4$. We can conclude that the yield of 5.3 given in Abbas et al. (2010) contradicts to energy conservation.

From this short discussion, it is clear that the results in Figure 4(d) of Abbas et al. (2010) are based on a wrong interpretation of measurements in their Figure 4(c) and that some important factor(s) is(are) neglected. After a careful examination of the conditions of our and Abbas et al. (2010) experiments, we have identified three principal factors that can influence the interpretation of experimental results: (1) the effect of the quadrupole AC electric field on the energy distribution of the primary electrons, (2) influence of the residual gas in the quadrupole, and (3) the method of determining the mass/size of the grains. Thus, following three subsections address these points.

4.1. Quadrupole AC Electric Field and Energy Distributions of Primary Electrons

The Abbas et al. (2010) experiment is based on the trapping of a single dust grain inside the quadrupole-like trap that consists of upper and lower spherical cups and a ring electrode. Unfortunately, an important information on the design of the trap, frequency, and amplitude of the AC voltage applied on the ring electrode as well as the DC voltage used for charge measurements cannot be found neither in the article nor in given references (i.e., Spann et al. 2001; Abbas et al. 2002,

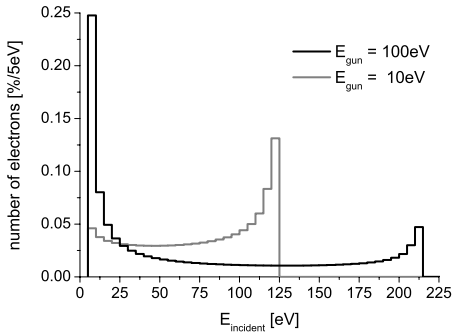

Figure 7. Distribution of electrons launched with the energies of 10 eV (gray) and 100 eV (black), respectively, on the 1 μm grain. The amplitude of the AC voltage is 500 V and geometry of the used model is described in the text. The simulation was performed using the SIMION® software package.

2004; Tankosic & Abbas 2008), thus the discussion is based on the information found in the mentioned papers and on our best estimates.

The electrons enter the trap along its vertical axis and they are influenced by the electric field resulting from the quadrupole AC voltage supplied to the ring electrode. We have used the geometry described in Spann et al. (2001) and modeled the trajectories of electrons within such trap. The amplitude of the AC voltage is 500 V and the top and bottom electrodes are grounded in our model. The electrons were launched from a spot of 1 mm in diameter at the center of the top electrode and the differential flux of electrons on a 1 μm grain placed in the trap center was recorded. Figure 7 shows the energy distribution of electrons launched with energies 10 and 100 eV, respectively. When the AC voltage is negative, primary electrons are decelerated and their energy decreases. Moreover, the negative ring electrode serves as a focusing electrostatic lens and increases the flux of electrons that fall onto the grain. On the other hand, the defocusing effect of the positive voltage decreases the primary flux and (at the same time) accelerates the electrons. It means that the grain is bombarded by electrons over a broad spectrum of energies.

The actual energies of impinging electrons depend on the trap geometry and the AC voltage, thus Figure 7 serves only as an example. Nevertheless, it is clear that considerations made in Abbas et al. (2010) that are based on the knowledge of the primary beam energy are not substantiated.

Moreover, if the numbers used in our model are realistic, the resulting spectrum of electrons launched with the energy of 10 eV will peak at ≈125 eV, whereas a much higher flux of 10 eV electrons will reach the grain when the electrons are launched with the energy of 100 eV. It could explain why Abbas et al. (2010) found a larger secondary emission yield for 10 eV than for 100 eV of the primary energy.

4.2. Influence of the Residual Gas Pressure

Figure 4(c) of Abbas et al. (2010) shows that the positive charge of the grain increases with time. The positive charging can be caused either by electrons leaving the grain or by positive ions falling onto it. Our Figure 7 demonstrates that even in the case of 10 eV primary electrons, the portion of energetic electrons is large enough to cause the SEE and thus it can be a source of the charging current. On the other hand, the energies of primary electrons are sufficient for ionization of the residual gas inside the trap. Moreover, the primary electrons are partly scattered in collisions with the molecules out of the trap axis and accelerated in the AC field to energies even higher than those shown in Figure 7. Since the mean free path of electrons is of the order of 10 m under experimental conditions of Abbas et al. (2010; pressure 10^{-5} to 10^{-6} torr), the ratio of the numbers of primary electrons falling on the grain and electrons colliding with the molecules of the residual gas would be $\approx 10^{-3}$. These collisions create electrons and positive or negative ions that can in turn alter the grain charge. The exact evaluation of the processes in the trap is impossible because the ongoing processes are complex and the boundary conditions are unknown. However, we would like to point out that the influence of the residual gas on the grain charging (especially to negative potentials) was investigated in Pavlů et al. (2004a) and it was shown (in their Figure 2) that the ion contribution should be considered even for pressures of the order of 10^{-8} torr under similar experimental conditions. We can suggest that aforementioned changes of the grain charge are connected with the contribution of the ion current rather than with variations of the secondary emission yield.

4.3. Determination of the Grain Mass and Potential

The mass of investigated lunar dust grains varies in a broad range but the methods of determination of the grain charge is based on knowledge of the mass of the particular grain. Our technique of the elementary charge (Figure 2) provides the grain mass with an uncertainty of the order of 1%.

The authors of Abbas et al. (2010) used the "spring-point method" (Davis 1985; Spann et al. 2001; Abbas et al. 2004; Tankosic & Abbas 2008, and references therein) that is based on a balance between the drag force and "heating" of the grain by the AC electric field in the quadrupole. However, the drag force strongly depends on the grain shape that is unknown. The authors of Abbas et al. (2010) apply a spherical approximation. They use the viscosity of the surrounding gas and experimental corrections that are based on the measurements with the spheres of known diameters. However, depending on the actual grain shape and direction of its motion, the drag coefficient can differ by an order of magnitude. Typical values of the drag coefficients are 0.42 for a sphere, 0.8–1.4 for a cube (depending on spatial orientation), and 2 for a plate perpendicular to the gas flow (e.g., Loth 2008). Neglecting the shape effect leads to overestimating the grain dimensions. For example, twice larger drag coefficient results in an overestimation of the effective diameter of the grain by a factor of $\sqrt{2}$. Since this diameter is used for an estimation of the grain mass, it would differ by a factor of ≈3 and the same uncertainty would apply to the determination of the grain charge.

Taking into account the experimental conditions inside the trap (pressure 10^{-3} torr), the molecular regime would be more appropriate for the drag force estimation because the mean free path of molecules is much larger than the characteristic dimensions of the grain. The exact calculations of the drag force is difficult but it can be simply shown (e.g., Dahneke 1973) that the drag exerting on a sphere and on a cylinder of the same volume (and mass) and twice larger diameter differ by a factor exceeding two and the consequences for the determination of the grain mass would be the same as in the case of viscous interaction discussed above.

5. CONCLUSION

We report the results of the measurements of the secondary emission yield and surface potential carried out on dust samples

from LHT lunar regolith simulants with sizes between 0.3 and 3 μm. We focused on an electron beam with energy below 700 eV. The interpretation of experimental results is supported by the computer model of the secondary emission from spherical samples that reflects the LHT mass composition. The conclusions listed below are different from those that Abbas et al. (2010) derived from their laboratory experiment and we point out some of physical inconsistencies in their data interpretation.

We can briefly summarize our investigations as follows.

1. The secondary emission yield rises with the primary beam energy up to a maximum of ≈3 at 350 eV (Figure 5).
2. The surface potential follows the increase of the secondary emission yield with the primary energy (Figure 4).
3. The surface potential does not depend on the dust grain mass, shape, and dimensions for the grains larger than 0.3 μm (effective diameter) and electron energies lower than ≈200 eV (Figure 6).

Finally, we would like to note that in our experiment, determined secondary emission yield is larger than that inferred from Lunar Prospector measurements above the lunar surface (Halekas et al. 2009a). The authors attributed the low value of the yield to the surface roughness and we are preparing investigations of this effect in the laboratory experiment as well as in simulations.

The work was supported by the Research Plan MSM 0021620860 that is financed by the Ministry of Education of the Czech Republic and partly by the Czech Grant Agency under Contracts 202/08/0063, 202/08/H057, and 209/11/1412. Students M.B. and J.V. thank for support of the Grant Agency of Charles University under Project No. GAUK 171410.

REFERENCES

Abbas, M., Craven, P., Spann, J., West, E., Pratico, J., Tankosic, D., & Venturini, C. 2002, Phys. Scr. T, 98, 99
Abbas, M. M., Craven, P. D., Spann, J. F., West, E., Pratico, J., Tankosic, D., & Venturini, C. C. 2004, ApJ, 614, 781
Abbas, M. M., Tankosic, D., Craven, P. D., LeClair, A. C., & Spann, J. F. 2010, ApJ, 718, 795
Čermák, I. 1994, PhD thesis, Naturwissenschaftlich-Mathematischen Gesamtfakultät, Ruprecht-Karls-Universität, Heidelberg
Čermák, I., Grün, E., & Švestka, J. 1995, Adv. Space Res., 15, 59
Dahneke, B. E. 1973, J. Aerosol Sci., 4, 147
Davis, E. J. 1985, Langmuir, 1, 379
Halekas, J. S., Delory, G. T., Lin, R. P., Stubbs, T. J., & Farrell, W. M. 2008, J. Geophys. Res., 113, A09102
Halekas, J. S., Delory, G. T., Lin, R. P., Stubbs, T. J., & Farrell, W. M. 2009a, Planet. Space Sci., 57, 78
Halekas, J. S., Delory, G. T., Lin, R. P., Stubbs, T. J., & Farrell, W. M. 2009b, J. Geophys. Res., 114, A05110
Halekas, J. S., Lin, R. P., & Mitchell, D. L. 2005, Geophys. Res. Lett., 32, L09102
Halekas, J. S., et al. 2007, Geophys. Res. Lett., 34, L02111
Horanyi, M., & Goertz, C. 1990, ApJ, 361, 155
Horányi, M., Walch, B., Robertson, S., & Alexander, D. 1998, J. Geophys. Res., 103, 8575
Jurac, S., Baragiola, R. A., Johnson, R. E., & Sittler, E. C. 1995, J. Geophys. Res., 100, 14821
Kimura, H., & Mann, I. 1998, ApJ, 499, 454
Loth, E. 2008, Powder Technol., 182, 342
Meyer-Vernet, N. 1982, A&A, 105, 98
Mukai, T. 1981, A&A, 99, 1
Pavlů, J., Němeček, Z., Šafránková, J., & Čermák, I. 2004a, IEEE Trans. Plasma Sci., 32, 607
Pavlů, J., Richterová, I., Němeček, Z., Šafránková, J., & Čermák, I. 2008, Faraday Discuss., 137, 139
Pavlů, J., Šafránková, J., Němeček, Z., & Richterová, I. 2009, Contrib. Plasma Phys., 49, 169
Pavlů, J., Velyhan, A., Richterová, I., Němeček, Z., Šafránková, J., Čermák, I., & Žilavý, P. 2004b, IEEE Trans. Plasma Sci., 32, 704
Richterová, I., Beránek, M., Pavlů, J., Němeček, Z., & Šafránková, J. 2010, Phys. Rev. B, 81, 075406
Richterová, I., Němeček, Z., Šafránková, J., & Pavlů, J. 2004, IEEE Trans. Plasma Sci., 32, 617
Richterová, I., Němeček, Z., Šafránková, J., Pavlů, J., & Beránek, M. 2007, IEEE Trans. Plasma Sci., 35, 286
Richterová, I., Pavlů, J., Němeček, Z., & Šafránková, J. 2006, Phys. Rev. B, 74, 235430
Spann, J., Abbas, M., Venturini, C., & Comfort, R. 2001, Phys. Scr. T, 89, 149
Sternovsky, Z., Horányi, M., & Robertson, S. 2001, J. Vac. Sci. Technol. A, 19, 2533
Stubbs, T. J., Vondrak, R. R., & Farrell, W. M. 2006, Adv. Space Res., 37, 59
Tankosic, D., & Abbas, M. M. 2008, in Lunar and Planetary Institute Science Conference (Lunar and Planetary Science XXXIX) (League City, TX: LPI), 1391
Velyhan, A., Žilavý, P., Pavlů, J., Šafránková, J., & Němeček, Z. 2004, Vacuum, 76, 447
Walch, B., Horanyi, M., & Robertson, S. 1998, in AIP Conf. Proc. 446, Physics of Dusty Plasmas—Seventh Workshop, Boulder, CO, 1998 April, ed. M. Horanyi, S. Robertson, & B. Walch (Melville, NY: AIP), 271
Whipple, E. C. 1981, Rep. Prog. Phys., 44, 1197
Žilavý, P., Sternovský, Z., Čermák, I., Němeček, Z., & Šafránková, J. 1998, Vacuum, 50, 139

L. Vaverka et al. [2013]

Vaverka, J., Richterova, I., Pavlu, J., Safrankova, J., Nemecek, Z., Numerical Calculation of an Equilibrium Dust Grain Potential in Lunar Environment. *IEEE Trans. Plasma Sci.* 41 (4, 2, SI): 740–744, 2013.

Numerical Calculation of an Equilibrium Dust Grain Potential in Lunar Environment

Jakub Vaverka, Ivana Richterová, Jiří Pavlů, Jana Šafránková, and Zdeněk Němeček

***Abstract*—The interaction of plasma particles with dust grains leads to their charging. An equilibrium grain potential depends on a plasma environment, as well as on the grain composition, size, shape, and charging history. We present results of calculations of the equilibrium potential of the grain immersed in the plasma simulating a lunar environment. In calculations, we apply a modified model of the secondary electron emission from dust grains, which takes into account grain sizes, their material, and surface roughness. Since this model describes the increase in the secondary emission yield caused by a finite dimension of the dust grain, the calculations provide a realistic estimation of the dust grain charge in the near-Earth environment. We show that the grain surface potential is a descending function of the grain size and this effect can even lead to opposite polarities of small and large grains.**

***Index Terms*—Dust charging, interplanetary dust, lunar charging.**

I. Introduction

THE LUNAR surface is covered with a layer of dust grains from centimeters to submicrometer scales (e.g., [1]) formed by meteoroid impact over years. This layer is exposed to solar ultraviolet (UV) and X-rays as well as solar and magnetospheric plasma and energetic particles. These processes affect charging currents to the surface and can produce an escaping flux of secondary electrons. The charging currents depend on the electrostatic potential of the surface layer with respect to the surrounding plasma [2]. Evidence strongly suggests that electrostatic potential of such dust grains plays an important role in physical and dynamic processes in the lunar environment.

However, during its orbit around the Earth, dust grains at or above the moon surface are exposed to highly variable charging currents; thus, surface potentials can vary over orders of magnitude [3], [4]. The terrestrial magnetosphere contains very rarefied plasma in the tail lobes, with denser and more energetic electrons and ions in the plasma sheet. Energetic particles (with the energy of tens of kiloelectronvolts) of different origins are trapped in radiation belts. Moreover, their content can be significantly enhanced during geomagnetic substorms and storms, and they can penetrate into the magnetotail [5].

On the other hand, the solar wind consists of relatively cool streaming plasma, whereas the lunar wake (which forms downstream of the moon in the solar wind) contains high-energy, but significantly rarefied, plasma. Moreover, through solar energetic particle events, enhanced fluxes of very energetic particles can impact the dayside moon surface.

On the sunlit side of the moon, a dominating photoelectron current charges the surface to a small positive potential. On the nightside, currents of plasma electrons tend to dominate, and thus, the surface is charged to a negative potential. However, secondary electron emission can play a role in this process providing an additional positive current; thus, the nightside surface could be even positively charged [6]–[8]. Uncertainties in secondary emission yields may contribute to poor predictions of the resulting surface potential; thus, laboratory measurements of the secondary emission from a lunar regolith with realistic charging conditions could help to understand charging processes.

The lunar dust is exposed to the solar wind and UV radiation on the dayside of the moon during the most time from a 29.6-day orbit, but the moon spends also around four days in the Earth's magnetosphere. The typical plasma sheet exposure in each tail crossing may vary from 10 to 40 h [9]. The average density of the solar wind ($n \approx 5$ cm^{-3}) is approximately ten times higher than that of the plasma sheet, but the plasma temperature can reach up to 2 keV for the plasma sheet instead of 10 eV for the solar wind [10]).

For these reasons, an interaction of dust grains with the ions and electrons has been widely studied (e.g., [11]–[17]). Laboratory experiments with small (submicrometer) dust grains have shown that the yield of the secondary electron emission differs from that of large planar samples and strongly depends on the grain size and thus can lead to different equilibrium potentials. Horanyi [14] discussed how a single isolated dust grain collects its electrostatic charge due to relevant charging currents, i.e., electron and ion bombardments, and the production of secondary electrons and photoelectrons. His estimation of the secondary emission yield was approximated by the Sternglass model [18] (hereafter denoted as the S model) and a Maxwellian energy distribution of the emitted electrons. Our paper follows this approach, but the S model is replaced with a more realistic model of Richterova *et al.* [19] (hereafter referred as the R model) that includes an influence of finite dust grain dimensions.

Manuscript received July 31, 2012; revised October 19, 2012; accepted October 23, 2012. Date of publication November 29, 2012; date of current version April 6, 2013. This work was supported in part by the Ministry of Education of the Czech Republic under Research Plan MSM 0021620860 and in part by the Czech Grant Agency under Contract 202/08/0063 and Contract 209/11/1412. The work of J. V. was supported by the Grant Agency of Charles University under Project GAUK 171410.

The authors are with the Department of Surface and Plasma Science, Faculty of Mathematics and Physics, Charles University, 180 00 Prague, Czech Republic (e-mail: jiri.pavlu@mff.cuni.cz).

Digital Object Identifier 10.1109/TPS.2012.2226757

II. Dust Grain Charging in Plasmas

The total current to a dust grain immersed in a plasma is described by the current balance equation, i.e., a sum of all charging/discharging currents

$$\frac{dQ}{dt} = J = J_{\rm e} + J_{\rm i} + J_{\rm pho} + J_{\rm sec}. \tag{1}$$

In typical space environments, electron $J_{\rm e}$ and ion $J_{\rm i}$ currents, the secondary electron current caused by an impact of energetic electrons $J_{\rm sec}$, and the photoemission current $J_{\rm pho}$ dominate, and the other processes such as thermoemission, triboelectric charging, and secondary electron emission caused by ion impacts can be neglected. The currents depend on parameters of plasma (density, energy distribution, velocity, and temperature) and dust grain properties (composition, size, shape, and surface roughness). A very important parameter is the surface potential of a dust grain. A positive charge of the grain enhances the electron flux and lowers the ion flux. The numbers of secondary electrons and photoelectrons are also reduced for positively charged grains. The grain immersed to a plasma reaches an equilibrium surface potential where a sum of all currents to the grain is equal to zero. For simplification, we assume the plasma with the Maxwellian energy distribution parametrized with temperature T and electron and ion densities $n_{\rm e}$ and $n_{\rm i}$, respectively.

We handle with spherical glass grains of a radius a for this particular study. The reasons are following: 1) there are enough data on the secondary emission obtained from laboratory experiments; 2) well-defined geometry; and 3) the glass composition resembles the composition of a typical space dust.

In the case of the Maxwellian plasma and particles smaller than the Debye length, the electron flux $J_{\rm e}$ can be estimated according to [11] as

$$J_{\rm e} = J_{0\rm e} \times \begin{cases} \exp(eU/kT_{\rm e}), & U < 0 \\ (1 + eU/kT_{\rm e}), & U \geq 0 \end{cases} \tag{2}$$

where U is the surface potential of the grain, e is the elementary charge, k is Boltzmann's constant, and $J_{0\rm e} = 4\pi a^2 n_{\rm e}(kT_{\rm e}/2\pi m_{\rm e})^{1/2}$.

The ion flux can be generally calculated by the same way as the electron flux as

$$J_{\rm i} = J_{0\rm i} \times \begin{cases} \exp(-eU/kT_{\rm i}), & U \geq 0 \\ (1 - eU/kT_{\rm i}), & U < 0. \end{cases} \tag{3}$$

When dust–plasma relative velocity w can be comparable or even larger than the ion thermal speed, it is necessary to use equations with a drifting Maxwellian distribution for ion current calculations [14], [20]. Thus, for negatively charged grains, the ion flux is

$$J_{\rm i} = \frac{J_{0\rm i}}{2}\left[\left(M^2 + \frac{1}{2} - \frac{eU}{kT_{\rm i}}\right)\frac{\sqrt{\pi}}{M}{\rm erf}(M) + \exp(-M^2)\right] \tag{4}$$

where $M = w/(2kT_{\rm i}/m_{\rm i})^{1/2}$ is the relative Mach number (the ratio of the dust–plasma relative velocity over the ion thermal speed), and erf stands for error function.

For positively charged grains, the ion flux is given by

$$\begin{aligned} J_{\rm i} = \frac{J_{0\rm i}}{4}\Bigg\{&\left(M^2 + \frac{1}{2} - \frac{eU}{kT_{\rm i}}\right)\frac{\sqrt{\pi}}{M} \\ &\cdot\left[{\rm erf}(M + \sqrt{eU/kT_{\rm i}}) + {\rm erf}(M - \sqrt{eU/kT_{\rm i}})\right] \\ &+ \left(\sqrt{\frac{eU}{kT_{\rm i}M}} + 1\right)\exp\left[-\left(M - \sqrt{\frac{eU}{kT_{\rm i}M}}\right)^2\right] \\ &- \left(\sqrt{\frac{eU}{kT_{\rm i}M}} - 1\right)\exp\left[-\left(M + \sqrt{\frac{eU}{kT_{\rm i}M}}\right)^2\right]\Bigg\}. \end{aligned} \tag{5}$$

Dust grains exposed to the solar light are charged by a UV part of the spectrum. We assume the Maxwellian energy distribution of photoelectrons with the average energy of $kT_{\rm pho}$ ($\approx$1–3 eV). The photoelectron flux from the grain can be written as

$$J_{\rm pho} = 2.5 \times 10^{10}\pi a^2 e\kappa/d^2 \begin{cases} 1, & U < 0 \\ \exp(-eU/kT_{\rm pho}), & U \geq 0 \end{cases} \tag{6}$$

where d is the distance from the Sun measured in astronomical unit (AU), and κ is the efficiency factor close to unity for conductive and to 0.1 for dielectric materials [2].

The yield of the secondary electron emission (the ratio of secondary electrons to primary electrons) depends on the grain material and the energy of primary electrons. The S model approximates the yield of secondary emission by the formula

$$\delta(E) = \epsilon^2 \delta_{\rm M}(E/E_{\rm M})\exp\left[-2(E/E_{\rm M})^{1/2}\right] \tag{7}$$

where ϵ is the Euler number, and $\delta_{\rm M}$ is the maximum of the secondary electron yield at energy $E_{\rm M}$. For a glass sample, $\delta_{\rm M} = 3.4$ and $E_{\rm M} = 350$ eV. This formula describes the yield of true secondary electrons from semi-infinite planes and neglects the yield of backscattered primary electrons.

However, we apply the R model because it provides both components of the secondary emission yield σ: a true secondary electron emission yield δ and a backscattered primary electron yield η. These coefficients obtained by the R model are depicted in Fig. 1 for several diameters of spherical grains and compared with the S model that does not consider the grain size. We can see that the yield of the secondary electron emission σ [see Fig. 1(c)] is significantly higher in the R model than in the S model for primary electron energies above $\approx$1 keV and for all grain diameters due to an increased portion of backscattered electrons [see Fig. 1(b)]. Note that the energy corresponding to the secondary maximum (that is most prominent at the σ profile for a 100-nm grain) increases with the grain diameter. This maximum appears at the energy for which the penetration depth of primary electrons becomes equal to the beam energy. Under this condition, the yield of backscattered electrons increases toward unity, and the emission of true secondary electrons becomes more intensive.

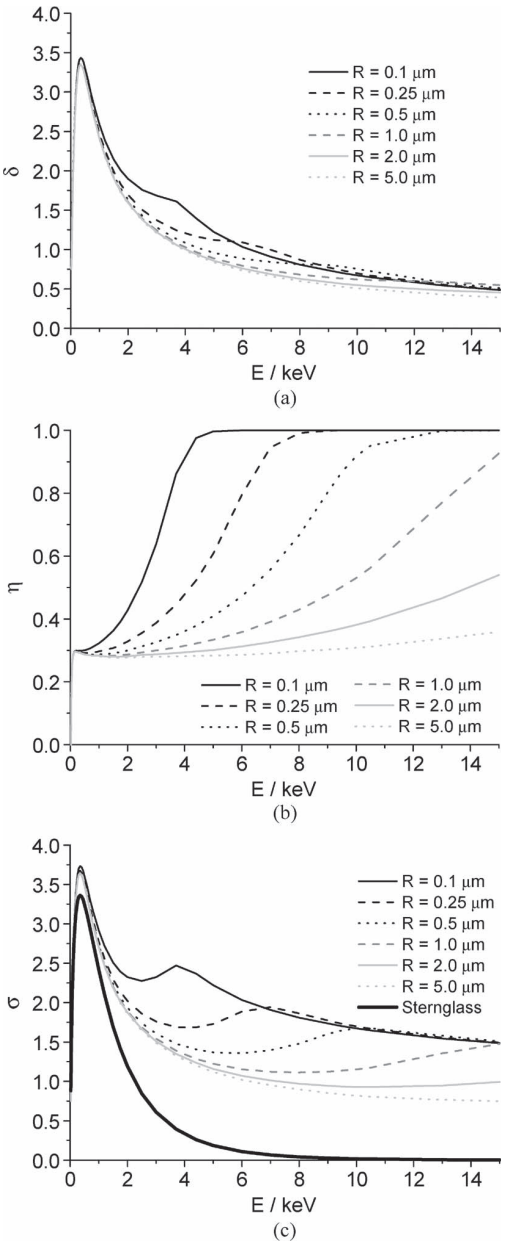

Fig. 1. (a) True secondary electron emission yield. (b) Backscattered electron yield. (c) Total yield of secondary emission. All panels for several radii of glass grains with respect to the primary electron energy.

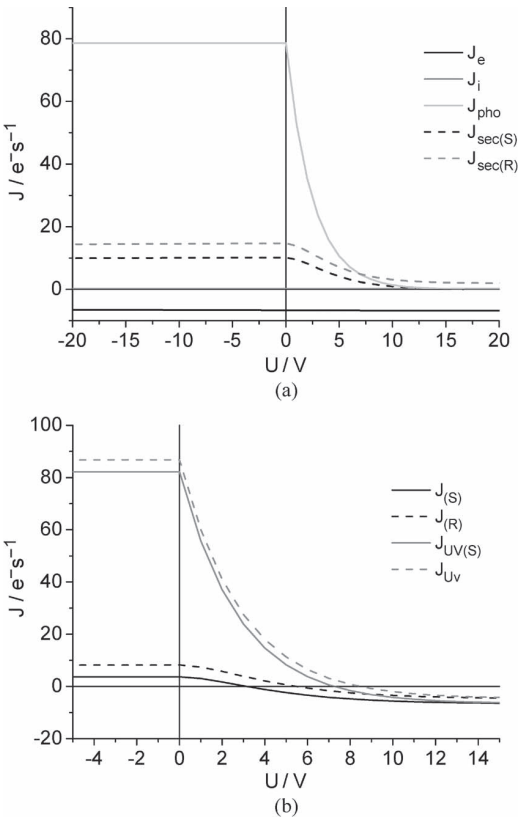

Fig. 2. (a) Charging currents for the spherical glass grain ($r = 1$ μm) and plasma sheet conditions with respect to the grain surface potential. $J_{\rm e}$ is the electron current, $J_{\rm i}$ is the ion current, $J_{\rm sec(S)}$ is the secondary electron current calculated according to [18], $J_{\rm sec(R)}$ is the secondary electron current according to [19], and $J_{\rm pho}$ is the photocurrent. (b) Total charging currents for the same spherical glass grain and the same plasma environment with respect to the grain surface potential. $J_{\rm (S)} = J_{\rm e} + J_{\rm i} + J_{\rm sec(S)}$, $J_{\rm (R)} = J_{\rm e} + J_{\rm i} + J_{\rm sec(R)}$, $J_{\rm UV(S)} = J_{\rm e} + J_{\rm i} + J_{\rm pho} + J_{\rm sec(S)}$, and $J_{\rm UV(R)} = J_{\rm e} + J_{\rm i} + J_{\rm pho} + J_{\rm sec(R)}$.

III. Estimation of the Grain Equilibrium Potential Under Plasma Sheet Conditions

Charging currents of the spherical glass grain ($r = 1$ μm) immersed in the plasma under conditions such as those in the plasma sheet ($n_{\rm i} = n_{\rm e} = 0.1$ cm^{-3}, $T_{\rm e} = T_{\rm i} = 1$ keV, $w =$ 200 km/s) calculated using (2)–(6) are shown in Fig. 2(a). The secondary emission current is calculated in two ways: $J_{\rm sec(S)}$ uses the S formula, whereas $J_{\rm sec(R)}$ uses the R model. Fig. 2(b) shows the sum of the currents in a particular environment (subscript UV stands for daylight conditions, no subscript means a shadow) calculated with the S approximation of the secondary emission (subscript S) or with the R model (subscript R). The equilibrium grain potential is set if the sum of all currents is zero, and one can note that the application of the R model leads to an increase in the grain potential because the secondary electron current that charges the grain positively is larger.

The equilibrium surface potentials U for spherical glass grains and plasma sheet conditions and with and without UV radiation as a function of the plasma temperature are depicted in Fig. 3. Fig. 3(a) shows that, if the photoemission is in operation, all grains are positively charged and the grain potential is a descending function of the grain diameter for temperatures above 1 keV; the differences are not too large for typical plasma sheet temperatures of about 2 keV because the photocurrent is a dominating component of the total current. On the other hand, the secondary emission current dominates in absence of UV radiation, and thus, the difference between the S (thick line) and R (thin lines) models becomes significant. The thick line crosses the zero level of the grain potential at ≈1.5 keV. It means that all dust grains regardless of their dimensions would be negatively charged for all temperatures exceeding this threshold if the S model is used. However, an application of the R model leads to enhancement of the secondary emission current that increases the dust grain potential. Consequently,

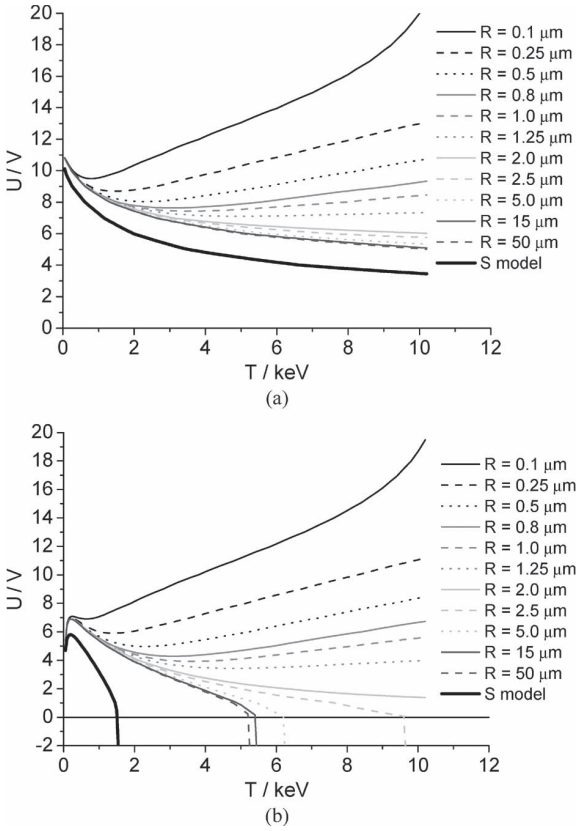

Fig. 3. Equilibrium potential of spherical glass grains in plasma sheet conditions (a) with and (b) without the solar radiation with respect to the plasma temperature. The dotted line stands for a comparison with [18].

small grains (below ≈ 2 μm of diameter) would be positively charged regardless of the temperature. An interesting effect can be expected for temperatures above $\approx$3 keV because the large grains would be negatively charged, whereas the smaller grains positively. Negative potentials of the grains can be rather large, but their determination requires a corresponding modification of the equation for the ion current and addition of other effects such as field emission, and it is out of scope of this short paper.

IV. Discussion

We calculated charging currents and equilibrium surface potentials for spherical glass grains under plasma sheet conditions using the model of the secondary electron emission from dust grains (R model) or the model of the secondary electron emission from planar samples (S model). We should note that the latter approach generally repeats the calculations made by [14]. Since the secondary emission yield does not depend on the dust grain size in the S model, the same does the dust grain potential. Our results show that a more realistic description of the secondary emission process in the R model leads to dependence of the grain potential on its size that is observable in the high-temperature environments.

The presented calculations use a Maxwellian distribution of plasma electrons, but it is well known that space plasmas often exhibit an enlarged portion of energetic electrons. We have simulated this distribution by addition of up to 10% of electrons with ten times higher temperature, but the results shown in Fig. 3 did not substantially change.

Our calculations reveal that the equilibrium potential of the dust grain is a function of the grain size and that this effect can even lead to different polarities of the potential of small and large dust grains and to their spatial separation. Such separation can occur only in the shadow at 1 AU because the photocurrent charges the grains positively regardless of their size. On the other hand, the solar UV radiation decreases with increasing distance from the Sun much faster than the densities in magnetospheres of outer planets (e.g., [21]), and thus, the effects similar to those shown in Fig. 3(b) would be applicable on such an environment, even under sunlight.

The calculations were done for glass spheres, but the results for any typical space dust material (excluding ice) would be similar. On the other hand, the recent paper [22] has shown that the smallest dimension of a nonspherical dust grain determines its secondary emission properties rather than its mass, and thus, the results shown in Fig. 3 should be interpreted in this view.

V. Conclusion

This paper has presented the results of calculations of the surface potential of dust grains in high-temperature plasmas such as that in the Earth's plasma sheet. The calculation reveals that the grain potential is a function of its size. Large (> 100 μm) grains would be negatively charged by hot electrons, whereas the positive potential of smaller grains is a descending function of their size. The negative potentials can be observed only in the shadow because the photocurrent caused by the solar UV radiation is large enough to compensate effects of the secondary emission. Nevertheless, the size dependence of the secondary emission current would cause different positive potentials of grains of different sizes even under sunlight. It has been suggested that the secondary emission can lead to multiple roots of the charging equations, but we did not find such behavior under the conditions studied in this paper.

References

[1] T. J. Stubbs, R. R. Vondrak, and W. M. Farrell, "A dynamic fountain model for lunar dust," *Adv. Space Res.*, vol. 37, no. 1, pp. 59–66, 2006.

[2] E. C. Whipple, "Potentials of surfaces in space," *Rep. Prog. Phys.*, vol. 44, no. 11, pp. 1197–1250, Nov. 1981.

[3] J. S. Halekas, R. P. Lin, and D. L. Mitchell, "Large negative lunar surface potentials in sunlight and shadow," *Geophys. Res. Lett.*, vol. 32, no. 9, pp. L09102-1–L09102-4, May 2005.

[4] J. S. Halekas, D. A. Brain, D. L. Mitchell, R. P. Lin, and L. Harrison, "On the occurrence of magnetic enhancements caused by solar wind interaction with lunar crustal fields," *Geophys. Res. Lett.*, vol. 33, pp. L08106-1–L08106-4, Apr. 2006.

[5] Y. Asano, I. Shinohara, A. Retinò, P. W. Daly, E. A. Kronberg, T. Takada, R. Nakamura, Y. V. Khotyaintsev, A. Vaivads, T. Nagai, W. Baumjohann, A. N. Fazakerley, C. J. Owen, Y. Miyashita, E. A. Lucek, and H. Rème, "Electron acceleration signatures in the magnetotail associated with substorms," *J. Geophys. Res.*, vol. 115, pp. A05215-1–A05215-19, May 2010.

[6] J. S. Halekas, G. T. Delory, R. P. Lin, T. J. Stubbs, and W. M. Farrell, "Lunar Prospector observations of the electrostatic potential of the lunar surface and its response to incident currents," *J. Geophys. Res.*, vol. 113, no. A9, pp. A09102-1–A09102-16, Sep. 2008.

[7] J. S. Halekas, G. T. Delory, R. P. Lin, T. J. Stubbs, and W. M. Farrell, "Lunar surface charging during solar energetic particle events: Measurement and prediction," *J. Geophys. Res.*, vol. 114, no. A5, pp. A05110-1–A05110-16, May 2009.
[8] J. S. Halekas, G. T. Delory, R. P. Lin, T. J. Stubbs, and W. M. Farrell, "Lunar Prospector measurements of secondary electron emission from lunar regolith," *Planet. Space Sci.*, vol. 57, no. 1, pp. 78–82, Jan. 2009.
[9] M. Hapgood, "Modelling long-term trends in lunar exposure to the Earth's plasmasheet," *Ann. Geophys.*, vol. 25, no. 9, pp. 2037–2044, Oct. 2007.
[10] J. Halekas, V. Angelopoulos, D. Sibeck, K. Khurana, C. Russell, G. Delory, W. Farrell, J. McFadden, J. Bonnell, D. Larson, R. Ergun, F. Plaschke, and K. Glassmeier, "First results from artemis, a new two-spacecraft lunar mission: Counter-streaming plasma populations in the lunar wake," *Space Sci. Rev.*, vol. 165, no. 1–4, pp. 93–107, Dec. 2011.
[11] N. Meyer-Vernet, ""Flip-flop" of electric potential of dust grains in space," *Astron. Astrophys.*, vol. 105, no. 1, pp. 98–106, Jan. 1982.
[12] V. Chow, D. Mendis, and M. Rosenberg, "Secondary emission from small dust grains at high electron energies," *IEEE Trans. Plasma Sci.*, vol. 22, no. 2, pp. 179–186, Apr. 1994.
[13] J. Svestka, I. Cermak, and E. Grün, "Electric charging and electrostatic fragmentation of dust particles in laboratory," *Adv. Space Res.*, vol. 13, no. 10, pp. 199–202, Oct. 1993.
[14] M. Horanyi, "Charged dust dynamics in the solar system," *Annu. Rev. Astron. Astrophys.*, vol. 34, pp. 383–418, 1996.
[15] I. Čermák, E. Grün, and J. Švestka, "New results in studies of electric charging of dust particles," *Adv. Space Res.*, vol. 15, no. 10, pp. 59–64, May 1995.
[16] J. Pavlů , I. Richterová, Z. Němeček, J. Šafránková, and I. Čermák, "Interaction between single dust grains and ions or electrons: Laboratory measurements and their consequences for the dust dynamics," *Faraday Discuss.*, vol. 137, pp. 139–155, 2008.
[17] X. Wang, M. Horányi, and S. Robertson, "Investigation of dust transport on the lunar surface in a laboratory plasma with an electron beam," *J. Geophys. Res.*, vol. 115, pp. A11102-1–A11102-6, Nov. 2010.
[18] E. Sternglass, "Theory of secondary electron emission under electron bombardment," Westinghouse Res. Lab., Pittsburgh, PA, Scientific Paper 6-94410-2-P9, Jul. 1957.
[19] I. Richterová, M. Beránek, J. Pavlů , Z. Němeček, and J. Šafránková, "Electrons scattered inside small dust grains of various materials," *Phys. Rev. B*, vol. 81, no. 7, pp. 075406-1–075406-7, Feb. 2010.
[20] T. G. Northrop and T. J. Birmingham, "Equilibrium electric potential of spherical, cylindrical, and planar dust grains moving through a plasma," *J. Geophys. Res.*, vol. 101, no. A5, pp. 10 793–10 796, May 1996.
[21] J. D. Scudder, E. C. Sittler, and H. S. Bridge, "A survey of the plasma electron environment of Jupiter: A view from Voyager," *J. Geophys. Res.*, vol. 86, no. A10, pp. 8157–8179, Sep. 1981.
[22] I. Richterová, Z. Němeček, M. Beránek, J. Šafránková, and J. Pavlů , "Secondary emission from non-spherical dust grains with rough surfaces application to lunar dust," *Astrophys. J.*, vol. 761, no. 1, 2012, accepted.

Jakub Vaverka was born in Prague, Czech Republic, in 1983. He received the M.S. degree in 2008 from Charles University, Prague, Czech Republic, where he is currently working toward the Ph.D. degree.

His current research interests include the laboratory simulation of elementary processes in dusty plasmas.

Ivana Richterová was born in Český Brod, Czech Republic, in 1979. She received the M.S. and Ph.D. degrees from Charles University, Prague, Czech Republic, in 2003 and 2012, respectively.

She is currently a Senior Assistant with the Space Physics Laboratory, Department of Surface and Plasma Science, Faculty of Mathematics and Physics, Charles University. Her research is devoted to the laboratory investigation and modeling of elementary charging processes on dust grains.

Jiří Pavlů was born in Pardubice, Czech Republic, in 1977. He received the M.S. and Ph.D. degrees from Charles University, Prague, Czech Republic, in 2001 and 2005, respectively.

He is currently a Senior Assistant with the Space Physics Laboratory, Department of Surface and Plasma Science, Faculty of Mathematics and Physics, Charles University. His research interests include the laboratory investigations of elementary processes on dust grains induced by electron, ion, and photon irradiations.

Jana Šafránková was born in Teplice, Czech Republic, in 1947. She received the M.S., Ph.D., and Dr.Sc. degrees from Charles University, Prague, Czech Republic, in 1972, 1982, and 1996, respectively.

Since 1971, she has held several positions with the Faculty of Mathematics and Physics, Charles University, where she is currently Director of the Department of Surface and Plasma Science and the Head of the Space Physics Laboratory. Her current research interests include the magnetospheric physics and laboratory simulation of elementary processes in dusty plasmas.

Zdeněk Němeček was born in Prague, Czech Republic, in 1947. He received the M.S., Ph.D., and Dr.Sc. degrees from Charles University, Prague, in 1971, 1982, and 1996, respectively.

Since 1971, he has been holding several positions with the Faculty of Mathematics and Physics, Charles University, where he currently serves as the Dean. His research interests include the solar wind interaction with the Earth's magnetosphere and the laboratory simulations of plasma processes.

M. Pavlů et al. [2014]

Pavlů, J., Beránek, M., Vaverka, J., Šafránková, J., Němeček, Z., Richterová, I., Secondary electron emission from martian soil simulant. *J. Geophys. Res.* 119 (1): 199–209, 2014.

AGU PUBLICATIONS

JGR

Journal of Geophysical Research: Planets

RESEARCH ARTICLE

10.1002/2013JE004522

Key Points:
- Mars dust simulant charging by energetic electrons is investigated
- Comparison of secondary emission model with laboratory experiment is presented
- Importance of dust sizes and shapes in presence of energetic electrons is shown

Correspondence to:
Z. Němeček,
zdenek.nemecek@mff.cuni.cz

Citation:
Pavlů, J., M. Beránek, J. Vaverka, J. Šafránková, Z. Němeček, and I. Richterová (2014), Secondary electron emission from Martian soil simulant *J. Geophys. Res. Planets*, *119*, 199–209, doi:10.1002/2013JE004522.

Received 23 SEP 2013
Accepted 24 DEC 2013
Accepted article online 1 JAN 2014
Published online 28 JAN 2014

Secondary electron emission from Martian soil simulant

J. Pavlů[1], M. Beránek[1], J. Vaverka[1], J. Šafránková[1], Z. Němeček[1], and I. Richterová[1]

[1]Department of Surface and Plasma Science, Faculty of Mathematics and Physics, Charles University in Prague, Prague, Czech Republic

Abstract In the recent years, growing interest in dust charging physics is connected with several lander missions running on or planned to the Moon, Mars, and Mercury for a near future. In support of these missions, laboratory simulations are a potential tool to optimize in situ exploration and measurements. In the paper, we have investigated electrical properties of a Martian soil simulant prepared at the Johnson Space Center under name JSC Mars-1 using the dust charging experiment when a single dust grain is trapped in a vacuum chamber and its secondary electron emission is studied. The exposure of the grain to the electron beam revealed that the grain surface potential is low and generally determined by a mean atomic number of the grain material at a low-energy range ($<$ 1 keV), whereas it can reach a limit of the field ion emission being irradiated by more energetic electrons. A comparison of model and experimental results reveals an influence of the grain shape and size predominantly in the range of higher ($>$ 2 keV) electron energies. We discuss possible implications of the secondary electron emission for the presence of lightnings on Mars.

1. Introduction

Mars as well as the Moon, Mercury, and other solar system objects (e.g., asteroids and satellites) are covered by a layer of granular material—dust which is called regolith. Being charged by winds and triboelectricity, dust grains can levitate, interact with another grain, or with other surfaces (e.g., meteorites, surface of landers, rovers, drills, and sampling devices). Massive dust clouds that may reach 60–80 km above the Martian surface and surround the entire planet for long periods of time were reported by many authors [e.g., *Gierasch and Goody*, 1973; *Conrath*, 1975; *Clancy et al.*, 2010; *Guzewich et al.*, 2013]. A less dense dusty environment can thus extent to higher altitudes.

The triboelectric charging in the intense dust devils and dust storms are believed to generate large electrostatic fields that significantly influence geophysical and geochemical processes at the surface or in the atmosphere of the planet. This field can exceed 100 kV/m within the Earth [*Freier*, 1960; *Stow*, 1969; *Crozier*, 1964; *Farrell et al.*, 2004] devils. There are no experimental data for Mars but simulations of *Farrell et al.* [2006a] revealed that it can reach 20–40 kV/m. Since the electrical breakdown of the Mars atmosphere is 20 kV/m (in comparison to 3000 kV/m for Earth [*Melnik and Parrot*, 1998]), electrification of windblown sand and dust could trigger electrical discharges. The electrostatic charge of particles can enhance saltation [*Kok and Renno*, 2006, 2008] that can result in the formation of new geological features [*Shinbrot et al.*, 2006].

Recent studies suggest that large electric fields produce energetic electrons and these electron avalanches can activate chemical reactions such as the formation of hydrogen peroxide and the dissociation of methane, and thus alter the composition of the Martian atmosphere [*Atreya et al.*, 2006; *Farrell et al.*, 2006b; *Kok and Renno*, 2009; *Jackson et al.*, 2010]. Moreover, the Martian atmosphere is tenuous (about 4.5–6 torr), and it permits a creation of glow discharges [*Hintze et al.*, 2006] that can lead to charging [*Krauss et al.*, 2003] as well as to degradation of possible organic materials [*Snyder et al.*, 2008]. In robotic and human missions to Mars, charged dust can adhere to equipment and temporarily disrupt its operation (e.g., by covering solar panels) or cause a permanent damage [e.g., *Agui and Nakagawa*, 2005; *Hyatt et al.*, 2007; *Calle et al.*, 2011].

The dominant charging processes at the Mars surface are the triboelectric charging during wind-driven saltation, liftoff processes involving interparticle collisions or separations, and photoionization by UV radiation [*Stow*, 1969; *Sickafoose et al.*, 2001; *Gross et al.*, 2001; *Gross*, 2003; *Krauss et al.*, 2003]. In the absence of direct measurements, the researchers have used laboratory simulation experiments and numerical models that are crucial to optimize in situ exploration and measurements. Many studies have been directed to the electrostatic charging of Martian regolith simulant. The effective work function of regolith was

determined by contact, charging the simulant with various materials [*Gross et al*., 2001; *Sternovsky et al*., 2002; *Sharma et al*., 2008]. Laboratory experiments examined the electrostatic discharges in the mixture of the simulant with other materials [*Krauss et al*., 2006] that are developed during a flow through the wind tunnel [*Merrison et al*., 2004]. On the other hand, effects of triboelectric charging due to fine grain ($<$ 150 μm) movement under simulated Martian conditions have been reported by *Anderson et al*. [2009]. *Forward et al*. [2009a, 2009b] presented the experiments on the charging of regolith simulant and confirmed that smaller particles tend to charge negatively and larger particles charge positively. It provides a mechanism for the charge separation that creates electric fields in Martian dust events (similarly as in a numerical model of *Kok and Renno* [2009]).

From this very brief survey it follows that electrical charging of individual dust grains is an important process because it affects the grain sticking to surfaces and to each other and influences the grain surface chemistry by the flow of ions and electrons. Although the triboelectric effect and photoemission were identified as dominant processes charging the dust of a Martian origin, secondary electron emission (SEE) can play a role under specific circumstances [*El-Taibany and Wadati*, 2007]. The electrons accelerated during dust storm events cause the secondary emission from dust grains, and their influence should be taken into account for self-consistent description of the electric discharges. Moreover, there are another sources of energetic electrons in the Martian environment. Fluxes of suprathermal electrons (of the order of hundred eV) in the regions with a strong crustal magnetization were found at the altitudes of $\approx$ 150 km [*Dubinin et al*., 2008]. *Lundin et al*. [2006] registered an electron acceleration above Mars near the local midnight and found that the electron energy flux is sufficient to cause even weak to moderately strong auroras. Electron densities in the Martian ionosphere increase substantially during solar flares in response to the increased solar irradiation [*Lollo et al*., 2012]. Thus, the electrons accelerated at the magnetospheric boundaries or solar energetic particles [e.g., *McKenna-Lawlor et al*., 2005; *Ulusen et al*., 2012; *Sheel et al*., 2012] penetrate to low altitudes along the magnetic cusps, and they can interact with the dust lifted to these altitudes.

Since secondary emission properties of the Martian dust were not determined yet, we have performed the present study. Several previous studies were oriented on dust grains from silicates (glass – *Richterová et al*. [2007], lunar dust simulant – *Němeček et al*. [2011], and others) that are main constituents of the Mars dust, but there are several differences that can be of importance for the secondary emission (presence of heavy elements, significant volatile content, and larger work function). A further motivation to this investigation is that a regolith simulant JSC Mars-1 can be considered as a typical prototype of a class of the interplanetary dust and the results and conclusions drawn from our laboratory experiments can be applied on such grains. Many of above mentioned studies used JSC Mars-1 which reproduces most of the known properties (spectral characteristics, mineralogy, chemical composition, grain size, density, porosity, and magnetic properties) of the dust on Mars. It is composed of weathered volcanic ash grains $<$ 1 mm in diameter which contain about 43.5 % of SiO_2 [*Allen et al*., 1998a, 1998b].

In this study, we focus on the secondary electron emission from small (in the range of 1–10 μm) JSC Mars-1 grains, similarly as the fine atmospheric dust on Mars, which has a diameter of around 2–4 μm [*Pollack et al*., 1995]. We compare experimental investigations with the results of numerical simulations that include both spherical and nonspherical grains. Finally, we discuss a role of the secondary electron emission of grains of different shapes in specific Martian conditions.

2. Experimental Setup

The experimental apparatus is based on trapping of a single dust grain in an electrodynamic quadrupole and its influencing by monoenergetic ion and/or electron beams. The present experiment uses the electron beam tunable in the range of 60 eV–10 keV. The electrodynamic quadrupole and the dust reservoir are placed inside an ultrahigh vacuum (10^{-6} Pa) chamber. A levitated grain is irradiated by a 635 nm diode laser light modulated by 10 kHz to reduce a noise. The laser light scattered by the grain is collected by a simple lens system, and the magnified image of grain motion is projected onto the entrance fiber optics of an image intensifier. The intensifier output is optically coupled to a position sensitive 2-D detector. Signals from this 2-D detector are amplified by narrow band lock-in amplifiers prior to the coordinates of the light spot are determined. These coordinates are used to control the motion of the particle by a damping system. The current charge-to-mass ratio, Q/m is calculated from the measured particle secular frequency, f_z, the value

of the quadrupole supply voltage, V_{ac}, and its frequency, f_{ac}. According to *Čermák* [1994], the Q/m ratio is given by

$$\frac{Q}{m} = \pi^2 r_0 \frac{f_{ac} \cdot f_z}{V_{ac}} \cdot c(f_z/f_{ac}) \quad (1)$$

where r_0 stands for the inner radius of the middle quadrupole electrode and c is a correction function (close to unity) which reflects the f_z/f_{ac} ratio and actual field geometry inside the trap. In order to ensure the stability of the trapped particle, the information on the Q/m ratio is used to control the frequency of the quadrupole voltage.

The grain oscillation frequency is the only measurable quantity, and we have developed several techniques to determine the grain size, mass, charge, capacitance, and other parameters. The details of the experiment as well as the description of these techniques could be found in *Čermák* [1994], *Žilavý et al*. [1998], *Pavlů et al*. [2004, 2008], and *Němeček et al*. [2011].

3. Results and Discussion

We investigate the secondary electron emission from the JSC Mars-1 simulant. Since small grains used in this study were made by grinding of large pieces, we have applied the EDX (Energy Dispersive X-ray) spectroscopy and check the elemental composition of several grains. We have found a similar composition as *Allen et al*. [1998b] with negligible deviations among individual grains. Nevertheless, a direct comparison is difficult because *Allen et al*. [1998b] provide the abundance of molecular components (SiO_2, Al_2O_3, Fe_2O_3, etc.), whereas only an elemental composition can be estimated by the EDX technique. Moreover, *Allen et al*. [1998b] show the results for two samples with mass percent compositions differing by several wt %. The most important parameter for the secondary electron emission is the mean atomic number (see section 3.3) that is influenced dominantly by the abundance of heavy elements (Mn and Fe in this particular case). *Allen et al*. [1998b] have found about 10–15 wt % and our analysis provided 11–13 wt %.

The description of our investigations is divided into several parts. First of them is devoted to a possible change of the dust grain mass in the experiment, the second one describes the measurements of the grain effective charge and the grain surface potentials are discussed in the third subsection. The last two parts deal with model calculations that represent a principal support for an interpretation of experimental results.

3.1. Mass Changes of Grains

Allen et al. [1998b] reported a notable portion of a volatile content in the Martian soil simulant. They found up to 20% of the mass loss after heating to 600°C and attributed it to water and sulfur dioxide evaporation. Since we would like to attribute the observed changes of the Q/m ratio to variations of the grain charge, a change of the grain mass in the course of the experiment should be negligible. For this reason, we discuss possible long-term changes of the grain mass through the experiment first.

A grain released from a reservoir was preliminary charged by the electron beam during its free fall, consequently trapped in the quadrupole and the equilibrium values of Q/m were recorded. A determination of the grain mass is based on the observation of stepwise changes of the Q/m ratio that can be ascribed to grain charging in steps of integral numbers of the elementary charge (such technique is called the method of elementary charge [*Žilavý et al*., 1998]. An accuracy of a mass determination is given by the noise of the frequency signal from the coordinate detector. This frequency can be measured with the accuracy of $\approx 10^{-3}$, and the same is held for a relative error of the mass determination.

In order to check the grain mass changes through our investigations, we kept the container with grains in the vacuum system (with the pressure of $\approx 10^{-6}$ Pa) at the room temperature for 10 days. After it, one grain was trapped and heated by the red laser beam to the temperature $\approx$ 70°C (see *Beránek et al*. [2010] for discussion of the grain temperature).

A mass of the grain was determined by the aforementioned method of the elementary charge, and the evolution of the Q/m ratio was recorded for next 5 days. Figure 1 shows these data after recalculation into the grain mass. We should note that the grain was charged by about 500 electrons in the course of these measurements. The change of the charge by one elementary charge thus would appear as a stepwise jump (up or down) of the grain mass by $\approx$ 0.2% in Figure 1. Since the figure shows about exponential decay of the grain mass in the course of the whole experiment and the total Q/m change is lower than this value, the

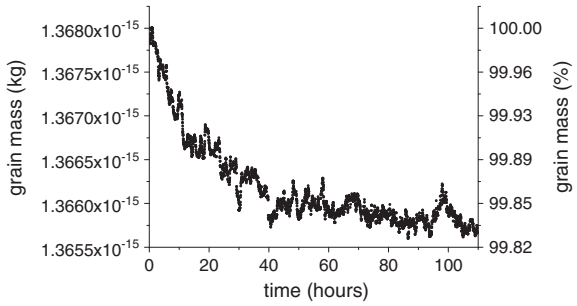

Figure 1. Mass evolution of a grain over 5 days in the UHV vessel.

observed decrease should be ascribed to the decrease of the grain mass. We can conclude that approximately 2 days are needed for setting of an equilibrium state and that the mass changes are negligible even within these 2 days. We think that there is no contradiction between our and *Allen et al.* [1998b] results because the heating used in *Allen et al.* [1998b] can lead to changes of the structure and, for example, the crystalline water can be released [*Seiferlin et al.*, 2008].

3.2. Dust Charging by Electrons

As a next step, we present the measurements of the grain charging by the electron beam. A trapped grain was bombarded by the electron beam of a particular energy. The values of Q/m were recorded for 10 min at each level of the electron beam energy from the range of 60 eV to 10 keV. Ten minutes guarantee a sufficient time for setting of the equilibrium charge. The electron beam current was stabilized, and the corresponding current density was of the order 0.1 A/m^2. The current density is low enough to influence the grain temperature because it brings 1 order of magnitude lower power than the laser beam [*Beránek et al.*, 2010].

The charging procedure was repeated with new grains to receive a representative set of Q/m ratios for a further processing. We should note that the secondary emission yield was larger than unity in the whole energy range; thus, the grains were charged positively.

The results of charging of several dust grains are shown in Figure 2 where the Q/m ratios are plotted as a function of the primary electron energy, E. Note that this energy is larger than the beam energy due to acceleration of the beam electrons in the electric field caused by the grain charge. The investigated grains differ by their masses that are given in the figure caption. All charging characteristics exhibit generally the same trend—an initial rise of the grain charge with the beam energy in the low-energy range (up to 0.3 keV), a slightly decreasing plateau between 0.3 and 4 keV, and a new rise of the grain charge for higher (> 4 keV) energies. Let us discuss the low-energy part because the charging characteristics of different grains are nearly self-similar up to ≈ 1 keV.

The equilibrium charge is given by a balance of incoming (beam) and outgoing (backscattered and secondary) electron currents. Both these currents are proportional to the beam current for a noncharged grain but the number of outgoing electrons is further reduced by the grain potential, ϕ.

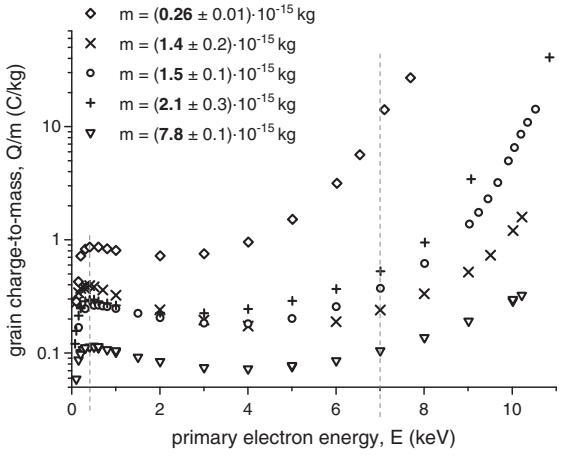

Figure 2. The Q/m ratio as a function of the primary beam energy for JSC Mars-1 grains of various masses.

Pavlů et al. [2008] have shown that the grains are charged to a surface potential that is given exclusively by their material properties in the low-energy range. Assuming a spherical shape of grains, the Q/m ratio would scale with the grain mass as $m^{-2/3}$ because Q/m is proportional to square of the grain diameter, D and the grain mass rises as D^3. Since the quantitative analysis of the data in Figure 2 is roughly consistent with this scaling law, we will apply a spherical approximation of the irregular shape of individual grains (see Figure 3, smaller grains in the SEM photo) in the first step.

Although the secondary electron emission yield would decrease with the increasing primary energy in the kiloelectronvolt range [*Sternglass*, 1957], one can note a rapid increase of the grain charge in Figure 2.

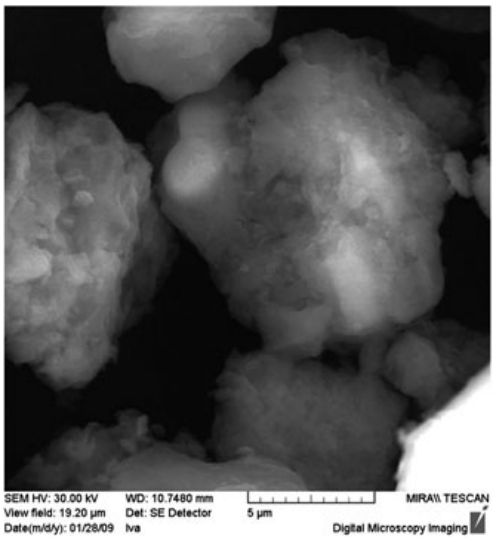

Figure 3. SEM image of Mars soil simulant (JSC Mars-1) grains used in the experiment.

However, the above statement about the scaling law is not held for higher primary energies. For example, the profile denoted in Figure 2 (plus symbol) belongs to a heavier grain than that plotted by cross, and its equilibrium Q/m ratio is lower in the low-energy range. On the other hand, the Q/m ratio for the heavier grain rapidly rises, and for energies above 4 keV it is larger than that for the lightweight grain. According to *Richterová et al*. [2007], this enhancement would be caused by increased numbers of backscattered electrons, and this rise would be more pronounced for smaller (lightweight) grains. In the next sections, we will try to show that this effect is probably connected with an irregular shape of a particular grain. As a working hypothesis, we suggest that if the grain (or a part of it) is highly elongated, the primary electrons can penetrate through, and their charges do not compensate the charge of leaving secondary electrons.

The above mentioned decrease of the secondary electron emission yield in the kiloelectronvolt range can be observed for large dust grains (above $\approx$ 10 µm, [e.g., *Vaverka et al*., 2013) and such grains are charged negatively. It means that a sign of the grain charge is size dependent, but this dependence is opposite than that expected for triboelectric charging [*Forward et al*., 2009b].

3.3. Grain Surface Potential

The rise of the grain charge leads to an increase of the grain surface potential. The proportionality constant between the charge and potential is the grain capacitance that can be determined by a special technique [*Pavlů et al*., 2004]. This procedure is complicated, and it was applied only to one of the samples because we can expect, in accord with *Pavlů et al*. [2004], that only material properties play a significant role in the low-energy range (up to $\approx$ 1 keV), and the surface potential of all grains would be the same.

The surface potentials determined by this way for three grains from Figure 2 are plotted in Figure 4 by the same symbols as a function of the primary electron energy. As it could be expected, the potentials are approximately equal up to $\approx$ 2 keV of the primary energy. The study of *Pavlů et al*. [2008] suggests that a best parameter that determines the maximum grain surface potential in the low-energy range of primary electrons (the grain potential at the peak of the secondary emission yield) is a mean atomic number, Z of the grain material. As it can be seen in Figure 5, JSC Mars-1 fits rather well to this dependence despite the fact that it is composed from several compounds and its crystalline structure is unknown.

Although nearly identical at low energies, surface potentials of individual grains in Figure 4 strongly differ in the high-energy range. In order to elucidate the reason for a rise of the grain surface potential with the increasing energy of primary electrons, we added surface potential profiles of several glass grains calculated by the *Richterová et al*. [2010] model into Figure 4 for the comparison.

The model traces a primary electron path inside the grain and provides a description of the secondary emission process for spherical grains. It was successfully applied for an interpretation of the experimental data measured in a broad energy range on spherical samples of different materials ranging from gold, glass to the lunar simulant [*Richterová et al*., 2006, 2007; *Němeček et al*., 2011]. Here, we are showing the model results for SiO_2 spheres [*Richterová et al*., 2007] because SiO_2 is a principal constituent of the investigated simulant. A comparison shows that grains from the Martian simulant behave approximately as SiO_2 spheres of a smaller (approximately by a factor of 0.5) size.

Another interesting difference between the model and experiment is that the model surface potential at a given primary energy monotonically increases with decreasing grain diameter, D. Since the dimensions of the grains trapped in the experiment are unknown, we have calculated an effective grain diameter, D_{eff} assuming its spherical shape and mass density equal to $\approx$ 1910 kg/m^3 (according to *Allen et al*. [1998b]).

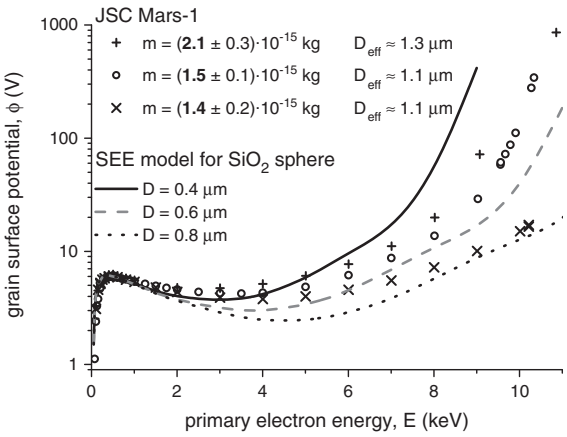

Figure 4. Surface potentials as a function of the primary electron energy for the selected grains from Figure 2 together with the results calculated according to the *Richterová et al.* [2007] model for glass spheres. The diameters of JSC Mars-1 grains are at the top part of the figure.

Even a very brief inspection of Figure 4 shows that a smaller grain (Figure 4, cross) exhibits a lower surface potential than a larger one (Figure 4, plus). This observation is not surprising, we have already commented an analogous effect in the description of Figure 2 and attributed it to a nonspherical shape of the grain.

3.4. Influence of the Grain Shape

The model calculations in *Richterová et al.* [2010] are based on an assumption of the spherical symmetry; thus, it does not allow us to check directly the hypothesis of a nonspherical shape of the grain. For this reason, we have changed the coordinate system used in the model and applied a new modification that includes a nonspherical shape of grains (see *Richterova et al.* [2012] for a detailed description). Figure 6 presents calculated potentials of cuboids from SiO_2. The masses of cuboids were chosen to approximately match the masses of the grains in Figure 4. One can note that the model even quantitatively reproduces the measured potentials if the ratio of cuboid edges is chosen properly. The resulting grain surface potential is determined rather by the grain shape than by its mass as it immediately follows from a comparison in Figure 6 (two red profiles). Both profiles belong to grains of the same mass, and they differ by the ratios of cuboid edges that are given in the figure caption. The profile plotted in blue belongs to a heavier grain, but its surface potential is much larger because this grain possesses a form of a thin flake.

To summarize this section, we can conclude that any deviation of the dust grain shape from a sphere increases its surface potential in the high-energy range of primary electrons. Since the spherical grain is a popular approximation of grain shape in many models of the dust grain charging, the effect of the secondary emission on the dust grain potential (charge) is underestimated in these models. Grains of arbitrary forms can be produced by primary collisions of large bodies, and they can be present in the interplanetary space or on surfaces of bodies without the atmosphere like a Moon. On the other hand, the frequent mutual collisions of the dust grains lifted from the Mars surface occurring during storms would shape them toward spheres.

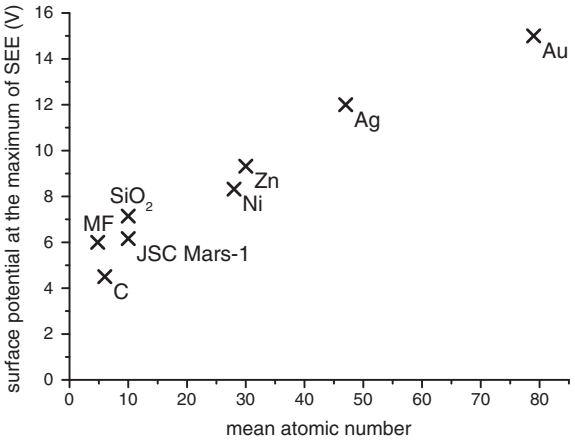

Figure 5. The surface potential at the maximum of the secondary electron emission, ϕ_{max}, for different kinds of grain materials as a function of the (mean) atomic number, Z. MF stands for the melamine formaldehyde resin grains. All data except JSC Mars-1 are taken from *Pavlů et al.* [2008].

3.5. Significance of Secondary Electron Energy Spectrum

Figure 6 suggests that the surface potential of an irregularly shaped grain is determined mainly by its smallest dimension. However, another equally important parameter is the energy spectrum of secondary electrons. This spectrum is often divided into two parts. A low-energy part is attributed to so-called true secondary electrons, whereas the high-energy tail represents a contribution of backscattered primary electrons to the outgoing current. Although a breakpoint of 50 eV is frequently used to distinguish these two populations, this division is not exact. There is a (negligible) portion of primary electrons slowed down below 50 eV prior

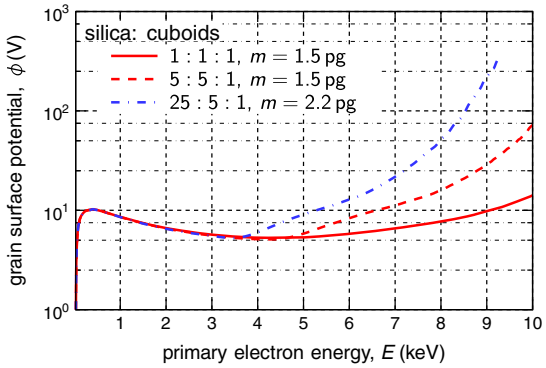

Figure 6. Surface potentials of cuboids from SiO_2 calculated according to *Richterova et al.* [2012]. See text for a detailed description.

to their escape from the grain, and several grain electrons can reach this threshold due to collision cascades [e.g., *Sickafus*, 1977; *Ding et al.*, 2001].

The energy spectrum of secondary electrons is often described by the Maxwellian distribution with a temperature T_M that depends on the target material, but *Draine and Salpeter* [1979] argued that this approximation underestimates the contribution of backscattered electrons and suggested a modified functional form. The free parameter of this function, T_D, has approximately the same meaning as the temperature in the Maxwellian distribution. A comparison of the Maxwellian and Draine and Salpeter distributions is shown in Figure 7 together with experimental points derived from measurements on a 1 μm SiO_2 sphere. These points were obtained from measurements of the surface potential profile similar to that described in the previous section under assumptions of the validity of the *Richterova et al.* [2012] model. One can note that neither Maxwell (Figure 7, red) nor Draine and Salpeter (Figure 7, blue) distributions match the data in the full energy range. Our fits suggest that the Maxwell distribution provides a very good description at low energies of secondary electrons, whereas the Draine and Salpeter distribution seems to show a better approximation of the whole spectrum.

Sickafus [1977] suggested a simple power law form of the energy spectrum of backscattered electrons from metals:

$$f(\varepsilon) = \frac{A}{\varepsilon^{\mu}} \tag{2}$$

where ε denotes the energy of secondary electrons, μ is the Sickafus index, and A is an arbitrary constant scaling the spectrum. A and μ are constants for a particular material at a given primary energy. Note that *Sickafus* [1977] found μ to be typically ≈ 1; *Greenwood et al.* [1994] measured experimentally the parameters A and μ with an incident beam of 20 keV for 32 various elements and found that the values of μ fell within the extremes of 0.5 and 1.5.

However, the mentioned measurements used planar samples; thus, they cannot reflect a possible change of the energy spectrum when the electrons are emitted from a highly curved surface like a grain. Moreover, such measurements were never done for compounds or blends of different elements.

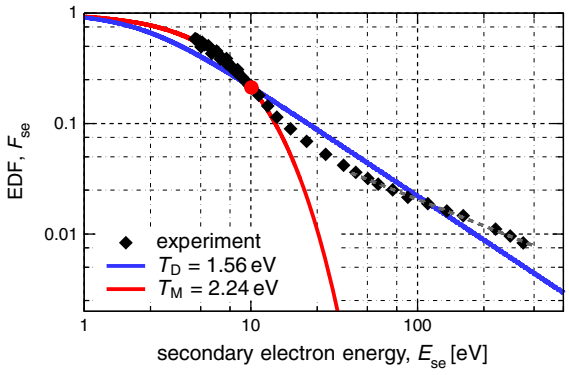

Figure 7. The electron distribution of secondary electrons. Points = experimental data; red curve = the Maxwellian fit to a low-energy part; blue line = the best fit to all experimental data by the Draine and Salpeter distribution; grey dashed line = the fit to experimental points with $E_{se} > 50$ eV by the power law form.

Our estimation shown in Figure 7 (grey dashed line) reveals that this description can be applied on the glass spheres. The best fit to the experimental points above $E_{se} = 50$ eV leads to $A = 0.158$ and $\mu \approx 0.6$. We should note that although the Sickafus form provides the best approximation of the energetic tail of secondary electrons, we have used the Draine and Salpeter distribution for calculations shown in Figure 7 because we intended to describe the grain surface potential in a broad range from 7 to 400 eV. The measurements in Figure 7 were done on SiO_2 spheres but the result (effective temperature of the distribution, T_D) was applied on JSC Mars-1 in Figure 6 because there is no possibility to have JSC Mars-1 grains of a defined shape. We believe that

the difference between secondary emissions from JSC and from pure SiO_2 would be small, since SiO_2 is a principal component of the JSC Mars-1 samples.

3.6. Discussion

The present paper deals with a complex investigation of the secondary electron emission, but it is only one of numerous processes charging the dust grains in real Martian conditions. *Yair* [2012] notes that while triboelectric charging is considered the best candidate for electrification of dust on Mars, other processes may be of potential importance. The secondary electron emission requires impacts of energetic (> 100 eV) electrons that are not present in a relatively dense Martian atmosphere under quiet conditions. However, severe dust storms [*Cantor et al*., 2001] or weaker but more frequent dust devils [e.g., *Thomas and Gierasch*, 1985] lift the dust from the surface. The collisions of the grains inside such events lead to their charging. Laboratory experiments have shown that the average charge carried by a grain can be as large as $\approx 10^4$ elementary charges [*Eden and Vonnegut*, 1973; *Sternovsky et al*., 2002; *Krauss et al*., 2003]. The small grains tend to be charged negatively, whereas the larger ones positively [*Forward et al*., 2009a, 2009b]. The competition of the uplifting and gravity forces leads to a charge separation and creation of a large electric field inside the dust cloud. Based on in situ observations in the Nevada desert, *Farrell et al*. [2004] concluded that the voltages can be possibly in excess of 0.5 MV. Such voltages would lead to electrical discharges—lightnings that are frequently observed on the Earth, and their presence on the Mars was inferred from observations of the radio emissions during a storm [*Ruf et al*., 2009]. On the other hand, *Gurnett et al*. [2010] searched for impulsive radio signals caused by lightnings in the data of Mars-Advanced Radar for Subsurface and Ionosphere Sounding on board the Mars Express mission, and they reported negative results.

The lightning is accompanied with (or, probably, initiated by, according to *Gurevich et al*. [2004]) the beams of runaway electrons with energies in the keV range. The initiation of the runaway avalanche needs a seed population of energetic electrons that is expected to be generated by cosmic rays on the Earth. On Mars, ionization caused by solar energetic particles (SEPs, *Lillis et al*. [2012]) and emitted secondary electrons can serve as additional sources. These electrons are accelerated in the electric field created by the charge separation and, consequently, we can expect electrons with energies sufficient for the secondary electron emission (> 100 eV) within the dust clouds.

Our investigations show that the secondary electron emission would charge small grains positively and thus, it would compete with the triboelectric charging that tends to charge them negatively. This effect would lead to the decrease of the grain charges and to the decrease of the electric field within the cloud. The secondary electron emission produces low-energy electrons from the grain surface (Figure 7) that can be captured by the positively charged large grains with the same effect on the electric field within the cloud. A self-consistent description should take into account the ionization of the atmosphere caused by energetic electrons. The resulting products (low-energy electrons and ions) again decrease the large-scale electric field by decreasing and/or shielding of dust grain charges.

All these processes act inside dust clouds produced by volcanic eruptions on the Earth and the lightnings are regularly observed within these clouds. It means that the production of runaway electrons is sufficient for their ignition. However, the mean free path for collisions of energetic electrons with atoms that is necessary for a development of runaway avalanches is two orders of magnitude larger in the rarefied Martian atmosphere, thus the collisions of energetic electrons with dust grains (and, consequently, the secondary electron emission) would play a much more important role.

Other charging currents (a collection of electrons and ions) can be treated in terms of the atmospheric conductivity [e.g., *Renno and Kok*, 2008]. This approach leads to a limitation of the achievable electric field in the Mars atmosphere. The model of *Farrell et al.* [2006a] suggests a decrease of this field from $\approx$ 35 kV/m to about 20 kV/m under the same conditions if the typical conductance is taken into account, but such field is still large enough for the mechanisms discussed above. On the other hand, the pressure at the Martian atmosphere is close to the minimum of the Paschen's law; thus, the presence of electrons emitted from dust grains can represent a seed population needed for ignition of the glow discharges expected by *Hintze et al*. [2006].

It is hard to draw a conclusion without a quantitative model, but it is possible that the above described processes can stabilize the electric field within dust clouds to a value insufficient for the runaway breakdown [*Milikh and Roussel-Dupré*, 2010]. It can explain the lack of radio signals from lightnings reported by *Gurnett*

et al. [2010]. Nevertheless, such model should include a proper description of the secondary electron emission because a majority of the present models does not take into account the effects caused by finite dimensions of the grains [see *Vaverka et al*., 2013, discussion].

The secondary electron emission can be an important (or even dominant) process not only within dust clouds/devils but also in all places where the dust grains can encounter energetic electrons. Such regions were found for example at the Martian nightside near strong crustal magnetic sources [*Brain et al*., 2006] where the energetic electrons were observed down to 100 km of altitude during passages of strong space weather events [*Fox and Weber*, 2012; *Ulusen et al*., 2012]. However, their density is low, and thus, the secondary electron emission contribution to the dust grain charging would be small in comparison with the current of low-energy ionospheric electrons at such low altitudes. On the other hand, the high-energy electron population is a principal plasma component in the Martian tail [*Mitchell et al*., 2000] and the secondary electron emission would be a leading charging process there.

4. Summary and Conclusion

We have performed a series of measurements of electron charging on JSC Mars-1 grains. The results can be summarized as follows:

1. The determination of the volatile content has shown that a significant part of previously determined volatile content is well bonded at low temperatures and can be released only by a moderate heating.
2. The charging of dust grains by electrons revealed a significant rise of the grain charge if the energy of primary electrons exceeds $\approx$ 4 keV. The density of energetic electrons is negligible near the Mars surface during quiet times, but it would be significantly increased within the dust devils and/or storms.
3. Recalculation of the grain charge into the surface potential and a comparison of the results with the Monte Carlo model of the secondary emission from grains has shown the principal importance of the grain shape for its potential and resulting equilibrium charge. This conclusion is significant because dust grains in the space are spherical only exceptionally, and any deviation from the spherical shape leads to increase of the grain surface potential. We would like to point out that these calculations are important for an interpretation of our experimental results and for an estimation of the secondary electron emission from dust grains in a general sense, but such effects would be probably weak at the Mars surface. The Martian dust grains collide each with another during dust storms, and these collisions shape the irregular grains.
4. Generally used Maxwellian approximation of the energy spectrum of secondary electrons cannot be applied for the dust grains from SiO_2 or similar (e.g., JSC Mars-1) materials. The Draine and Salpeter [*Draine and Salpeter*,1979] distribution provides a better approximation in a broad range of energies, whereas the Sickafus distribution [*Sickafus*, 1977] with $\mu \approx 0.5$ is appropriate for the description of a contribution of backscattered electrons (above 50 eV).
5. The models of electric circuits within the Martian dust clouds should include a description of the secondary electron emission that should reflect the effects of finite dimensions of dust grains.

Acknowledgments
The authors would like to thank their friends from Center for Integrated Plasma Studies, University of Colorado Boulder (CO, USA) for providing them with the Martian simulant samples. This work was supported partly by the Research plan MSM 0021620860 financed by the Ministry of Education of the Czech Republic, partly supported by the Czech Grant Agency under contract 209/11/1412, and partly funded by the Grant Agency of Charles University (GAUK 1410213).

References

Agui, J., and M. Nakagawa (2005), Dust on the Moon and Mars, in *43rd AIAA Aerospace Sciences Meeting and Exhibit—Meeting Papers Reno, Nevada*, pp. 7411–7418, American Institute of Aeronautics and Astronautics, Alexander Bell Drive, Reston, Va., doi:10.2514/6.2005-539.

Allen, C. C., K. M. Jager, R. V. Morris, D. J. Lindstrom, M. M. Lindstrom, and J. P. Lockwood (1998a), JSC Mars-1: A Martian soil simulant, in *Sixth ASCE Specialty Conference and Exposition on Engineering, Construction, and Operations in Space*, vol. 206, edited by R. G. Galloway and S. Lokaj, pp. 469–476, American Society of Civil Engineers, Albuquerque, New Mexico, United States, doi:10.1061/40339(206)54.

Allen, C. C., K. M. Jager, R. V. Morris, D. J. Lindstrom, M. M. Lindstrom, and J. P. Lockwood (1998b), Martian soil stimulant available for scientific, educational study, *EOS Trans. AGU*, *79*, 405, doi:10.1029/98EO00309.

Anderson, R. C., et al. (2009), Particle transport and distribution on the Mars Science Laboratory mission: Effects of triboelectric charging, *Icarus*, *204*, 545–557, doi:10.1016/j.icarus.2009.07.006.

Atreya, S. K., et al. (2006), Oxidant enhancement in Martian dust devils and storms: Implications for life and habitability, *Astrobiology*, *6*, 439–450, doi:10.1089/ast.2006.6.439.

Beránek, M., M. Vyšinka, J. Pavlů, I. Richterová, Z. Němeček, and J. Šafránková (2010), Dust as a gas carrier, *IEEE Trans. Plasma Sci.*, *38*(4), 886–891, doi:10.1109/TPS.2009.2038219.

Brain, D. A., J. S. Halekas, L. M. Peticolas, R. P. Lin, J. G. Luhmann, D. L. Mitchell, G. T. Delory, S. W. Bougher, M. H. Acuña, and H. Rème (2006), On the origin of aurorae on Mars, *Geophys. Res. Lett.*, *33*, L01201, doi:10.1029/2005GL024782.

Calle, C. I., C. R. Buhler, M. R. Johansen, M. D. Hogue, and S. J. Snyder (2011), Active dust control and mitigation technology for lunar and Martian exploration, *Acta Astronaut.*, *69*, 1082–1088, doi:10.1016/j.actaastro.2011.06.010.

Cantor, B. A., P. B. James, M. Caplinger, and M. J. Wolff (2001), Martian dust storms: 1999 Mars Orbiter Camera observations, *J. Geophys. Res.*, *106*, 23,653–23,688, doi:10.1029/2000JE001310.
Čermák, I. (1994), Laboruntersuchung elektrischer Aufladung kleiner Staubteilchen, PhD thesis, Naturwissenschaftlich-Mathematischen Gesamtfakultät, Ruprecht-Karls-Universität, Heidelberg.
Clancy, R. T., M. J. Wolff, B. A. Whitney, B. A. Cantor, M. D. Smith, and T. H. McConnochie (2010), Extension of atmospheric dust loading to high altitudes during the 2001 Mars dust storm: MGS TES limb observations, *Icarus*, *207*, 98–109, doi:10.1016/j.icarus.2009.10.011.
Conrath, B. J. (1975), Thermal structure of the Martian atmosphere during the dissipation of the dust storm of 1971, *Icarus*, *24*, 36–46, doi:10.1016/0019-1035(75)90156-6.
Crozier, W. D. (1964), The electrical field of a New Mexico dust devil, *J. Geophys. Res.*, *69*, 5427–5429, doi:10.1029/JZ069i024p05427.
Ding, Z. J., X. D. Tang, and R. Shimizu (2001), Monte Carlo study of secondary electron emission, *J. Appl. Phys.*, *89*, 718–726.
Draine, B., and E. Salpeter (1979), On the physics of dust grains in hot gas, *Astrophys. J.*, *231*(1), 77–94.
Dubinin, E., M. Fraenz, J. Woch, J. Winnigham, R. Frahm, R. Lundin, and S. Barabash (2008), Suprathermal electron fluxes on the nightside of Mars: ASPERA-3 observations, *Planet. Space Sci.*, *56*(6), 846–851, doi:10.1016/j.pss.2007.12.010.
Eden, H. F., and B. Vonnegut (1973), Electrical breakdown caused by dust motion in low-pressure atmospheres: Considerations for Mars, *Science*, *180*, 962–963, doi:10.1126/science.180.4089.962.
El-Taibany, W. F., and M. Wadati (2007), Sagdeev potential analysis for positively charged dust grains in nonthermal dusty plasma near Mars, *Phys. Plasmas*, *14*(10), 103–703, doi:10.1063/1.2784764.
Farrell, W. M., M. L. Kaiser, W. S. Kurth, M. D. Desch, D. A. Gurnett, G. B. Hospodarsky, and R. J. MacDowall (2004), Remote sensing of possible plasma density bubbles in the inner Jovian dayside magnetosphere, *J. Geophys. Res.*, *109*, A09S14, doi:10.1029/2003JA010130.
Farrell, W. M., N. Renno, G. T. Delory, S. A. Cummer, and J. R. Marshall (2006a), Integration of electrostatic and fluid dynamics within a dust devil, *J. Geophys. Res.*, *111*, E01006, doi:10.1029/2005JE002527.
Farrell, W. M., G. T. Delory, and S. K. Atreya (2006b), Martian dust storms as a possible sink of atmospheric methane, *Geophys. Res. Lett.*, *33*, L21203, doi:10.1029/2006GL027210.
Forward, K. M., D. J. Lacks, and R. M. Sankaran (2009a), Charge segregation depends on particle size in triboelectrically charged granular materials, *Phys. Rev. Lett.*, *102*(2), 028,001, doi:10.1103/PhysRevLett.102.028001.
Forward, K. M., D. J. Lacks, and R. M. Sankaran (2009b), Particle-size dependent bipolar charging of Martian regolith simulant, *Geophys. Res. Lett.*, *36*, L13201, doi:10.1029/2009GL038589.
Fox, J. L., and A. J. Weber (2012), MGS electron density profiles: Analysis and modeling of peak altitudes, *Icarus*, *221*(2), 1002–1019, doi:10.1016/j.icarus.2012.10.002.
Freier, G. D. (1960), The electric field of a large dust devil, *J. Geophys. Res.*, *65*, 3504, doi:10.1029/JZ065i010p03504.
Gierasch, P. J., and R. M. Goody (1973), A model of a Martian great dust storm, *J. Atmos. Sci.*, *30*(2), 169–179, doi:10.1175/1520-0469(1973)030<0169:AMOAMG>2.0.CO;2.
Greenwood, J. C., M. Prutton, and R. H. Roberts (1994), Atomic-number dependence of the secondary-electron cascade from solids, *Phys. Rev. B*, *49*(18), 12,485–12,495, doi:10.1103/PhysRevB.49.12485.
Gross, F. B. (2003), JSC Mars-1 Martian regolith simulant particle-charging experiments in the presence of AC and DC corona fields, *J. Electrostat.*, *58*(1–2), 147–156, doi:10.1016/S0304-3886(02)00206-1.
Gross, F. B., S. B. Grek, C. I. Calle, and R. U. Lee (2001), JSC Mars-1 Martian regolith simulant particle charging experiments in a low pressure environment, *J. Electrostat.*, *53*(4), 257–266, doi:10.1016/S0304-3886(01)00152-8.
Gurevich, A. V., Y. V. Medvedev, and K. P. Zybin (2004), New type discharge generated in thunderclouds by joint action of runaway breakdown and extensive atmospheric shower, *Phys. Lett. A*, *329*, 348–361, doi:10.1016/j.physleta.2004.06.099.
Gurnett, D. A., D. D. Morgan, L. J. Granroth, B. A. Cantor, W. M. Farrell, and J. R. Espley (2010), Non-detection of impulsive radio signals from lightning in Martian dust storms using the radar receiver on the Mars Express spacecraft, *Geophys. Res. Lett.*, *37*, L17802, doi:10.1029/2010GL044368.
Guzewich, S. D., E. R. Talaat, A. D. Toigo, D. W. Waugh, and T. H. McConnochie (2013), High-altitude dust layers on Mars: Observations with the Thermal Emission Spectrometer, *J. Geophys. Res. Planets*, *118*, 1177–1194, doi:10.1002/jgre.20076.
Hintze, P. E., C. R. Buhler, L. M. Calle, C. I. Calle, S. Trigwell, J. W. Starnes, and A. C. Schuerger (2006), Degradation of organics in a glow discharge under Martian conditions, in *37th Annual Lunar and Planetary Science Conference, Lunar and Planetary Inst. Technical Report*, vol. 37, edited by S. Mackwell and E. Stansbery, pp. 2098–2099.
Hyatt, M., P. Greenberg, V. Pines, A. Chait, W. Farrell, T. Stubbs, and J. Feighery (2007), Lunar and Martian dust: Evaluation and mitigation, in *45th AIAA Aerospace Sciences Meeting and Exhibit 8-1 January 2007, Reno, Nevada*, vol. 6, pp. 4246–4260, American Institute of Aeronautics and Astronautics, Alexander Bell Drive, Reston, VA, doi:10.2514/6.2007-347.
Jackson, T. L., W. M. Farrell, G. T. Delory, and J. Nithianandam (2010), Martian dust devil electron avalanche process and associated electrochemistry, *J. Geophys. Res.*, *115*, E05006, doi:10.1029/2009JE003396.
Kok, J. F., and N. O. Renno (2006), Enhancement of the emission of mineral dust aerosols by electric forces, *Geophys. Res. Lett.*, *33*, L19S10, doi:10.1029/2006GL026284.
Kok, J. F., and N. O. Renno (2008), Electrostatics in wind-blown sand, *Phys. Rev. Lett.*, *014,501*(1), doi:10.1103/PhysRevLett.100.014501.
Kok, J. F., and N. O. Renno (2009), Electrification of wind-blown sand on Mars and its implications for atmospheric chemistry, *Geophys. Res. Lett.*, *36*, L05202, doi:10.1029/2008GL036691.
Krauss, C. E., M. Horányi, and S. Robertson (2003), Experimental evidence for electrostatic discharging of dust near the surface of Mars, *New J. Phys.*, *5*(1), 70, doi:10.1088/1367-2630/5/1/370.
Krauss, C. E., M. Horányi, and S. Robertson (2006), Modeling the formation of electrostatic discharges on Mars, *J. Geophys. Res.*, *111*, E02001, doi:10.1029/2004JE002313.
Lillis, R. J., D. A. Brain, G. T. Delory, D. L. Mitchell, J. G. Luhmann, and R. P. Lin (2012), Evidence for superthermal secondary electrons produced by SEP ionization in the Martian atmosphere, *J. Geophys. Res.*, *117*, E03004, doi:10.1029/2011JE003932.
Lollo, A., P. Withers, K. Fallows, Z. Girazian, M. Matta, and P. C. Chamberlin (2012), Numerical simulations of the ionosphere of Mars during a solar flare, *J. Geophys. Res.*, *117*, A05314, doi:10.1029/2011JA017399.
Lundin, R., et al. (2006), Plasma acceleration above Martian magnetic anomalies, *Science*, *311*(5763), 980–983, doi:10.1126/science.1122071.
McKenna-Lawlor, S. M. P., et al. (2005), Predictions of energetic particle radiation in the close Martian environment, *J. Geophys. Res.*, *110*, A03102, doi:10.1029/2004JA010587.
Melnik, O., and M. Parrot (1998), Electrostatic discharge in Martian dust storms, *J. Geophys. Res.*, *103*, 29,107–29,118, doi:10.1029/98JA01954.

Merrison, J., J. Jensen, K. Kinch, R. Mugford, and P. Nørnberg (2004), The electrical properties of Mars analogue dust, *Planet. Space Sci.*, *52*, 279–290, doi:10.1016/j.pss.2003.11.003.
Milikh, G., and R. Roussel-Dupré (2010), Runaway breakdown and electrical discharges in thunderstorms, *J. Geophys. Res.*, *115*, A00E60, doi:10.1029/2009JA014818.
Mitchell, D. L., R. P. Lin, H. Rème, D. H. Crider, P. A. Cloutier, J. E. P. Connerney, M. H. Acuña, and N. F. Ness (2000), Oxygen auger electrons observed in Mars' ionosphere, *Geophys. Res. Lett.*, *27*, 1871–1874, doi:10.1029/1999GL010754.
Němeček, Z., J. Pavlů, J. Šafránková, M. Beránek, I. Richterová, J. Vaverka, and I. Mann (2011), Lunar dust grain charging by electron impact: Dependence of the surface potential on the grain size, *Astrophys. J.*, *738*(1), 14, doi:10.1088/0004-637X/738/1/14.
Pavlů, J., A. Velyhan, I. Richterová, Z. Němeček, J. Šafránková, I. Čermák, and P. Žilavý (2004), Mass-loss rate for MF resin microspheres, *IEEE Trans. Plasma Sci.*, *32*(2), 704–708, doi:10.1109/TPS.2004.826120.
Pavlů, J., I. Richterová, Z. Němeček, J. Šafránková, and I. Čermák (2008), Interaction between single dust grains and ions or electrons: Laboratory measurements and their consequences for the dust dynamics, *Faraday Discuss.*, *137*, 139–155, doi:10.1039/b702843a.
Pollack, J. B., M. E. Ockert-Bell, and M. K. Shepard (1995), Viking Lander image analysis of Martian atmospheric dust, *J. Geophys. Res.*, *100*(E3), 5235–5250, doi:10.1029/94JE02640.
Renno, N. O., and J. F. Kok (2008), Electrical activity and dust lifting on Earth, Mars, and beyond, *Space Sci. Rev.*, *137*, 419–434, doi:10.1007/s11214-008-9377-5.
Richterová, I., J. Pavlů, Z. Němeček, and J. Šafránková (2006), Model of secondary emission and its application on the charging of gold dust grains, *Phys. Rev. B*, *74*(23), 235430, doi:10.1103/PhysRevB.74.235430.
Richterová, I., Z. Němeček, J. Šafránková, J. Pavlů, and M. Beránek (2007), Secondary emission from glass grains: Comparison of the model and experiment, *IEEE Trans. Plasma Sci.*, *35*(2), 286–291, doi:10.1109/TPS.2007.892131.
Richterová, I., M. Beránek, J. Pavlů, Z. Němeček, and J. Šafránková (2010), Electrons scattered inside small dust grains of various materials, *Phys. Rev. B*, *81*(7), 075406, doi:10.1103/PhysRevB.81.075406.
Richterova, I., Z. Nemecek, M. Beranek, J. Safrankova, and J. Pavlu (2012), Secondary emission from non-spherical dust grains with rough surfaces: Application to lunar dust, *Astrophys. J.*, *761*(2), 108, doi:10.1088/0004-637X/761/2/108.
Ruf, C., N. O. Renno, J. F. Kok, E. Bandelier, M. J. Sander, S. Gross, L. Skjerve, and B. Cantor (2009), Emission of non-thermal microwave radiation by a Martian dust storm, *Geophys. Res. Lett.*, *36*, L13202, doi:10.1029/2009GL038715.
Seiferlin, K., P. Ehrenfreund, J. Garry, K. Gunderson, E. Hütter, G. Kargl, A. Maturilli, and J. P. Merrison (2008), Simulating Martian regolith in the laboratory, *Planet. Space Sci.*, *56*(15), 2009–2025, doi:10.1016/j.pss.2008.09.017.
Sharma, R., D. Clark, P. Srirama, and M. Mazumder (2008), Tribocharging characteristics of the Mars dust simulant (JSC Mars-1), *IEEE Trans. Ind. Appl.*, *44*(1), 32–39, doi:10.1109/TIA.2007.912761.
Sheel, V., S. A. Haider, P. Withers, K. Kozarev, I. Jun, S. Kang, G. Gronoff, and C. Simon Wedlund (2012), Numerical simulation of the effects of a solar energetic particle event on the ionosphere of Mars, *J. Geophys. Res.*, *117*, A05312, doi:10.1029/2011JA017455.
Shinbrot, T., K. Lamarche, and B. J. Glasser (2006), Triboelectrification and Razorbacks: Geophysical patterns produced in dry grains, *Phys. Rev. Lett.*, *96*(17), 178,002, doi:10.1103/PhysRevLett.96.178002.
Sickafoose, A. A., J. E. Colwell, M. Horányi, and S. Robertson (2001), Experimental investigations on photoelectric and triboelectric charging of dust, *J. Geophys. Res.*, *106*(A5), 8343–8356, doi:10.1029/2000JA000364.
Sickafus, E. N. (1977), Linearized secondary-electron cascades from the surfaces of metals. I. clean surfaces of homogeneous specimens, *Phys. Rev. B*, *16*(4), 1436–1447, doi:10.1103/PhysRevB.16.1436.
Snyder, S. J., P. E. Hintze, J. L. McFall, C. R. Buhler, J. S. Clements, and C. I. Calle (2008), Triboelectric charging of dust and its relation to organic degradation on Mars, in *Proceedings of the ESA Annual Meeting on Electrostatics, Paper F2 (8 pages)*, edited by A. Seaver, Electrostatics Society of America (ESA), Minneapolis, Minn.
Sternglass, E. (1957), Theory of secondary electron emission under electron bombardment, *Scientific Paper 6-94410-2-P9*, Westinghouse Research Laboratories, Pittsburgh 35, Pennsylvania.
Sternovsky, Z., S. Robertson, A. Sickafoose, J. Colwell, and M. Horányi (2002), Contact charging of lunar and Martian dust simulants, *J. Geophys. Res.*, *107*(E11), 5105, doi:10.1029/2002JE001897.
Stow, C. D. (1969), Dust and sand storm electrification, *Weather*, *24*, 134–140.
Thomas, P., and P. J. Gierasch (1985), Dust devils on Mars, *Science*, *230*, 175–177, doi:10.1126/science.230.4722.175.
Ulusen, D., D. A. Brain, J. G. Luhmann, and D. L. Mitchell (2012), Investigation of Mars' ionospheric response to solar energetic particle events, *J. Geophys. Res.*, *117*, A12306, doi:10.1029/2012JA017671.
Vaverka, J., I. Richterova, J. Pavlu, J. Safrankova, and Z. Nemecek (2013), Numerical calculation of an equilibrium dust grain potential in lunar environment, *IEEE Trans. Plasma Sci.*, *41*, 740–744, doi:10.1109/TPS.2012.2226757.
Yair, Y. (2012), New results on planetary lightning, *Adv. Space Res.*, *50*, 293–310, doi:10.1016/j.asr.2012.04.013.
Žilavý, P., Z. Sternovský, I. Čermák, Z. Němeček, and J. Šafránková (1998), Surface potential of small particles charged by the medium-energy electron beam, *Vacuum*, *50*(1–2), 139–142.

N. Richterová et al. [2011]

Richterová, I., Němeček, Z., Pavlů, J., Beránek, M., Šafránková, J., Modeling the secondary emission yield of salty ice dust grains. *Icarus* 212 (1): 367–372, 2011.

Icarus 212 (2011) 367–372

Contents lists available at ScienceDirect

Icarus

journal homepage: www.elsevier.com/locate/icarus

Modeling the secondary emission yield of salty ice dust grains

I. Richterová, Z. Němeček, J. Pavlů *, M. Beránek, J. Šafránková

Charles University, Faculty of Mathematics and Physics, Department of Surface and Plasma Science, V Holešovičkách 2, 180 00 Prague, Czech Republic

ARTICLE INFO

Article history:
Received 25 August 2010
Revised 25 November 2010
Accepted 27 December 2010
Available online 31 December 2010

Keywords:
Interplanetary dust
Ices

ABSTRACT

Secondary emission is one of important processes leading to dust grain charging in many plasma environments. The secondary yield varies with the grain material, shape, and size. Several experiments confirmed that the yield of small grains differs from that of planar samples. Among other materials, ices of different compositions can be frequently found in the interplanetary space and/or planetary magnetospheres. However, the admixtures can significantly influence the inner structure of such materials and thus may change their yield. We present numerical simulations that provide a realistic description of the secondary emission process from water ice grains. The simulations reveal that the secondary emission yield increases as the grain dimension decreases to tens of nanometers. The yield of backscattered primary electrons approaches unity and the grain can be charged to high positive potentials under these conditions. We found that any reasonable admixture of NaCl does not alter secondary electron emission properties significantly.

1. Introduction

In the Solar System, vapor-deposited water ice in the amorphous or cubic phases is the principal constituent of the surface of many satellites and rings (Schmitt et al., 1998). Water coexists with other condensed gases and is mixed with mineral grains. The ice surface is a subject to bombardment by energetic particles and UV radiation from the Sun, planetary magnetospheric ions, cosmic rays, and meteorites. These energetic impacts induce many effects on the ice surface, like chemical reactions, electrostatic charging, lattice damage, desorption, and evaporation, some of which alter the surface properties (Johnson, 1998).

Many new results concerning composition and charging properties of dust grains in the Solar System and near the planets were discovered by the Cassini mission. The Cosmic Dust Analyser (CDA) provides information about speed, mass, direction, and chemical composition of impacting dust grains (Srama et al., 2004). To determine the chemical composition of particles, a comprehensive statistical analysis of the data sets was performed and the results imply that the vast majority (>95%) of the observed particles originate from the Jupiter active volcanic satellite Io. Sodium chloride (NaCl) was identified as a significant particle constituent accompanied by sulfur and potassium. Na_2SO_4 and K_2SO_4 are minor constituents, each representing 5–10% of the observed NaCl mass (Postberg et al., 2006).

CDA measured also the mass spectra in the Saturn's E-ring (e.g., Postberg et al., 2008). An initial interpretation of the data shows that the population of this outermost tenuous E-ring is dominated by tiny water ice particles, some of which contain organic or mineral impurities (e.g., silicates, carbon dioxide, ammonia, molecular nitrogen, hydrocarbons and perhaps carbon monoxide—according to Hillier et al. (2007)). The determination of grain size distribution from CDA measurements is difficult, however, the data suggest a significant portion of grains below 0.5 μm (Kempf et al., 2008). Optical observations revealed that the water ice grains that are predominantly 0.3–3 μm in size (Hansen et al., 2006) extend from about three to at least eight Saturn radii, with a peak density at the Enceladus orbit (Showalter et al., 1991).

Active volcanism on Enceladus emits plumes of water vapor and water ice grains from fractures near its south pole (e.g., Hansen et al., 2006; Spahn et al., 2006; Waite et al., 2006) and these particles are the dominant source of the Saturn's E-ring (Schmidt et al., 2008; Kempf et al., 2008). Recently, Postberg et al. (2009) reported populations of E-ring grains that are rich in sodium salts (approximately to 0.5–2% of mass). The authors suggested that the Na-rich grains are directly frozen submicrometer droplets and they presented spectra of E-ring particles with different Na/H_2O ratios. Their results were confirmed by the experiment where mass spectra of water aggregates generated from a laser-dispersed liquid solution with different sodium salt concentrations were recorded (Charvat and Abel, 2007).

However, having different salt concentration, ice dust grains can accumulate different charges from the surrounding plasma environment. The charging of 1 μm spherical water ice grains in the plasma environment in different parts of the saturnian E-ring was analytically modeled by Jurac et al. (1995). The authors have shown that the grain surface potential is predominantly deter-

* Corresponding author.
E-mail address: jiri.pavlu@mff.cuni.cz (J. Pavlů).

0019-1035/$ - see front matter © 2011 Elsevier Inc. All rights reserved.
doi:10.1016/j.icarus.2010.12.027

mined by the secondary emission and varies from −5 V at $4R_S$ (saturnian radii) to +5 V at distances exceeding $8R_S$. The authors stress out the importance of the backscattered (reflected) primary electrons that dominate the charging process especially at the outer parts of the E-ring.

The calculations of Jurac et al. (1995) are based on present knowledge of the secondary electron emission but they cannot properly describe the charging of small (tens/hundreds of nm) grains as well as a possible influence of the salt admixture to the grain charging. With motivation to contribute to these investigations, we have applied a corrected version (Richterová et al., 2010) of the dust grain charging model (Richterová et al., 2006; Richterová et al., 2007) and studied the changes of the secondary emission yield of micron and sub-micron spherical grains from water ice caused by gradually increasing salt admixtures. We present results of calculation of the yields of true as well as backscattered electrons from ice grains of sizes ranging from 50 nm to 10 μm. A comparison of calculations for a planar ice surface with the experimental data is shown and further used for a model adjustment. The results reveal that the effect of the salt admixture is small even for saturated solution.

2. The model of SEE from spherical grains

Secondary electron emission (SEE) plays a prominent role when a portion of energetic (>10 eV) electrons is present in the medium surrounding the grain. The SEE contributes to charging of the spacecraft surface (e.g., Němeček et al., 1997) as well as to charging of dust grains exposed to cosmic radiation (e.g., Weingartner and Jordan, 2008). Many other examples of importance of SEE in space processes can be found in Mann et al. (2004, 2007).

Theoretical assessments of SEE have been based on the elementary theories of Salow (1940a,b), Baroody (1950), and Bruining (1954). One of the first complex studies (Sternglass, 1957) describes the SEE from planar metal surfaces in the range from hundreds of electronvolts to a few kiloelectronvolts. Primary electrons impacting the surface interact with the bulk material and lose their energy in many types of collisions what often result in excitations of material electrons and some of the excited electrons can leave the surface. These electrons, the so-called true secondary electrons, have typical energies of a few electronvolts.

For large planar samples, the energy dependence of the SEE yield, $\delta(E)$ (defined as the mean number of secondary electrons per one primary electron) can be described by the Sternglass universal curve (Sternglass, 1957) where the maximum SEE yield, δ_{max}, and the corresponding primary electron energy, E_{max}, depend only on the sample material at a given incident angle. During collisions with solids, primary electrons change their direction and may be back-scattered from the material, often without a significant loss of their initial energy. The yield of backscattered electrons, η, increases with the material density and atomic number. It grows slowly with the beam energy above a few hundred of electronvolts for heavy species whereas a decrease of the yield with the energy was observed for light materials like water (see for example the lower curve in Fig. 1). Thus, the total SEE yield, $\sigma = \delta + \eta$, and δ vary in a similar way with the primary beam energy.

In the case of small bodies, the process of SEE is very sensitive to the surface curvature (Draine and Salpeter, 1979). The secondary emission yield increases with an incident angle (Bruining, 1954) because the main interaction region is nearer to the surface and thus the highly curved surface of dust grains leads to a yield enhancement (Draine and Salpeter, 1979; Jurac et al., 1995; Richterová et al., 2007). Another important effect is related to the grain size—when the size becomes comparable to the beam penetration

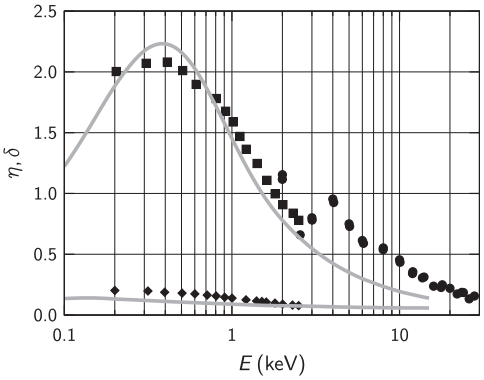

Fig. 1. A comparison of modeled profile of the true secondary electron emission yield, δ (top curve) and backscattered yield, η (bottom curve) with experimental data (diamonds – η according to Matskevich and Mikhailova (1960) for pure water ice; squares – δ according to Matskevich and Mikhailova (1960); and circles – δ according to Suszcynsky et al. (1992)).

depth, more primary electrons can leave the grain. Decreasing further the grain size, no beam electrons can be captured inside the grain, thus they do not deposit their charge inside the grain. On the other hand, they lose a part of their energy by excitation of secondary electrons. As a consequence, a surface potential of very small grains can reach large positive values (e.g., Pavlů et al., 2008; Beránek et al., 2011).

Secondary electrons charge the dust grain positively; negative potentials can be reached only when the total SEE yield is lower than unity. This is generally the case of low beam energies (tens of electronvolts), and in the kiloelectronvolt range, for grain materials with a specific combination of true and backscattered SEE yields.

During the past several years, an enhanced attention has been directed toward numerical simulations of an electron interaction with solids. This interest arises from the application of scanning electron microscopy (SEM) to the analysis of conductors as well as non- or poorly conducting materials such as polymers, ceramics, biological material, and composites.

In widely used Monte Carlo simulations, two phenomena should be modeled: elastic collisions and energy losses. Scattering by inelastic collisions is usually neglected due to a small deflection angle resulting from such events (Drouin et al., 1997) and they are considered to be uniformly distributed along the paths of the electrons. Thus, a continuous slowing-down equation based on the Bethe stopping power expression (Bethe, 1933) usually simulates the energy losses. However, in the low-energy range, this expression must be reevaluated since the number of inelastic events is decreasing (e.g., Hovington et al., 1997b).

For elastic events, the Rutherford theory (Rutherford, 1911) has been widely used due to its simplicity and its short computation time (Joy and Luo, 1989). This model is accurate for a high-energy interaction (>10 keV) but it is not valid for low energies. At the low-energy range, the more accurate Mott theory (Mott and Massey, 1965) is preferable. Empirical forms of the Mott cross section have been developed recently (e.g., Browning et al., 1995). The differential Mott cross sections for each element of the periodic table were computed by Czyżewski et al. (1990).

However, the majority of models were applied to the planar metal or insulating targets but only a few papers dealt with spherical samples. A complex analytical calculation (Jurac et al., 1995) of the charge accumulated by spherical ice grains under saturnian E-ring conditions involves both true and backscattered (called reflected therein) electrons and the influence of the grain curvature but it is not able to reproduce size effects. The authors limited

the validity of their calculations to 1 μm of the grain diameter but the saturnian environment contains significantly smaller grains.

Ziemann et al. (1995) and Chow et al. (1993, 1994) developed different analytical models but none of them match the experimental data when the size effect becomes notable. A simple numerical model of secondary emission from small dust grains developed by Richterová et al. (2004) has revealed also the importance of backscattered electrons to the determination of the equilibrium surface potential, especially for high primary energies. The main assumptions of the Richterová et al. (2004) model were that primary electrons inside the grain travel a mean free path (energy dependent), collide with an atom, loss a constant portion of its energy and change the direction of their motion according to cosine law.

Since the model assumptions were very simplified, the authors have revised it in order to include more complex principles of the electron–solid interaction that will be specified bellow. The improved model (Richterová et al., 2006) provides the charge accumulated in the grain as a function of the primary beam energy which is directly measurable as well as the energetic dependence of the secondary and backscattered yields. The new model was successfully verified by laboratory experiments with charging of gold (Richterová et al., 2006) and glass (Richterová et al., 2007) dust grains. However, further investigations revealed a small disagreement of model predictions and experiments for light materials like carbon, thus Richterová et al. (2010) suggested several model corrections. Since the present paper deals with the water ice and the corrections are substantial for this material, we briefly review their approach that is applied to calculations presented in the next section.

The model follows trajectories of primary electrons inside the spherical grain of a given composition. A deflection angle is generated according to energy-dependent Mott differential cross-sections (Mott and Massey, 1965). Note that these cross-sections are calculated in 2D and provide only the total deflection angle. Since our model is 3D, we use this angle as a polar angle and generate the azimuthal angle in a random way. In the case of compounds, we do not compute a new weighted differential cross-section but a random number is generated to decide which of particular species cause the electron deflection at each collision.

Integrating radial cross-section over a whole space angle, we can obtain the total cross-section, $\sigma_T(E)$, where σ_T decreases monotonously with the energy and can be well interpolated via cubic splines.

A path length between two subsequent collisions, $\lambda(E)$, is generated according to $\sigma_T(E)$. The energy of primary electrons decreases continuously along its path. Since a corresponding change of $\sigma_T(E)$ between two subsequent collisions can be often neglected, the mean free forceless path, $\lambda(E)$ was used in Richterová et al. (2006, 2007):

$$\lambda(E) = \left(\sum n_j \sigma_{Tj}(E)\right)^{-1}, \tag{1}$$

where n_j is a number density of deflecting atoms of jth elemental species.

For a given uniform random number, ξ, from the interval $(0,1)$ we can write

$$\Delta s = -\lambda(E)\ln(\xi). \tag{2}$$

When the σ_T increase along electron path is not omitted, electrons travel a shorter path than that given by a mean free path, $\lambda(E)$ from Eq. (1). In present calculations, the probability P that an electron of the energy E does not undergo any collision decreases with the path length, Δs exponentially:

$$P(E,\Delta s) = \exp(-f(E,\Delta s)). \tag{3}$$

The accumulation function, $f(E,\Delta s)$ can be written as:

$$f(E,\Delta s) = \int_{s(E)}^{s(E)+\Delta s} \sum n_j \sigma_{Tj}(s')ds'. \tag{4}$$

Generation of the path segment between subsequent collisions requires to solve an expression

$$f(E,\Delta s) = -ln(\xi). \tag{5}$$

For calculations of the traveling path of primary electrons, we use modified Bethe stoping power formula (Joy and Luo, 1989):

$$\frac{dE}{ds} \sim -\frac{\varrho}{N}\frac{A_{eff}(E)}{E}\ln\frac{1.166E}{J_{eff}(E)}. \tag{6}$$

where E is an actual electron energy, s is the traveled path, ϱ is a mass density, and N is the nucleon number. The effective number of atom electrons, $A_{eff}(E)$ and the effective mean ionization potential, $J_{eff}(E)$ are calculated using the Hovington et al. (1997a) approach and optical absorbtion data for water and ice (Palik, 1991; Warren and Brandt, 2008).

Integration of Eq. (6) provides the energy of primary electrons as a function of the path traveled inside the grain, $E(s)$, that does not depend on the actual trajectory of a particular electron. Using inverse function, $s(E)$, we can then determine the accumulation function, $f(E,\Delta s)$ and obtain Δs for a given ξ.

To test the model performance, we have calculated the yields δ and η as a function of the primary beam energy for a planar sample from pure water ice and compared them with available experimental data. Fig. 1 shows a good agreement of modeled and measured profiles. We should point out that the values of η follow directly from the model calculation, whereas the δ values were scaled by fitting of the computed profile to the experimental data because the absorbtion length of excited electrons inside the grain, Λ, is a free parameter of the model. The fit shown in Fig. 1 as a gray line provides a value of Λ = 4.5 nm that is a mean value for the whole energy spectrum of true secondary electrons. Experimentally and theoretically determined values for ice films (≈2 monolayers for ≈1 eV electrons and ≈4 monolayers for ≈3 eV electrons (Gilton et al., 1989, experiment); ≈2.3 monolayers for ≈3.5 eV, i.e., ≈0.87 nm (Jo and White, 1991, experiment); ≈1.3 monolayers for 1 eV electrons and ≈5 monolayers for 4.7 eV electrons, i.e., ≈0.49 nm and ≈1.89 nm, respectively, (Barnett et al., 1990, theory) show an increase of this length with the energy. Since our fit provides an average value for the whole spectrum of secondary electrons (i.e., in the range of ≈0–50 eV), we believe that our result is in a good agreement with the aforementioned data.

3. Water ice grain with varying salt content

The modified model described above was applied on water ice grains of different diameters and salinity. The presented model results are based on following assumptions:

- spherical ice grains (with ϱ = 0.92 g cm^{-3}) of a given diameter are bombarded by the parallel electron beam;
- Na and Cl atoms are distributed uniformly inside the grain, the grain mass density increases in accord with the portion of NaCl;
- free path of excited electrons is not altered by the salt admixture;
- the energetic distribution of the true secondary electrons according to Chung and Everhart (1974) with the ice work function of 4.2 eV is used;
- the results for water ice were calibrated to match measurements on planar samples at 77 K (Matskevich and Mikhailova, 1960).

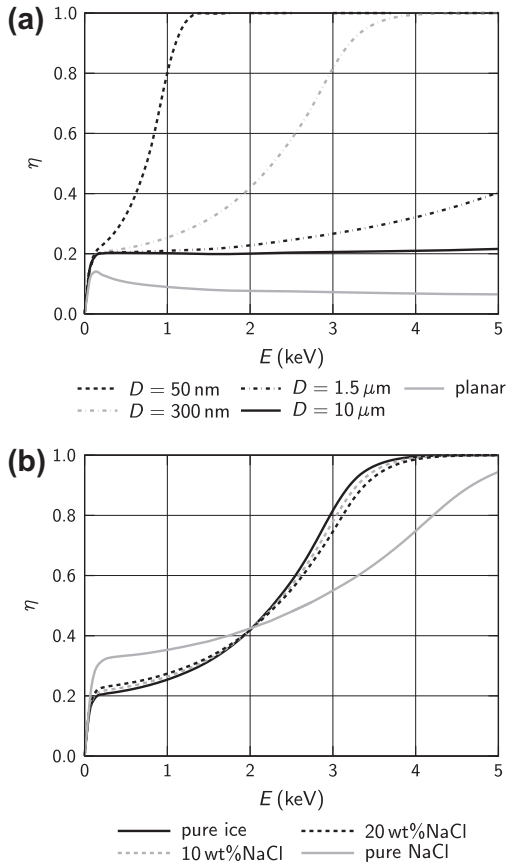

Fig. 2. Modeled backscattered electron yields for water ice grains of different diameters (a) and for a 300 nm ice grain with different salt admixtures (b).

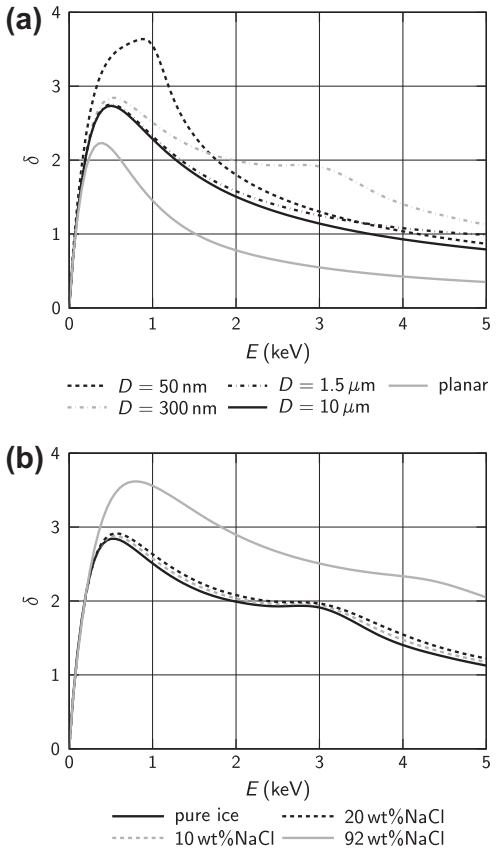

Fig. 3. Modeled true secondary emission yield for water ice grains of different diameters (a) and a 300 nm ice grain with different salt admixtures (b).

We are analyzing effects of the grain size and the salt admixtures. For this reason, results are shown in three pairs of figures. Each of them presents the size dependence as modeled for the water ice grains in the (a) panels, whereas the influence of the NaCl admixture is shown for a 300 nm grain in the (b) panels.

Fig. 2 shows the backscattered yield, η, as a function of the primary energy. The profile computed for a planar sample is given as a reference in Fig. 2a. The increase of η for water ice grains with dimensions equal to (or larger than) 10 μm is caused by the surface curvature and is independent on the grain size because it is given by the distribution of incidence angles of the parallel beam along the spherical surface. A further decrease of the grain diameter leads to a rapid increase of η towards unity. The energy at which the increase becomes observable decreases, whereas the slope of this rise enhances for small grains. As it can be seen from Fig. 2b, the salt admixture exhibits a similar effect as the increase of the grain diameter but the effect is nearly negligible. The results shown for a 300 nm grain and 20% of the salt reveal that this admixture causes an effect similar to increase of the grain diameter by ≈2%.

Fig. 3a shows how the yield of true secondary electrons changes with the decreasing grain diameter. Similarly to the η profiles in Fig. 2a, the increase of δ from values calculated for a planar surface to those for the 10 μm grain are connected with the curved surface and this effect does not depend on the diameter.

For smaller grains, the maximum of δ increases and its position shifts toward higher energies. The "bump" on the profile computed for 300 nm is caused by the fact that a great majority of primary electrons is leaving the grain with a small energy, thus they excite a large number of secondary electrons near the surface. Note that this effect causes δ being larger for the 300 nm grain than for the 50 nm grain for energies above ≈2 keV. On the other hand, the salt admixture (Fig. 3b) increases the secondary electron yield by a small factor that is a rising function of this admixture but that only slightly depends on the primary beam energy.

Combining the above results together and adding the energetic spectrum of true secondary electrons, we can compute the surface potential that a grain acquires. These potentials reached by the grain charging with a parallel beam of primary electrons are plotted in Fig. 4 as a function of their energy for water ice and ice with different salt admixtures. The energetic spectrum and the yield of true secondary electrons influence the grain potential at a low-energy range, whereas the backscattered electrons are responsible for the sharp rise of the potential when η approaches unity. We stopped our computations at 25 V but the limit is close to a half of the beam energy (Reid et al., 2008). This result is very important because the backscattered yield and the energetic spectrum of the back-scattered electrons are modeled without any additional assumption and the rise of the potential is realistic. We can note that a similar rise of the grain potential was recorded by Beránek et al. (2011) in experimental investigations of the JCS-1 Mars soil simulant.

Fig. 4a shows that 10 μm grains can reach a potential of about 7.6 V at 500 eV of the primary energy and that the potential decreases for higher energies being nearly zero at 5 keV because the charge of primary electrons deposited in the grain (about 25%, Fig. 2a) is compensated by the charge of outgoing true secondary electrons. A decrease of the grain diameter up to 300 nm does not alter the potential profile at low (below 1 keV) energies; both δ and η do not change with the grain diameter in this energy range.

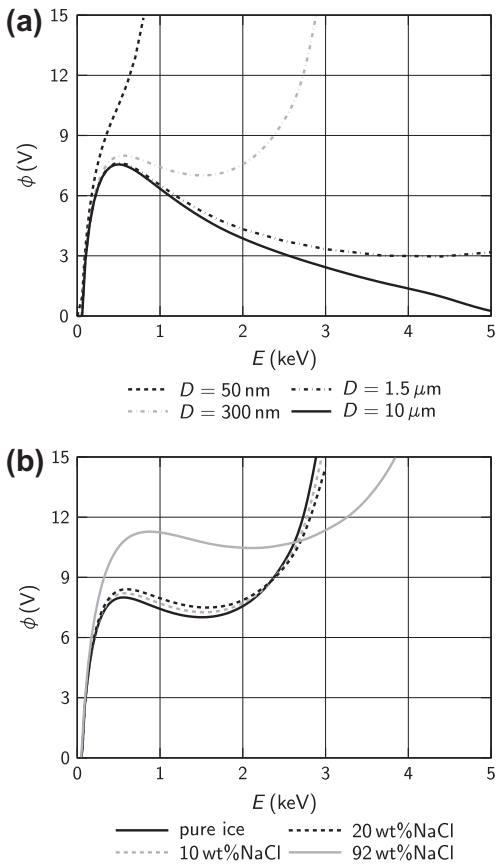

Fig. 4. Computed surface potentials for water ice grains of different diameters (a) and a for 300 nm ice grain with different salt admixtures (b).

High potentials observed for smaller grains and/or higher primary energies are connected with the sharp rise of η (Fig. 2a) as discussed above. Fig. 2b and Fig. 3b show that the changes of δ and η with the salt admixture are small, the same is true for the grain potential as demonstrated in Fig. 4b.

4. Discussion

We have developed a simple model of SEE that well describes and follows trajectories of primary electrons, and thus it gives a reliable number of scattered electrons. The conversion of the deposited energy to emitted true secondary electrons is treated only statistically through the mean transferred energy and the attenuation length of excited electrons (e.g., Lin and Joy, 2005). We successfully applied this approach to modeling of charging of another insulating compound—glass grains (Richterová et al., 2007).

Other possibility is to follow particular products of each inelastic collision (Schreiber and Fitting, 2002; Kieft and Bosch, 2008). Corresponding scattering cross-sections can be derived using optical data for dispersion relations (including the acoustic deformation potential and longitudinal optical phonos properties for insulators). However, a lack of input data and approximate relations would cause large errors in determination of electron cascades for complex materials.

Taking into account these constrains, we believe that our approach provides more reliable results. Our calculations assume that Na and Cl atoms are distributed uniformly inside the grain for the purpose of the scattering of the primary beam, whereas the emission of true secondary electrons is adjusted to data measured on a pure water ice (Fig. 1). These two assumptions are apparently contradictory. However, the theory of Onsager and Samaras (1934) demonstrates that the dissolved ions are repulsed from the water surface by electrostatic image forces. These results were confirmed for light species by molecular dynamics calculations (Vrbka and Jungwirth, 2005). Their calculations reveal that we can expect several atomic layers of pure water at the grain surface in liquid phase and, because the freezing is rapid (Postberg et al., 2009), the same would be true for icy grains. The emission of true secondary electrons is governed by the surface properties that are given by composition of several uppermost atomic layers, thus our simplification is substantiated. On the other hand, the scattering of primary electrons proceeds in the whole volume of small grains. The first collision occurs in a depth where Na and Cl atoms are already uniformly distributed, thus our omission of several atomic layers at the grain surface cannot spoil the results.

The potential of water ice dust grains in the saturnian E ring was modeled by Jurac et al. (1995). The authors used available experimental data on the secondary emission yield from planar samples and the angular dependence of the yield and compute the secondary emission yield from a sphere. They obtained the increase of δ by a factor of $\approx$1.5; slightly larger than that following from our model ($\approx$1.2, see Fig. 3a). This difference is small and it is connected with the angular dependence of δ. Jurac et al. (1995) used the experimental data that hold for heavier species but the smaller deflection of primary electrons in collisions with light elements leads to a little different result. Larger values of δ compensate the omission of the increase of the yield of backscattered electrons (Fig. 2a) due to grain surface curvature. Consequently, they obtained the same σ but slightly smaller positive equilibrium potentials than our results. Nevertheless, we show that Jurac et al. (1995) calculations can be used without notable corrections for the grain diameter exceeding $\approx$1 μm, whereas smaller grains would charge to larger positive potentials. On the other hand, the presence of the salt in the water-ice grains does not alter their potential substantially.

5. Conclusion

Our simulations of the secondary electron emission yield of water ice grains show that the yield is greater than unity from $\approx$30 eV to several keV. Thus, these grains can achieve a negative equilibrium potential only if the Saturn E-ring plasma is cold enough (i.e., the secondary electron emission does not contribute significantly to the charging current) and the contribution of photoemission would be negligible.

Furthermore, the calculations reveal that any reasonable admixture of NaCl does not change the secondary emission properties of small icy dust grains of a given diameter. We would like to note that from our discussion of a probable grain structure it follows that the same conclusions would be valid for the photoemission because the emission of electrons excited by energetic photons proceeds by the same way as the emission of true secondary electrons.

Acknowledgments

This work was supported partly by the Research Plan MSM 0021620860 financed by the Ministry of Education of the Czech Republic, partly by the Czech Grant Agency under Contracts 202/08/0063, 202/08/P066, and 202/08/H057. M. Beránek thanks for a support by the Grant Agency of Charles University (project No. 171410).

References

Barnett, R.N., Landman, U., Nitzan, A., 1990. Primary events following electron injection into water and adsorbed water layers. J. Chem. Phys. 93, 6535–6542.

Baroody, E.M., 1950. A theory of secondary electron emission from metals. Phys. Rev. 78, 780–787.

Beránek, M., Pavlů, J., Vaverka, J., Richterová, I., Šafránková, J., Němeček, Z., 2011. Properties of martian soil simulant. J. Geophys. Res., submitted for publication.

Bethe, H.A., 1933. Handbook of Physics, vol. 24. Springer, Berlin.

Browning, R., Li, T.Z., Chui, B., Jun, Y., Pease, R.F.W., Czyzewski, Z., Joy, D.C., 1995. Low energy electron/atom elastic scattering cross section from 0.1–30 keV. Scanning 17, 250–253.

Bruining, H., 1954. Physics and Applications of Secondary Emission. Pergamon, London.

Charvat, A., Abel, B., 2007. How to make big molecules fly out of liquid water: Applications, features and physics of laser assisted liquid phase dispersion mass spectrometry. Phys. Chem. Chem. Phys. 9, 3335–3360.

Chow, V., Mendis, D., Rosenberg, M., 1993. Role of grain size and particle velocity distribution in secondary electron emission in space plasmas. J. Geophys. Res. 98, 19065–19076.

Chow, V., Mendis, D., Rosenberg, M., 1994. Secondary emission from small dust grains at high electron energies. IEEE Trans. Plasma Sci. 22, 179–186.

Chung, M.S., Everhart, T.E., 1974. Simple calculation of energy distribution of low-energy secondary electrons emitted from metals under electron bombardment. J. Appl. Phys. 45, 707–709.

Czyżewski, Z., O'Neill MacCallum, D., Romig, A., Joy, D.C., 1990. Calculations of Mott scattering cross sections. J. Appl. Phys. 68, 3066–3072.

Draine, B., Salpeter, E., 1979. On the physics of dust grains in hot gas. Astrophys. J. 231, 77–94.

Drouin, D., Hovington, P., Gauvin, R., 1997. CASINO: A new Monte Carlo code in C language for electron beam interaction. 2. Tabulated values of the Mott cross section. Scanning 19, 20–28.

Gilton, T.L., Dehnbostel, C.P., Cowin, J.P., 1989. Electron transmission through layers of H_2O and Xe in the ultrahigh vacuum photoreduction of CH_3Cl on Ni(1 1 1). J. Chem. Phys. 91, 1937–1938.

Hansen, C.J., Esposito, L., Stewart, A.I.F., Colwell, J., Hendrix, A., Pryor, W., Shemansky, D., Wast, R., 2006. Enceladus' water vapor plume. Science 311, 1422–1425.

Hillier, J.K., Green, S.F., McBride, N., Schwanethal, J.P., Postberg, F., Srama, R., Kempf, S., Moragas-Klostermeyer, G., McDonnell, J.A.M., Grün, E., 2007. The composition of Saturn's E ring. Mon. Not. R. Astron. Soc. 377, 1588–1596.

Hovington, P., Drouin, D., Gauvin, R., 1997a. CASINO: A new Monte Carlo code in C language for electron beam interaction. 1. Description of the program. Scanning 19, 1–14.

Hovington, P., Drouin, D., Gauvin, R., Joy, D.C., Evans, N., 1997b. CASINO: A new Monte Carlo code in C language for electron beam interaction. 3. Stopping power at low energies. Scanning 19, 29–35.

Jo, S.K., White, J.M., 1991. Low energy (<1 eV) electron transmission through condensed layers of water. J. Chem. Phys. 94, 5761–5764.

Johnson, R.E., 1998. Sputtering and desorption from icy surfaces. In: Schmitt, B., De Bergh, C., Festou, M. (Eds.), Solar System Ices. Kluwer, Dordrecht, pp. 303–336.

Joy, D.C., Luo, S., 1989. An empirical stopping power expression for low energy electrons. Scanning 11, 176–180.

Jurac, S., Baragiola, R.A., Johnson, R.E., Sittler, E.C., 1995. Charging of ice grains by low-energy plasmas: Application to Saturn's E ring. J. Geophys. Res. 100, 14821–14832.

Kempf, S., Beckmann, U., Moragas-Klostermeyer, G., Postberg, F., Srama, R., Economou, T., Schmidt, J., Spahn, F., Grün, E., 2008. The E ring in the vicinity of Enceladus. I. Spatial distribution and properties of the ring particles. Icarus 193, 420–437.

Kieft, E., Bosch, E., 2008. Refinement of Monte Carlo simulations of electron specimen interaction in low-voltage SEM. J. Phys. D 41, 215310.

Lin, Y., Joy, D.C., 2005. A new examination of secondary electron yield data. Surf. Interface Anal. 37, 895–900.

Mann, I. et al., 2004. Dust near the Sun. Space Sci. Rev. 110, 269–305.

Mann, I., Murad, E., Czechowski, A., 2007. Nanoparticles in the inner Solar System. Planet. Space Sci. 55, 1000–1009.

Matskevich, T.L., Mikhailova, E.G., 1960. Secondary electron emission in ice and anthracene films. Solid State Phys. 2, 709–715.

Mott, N., Massey, H., 1965. Theory of Atomic Collisions. Oxford University Press, New York.

Němeček, Z. et al., 1997. Artificial electron and ion beam effects: Active plasma experiment. J. Geophys. Res. 102, 2201–2211.

Onsager, L., Samaras, N.N.T., 1934. The surface tension of Debye–Hückel electrolytes. J. Chem. Phys. 2, 528–536.

Palik, E.D., 1991. Handbook of Optical Constants of Solids II. Academic Press, Boston.

Pavlů, J., Richterová, I., Němeček, Z., Šafránková, J., Čermák, I., 2008. Interaction between single dust grains and ions or electrons: Laboratory measurements and their consequences for the dust dynamics. Faraday Discuss. 137, 139–155.

Postberg, F., Kempf, S., Hillier, J.K., Srama, R., Green, S.F., McBride, N., Grün, E., 2008. The E-ring in the vicinity of Enceladus: II. Probing the Moon's interior—The composition of E-ring particles. Icarus 193, 438–454.

Postberg, F., Kempf, S., Schmidt, J., Brilliantov, N., Beinsen, A., Abel, B., Buck, U., Srama, R., 2009. Sodium salts in E-ring ice grains from an ocean below the surface of Enceladus. Nature 459, 1098–1101.

Postberg, F., Kempf, S., Srama, R., Green, S.F., Hillier, J.K., McBride, N., Grün, E., 2006. Composition of jovian dust stream particles. Icarus 183, 122–134.

Reid, J.P. et al., 2008. General discussion. Faraday Discuss. 137, 193–204.

Richterová, I., Beránek, M., Pavlů, J., Němeček, Z., Šafránková, J., 2010. Electrons scattered inside small dust grains of various materials. Phys. Rev. B 81, 075406.

Richterová, I., Němeček, Z., Šafránková, J., Pavlů, J., 2004. A model of secondary emission from dust grains and its comparison with experiment. IEEE Trans. Plasma Sci. 32, 617–622.

Richterová, I., Němeček, Z., Šafránková, J., Pavlů, J., Beránek, M., 2007. Secondary emission from glass grains: Comparison of the model and experiment. IEEE Trans. Plasma Sci. 35, 286–291.

Richterová, I., Pavlů, J., Němeček, Z., Šafránková, J., 2006. Model of secondary emission and its application on the charging of gold dust grains. Phys. Rev. B 74, 235430.

Rutherford, E., 1911. The scattering of α and β particles by matter and the structure of the atom. Philos. Mag. 21, 669–688.

Salow, H., 1940a. Angular dependence of the secondary electron emission from insulators. Phys. Z. 41, 434–442 (in German).

Salow, H., 1940b. On the secondary electron yield of electron bombarded insulators. Z. Tech. Phys. 21, 8–15 (in German).

Schmidt, J., Brilliantov, N., Spahn, F., Kempf, S., 2008. Slow dust in Enceladus' plume from condensation and wall collisions in tiger stripe fractures. Nature 451, 685–688.

Schmitt, B., De Bergh, C., Festou, M. (Eds.), 1998. Solar System ices. Astrophysics and Space Science Library, vol. 227. Kluwer, Dordrecht.

Schreiber, E., Fitting, H.J., 2002. Monte Carlo simulation of secondary electron emission from the insulator SiO_2. J. Electron Spectrosc. Relat. Phenom. 124, 25–37.

Showalter, M.R., Cuzzi, N.J., Larson, S.M., 1991. Structure and particle properties of Saturn's E ring. Icarus 94, 451–473.

Spahn, F. et al., 2006. Cassini dust measurement at Enceladus and implications for the origin of the E ring. Science 311, 1416–1418.

Srama, R., Ahrens, T., Altobelli, N., Auer, S., Bradley, J., et al., 2004. The Cassini Cosmic Dust Analyzer. Space Sci. Rev. 114, 465–518.

Sternglass, E., 1957. Theory of Secondary Electron Emission under Electron Bombardment. Scientific Paper 6-94410-2-P9. Westinghouse Research Laboratories, Pittsburgh, p. 35.

Suszcynsky, D.M., Borovsky, J.E., Goertz, C.K., 1992. Secondary electron yields of Solar System ices. J. Geophys. Res. 97, 2611–2619.

Vrbka, L., Jungwirth, P., 2005. Brine rejection from freezing salt solutions: A molecular dynamics study. Phys. Rev. Lett. 95, 148501.

Waite Jr., J.H. et al., 2006. Cassini ion and neutral mass spectrometer: Enceladus plume composition and structure. Science 311, 1419–1422.

Warren, S.G., Brandt, R.E., 2008. Optical constants of ice from the ultraviolet to the microwave: A revised compilation. J. Geophys. Res. 113, 14220.

Weingartner, J.C., Jordan, M.E., 2008. Torques on spheroidal silicate grains exposed to anisotropic interstellar radiation fields. Astrophys. J. 672, 382–390.

Ziemann, P., Liu, P., Kittelson, D., McMurry, P., 1995. Electron impact charging properties of size-selected, submicrometer organic particles. J. Phys. Chem. 99, 5126–5138.

O. Vaverka et al. [2014]

Vaverka, J., Richterová, I., Vyšinka, M., Pavlů, J., Šafránková, J., Němeček, Z., The influence of secondary electron emission on the floating potential of tokamak-born dust. *Plasma Phys. Contr. F.* 56 (2): 025001, 2014.

IOP Publishing Plasma Physics and Controlled Fusion
Plasma Phys. Control. Fusion **56** (2014) 025001 (11pp) doi:10.1088/0741-3335/56/2/025001

The influence of secondary electron emission on the floating potential of tokamak-born dust

J Vaverka, I Richterová, M Vyšinka, J Pavlů, J Šafránková and Z Němeček

Faculty of Mathematics and Physics, Charles University, Prague, Czech Republic

E-mail: jakub.vaverka@mff.cuni.cz

Received 30 September 2013, revised 29 October 2013
Accepted for publication 7 November 2013
Published 6 January 2014

Abstract

Dust production and its transport into the core plasma is an important issue for magnetic confinement fusion. Dust grains are charged by various processes, such as the collection of plasma particles and electron emissions, and their charge influences the dynamics of the dust. This paper presents the results of calculations of the surface potential of dust grains in a Maxwellian plasma. Our calculations include the charging balance of a secondary electron emission (SEE) from the dust. The numerical model that we have used accounts for the influence of backscattered electrons and takes into account the effects of grain size, material, and it is also able to handle both spherical and non-spherical grains. We discuss the role of the SEE under tokamak conditions and show that the SEE is a leading process for the grains crossing the scrape-off layer from the edge to core plasma. The results of our calculations are relevant for materials related to fusion experiments in ITER.

Keywords: dust in tokamak, dust charging model, materials for tokamak

(Some figures may appear in colour only in the online journal)

1. Introduction

One of the most important challenges of present physics is addressing the problem of materials related to the next generation of fusion experiments. Large energy fluxes are directed toward the walls of the vessel and these cause the erosion of the plasma-facing components. This process leads to the introduction of impurities into the plasma and it also leads to their degradation [1, 2]. The resulting production of solid grains and their transport into the plasma is, thus, important for magnetic confinement fusion. Previous studies have shown the origin of a considerable amount of dust [3–5] that may vary according to its formation mechanism and the plasma conditions at a particular region. Small dust grains are observed mainly in the edge plasma region but some grains can penetrate deeply into the core plasma after disruption [1, 6–10]. It is known that dust collected from a tokamak exhibits a large variety of shapes and sizes [1] and that, after a series of discharges, it has a log-normal size distribution [1, 11] with an average radius of the order of 1 μm. Hence, the composition of the dust grains reflects the composition of the plasma-facing components [5, 10].

Various scenarios have been considered for the construction of the ITER divertor and first wall [12] and all of these scenarios are planned to be adopted in different stages of the project's development. These options are (1) a combination of carbon fibre composite, tungsten and beryllium for the divertor and the first wall; (2) W divertor with the Be first wall; and (3) the whole vessel from W. The choice of carbon for the parts of the divertor where the scrape-off layer (SOL) strikes the vertical target and where energy deposition from disruptions and edge-localized modes (ELMs) will occur is mainly due to its good power handling and thermal shock resistance. In other words, it does not melt and preserves its shape even under extreme temperature excursions [13]. However, there is concern about the absorption of tritium in the carbon components. Consequently, the induced dust grains in ITER will be mainly composed of carbon, tungsten and beryllium [2, 12].

The scaling of existing tokamak data to other reactors, in particular to ITER, including all relevant physical processes

(charging, sputtering, evaporation, radiation, transport, etc) is not yet advanced enough, although significant progress has recently been made ([14–16] and references therein). Thus, both the experimental results on dust generation, mobilization, and transport in existing devices and theoretical predictions for ITER are highly uncertain and require additional intensive studies.

Dust moving in a high-temperature plasma becomes electrically charged due to various processes, such as the collection of plasma particles and electron emissions. In low-temperature and low-density plasmas, dust grains are generally negatively charged due to plasma particle collection since the electrons have higher thermal mobility in comparison with heavier ions. In tokamak plasmas where strong electric fields can be formed due to plasma temperature gradients, drifts, induced currents, and in the electrostatic sheaths near the plasma-facing components, the charge of a micrometer-sized grain can vary from slightly positive to highly negative depending on the plasma conditions and the electron emission currents (e.g. [10]). Generally, the photoemission or thermionic emission positively charges the grain, whereas an interaction of grains with energetic electrons, which is called secondary electron emission (SEE), can lead to more positive but, in some cases, also to negative grain charges.

1.1. The role of SEE in tokamaks

If the electron flux is significant (in hot plasma regions), the sign and value of the dust grain surface potential will be determined by the energy of the impinging electrons. An electron attachment dominates in the eV range but SEE becomes important and results in a reduction of the negative potential at electron energies above about 10 eV. At a few tens of electronvolts, the total SEE yield (which is defined as the number of outgoing electrons per primary electron) can reach values larger than unity, which causes a sign change of the potential from negative to positive. Generally, the SEE yield reaches a maximum value at energies between 300 and 2000 eV. At higher energies, the SEE yield decreases again below unity, resulting in a negative surface potential. However, if the size of the grains is comparable with the mean free path of the primary electrons and with the diffusion length of excited electrons, then the SEE yield may be substantially enhanced. Moreover, the surface quality, and even material properties, of the grain can be modified by an interaction with the tokamak plasma.

Theoretical studies and models of SEE are often based on Monte Carlo simulations of electron trajectories [17–20]. However, these studies expect planar metal or insulating targets, and/or clean and smooth grains from well defined materials.

Measurements of a SEE yield are reported for fresh graphite samples and for the same material exposed for some months in the JET tokamak. The exposed samples exhibited substantially higher (by a factor of 1.3) values of the SEE yield than the fresh samples [21]. Clean conducting surfaces usually have a maximum SEE yield slightly above unity. For light materials, such as graphite and beryllium, the SEE yield for clean surfaces is lower but the presence of hydrogen in the surface increases the yield values to about unity. The experimental yields are in a good agreement with relatively simple models for primary electrons at nearly normal incidence [22].

Since SEE influences the grain floating potential, this process is an important part of the models describing the dust dynamics in tokamaks. At present, there are two main codes simulating the interactions of an isolated spherical dust grain with a non-magnetized plasma (e.g. [10] and references therein): DUSTT [23] and DTOKS [24], which include dust grain charging, heating, and motion. In such simulation codes, a plasma background is coupled with a dust model (charging, forces, etc) to solve the grain equation of motion and to determine its trajectory, and with a dust heating model to include a presence of large energy fluxes on the grain that can heat the dust grains to high temperatures. The charging model is based on the orbital motion limited (OML) approach [25] and is complemented with additional mechanisms; namely, thermionic and secondary electron emissions. Other charging mechanisms, such as photoemission and radioactivity, have been considered as minor in comparison with the secondary and thermionic emission currents (see [26–28] for details).

Smirnov *et al* [27] modeled the dynamics and transport of carbon dust particles in tokamak fusion devices using computer simulations with the DUSTT code from small grains and the presence of impurities. It was shown that thermionic emission leads to enhanced dust heating by the plasma, which increases the destruction of the dust particles. In addition, the transport of dust in tokamaks can significantly enhance the penetration of carbon impurities towards the core plasma.

Bacharis *et al* [29] used the dust transport code, DTOKS, to simulate the penetration of tungsten and beryllium dust grains into the ITER plasma. They found that grains with a radius larger than 10 μm and with an injection velocity of 10 m s^{-1} can survive long enough to reach the separatrix. Generally, smaller particles with lower injection velocities deposit most of their initial mass within the SOL and larger particles with high injection velocities have a higher probability of reaching the last closed magnetic surface and the core.

In these, and many other, simulations (e.g. [28, 30–32]), the SEE yield is calculated using an original Sternglass approach [33] that does not reflect the effects of dust radius. However, when the size of the grain is comparable with the penetration depth of the incident electrons the SEE yield, and especially the floating potential and the grain charge, depends significantly on the grain size [34–36].

1.2. Motivation

Laboratory experiments devoted to SEE investigations have shown that the charge of micrometer-sized grains can be either positive or negative and the charge sign depends on their shape, dimensions, and material even under the same parameters of the ambient plasma (e.g. [37–43]). This fact lies behind the main motivation for our study.

We have investigated dust samples collected during a technical shutdown of the COMPASS-D tokamak [44]. A

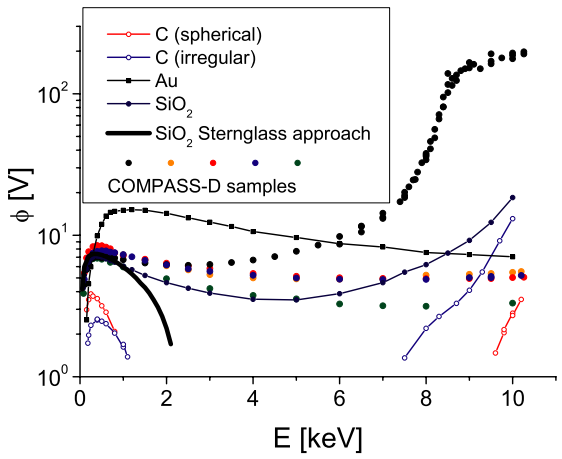

Figure 1. The surface potential as a function of the primary electron energy for several grains collected from the COMPASS-D tokamak (dots) and their comparison with glassy carbon, gold and glass samples (lines). The full line presents the theoretical floating potential of the 1 μm SiO_2 grain computed according to the Sternglass theory [33].

basic analysis by an electron microscope (SEM) has confirmed that the COMPASS-D grains exhibit various shapes and that their typical sizes are of the order of micrometers. These results correspond well with other analyses of the tokamak-born dust [1, 10]. The elemental composition determined by the energy dispersive x-ray (EDX) spectroscopy corresponded to that of the vessel walls, divertor and diagnostic tools destroyed during a preceding active period. We should note that carbon is not used in this tokamak. The SEE investigation was carried out in the experimental set-up where a single dust grain is stored in an electrodynamic quadrupole for a long time in the UHV apparatus. The levitating grain is influenced by the electron beam with the energy adjustable in the range of 0.1–10 keV (the detailed description of the set-up and measurement techniques can be found in [42, 45]).

Figure 1 presents a collection of measurements of equilibrium surface potentials of several grains from the COMPASS-D tokamak. For a comparison with these grains we have plotted potential profiles measured on grains from two crystalline forms of C, Au and SiO_2 as representatives of metals and insulators, respectively (marked by the lines in figure 1). We should note that these samples were spherical and that their mass and diameter were known. On the other hand, neither compositions nor shapes are known for the investigated COMPASS-D grains (color dots in figure 1).

Figure 1 shows a large variability of surface potential profiles measured on tokamak grains. Their profiles are similar to those measured on the SiO_2 grain. We believe that this effect is caused by a partial oxidation of metallic grains during their exposition to the open air. The tokamak grain, which is marked by a black color, exhibits a large and nearly constant ($\approx$200 V) potential for the primary energy above $\approx$8 keV. This effect is well known for small grains or the grains of highly non-spherical shape [46]. The surface potential is limited by the field emission in such a case [47]. The heavy line shows the theoretical floating potential of the 1 μm SiO_2 grain computed using the Sternglass theory [33] and corrected on the angular dependence of the SEE yield. The Maxwellian distribution of true secondary electrons with the temperature of 3 eV was assumed in our calculations. One can see that the theory underestimates SEE from the dust grains and predicts negative potentials for primary energies above 2.2 keV but the measured potentials are positive in the whole range of examined energies.

For this reason, this paper presents the results of our calculations of the surface potential of dust grains in a high-temperature Maxwellian plasma. We include a numerical model [48] of the SEE that reflects the grain's size effects into the charging balance of the dust and consider dust produced by the sputtering of plasma-facing surfaces from ITER related materials. Our calculations include electron and ion currents, the SEE and thermionic currents, and a possible contribution of the field emission current due to a strong electric field at the grain surface.

2. Dust charging in fusion plasma

The charging of dust in fusion plasmas is a dynamic process that is described by the current balance equation (a sum of all discharging/charging currents). As in other models, we start with theoretical models for plasma–grain interaction ignoring magnetic field effects and assuming a spherical grain in a Maxwellian plasma [49]. We consider dust grain charging caused by ion, J_i and electron, J_e currents. We include the SEE current, J_{sec}, and the thermionic current, J_{therm}, because the grain can be heated by the hot dense plasma. A contribution of the field emission current, J_{fe} caused by the strong electric field above the grain surface [47] can be important for small grains charged to high negative potentials.

Since this paper mainly deals with the effects of secondary electron and field emissions, we will concentrate on hot dense plasma regions at, and inside, the SOL. This allows us to neglect a photoemission current that can be important only in the edge plasma where the electron and ion currents are relatively low [10]. Furthermore, although the intensity of the magnetic field can exceed 1 T, the OML theory provides a reasonable approximation of both electron and ion currents because the electron (ion) gyro-radius is of the order of hundreds of micrometers (tens of millimeters); that is, much larger than the dust grain radius. The collisions with the neutral gas can be neglected because a plasma is fully ionized in the considered temperature range. However, there would be a number (hopefully low) of neutrals in the grain vicinity because the ions that recombine on a surface would leave the grain as neutrals. The ratio of the dust grain radius and Debye length is <0.01, whereas Lampe [50] has shown that if this ratio is lower than 5 in the isothermal plasma, then the OML theory provides a good approximation of the particle current.

Based on these simplifications, we can estimate a total current to the dust grain as

$$\frac{\mathrm{d}Q}{\mathrm{d}t} = J = J_e + J_i + J_{therm} + J_{fe} + J_{sec}. \qquad (1)$$

The differential flux density of electrons or ions, $J_{e,i}$ toward a dust grain charged to a surface potential, ϕ can be generally written as

$$J_{e,i} = \int_{\max(0,\pm e\phi)}^{\infty} (1 \mp e\phi/E) \frac{\mathrm{d}j_{e,i}}{\mathrm{d}E} \mathrm{d}E, \quad (2)$$

where

$$\frac{\mathrm{d}j_{e,i}}{\mathrm{d}E} = \frac{2\pi E}{m_{e,i}^2} n_{e,i} \left(\frac{m_{e,i}}{2\pi k T_{e,i}}\right)^{3/2} \exp\left(-\frac{E}{kT_{e,i}}\right). \quad (3)$$

The positive and negative signs correspond to electrons and ions, respectively, e is the elementary charge, and E is the energy of impacting electrons. We assume the neutral $n_e = n_i = n$, isothermal $T_e = T_i = T$, hydrogen plasma with a Maxwellian energy distribution. When the spherical dust grain radius, a is smaller than the Debye length, the electron and ion currents, $J_{e,i}$, can be estimated according to [10, 37]. In this case, we can write for the electron current, J_e:

$$J_e = J_{0e} \times \begin{cases} \exp(+e\phi/kT), & \phi < 0, \\ (1 + e\phi/kT), & \phi \geqslant 0, \end{cases} \quad (4)$$

where k is the Boltzmann constant, and $J_{0e} = 4\pi a^2 en\,(kT/2\pi m_e)^{1/2}$.

Similarly, the ion current, J_i can be written as:

$$J_i = J_{0i} \times \begin{cases} \exp(-e\phi/kT), & \phi \geqslant 0, \\ (1 - e\phi/kT), & \phi < 0, \end{cases} \quad (5)$$

where J_{0i} is defined similarly to J_{0e}.

To include the thermionic J_{therm} and field electron J_{fe} emission currents, we use the Richardson–Dushman formula and the Fowler–Nordheim equation, respectively:

$$J_{\mathrm{therm}} = 4.8 \times 10^6 \pi a^2 e k T_d^2 \exp(-w_f/kT_d) \times \begin{cases} 1, & \phi < 0, \\ \exp(-e\phi/kT_d), & \phi \geqslant 0, \end{cases} \quad (6)$$

and

$$J_{\mathrm{fe}} = 13.7 \times 10^{-7} \pi a^2 e \left(\frac{\phi}{a}\right)^2 \exp\left(\frac{6.52 \times 10^{10} a}{\phi}\right), \quad (7)$$

where w_f is a material work function, T_d is the dust grain temperature. Both equations (6) and (7) are written in a form that is appropriate for the following calculations. To receive the current in amperes, the grain radius in meters and the potential in volts should be substituted. The work function is set to $w_f = 4.5$ eV in equation (7).

The SEE current is generally determined by the flux of impinging electrons (2), the total SEE yield, σ, and the energy distribution of secondary electrons. Since the SEE current is often a dominant current in hot plasma environments, we will discuss it in the next section.

2.1. SEE current estimation

The most frequently used theory [33] describes SEE from planar metal surfaces in the range of tens of eV to several keV. Primary electrons impacting the sample surface interact with the bulk material and lose their energy in many types of collisions. The energy losses often result in excitations of material electrons and some of the excited electrons can leave the surface. These electrons are usually called true secondary electrons. The energy dependence of the true SEE yield, $\delta(E)$ (which is defined as the ratio of numbers of true secondary and primary electrons) can be described by the Sternglass universal formula [33]:

$$\frac{\delta(E)}{\delta_M} = \frac{E}{E_M} \exp\left[2\left(1 - \sqrt{\frac{E}{E_M}}\right)\right], \quad (8)$$

where δ_M is the maximum of the true SEE yield at the energy E_M. For real materials, the curve exhibits a maximum at energies in the range from several hundred eV to a few keV, and decreases to zero at very high and low beam energies. For both parameters of the curve, the maximum yield and corresponding energy depend only on the sample material at a given incidence angle. For example, $\delta_M = 1.25$ and $E_M = 300$ eV for a glassy carbon sample. Although the author limited the validity of this universal curve to $E < 4E_M$ and planar metal samples, this formula is often used outside this range and it is also used for arbitrary targets.

However, the primary electrons undergo scattering and may be re-emitted from the solid without a significant loss of their initial energy. The yield of these backscattered electrons, η increases with the material density and with the atomic number up to $\eta \approx 0.5$ for a normal incidence angle. Thus, the total SEE yield, σ, is a sum of the true and backscattered yields, $\sigma = \delta + \eta$. Since both the yield of true SEE δ and total yield σ vary in a similar way with the beam energy, the contribution of the backscattered primary electrons is often omitted in calculations of the grain potential; that is, $\eta = 0$ and $\sigma = \delta$ are supposed.

Under assumptions that the energetic distribution of secondary electrons is Maxwellian and parametrized by the temperature T_s ($T_s = 3$ eV in our calculations), the SEE current from positively charged grain can be written as

$$J_{\mathrm{sec}} = nAe \times \begin{cases} \int_{-e\phi}^{\infty} (1 + e\phi/E) \frac{\mathrm{d}j_e}{\mathrm{d}E} \sigma(E + e\phi) \mathrm{d}E & \phi < 0. \\ \left(\int_0^{\infty} (1 + e\phi/E) \frac{\mathrm{d}j_e}{\mathrm{d}E} \eta(E + e\phi) \mathrm{d}E \right. & \\ \quad + (1 + e\phi/kT_s) \exp(-e\phi/kT_s) & \\ \left. \quad \cdot \int_0^{\infty} (1 + e\phi/E) \frac{\mathrm{d}j_e}{\mathrm{d}E} \delta(E + e\phi) \mathrm{d}E \right) & \phi \geqslant 0, \end{cases} \quad (9)$$

where A is the grain surface area. Note that the energy of scattered primary electrons is expected to be sufficient for their escape from positively charged grains.

Richterová *et al* [51] developed a hybrid Monte Carlo model explaining the increase of the grain potential for small spherical grains that is experimentally demonstrated in figure 1. This mechanism leads to the dust grain potential becoming a function of the grain size. This model was successfully verified by laboratory experiments dealing with charging of gold [36], glass (silica) [52] and glassy carbon [48] dust grains. A novel version [46] of the model was applied to non-spherical grains and to grains with defined surface roughness. It was shown that non-sphericity causes a rise of the SEE yield, whereas the

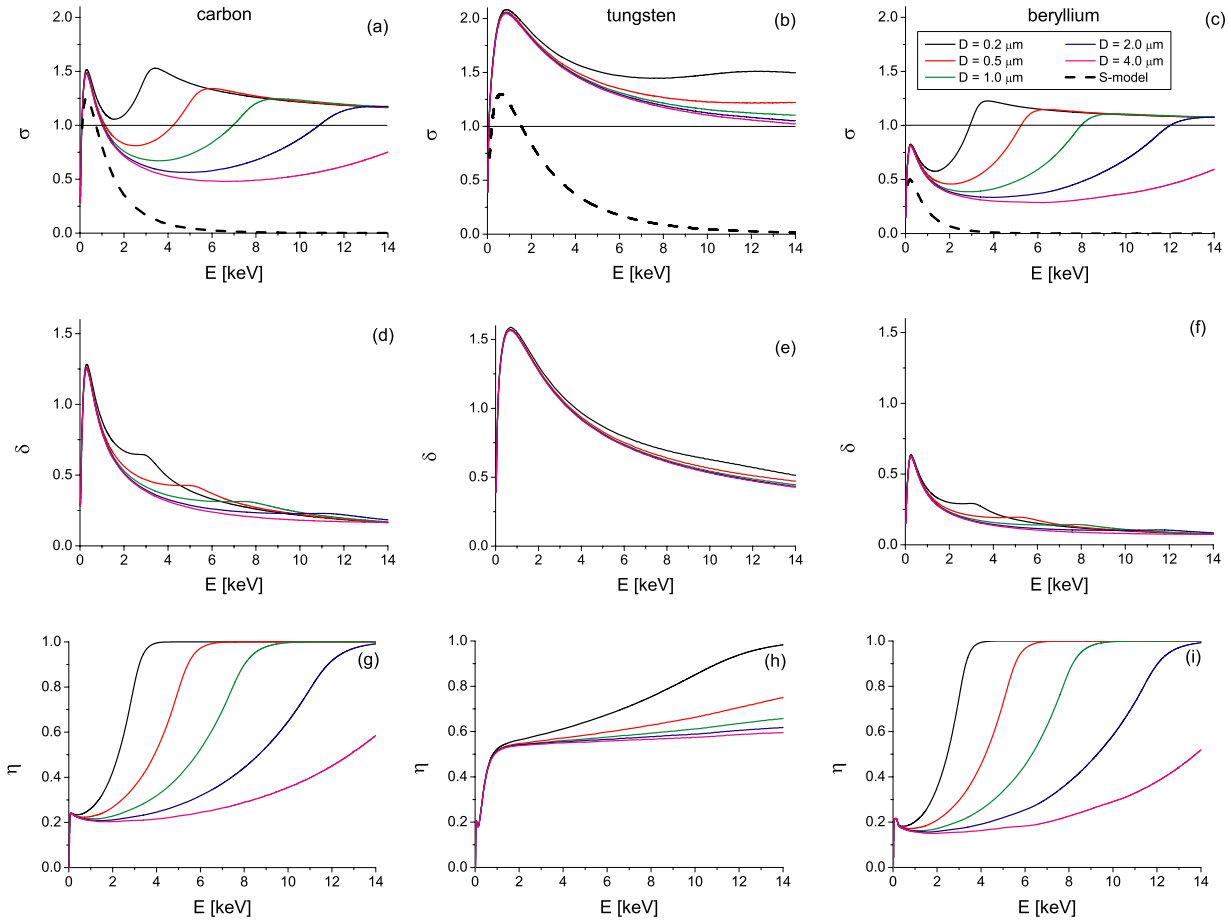

Figure 2. Energetic profiles of SEE yield for glassy carbon, tungsten and beryllium spherical dust grains of different diameters. Top panels (*a*), (*b*), (*c*) correspond to total SEE yields, middle panels (*d*), (*e*), (*f*) to true SEE yields, and lower panels (*g*), (*h*), (*i*) to backscattered SEE yields. The first column of the figure presents glassy carbon (*a*), (*d*), (*g*), the second column tungsten (*b*), (*e*, (*h*), and finally the third column beryllium (*c*), (*f*), (*i*). Profiles of σ are compared with the results of the S-model (black dashed lines in top panels).

surface roughness leads to a yield decrease. Moreover, these effects can be distinguished: the shape effect is prominent for high primary energies only, whereas the surface roughness predominantly affects the yield at the low-energy range.

The model describes both components of the SEE yield, δ and η for spherical grains of different materials and diameters. Since the model does not provide an analytical formula, we use $\delta(E)$ and $\eta(E)$ pre-calculated for a given material and grain diameter in discrete points. A linear interpolation between these points is used for a numerical solution of equation (9) (hereafter, the R-model).

Nevertheless, many authors use equation (8) for a description of the total SEE yield. To show the importance of the backscattered yield η, we plotted all components of the SEE yield calculated by the R-model for several diameters of spherical grains from (*a*) glassy carbon, (*b*) tungsten, (*c*) beryllium with respect to the primary electron energy in figure 2. The curves are compared with the approach using the theoretical Sternglass curve for the true SEE yield (hereafter, the S-model).

The profiles of σ provided by both models are similar in the low-energy range (up to $\approx$1 keV). The enhanced values provided by the R-model are caused partly by the neglection of backscattered electrons in the S-model and by the dependence of the SEE yield on the incident angle of primary electrons. An inclusion of the angular dependence into the S-model would enhance δ by a factor of $\approx$1.3 [34, 42] but the profile remains unchanged.

At high primary energies (above about 2 keV for $D = 0.2\,\mu$m grain), σ again increases and can reach values comparable to, or even exceeding, the first maximum. This effect is prominent for light materials but it can be hardly identified for tungsten grains. Note that the energy corresponding to the secondary maximum is a rising function of the grain size. The maximum appears at the energy for which the penetration depth of the primary electrons is comparable with the grain size. The yield of backscattered electrons η increases toward unity and the yield of true secondary electrons δ is also enhanced under this condition.

2.2. Estimation of the dust grain floating potential

This section presents our calculations of the floating potential of spherical grains ($D = 1\,\mu$m) immersed in a hydrogen plasma with a density corresponding to that in a small tokamak

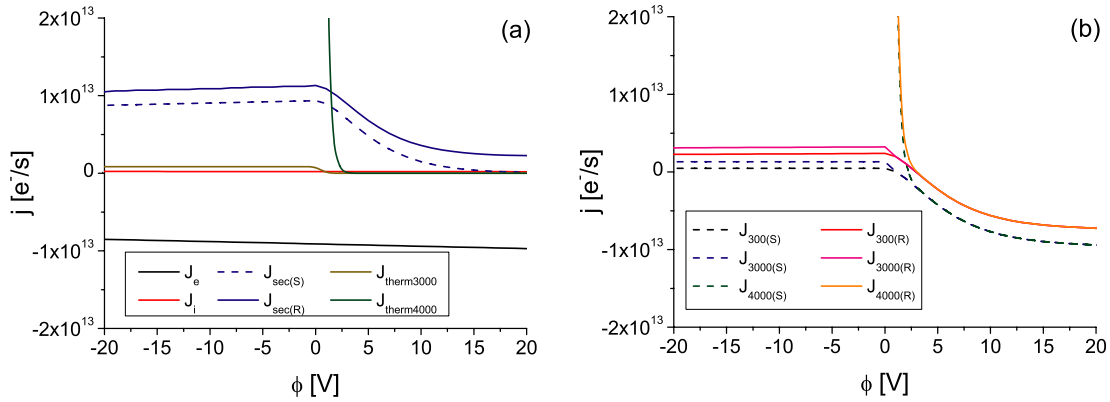

Figure 3. (*a*) Charging currents of the spherical glassy carbon grain ($D = 1\,\mu$m) for fusion related plasma conditions with respect to the grain surface potential; (*b*) the total charging current for the same grain and the same conditions as a function of the grain surface potential.

($n = 10^{18}\,\mathrm{m}^{-3}$). The charging currents J_e, J_i, J_therm and J_fe are computed according to the equations given in previous sections. Since the Sternglass formula for the SEE current is often applied for calculations of the dust charging in the tokamak plasma, we use both R- and S-models to contrast these two approaches: (1) the calculations of $J_{\mathrm{sec(S)}}$ use the S-model of SEE and analytical solution from [37]; whereas (2) $J_{\mathrm{sec(R)}}$ is computed numerically using the R-model (we use following SEE parameters for glassy carbon $\delta_\mathrm{M} = 1.25$ and $E_\mathrm{M} = 350\,\mathrm{eV}$, for beryllium $\delta_\mathrm{M} = 0.5$ and $E_\mathrm{M} = 200\,\mathrm{eV}$, and for tungsten $\delta_\mathrm{M} = 1.3$, $E_\mathrm{M} = 600\,\mathrm{eV}$).

Charging currents of the spherical glassy carbon grain ($D = 1\,\mu$m) and $T = 300\,\mathrm{eV}$ with respect to the grain surface potential are shown in figure 3(*a*). One can see that the SEE current calculated by the R-model, $J_{\mathrm{sec(R)}}$ is higher than $J_{\mathrm{sec(S)}}$ due to a larger SEE yield. The thermionic current is calculated for two different temperatures of dust: $J_{\mathrm{therm3000}}$ for 3000 K and $J_{\mathrm{therm4000}}$ for 4000 K. We would like to note that $J_{\mathrm{sec(R)}}$ is the largest charging current and SEE is a dominant process for a determination of the potential of the colder grain. Figure 3(*b*) shows a sum of the currents in the same environment for three different temperatures of the grain (300, 3000 and 4000 K) and for two ways of calculating the SEE current.

The equilibrium grain potential is set if the sum of all currents is equal to zero. It is possible to see that equilibrium potential is always higher when the R-model is applied. On the other hand, the effect of the grain temperature is notable only for 4000 K. This effect is clearly demonstrated in figure 4 where the equilibrium surface potential of the glassy carbon grain is plotted as a function of the plasma temperature for several grain temperatures (300, 3000, 3250 and 3500 K). For the middle range of plasma temperatures, the thermionic emission leads to the positive potential of the grain if its temperature exceeds 3200 K but SEE remains a dominant charging mechanism at low (<800 eV) and high (>4 keV plasma temperatures even for 3500 K of the grain temperature. It is important to note that the calculations use $n = 10^{18}\,\mathrm{m}^{-3}$ but that the expected plasma densities in tokamaks can reach $10^{20}\,\mathrm{m}^{-3}$. The influence of the thermionic emission will be even less significant because all charging currents except J_therm and J_fe are proportional to the plasma density. In order to decrease the number of free

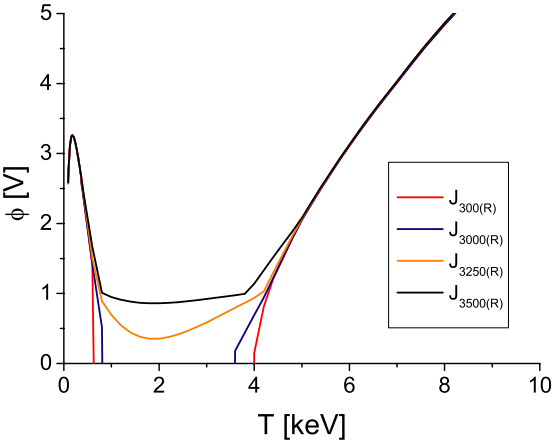

Figure 4. The equilibrium surface potential of glassy carbon dust ($D = 1\,\mu$m) for fusion related plasma conditions as a function of the plasma temperature calculated by the R-model for several dust grain temperatures (300, 3000, 3250 and 3500 K).

parameters, we expect a cold (<3000 K) grain and neglect the thermionic emission current in further calculations.

Figure 5(*a*) shows the equilibrium surface potentials for cold carbon dust grains of several radii calculated by the R-model with respect to the plasma temperature. The potential calculated with the S-model that does not depend on the grain size is shown for reference. Small ($D < 0.5\,\mu$m) carbon grains reach a positive equilibrium potential in the whole range of plasma temperatures. On the other hand, grains of intermediate ($0.5\,\mu\mathrm{m} < D < 2.0\,\mu\mathrm{m}$) sizes are charged negatively for the middle range of plasma temperatures and large ($D > 2.0\,\mu$m) grains are charged negatively for the temperatures exceeding 1 keV. These results correspond to SEE yield profiles shown in figure 2(*a*).

On the other hand, calculations that use the S-model are able to predict negative potentials for all grains and temperatures in excess of ≈0.7 keV. The rising negative potential increases the ion current, which would eventually stop its rise, but our estimation shows that the field emission is more effective even for relatively large grains. This effect is seen in the profile denoted as $\mathrm{S_{fe}}$-model for $D = 2.0\,\mu$m. The

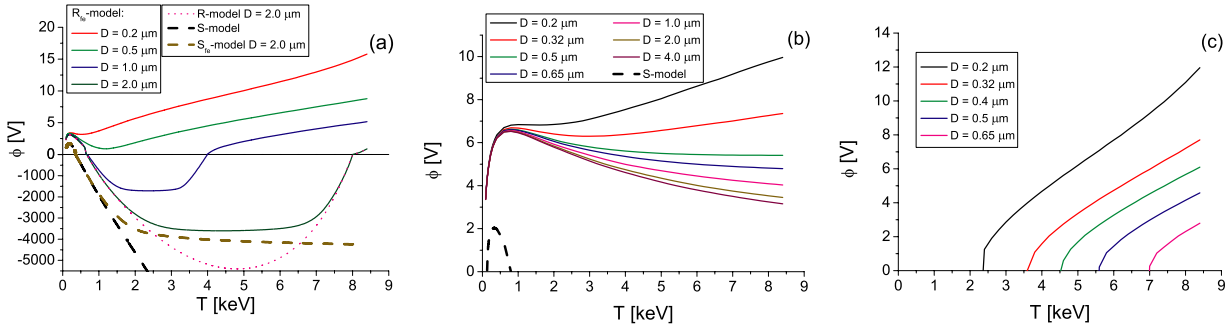

Figure 5. The equilibrium surface potentials for (*a*) glassy carbon, (*b*) tungsten and (*c*) beryllium dust grains of different diameters and their comparison with the S-model.

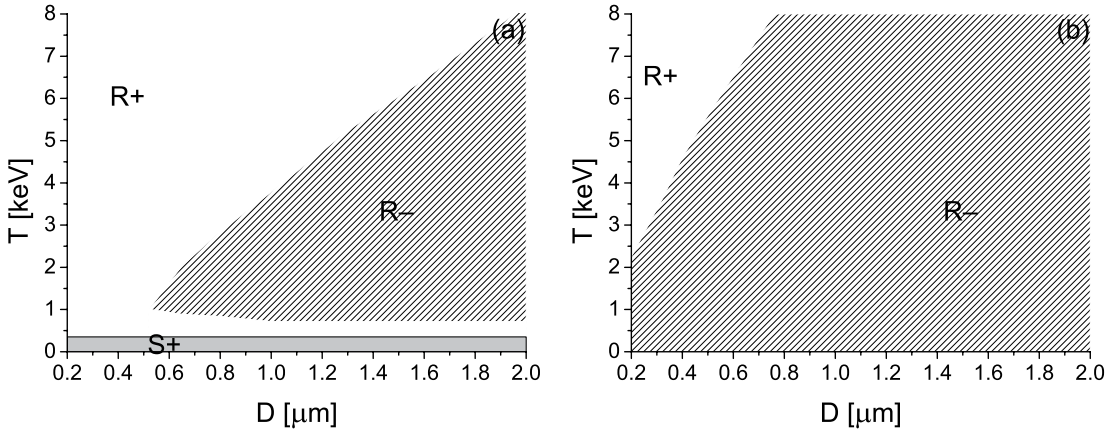

Figure 6. A map of the signs of surface potentials for (*a*) glassy carbon and (*b*) beryllium grains with respect to the grain size and plasma temperature.

field emission current increases with decreasing grain diameter (all profiles with subscripts 'fe'), thus the small grains exhibit lower but still highly negative potentials (a negative part of the vertical axis has a different scale than the positive one). It should be noted that the negative grain potentials accelerate the ions and that their impact causes emissions of electrons. This effect is not included in our calculations because the yield of the ion induced emission is very low.

Since negative potentials depend only weakly on the material, we present only the positive parts of the plots for tungsten (figure 5(*b*)) and beryllium (figure 5(*c*)). Tungsten grains would be charged negatively for plasma temperatures higher than 1 keV according to the S-model but they are charged positively for all plasma temperatures regardless of grain sizes when the R-model is used (figure 5(*b*)). The S-model leads to the negative potential for beryllium grains in the whole range of plasma temperatures. By contrast, the R-model (figure 5(*c*)) predicts that small grains would be charged positively in hot environments.

Figure 6 shows a floating potential sign map for (*a*) glassy carbon, and (*b*) beryllium grains with respect to grain sizes and plasma temperatures. The grains in a white area (R+) would have a positive equilibrium potential (typically a few V) and those in a hatched area (R−) would be negative (several kV). The shadowed area (S+) describes conditions where the grains are charged positively according to both models. This area is absent in figure 6(*b*) because all Be grains will be charged negatively when the S-model is used.

3. Discussion and conclusion

We have analyzed the dust grains collected from the COMPASS-D tokamak by electron microscope (SEM) and EDX. This analysis has shown that there are a large variety of dust shapes with a typical size of grains of the order of micrometers. The elemental composition of the collected dust corresponds to the materials used for the divertor and diagnostic tools. We did not show these results because they agree with previous studies of tokamak-born dust.

Many published calculations of the dust grain potential use the Sternglass approach (S-model) or similar formulas for a description of SEE, and they all tend to underestimate the SEE current. We have applied the R-model that is more realistic for the description of SEE from objects of a limited size, especially for the environments with hot electrons. An application of this SEE model reveals that the SEE current dominates all other charging currents for cold tungsten grains in the whole range of investigated plasma temperatures (0.1–10 keV); therefore, these grains will always be slightly positive, whereas the application of the S-model would lead to high (of the order of kV) negative potentials for cold (<3200 K) grains. Since W

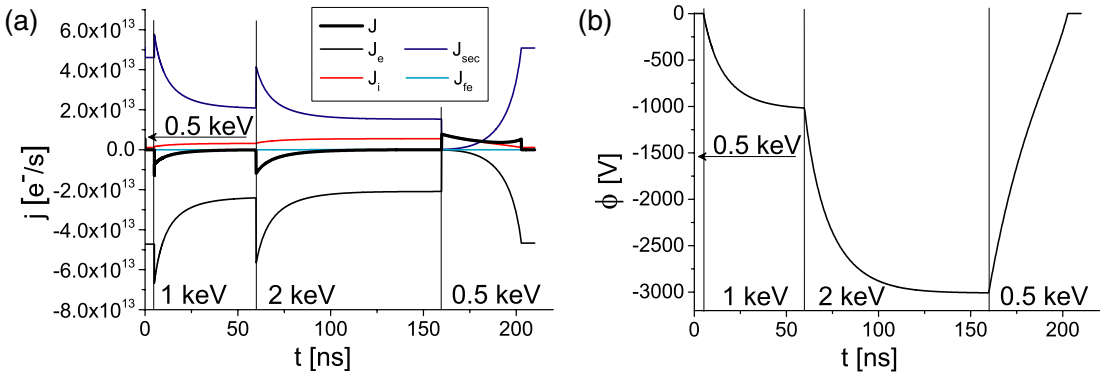

Figure 7. A temporal evolution of major charging currents after abrupt changes (*a*) of the plasma temperature and corresponding changes (*b*) of the floating potential of the 1 μm cold carbon grain.

is expected to be a principal material for ITER, we think that this result is very important.

The SEE yield of beryllium is rather low and, thus, the SEE effects are important only for small (<500 nm) cold grains that would be charged positively in fusion plasma. The plasma temperature at which the transition from high negative to weak positive potentials occurs ranges from ≈2.5 keV for a 100 nm grain to ≈7 keV for the 325 nm grain. The transition is a consequence of the size dependence of the SEE yield and, thus, it cannot be predicted if the S-model is used for surface potential calculations.

The most complicated potential profiles exhibits glassy carbon. Carbon grains would be charged positively in the low-temperature (<1 keV) plasma regardless of their sizes. Positive charges can be expected for small (<250 nm) grains in a whole range of temperatures, whereas the grains of an intermediate size (0.25–1 μm) exhibit a region of plasma temperatures where they acquire large negative potentials. The negative potentials of the grains are limited by the field emission, which strongly depends on the grain size and, to a lesser degree, by the ion induced SEE that was mentioned in the previous section.

To be consistent with the previous results of other authors, our calculations use the Maxwellian approximation for the energy distribution of secondary electrons. However, Richterová *et al* [53] have shown that this distribution is appropriate for a description of SEE from non-conducting grains, whereas the Draine–Salpeter distribution [34] better fits the measurements on conducting grains. Since this distribution exhibits a strongly enhanced tail above ≈10 eV, the positive potentials in figure 5 are underestimated. We will return to this topic later, after collecting a sufficient set of experimental data on the distribution of secondary electrons emitted from small grains.

The discussed calculations of the surface potential neglect the thermionic emission; therefore, we will examine the effects of the grain temperature in the next section.

3.1. The applicability of our calculations to tokamak conditions

The dust in tokamaks is produced at the walls of the vessel or at the divertor where the plasma temperature is generally

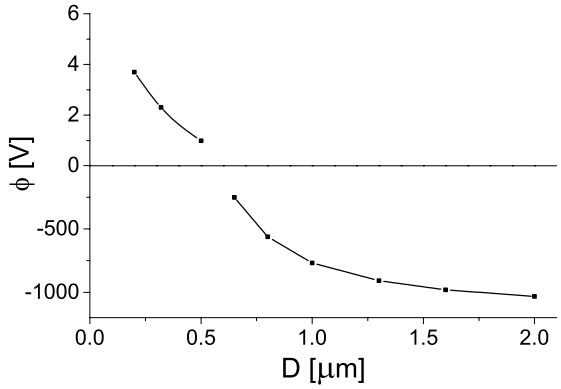

Figure 8. A change of the floating potential of the cold (T < 3000 K) carbon grain immersed into a hot (1 keV) plasma as a function of its size.

low, except when the confinement conditions are broken. On the other hand, our calculations show that SEE becomes a leading charging process for a relatively cold grain (i.e. below ≈3200 K) and electron temperature in the keV range that is typical for a core plasma. Krasheninnikov *et al* [14] have shown that the equilibrium temperature of the dust grain in the edge plasma varies between 1500 K for plasma densities $n = 10^{18}\,\mathrm{m}^{-3}$ and 4000 K for $n = 10^{20}\,\mathrm{m}^{-3}$ and that a significant portion of the dust produced at the divertor would reach the core. As we have shown in figure 3, the thermionic current dominates above 3200 K that corresponds to the density of about $n = 10^{19}\,\mathrm{m}^{-3}$. This means that all of the dust grains would be charged positively for this and larger densities; however, our calculations expect a plasma density of $n = 10^{18}\,\mathrm{m}^{-3}$ and, thus, our neglect of the thermionic current is well justified.

The estimated lifetime of a micrometer dust grain is 10 ms in a dense ($n = 10^{20}\,\mathrm{m}^{-3}$) edge plasma [14, 54], it would be significantly longer at lower densities. The ion drag accelerates dust grains to ≈10-–100 m s^{-1} [28] and a collision with the wall can direct the grain toward the core where it is rapidly charged. Figure 7(*a*) demonstrates a relaxation of charging currents (1 μm carbon grain and $n = 10^{18}\,\mathrm{m}^{-3}$ are assumed) after abrupt changes of the plasma temperature.

The calculation starts at $t = 0$ with a plasma temperature of 500 eV. The grain is slightly positive at this temperature.

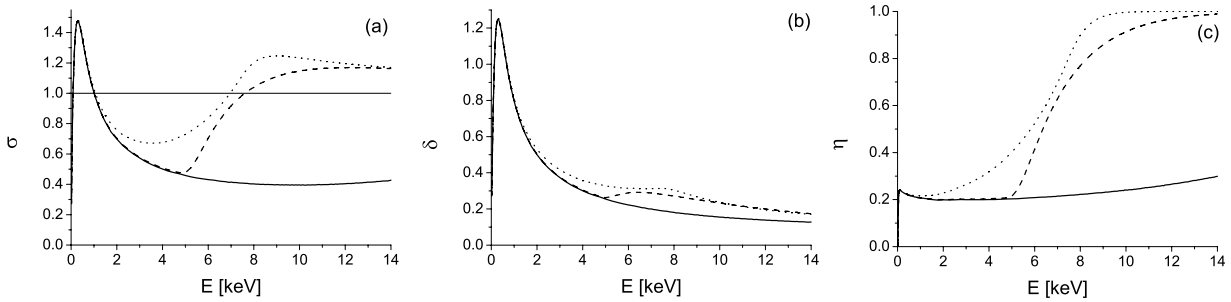

Figure 9. The total (*a*), true (*b*) and backscattered (*c*) yields for a 10 μm glassy carbon grain (solid), 1 μm glassy carbon grain (dotted), and glassy carbon flake with the thickness of 0.5 μm and the mass of 10 μm grain (dashed).

At $t = 10$ ns, the temperature was changed to 1 keV, then to 2 keV at $t = 60$ ns and, finally, back to 500 eV at $t = 160$ ns. The figure shows a competition between electron and SEE currents, with a relaxation time of about 10 ns. The resulting floating potential of the grain (figure 7(*b*)) is set within a 50 ns to the equilibrium level corresponding to the given plasma temperature (see figure 4). Since both major currents are directly proportional to the plasma density, the relaxation time would be shorter in a denser plasma. The calculations were carried out for a 1 μm grain, and the charging currents are proportional to the square of its radius, whereas the grain capacitance is directly proportional to the grain radius. This means that the relaxation time is inversely related to the grain size (a spherical grain is assumed).

These estimations show that the floating potential of dust grains moving toward the core would always be close to its equilibrium value corresponding to the local plasma temperature. On the other hand, when the heating of the grain is much slower, the corresponding time constants are of the order of milliseconds for 1 μm grains from the tokamak-relevant materials and the heat flux of 5×10^6 W m^{-2} [14]. Moreover, the heating of small grains would be even slower if the enhanced thermal radiation of small conductive grains is taken into account [55]. Consequently, we can conclude that the dust grains can reach the core plasma under conditions where their floating potential is determined by SEE. The size distribution of dust grains is very broad, the grains in the core plasma are quickly sputtered by energetic ions, and their dimensions affect the floating potential accordingly. Figure 8 shows the floating potential of a carbon grain immersed into the hydrogen plasma with a temperature of 1 keV as a function of the grain diameter. The figure shows that the negative potential depends only weakly on the grain size above $\approx$0.5 μm. We would like to point out that the corresponding specific charge of such grains is of the order of tens C kg^{-1}, thus, the electromagnetic forces are important for their dynamics.

3.2. The influence of grain shape

We expected spherical grains in calculations but the SEM analysis has shown that a spherical shape is more of an exception than a rule. Nevertheless, the modeling of SEE from the grains of irregular shapes and various surface roughness [46] has shown that the SEE yield of an irregular grain is determined by its smallest dimension. Since all other currents (except the field emission current) are proportional to the surface area and do not depend on the shape of a particular grain, we can expect that, for example, a thin flake would be charged to a potential similar to that of the spherical grain with diameter equal to the flake thickness. The influence of the grain shape illustrates figure 9 that presents the SEE yields of a 10 μm carbon sphere and compares them with the yields of a flake with the same mass but only 0.5 μm thick. A comparison in figure 9 reveals that the yields of the flake exhibit very similar profiles to those of the $\approx$1 μm spherical grain from the same material. Consequently, we can conclude that positive charges of grains at high temperatures shown in figure 5 can be expected for a large portion of grains in tokamaks.

The effects of a surface roughness discussed in [46] are not important for charging of grains in a hot plasma because they are prominent only for low electron energies ($<$100 eV).

On the other hand, the field emission current grows exponentially with the electric field at the grain surface, which can be considered as an equipotential surface. The electric field, thus, peaks at different tips or spikes and the stabilization effects of the field emission currents on the negative grain potential shown in figure 5(*a*) should be considered as a lower estimate.

Finally, we have shown that a realistic description of the SEE yield from the dust grains is principal for an estimation of their floating potential in hot plasmas. Since the Sternglass formula that underestimates the SEE yield for dust grains is a part of widely used numerical codes (e.g. DTOKS, DUSTT), calculations of the dust dynamics within tokamaks using these codes should be taken with care.

Acknowledgments

This work was supported partly by the Czech Grant Agency under Contracts 209/11/1412 and 209/13/25185P, and partly by the Charles University (UNCE 204020/2012 and GAUK 1410213).

References

[1] Sharpe J P, Petti D A and Bartels H 2002 A review of dust in fusion devices: implications for safety and operational performance *Fusion Eng. Des.* **63–64** 153–63
[2] Loarte A *et al* and the ITPA Scrape-off Layer and Divertor Physics Topical Group 2007 Chapter 4: power and particle control *Nucl. Fusion* **47** S203

[3] Winter J 1998 Dust in fusion devices—experimental evidence, possible sources and consequences *Plasma Phys. Control. Fusion* **40** 1201

[4] Chappuis P, Tsitrone E, Mayne M, Armand X, Linke H, Bolt H, Petti D and Sharpe J 2001 Dust characterization and analysis in Tore-Supra *J. Nucl. Mater.* **290** 245–9

[5] Tanaka Y, Pigarov A Yu, Smirnov R D, Krasheninnikov S I, Ohno N and Uesugi Y 2007 Modeling of dust-particle behavior for different materials in plasmas *Phys. Plasmas* **14** 052504

[6] Goodall D H J 1982 High-speed cine film studies of plasma behavior and plasma surface interactions in tokamaks *J. Nucl. Mater.* **111** 11–22

[7] Rubel M, Cecconello M, Malmberg J A, Sergienko G, Biel W, Drake J R, Hedqvist A, Huber A and Philipps V 2001 Dust particles in controlled fusion devices: morphology, observations in the plasma and influence on the plasma performance *Nucl. Fusion* **41** 1087

[8] Saito K *et al* 2007 ICRF long-pulse discharge and interaction with a chamber wall and antennas in LHD *J. Nucl. Mater.* **363–365** 1323–8

[9] Grisolia C, Rosanvallon S, Loarte A, Sharpe P and Arnas C 2009 From eroded material to dust: an experimental evaluation of the mobilised dust production in Tore Supra *J. Nucl. Mater.* **390–391** 53–6

[10] Krasheninnikov S I, Smirnov R D and Rudakov D L 2011 Dust in magnetic fusion devices *Plasma Phys. Control. Fusion* **53** 083001

[11] Sharpe J P, Humrickhouse P W, Skinner C H, Tanabe T, Masaki K, Miya N and Sagara A 2005 Characterization of dust collected from NSTX and JT-60U *J. Nucl. Mater.* **337–339** 1000–4

[12] Roth J *et al* 2009 Recent analysis of key plasma wall interactions issues for ITER *J. Nucl. Mater.* **390–391** 1–9

[13] Federici G *et al* 2001 Plasma-material interactions in current tokamaks and their implications for next step fusion reactors *Nucl. Fusion* **41** 1967

[14] Krasheninnikov S I, Tomita Y, Smirnov R D and Janev R K 2004 On dust dynamics in tokamak edge plasmas *Phys. Plasmas* **11** 3141–50

[15] Krasheninnikov S I *et al* and the LHD Experimental Group 2008 Recent progress in understanding the behavior of dust in fusion devices *Plasma Phys. Control. Fusion* **50** 124054

[16] Smirnov R D, Krasheninnikov S I, Pigarov A Yu, Benson D J, Rosenberg M and Mendis D A 2009 Modeling of velocity distributions of dust in tokamak edge plasmas and dust–wall collisions *J. Nucl. Mater.* **390–391** 84–7

[17] Joy D C 1987 A model for calculating secondary and backscattered electron yields *J. Microsc.* **147** 51–64

[18] Shimizu R and Ding Z-J 1992 Monte Carlo modelling of electron-solid interactions *Rep. Prog. Phys.* **55** 487–531

[19] Dubus A, Dehaes J-C, Ganachaud J-P, Hafni A and Cailler M 1993 Monte Carlo evaluation of the influence of the interaction cross sections on the secondary-electron-emission yields from polycrystalline aluminum targets *Phys. Rev.* B **47** 11056–73

[20] Renoud R, Mady F, Attard C, Bigarré J and Ganachaud J-P 2004 Secondary electron emission of an insulating target induced by a well-focused electron beam—Monte Carlo simulation study *Phys. Status Solidi* a **201** 2119–33

[21] Woods M E, Hopkins B J, Matthews G F, McCracken G M, Sewell P M and Fahrang H 1987 An investigation of the secondary-electron emission of carbon samples exposed to a hydrogen plasma *J. Phys. D: Appl. Phys.* **20** 1136

[22] Pedgley J M and McCracken G M 1993 Plasma sheath properties calculated using measured secondary electron emission coefficients *Plasma Phys. Control. Fusion.* **35** 397

[23] Pigarov A Y, Krasheninnikov S I, Soboleva T K and Rognlien T D 2005 Dust-particle transport in tokamak edge plasmas *Phys. Plasmas* **12** 122508

[24] Martin J D, Bacharis M, Coppins M, Counsell G F and Allen J E 2008 Modelling dust transport in tokamaks *Europhys. Lett.* **83** 65001

[25] Allen J E 1992 Probe theory—the orbital motion approach *Phys. Scr.* **45** 497

[26] Tsytovich V N 1997 Dust plasma crystals, drops, and clouds *Phys.—Usp.* **40** 53–94

[27] Smirnov R D, Pigarov A Y, Rosenberg M, Krasheninnikov S I and Mendis D A 2007 Modelling of dynamics and transport of carbon dust particles in tokamaks *Plasma Phys. Control. Fusion.* **49** 347–71

[28] Bacharis M, Coppins M and Allen J E 2010 Dust in tokamaks: an overview of the physical model of the dust in tokamaks code *Phys. Plasmas* **17** 042505

[29] Bacharis M, Coppins M, Fundamenski W and Allen J E 2012 Modelling of tungsten and beryllium dust in ITER *Plasma Phys. Control. Fusion* **54** 085010

[30] Filippov A V and Derbenev I N 2009 Microparticle charge screening in non-equilibrium plasmas with two types of positive ions *Contrib. Plasma Phys.* **49** 769–80

[31] Gunn J P 2012 Evidence for strong secondary electron emission in the tokamak scrape-off layer *Plasma Phys. Control. Fusion* **54** 085007

[32] Liu J, Chen L, Mao A, Sun G and Duan P 2013 Charging, movement and lifetime characteristics of dust in magnetic fusion devices *Vacuum* **88** 177–81

[33] Sternglass E J 1957 Theory of secondary electron emission under electron bombardment *Scientific Paper* 6-94410-2-P9 (Pittsburgh: Westinghouse Research Laboratories) p 35

[34] Draine B T and Salpeter E E 1979 On the physics of dust grains in hot gas *Astrophys. J.* **231** 77–94

[35] Chow V W, Mendis D A and Rosenberg M 1993 Role of grain size and particle velocity distribution in secondary electron emission in space plasmas *J. Geophys. Res.* **98** 19065–76

[36] Richterová I, Pavlů J, Němeček Z and Šafránková J 2006 Model of secondary emission and its application on the charging of gold dust grains *Phys. Rev.* B **74** 235430

[37] Meyer-Vernet N 1982 'Flip-flop' of electric potential of dust grain in space *Astron. Astrophys.* **105** 98–106

[38] Chow V W, Mendis D A and Rosenberg M 1994 Secondary emission from small dust grains at high electron energies *IEEE Trans. Plasma Sci.* **22** 179–86

[39] Svestka J, Cermak I and Grün E 1993 Electric charging and electrostatic fragmentation of dust particles in laboratory *Adv. Space Res.* **13** 199–202

[40] Horanyi M 1996 Charged dust dynamics in the solar system *Annu. Rev. Astron. Astrophys.* **34** 383–418

[41] Čermák I, Grün E and Švestka J 1995 New results in studies of electric charging of dust particles *Adv. Space Res.* **15** 59–64

[42] Pavlů J, Richterová I, Němeček Z, Šafránková J and Čermák I 2008 Interaction between single dust grains and ions or electrons: laboratory measurements and their consequences for the dust dynamics *Faraday Discuss.* **137** 139–55

[43] Wang X, Horányi M and Robertson S 2010 Investigation of dust transport on the lunar surface in a laboratory plasma with an electron beam *J. Geophys. Res.* **115** A11102

[44] Pánek R *et al* 2006 Reinstallation of the COMPASS-D tokamak in IPP ASCR *Czech. J. Phys.* **56** B125–37

[45] Nemecek Z, Pavlu J, Safrankova J, Beranek M, Richterova I, Vaverka J and Mann I 2011 Lunar dust grain charging by electron impact: dependence of the surface potential on the grain size *Astrophys. J.* **738** 14

[46] Richterová I, Němeček Z, Beránek M, Šafránková J and Pavlů J 2012 Secondary emission from non-spherical dust

grains with rough surfaces: application to lunar dust *Astrophys. J.* **761** 108
[47] Jerab M, Vaverka J, Vysinka M, Nemecek Z and Safrankova J 2010 Relation of charging history to field ion emission from gold and carbon dust *IEEE Trans. Plasma Sci.* **38** 798–802
[48] Richterova I, Beranek M, Pavlu J, Nemecek Z and Safrankova J 2010 Electrons scattered inside small dust grains of various materials *Phys. Rev.* B **81** 075406
[49] Whipple E C 1981 Potentials of surfaces in space *Rep. Prog. Phys.* **44** 1197–250
[50] Lampe M 2001 Limits of validity for orbital-motion-limited theory for a small floating collector *J. Plasma Phys.* **65** 171–80
[51] Richterová I, Němeček Z, Šafránková J and Pavlů J 2004 A model of secondary emission from dust grains and its comparison with experiment *IEEE Trans. Plasma Sci.* **32** 617–22
[52] Richterová I, Němeček Z, Šafránková J, Pavlů J and Beránek M 2007 Secondary emission from glass grains: comparison of the model and experiment *IEEE Trans. Plasma Sci.* **35** 286–91
[53] Richterová I, Pavlů J, Němeček Z and Šafránková J 2008 An application of the dust grain charging model to determination of secondary electron spectra *Eur. Phys. J.* D **48** 375–81
[54] Martin J D, Coppins M and Counsell G F 2005 Motion and lifetime of dust grains in a tokamak plasma *J. Nucl. Mater.* **337–339** 114–8
[55] Rosenberg M, Smirnov R D and Pigarov A Y 2008 On thermal radiation from heated metallic dust grains *J. Phys. D: Appl. Phys.* **41** 015202